

Ministry of Education and Science of Ukraine
Scientific Council on Laser Physics and Laser Technologies of NASU, Ukraine
International Center «Institute of Applied Optics» of NASU, Ukraine
V. Lashkarev Semiconductor Physics Institute of NASU, Ukraine
G. Karpenko Physical Mechanical Institute of NASU, Ukraine
Representative Office «Polish Academy of Sciences» in Kiev, Poland
Riga Technical University, Latvia
Lviv Polytechnic National University, Ukraine
University of Rzeszow, Poland
Ivan Franko Drohobych State Pedagogical University, Ukraine

MATERIALS

**OF INTERNATIONAL SCIENTIFIC
AND TECHNICAL CONFERENCE**

**LASER TECHNOLOGIES. LASERS
AND THEIR APPLICATION
LTLA-2019**

**June 11–13, 2019
Truskavets, Ukraine**

UDK 535.37(063)

BBK 22.3я43

M34

*Materials are recommended for publication by the Council on Science and
Technology at the International Center "Institute of Applied Optics"
National Academy of Sciences of Ukraine
(Protocol N 5 on 14 May 2019)*

Laser Technologies. Lasers and their Application (LTLA-2019):
Materials of International Scientific & Technical Conference. – Drohobych. –
2019. – 164 p.

ISBN 978-966-384-345-2

The book contains the abstracts of International Scientific and Technical Conference «Laser technologies. Lasers and their application» for such scientific topics:

- Physical and mathematical fundamentals of laser systems.
- Development of lasers and laser systems.
- Laser processing of materials.
- Laser deposition.
- Laser technical and technology applications.
- Lasers in nanotechnologies.
- Biomedical laser applications.

The book will be useful for scientists and post-graduate students working in the field of physics and technology of lasers and laser technologies.

Address of conference: Ivan Franko Drohobych State Pedagogical University, Institute of Physics, Mathematics, Economy and Innovation Technologies, 3 Stryjska Str., Drohobych, Lviv Region, 82100.

E-mail: laser-2019@ukr.net, isvirt@email.ua

Edited by
Dr. Sci., Prof. **V. Taranenko**,
Dr. Sci., Prof. **J. Cebulskii**
Dr. Sci., Prof. **I. Virt**

The abstracts are printed as submitted by authors

SCIENTIFIC PROGRAM COMMITTEE

Chairmen **prof. Taranenko V.** International Center «Institute of Applied Optics» of the NASU, Ukraine

Chairmen **prof. Cebulskii J.** University of Rzeszów, Poland

Chairmen **prof. Virt I. I.** Franko Drohobych State Pedagogical University, Ukraine

prof. Bobitski Ya. Lviv Polytechnic National University, Ukraine

prof. Bilynskyi I. I. Franko Drohobych State Pedagogical University, Ukraine

prof. Druzhinin A. Lviv Polytechnic National University, Ukraine

prof. Duriagina Z. Lviv Polytechnic National University, Ukraine

prof. Fekeshgazi I. Uzhhorod National University, Ukraine

prof. Medvid' A. Riga Technical University, Latvia

prof. Muravskyy L. Karpenko Physico-Mechanical Institute of the NASU, Ukraine

prof. Sobchuk H. RO in Kiev «Polish Academy of Sciences», Poland

prof. Padlyak B. University of Zielona Gora, Poland

prof. Polovinko I. I. Franko Lviv National University, Ukraine

prof. Teterkin V. Lashkaryov V. Institute of Semiconductor Physics, NASU, Ukraine

prof. Vlokh R. Institute of Physical Optics of the NASU, Ukraine

prof. Wal A. University of Rzeszów, Poland

prof. Wnuk M. University of Rzeszów, Poland

ORGANIZING & LOCAL COMMITTEE

Prof. I. Virt – **chairmen** (UR), Dr. Yu. Pavlovskyy – **secretary** (DSPU), Dr. P. Potera – **secretary** (UR).

MEMBERS:

Dr. S. Adamiak (UR), Dr. V. Luzhetskyy (DSPU), Dr. R. Lymarenko (ICIAO), Dr. I. Petrycyn (DSPU), Dr. I. Stefaniuk (UR), B. Cieniek (UR), O. Didovska (DSPU), S. Frolov (ICIAO), V. Khabinskyy (DSPU), Yu. Tur (DSPU), M. Vovchansky (DSPU).

CONTACT ADDRESS To:

Prof. I. Virt, Institute of Physics, Mathematics, Economy and Innovation Technologies, 3 Stryiska Str, Drohobych, 82100, Ukraine.

E-mail: laser-2019@ukr.net, isvirt@email.ua

Web-site: <http://drohobych.net/ddpu/>

PROGRAM
SCIENTIFIC AND TECHNICAL CONFERENCE
«LASER TECHNOLOGIES. LASERS AND THEIR APPLICATION»
LTLA-2019

June 11-13, 2019 Truskavets, Ukraine
(Conference-hall of Beskyd Hotel)

11.06.2019 Tuesday

10⁰⁰-10¹⁰ OPENING CEREMONY

PLENARE LECTURE		
1. Physical and mathematical fundamentals of laser systems		
2. Development of lasers and laser systems		
<i>Chairman prof. A. Suchocki</i>		
10¹⁵-11³⁰	1 TuP 10 ¹⁵ -10 ⁴⁰	R. Lymarenko ¹ , D. Gailevicius ² , V. Purlys ² , M. Peckus ² K. Staliunas ³ , V. Taranenko ¹ . MICROCHIP LASER WITH INTRACAVITY CIRCULAR GRATING. ¹ International center "Institute of Applied Optics" NAS of Ukraine, Ukraine, ² Laser Research Center, Vilnius University, Lithuania, ³ Universitat Politècnica de Catalunya, Spain
	1TuP 10 ⁴⁰ -11 ⁰⁵	V. Mitsa ¹ , A. Feher ² , V. Tkáč ² , R. Holomb ^{1,3} , M. Veres ³ , B.Matyashovska ¹ . THERMAL CONDUCTIVITY AT LOW TEMPERATURE OF OPTICAL MATERIALS FOR IR LASERS BASED ON WIDE GAP CHALCOGENIDE GLASSES. ¹ Uzhhorod National University, Ukraine, ² Pavol Jozef Šafárik University in Košice Slovak Republic, ³ Wigner Research Centre for Physics of the Hungarian Academy of Sciences, Budapest, Hungary
	1 TuP 11 ⁰⁵ -11 ³⁰	M. Kosmyna, A. Shekhovtsov. GROWTH AND PROPERTIES OF DISORDERED BORATE SINGLE CRYSTALS FOR LASER APPLICATION. <i>Institute for Single Crystals of the NAS of Ukraine, Ukraine</i>
11 ³⁰ -12 ⁰⁰ Coffee break		
<i>Chairman prof. V. Taranenko</i>		
12⁰⁰-14⁰⁵	1 TuP 12 ⁰⁰ -12 ²⁵	A. Czitrovszky ¹ , M. Veresh ¹ , R. Holomb ¹ , I. Rigo ¹ , I. Fekeshgazi ² , V. Mitsa ² . ABSORPTION SPECTRA OF SOLID OPTICAL FILTERS. ¹ Vigner Center for Physical Investigation of HAS, Budapest, Hungary, ² Ushhorod National University, Ushhorod, Ukraine
	1 TuP 12 ²⁵ -12 ⁵⁰	B. Padlyak ^{1,2} , I. Kindrat ¹ . EFFECT OF THE Ag IMPURITY ON LUMINESCENT AND LASER PROPERTIES OF THE Re ³⁺ IONS IN BORATE GLASSES. ¹ University of Zielona Góra Poland, ² Vlokh Institute of Physical Optics, Lviv, Ukraine
	1 TuP 12 ⁵⁰ -13 ¹⁵	S. Pokutnyi. EXCITON QUASIMOLECULES IN NANOHETEROSYSTEMS CONTAINING SEMICONDUCTOR AND DIELECTRIC QUANTUM DOTS: THEORY. <i>Chuiko Institute of Surface Chemistry, NAS of Ukraine, Ukraine</i>
	1 TuP 13 ¹⁵ -13 ⁴⁰	A. Suchocki. HIGH PRESSURE STUDIES OF PHOSPHOR MATERIALS INSTITUTE OF PHYSICS. <i>Institute of Physics, Polish Academy of Sciences, Poland Kazimierz Wielki University, Bydgoszcz, Poland</i>

	1 TuP 13 ⁴⁰ -14 ⁰⁵	<u>O. Gomonnai</u> ^{1,2} , M. Ludemann ³ , A. Gomonnai ^{1,4} , A. Slivka ¹ , I. Roman ⁴ , D. Zahn ³ . TEMPERATURE-DEPENDENT RAMAN STUDIES OF LAYERED TlIn(S _{1-x} Se _x) ₂ (0 ≤ x ≤ 0.25) SINGLE CRYSTALS. ¹ <i>Uzhhorod National University, Ukraine</i> , ² <i>Vlokh Institute of Physical Optics, Lviv, Ukraine</i> , ³ <i>Chemnitz University of Technology, Germany</i> , ⁴ <i>Institute of Electron Physics NASU, Uzhhorod, Ukraine</i>
14 ⁰⁵ –14 ⁴⁰ Lunch break		
SESSION		
1. Physical and mathematical fundamentals of laser systems		
2. Development of lasers and laser systems		
<i>Chairman prof. O. Melnichuk</i>		
14⁴⁰-15⁵⁰	2 TuP 14 ⁴⁰ -15 ⁰⁵	<u>I. Stefaniuk</u> . X- AND Q-BAND ELECTRON PARAMAGNETIC RESONANCE SPECTROSCOPY OF CO-DOPED YAP CRYSTAL. <i>University of Rzeszow, Poland</i>
	2 TuS 15 ⁰⁵ -15 ²⁰	<u>S. Ilchenko</u> , R. Lymarenko, V. Taranenko. ANGULAR SELECTIVE MULTILAYER DIELECTRIC STRUCTURE. <i>International Center "Institute of Applied Optics" NAS of Ukraine, Ukraine</i>
	2 TuS 15 ²⁰ -15 ³⁵	<u>A. Ostroukh</u> , R. Lymarenko, V. Taranenko. DEVELOPMENT OF COMPACT ENERGY-EFFICIENT PULSE LASERS ON CERAMICS FOR LAND-BASED AND SPACE-BASED LASER POSITIONING SYSTEMS. <i>International Center "Institute of Applied Optics" NAS of Ukraine, Ukraine</i>
	2 TuS 15 ³⁵ -15 ⁵⁰	<u>R. Lymarenko</u> ¹ , D. Gailevicius ² , V. Purlys ² , M. Peckus ² , K. Staliunas ³ , V. Taranenko ¹ . SUPER-COLLIMATION BY CIRCULAR GRATING PAIR. ¹ <i>International center "Institute of Applied Optics" NAS of Ukraine, Ukraine</i> , ² <i>Laser Research Center, Vilnius University, Lithuania</i> , ³ <i>Universitat Politècnica de Catalunya, Spain</i>
15 ⁵⁰ –16 ²⁰ Coffee break		
SESSION		
1. Physical and mathematical fundamentals of laser systems		
2. Development of lasers and laser systems		
<i>Chairman prof. A. Kul'ment'ev</i>		
16²⁰-17³⁵	1 TuS 16 ²⁰ -16 ³⁵	<u>I. Kindrat</u> ¹ , B. Padlyak ^{1,2} , R. Lisiecki ³ , V. Adamiv ² , I. Teslyuk ² . LUMINESCENCE PROPERTIES OF THE Tm ³⁺ -DOPED LiKB ₄ O ₇ GLASS. ¹ <i>University of Zielona Góra, Poland</i> , ² <i>Vlokh Institute of Physical Optics, Lviv, Ukraine</i> , ³ <i>Institute of Low Temperature and Structure Research of the Polish Academy of Sciences, Wrocław, Poland</i>
	1 TuS 16 ³⁵ -16 ⁵⁰	<u>V. Popovych</u> ¹ , P. Potera ² , M. Kuzma ² . INFRARED OPTICAL EXTINCTION IN HEAVILY DOPED CdTe:Cr SINGLE CRYSTALS. ¹ <i>Ivan Franko Drogobych State Pedagogical University, Ukraine</i> , ² <i>University of Rzeszow, Poland</i>
	2 TuS 16 ⁵⁰ -17 ⁰⁵	<u>Ye. Krasnoshchekov</u> , V. Yaparov, V. Taranenko. LASER EMITTING BEAM WITH ROTATING VORTICES. <i>International center "Institute of Applied Optics" NAS of Ukraine, Ukraine</i>
	2 TuS 17 ⁰⁵ -17 ²⁰	<u>O. Banzak</u> , G. Banzak. SIMULATION OF INSTRUMENTAL SPECTRA CdZnTe-DETECTORS FOR MEASURING THE INTRINSIC GAMMA- RADIATION OF SPENT NUCLEAR FUEL. <i>Odessa state academy of technical regulation and quality, Ukraine</i>

	2 TuS 17 ²⁰ -17 ³⁵	<u>H. Sobczuk</u> . POLISH SCIENTIFIC COOPERATION WITH UKRAINE. <i>Representative office „Polish Academy of Sciences in Kiev”, Polish Academy of Sciences, Poland</i>
POSTER SESSION 17³⁵-18³⁵ <i>Chairman prof. I. Stefaniuk</i>		
17 ³⁵ - 18 ³⁵	Topics 1 POSTER	<u>V. Hols'kyi</u> . ELECTRON IN MOLECULE OF THREE QUANTUM DOTS. <i>Drohobych Ivan Franko State Pedagogical University, Ukraine</i>
	Topics 2 POSTER	<u>O. Konoreva</u> ¹ , P. Lytovchenko ¹ , Yu. Pavlovskyy ² , V. Tartachnyk ¹ , V. Shlapatska ³ . APPLICATION OF THE POSITRON ANNIHILATION METHOD WITH PURPOSE IDENTIFY COMPLICATED STRUCTURE DAMAGE IN IRRADIATED GaP AND InP CRYSTALS. ¹ <i>Institute for Nuclear Research, NAS of Ukraine</i> , ² <i>Drohobych Ivan Franko State Pedagogical University</i> , ³ <i>L. Pisarzhevski Physical Chemistry Institute NAS of Ukraine</i>
	Topics 3 POSTER	H. Czyż, <u>P. Ciupak</u> , P. Sarzyńska, A. Barłowski, T. Jasiński. INTERACTION OF LASER BEAM OF YAG: ND ³⁺ LASER WITH BULK HEUSLER ALLOY. <i>Rzeszow University of Technology, Poland</i>
		<u>N. Pavlovska</u> ¹ , Yu. Pavlovskyy ² . NEW TECHNOLOGIES OF INCREASING THE RELIABILITY OF STRUCTURAL MATERIALS ¹ <i>Drohobych secondary school of I-III degrees №4, Drohobych, Ukraine</i> ² <i>Drohobych Ivan Franko State Pedagogical University, Ukraine</i>
		<u>Yu. Pavlovskyy</u> . INCREASING THE STRENGTH OF THE SURFACE OF MATERIALS BY LASER METHOD. <i>Drohobych Ivan Franko State Pedagogical University, Ukraine</i>
	Topics 4 POSTER	<u>Yu. Tur</u> , I. Virt. PULSE LASER DEPOSITION OF THIN CHALCOGENIDE FILMS OF LEAD. <i>Drohobych State University, Ukraine</i>
		T. Jasiński, <u>A. Barłowski</u> , P. Ciupak, M. Kuźma. ELECTRICAL PROPERTIES OF THIN LAYERS OF Ni ₂ MnIn OBTAINED BY PLD METHOD. <i>Rzeszow University of Technology, Poland</i>
		<u>B. Cieniek</u> ¹ , I. Stefaniuk ¹ , I. Virt ^{1,2} , I. Rogalska ¹ . STUDY OF ZnO THIN FILMS ON A QUARTZ AND SAPPHIRE SUBSTRATE DEPOSITED BY THE PLD METHOD MEASURED BY MEANS OF ELECTRON PARAMAGNETIC RESONANCE. ¹ <i>University of Rzeszow, Poland</i> , ² <i>Drohobych Ivan Franko State Pedagogical University, Ukraine</i>
		<u>Yu. Pavlovskyy</u> , I. Virt. TECHNOLOGY OF OBTAINING NANO CARBON FILMS BY LASER METHOD. <i>Drohobych Ivan Franko State Pedagogical University, Ukraine</i>
	Topics 5 POSTER	<u>I. Petricin</u> . APPLICATION OF LASERS IN SCIENCE AND TECHNOLOGY. <i>Drohobych State Pedagogical University, Ukraine</i>

18³⁵ - Dinner scientific discussion

12.06.2019 Wednesday

PLENARE LECTURE 3. Laser processing of materials 5. Laser technical and technology applications <i>Chairman prof. O. Gomonnai</i>		
10⁰⁰-12⁰⁵	3 WeP 10 ⁰⁰ -10 ²⁵	<u>M. Kuzma</u> . LASER MELTING OF POWDER METALS AT 3D PRINTING. <i>Uniwersity of Rzeszow, Poland</i>
	3 WeP 10 ²⁵ -10 ⁵⁰	<u>A. Kul'ment'ev</u> , A. Polishchuk. IN-LINE X-RAY PHASE CONTRAST IMAGING AND WELD POOL DYNAMICS FOR LASER WELDING OF PURE ALUMINIUM. <i>Institute of Applied Physics NAS of Ukraine, Sumy, Ukraine</i>
	5 WeP 10 ⁵⁰ -11 ¹⁵	Ye. Venger ¹ , N. Korsunsk ¹ , L. Melnichuk ² , <u>O. Melnichuk</u> ² , L. Khomenkova ¹ . INVESTIGATION OF PLASMON-PHONON INTERACTION IN THE INFRARED SPECTRAL RANGE FOR THIN TB-DOPED ZNO FILMS GROWN ON SiO ₂ SUBSTRATES ¹ V. Lashkaryov Institute of Semiconductor Physics of NAS of Ukraine, Ukraine, ² Mykola Gogol State University of Nizhyn, Ukraine
	5 WeP 10 ¹⁵ -11 ⁴⁰	<u>L. Muravsky</u> , O. Kuts. VISUALIZATION OF SUBSURFACE DEFECTS IN COMPOSITE STRUCTURES USING SPECKLE INTERFEROGRAMS AND DYNAMIC SPECKLE PATTERNS. <i>Karpenko Physico-Mechanical Institute of NAS of Ukraine, Ukraine</i>
	5 WeP 11 ⁴⁰ -12 ⁰⁵	<u>B. Mytsyk</u> ¹ , A. Andrushchak ² , N. Demyanyshyn ¹ , Ya. Kost ¹ . LASER CONOSCOPIC METHOD FOR INVESTIGATION OF PHOTOELASTICITY OF CRYSTALS. ¹ Karpenko Physico-Mechanical Institute NAS of Ukraine, ² Lviv Polytechnic National University, Ukraine
12 ⁰⁵ –12 ³⁵ Coffee break PLENARE LECTURE, SESSION 3. Laser processing of materials 5. Laser technical and technology applications <i>Chairman prof. B. Padlyak</i>		
12³⁵-14³⁰	5 WeP 12 ³⁵ -13 ⁰⁰	<u>V. Zemlyanskij</u> , M. Gusev, O. Zakrevskiy. THE MULTIWAVE LASER MEASUREMENT OF THE CRYOGENIC LIQUIDS FLOW. <i>National Aviation University, Ukraine</i>
	3 WeS 13 ⁰⁰ -13 ¹⁵	<u>D. Lesyk</u> ¹ , S. Martinez ² , B. Mordyuk ³ , V. Dzhemelinskyi ¹ , A. Lamikiz ² , G. Prokopenko ³ . IMPROVEMENT OF THE SURFACE PROPERTIES OF SLM-FABRICATED PARTS BY POST-PROCESSING. ¹ National Technical University of Ukraine "Igor Sikorsky Kyiv Polytechnic Institute", Ukraine, ² Aeronautics Advanced Manufacturing Center, University of the Basque Country, Zamudio, Spain, ³ Kurdyumov Institute for Metal Physics of the NAS of Ukraine, Ukraine
	5 WeS 13 ¹⁵ -13 ³⁰	V. Adamiv ¹ , <u>R. Gamernyk</u> ² , S. Malynych ^{3,4} . LASER STIMULATED Ag NANOPARTICLES GRATING FORMATION ON THE SURFACE OF Li ₂ B ₄ O ₇ –Ag ₂ O GLASS. ¹ O.G.Vlokh Institute of Physical Optics, ² Ivan Franko National University of Lviv, ³ National

		<i>University "Lviv Polytechnic", ⁴Hetman Petro Sahaidachnyi National Army Academy, Lviv, Ukraine</i>
5 WeS 13 ³⁰ -13 ⁴⁵		<u>J. Gradauskas</u> ^{1,2} , S. Ašmontas ¹ , A. Sužiedėlis ¹ , A. Šilėnas ¹ , E. Širmulis ¹ , A. Čerškus ^{1,2} , V. Švedas ¹ , V. Vaičiškauskas ¹ , O. Žalys ¹ , A. Opanasyuk ³ . LASER ASSISTED HOT CARRIER EVIDENCE IN SOLAR CELLS. ¹ Center for Physical Sciences and Technology, Vilnius, Lithuania, ² Vilnius Gediminas Technical University, Lithuania, ³ Sumy State University, Ukraine
5 WeS 13 ⁴⁵ -14 ⁰⁰		<u>S. Schukin</u> ¹ , S. Frolov ¹ , R. Lymarenko ¹ , L. Litvinuk ² , V. Taranenko ¹ . DETERMINATION OF THE CHEMICAL ELEMENTS IN THE SOIL BY LASER-INDUCED BREAKDOWN SPECTROSCOPY. ¹ International Center "Institute of Applied Optics" NAS of Ukraine, ² Nat. Scientific Center "Institute of Mechanization and Electrification of Agriculture" NAS of Ukraine, Ukraine
5 WeS 14 ⁰⁰ -14 ¹⁵		V. Zemlianski, M. Gusev, <u>A. Ovenko</u> . LASER DEVICE FOR MEASUREMENT OF ANGLES ATTACK AND SIDE SLIP (LDASS) OF AIRCRAFT. National Aviation University, Ukraine
5 WeS 14 ¹⁵ -14 ³⁰		V. Zemlianski, M. Gusev, S. Yegorov, <u>S. Poliak</u> . LASER FLOWMETER FOR OPTICALLY ACTIVE LIQUID-LUBRICANT MATERIALS. National Aviation University, Ukraine
14 ³⁰ -15 ¹⁵ Lunch break		
15 ¹⁵ -20 ¹⁵ Excursion		

13.06.2019 Thursday

PLENARE LECTURE		
6. Lasers in nanotechnologies		
7. Biomedical laser applications		
<i>Chairman prof. M. Kuzma</i>		
10⁰⁰-12⁰⁵	6 ThP 10 ⁰⁰ -10 ²⁵	<u>L. Fedorenko</u> , A. Evtukh, V. Naumov. LASER-STIMULATED PROCESSES OF NANOSTRUCTURING OF THE SURFACE OF A SOLID. CURRENT STATE AND PROSPECTS. V.E. Lashkaryov ISP NAS of Ukraine, Ukraine
	6 ThP 10 ²⁵ -10 ⁵⁰	<u>Y. Shopa</u> ¹ , D. Jakubczyk ² , M. Woźniak ² , G. Derkachov ² , K. Kolwas ² , K. Piekarski ³ . DYNAMIC LIGHT SCATTERING ON EVAPORATING MICRODROPLET OF SUSPENSION WITH NANOSPHERES. ¹ Cardinal Stefan Wyszyński University in Warsaw, Poland, ² Institute of Physics, Polish Academy of Sciences, Warsaw, Poland, ³ Białystok University of Technology, Poland
	6 ThP 10 ⁵⁰ -11 ¹⁵	<u>I. Stolyarchuk</u> , A. Stolyarchuk, I. Hadzaman. STRUCTURAL AND OPTICAL PROPERTIES OF COBALT AND CHROMIUM DOPED ZnO NANOSTRUCTURES GENERATED BY PULSED LASER ABLATION IN LIQUIDS. Drohobych Ivan Franko State Pedagogical University, Ukraine
	7 ThP 11 ¹⁵ -11 ⁴⁰	<u>M. Cholewa</u> ¹ , A. Banaś ² , J. Cebulski ¹ , M. Obrzut ² , I. Zawlik ² . DEVELOPMENT AND APPLICATIONS OF LASER TECHNIQUES IN BIOLOGY AND MEDICINE. ¹ Faculty of Mathematics and Natural

		<i>Sciences, The University of Rzeszow, Rzeszow, Poland, ²Faculty of Medicine, The University of Rzeszow, Rzeszow, Poland</i>
	7 ThP 11 ⁴⁰ -12 ⁰⁵	<u>I. Bilynskyi</u> , R. Leshko. ELECTRICAL AND OPTICAL PROPERTIES OF THE ARRAYS DIFFERENT FORM QUANTUM DOT. <i>Ivan Franko State Pedagogical University, Ukraine</i>
12 ⁰⁵ -12 ³⁵ Coffee break		
SESSION		
6. Lasers in nanotechnologies		
7. Biomedical laser applications		
<i>Chairman prof. Y. Shopa</i>		
12³⁵ - 13⁴⁵	6 ThS 12 ³⁵ -12 ⁵⁰	Yu. Azhniuk ^{1,2} , V. Lopushansky ¹ , V. Loya ¹ , <u>A. Gomonnai</u> ^{1,2} , D. Zahn ³ . SPECTROSCOPIC STUDY OF LASER-INDUCED FORMATION OF CdSe NANOCRYSTALS IN Cd-DOPED As ₂ Se ₃ FILMS. ¹ <i>Institute of Electron Physics NAS of Ukraine, Uzhhorod, Ukraine, ²Uzhhorod National University, Ukraine, ³Semiconductor Physics, Chemnitz University of Technology, Germany</i>
	7 ThS 12 ⁵⁰ -13 ⁰⁵	<u>Kul'ment'eva O.P.</u> ¹ , Kul'ment'ev A. ^{1,2} APPLICATION OF "SOFT LASERS" IN MEDICINE ¹ Ukrainian branch BIONET, concern BIYOVIS, Hungary, ² Institute of Applied Physics, Sumy, Ukraine
PLENARE LECTURE, SESSION		
4. Laser deposition		
<i>Chairman prof. L. Fedorenko</i>		
	4 ThP 13 ⁰⁵ -13 ³⁰	<u>I. Virt</u> ^{1,2} , S. Adamiak ² , B. Cieniek ² , A. Dziedzic ² , P. Potera ² , D. Zak ² . PULSED LASER TECHNIQUES FOR DEPOSITING NANOCARBON MATERIALS. ¹ <i>Drogobych State Pedagogical University, Drohobych, Ukraine, ²University of Rzeszow, Rzeszow, Poland</i>
	4 ThS 13 ³⁰ -13 ⁴⁵	<u>P. Potera</u> ¹ , I. Virt ^{1,2} , G. Wisz ¹ , B. Cieniek ¹ . OPTICAL PROPERTIES OF ZnO:TM (TM = Cr, Mn, Co) LAYERS OBTAINED BY PLD METHOD. ¹ <i>University of Rzeszow, Poland, ²Drogobych State Pedagogical University, Ukraine</i>

13⁴⁵-14⁰⁰ CLOSING

P – PLENARE LECTURE

S – SESSION

Tu – Tuesday

We – Wednesday

Th – Thursday

CONTENTS

SECTION 1. PHYSICAL AND MATHEMATICAL FUNDAMENTALS OF LASER SYSTEMS

A. Czitrovszky, M. Veresh, R. Holomb, I. Rigo, I. Fekeshgazi, V. Mitsa ABSORPTION SPECTRA OF SOLID OPTICAL FILTERS.....	16
O. Gomonnai, M. Ludemann, A. Gomonnai, A. Slivka, I. Roman, D. Zahn TEMPERATURE-DEPENDENT RAMAN STUDIES OF LAYERED TlIn(S _{1-x} Se _x) ₂ (0 ≤ x ≤ 0.25) SINGLE CRYSTALS.....	19
I. Kindrat, B. Padlyak, R. Lisiecki, V. Adamiv, I. Teslyuk LUMINESCENCE PROPERTIES OF THE Tm ³⁺ -DOPED LiKB ₄ O ₇ GLASS.....	22
O. Konoreva, P. Lytovchenko, Yu. Pavlovskyy, V. Tartachnyk, V. Shlapatska APPLICATION OF THE POSITRON ANNIHILATION METHOD WITH PURPOSE IDENTIFY COMPLICATED STRUCTURE DAMAGE IN IRRADIATED GaP AND InP CRYSTALS	25
M. Kosmyna, A. Shekhovtsov GROWTH AND PROPERTIES OF DISORDERED BORATE SINGLE CRYSTALS FOR LASER APPLICATION.....	29
V. Mitsa, A. Feher, V. Tkáč, R. Holomb, M. Veres, B. Matyashovska THERMAL CONDUCTIVITY AT LOW TEMPERATURE OF OPTICAL MATERIALS FOR IR LASERS BASED ON WIDE GAP CHALCOGENIDE GLASSES	32
B. Padlyak, I. Kindrat EFFECT OF THE Ag IMPURITY ON LUMINESCENT AND LASER PROPERTIES OF THE RE ³⁺ IONS IN BORATE GLASSES	35
S. Pokutnyi EXCITON QUASIMOLECULES IN NANOHETEROSYSTEMS CONTAINING SEMICONDUCTOR AND DIELECTRIC QUANTUM DOTS: THEORY	38
V. Popovych, P. Potera, M. Kuzma INFRARED OPTICAL EXTINCTION IN HEAVILY DOPED CdTe:Cr SINGLE CRYSTALS	41

I. Stefaniuk

X- And Q-BAND ELECTRON PARAMAGNETIC RESONANCE SPECTROSCOPY OF Co-DOPED YAP CRYSTAL	44
---------------------------------------------------------------------------------------------	----

A. Suchocki

HIGH PRESSURE STUDIES OF PHOSPHOR MATERIALS	47
---------------------------------------------------	----

SECTION 2. DEVELOPMENT OF LASERS AND LASER SYSTEMS**O. Banzak, G. Banzak**

SIMULATION OF INSTRUMENTAL SPECTRA CdZnTe-DETECTORS FOR MEASURING THE INTRINSIC GAMMA- RADIATION OF SPENT NUCLEAR FUEL	51
------------------------------------------------------------------------------------------------------------------------------------	----

S. Ilchenko, R. Lymarenko, V. Taranenko

ANGULAR SELECTIVE MULTILAYER DIELECTRIC STRUCTURE	54
---------------------------------------------------------	----

A. Ostroukh, R. Lymarenko, V. Taranenko

DEVELOPMENT OF COMPACT ENERGY-EFFICIENT PULSE LASERS ON CERAMIC FOR LASER-LOCATION SYSTEMS OF GROUND AND SPACE BASE	57
---------------------------------------------------------------------------------------------------------------------------------	----

**R. Lymarenko, D. Gailevicius, V. Purlys, M. Peckus, K. Staliunas,
V. Taranenko**

SUPER-COLLIMATION BY CIRCULAR GRATING PAIR	60
--------------------------------------------------	----

**R. Lymarenko, D. Gailevicius, V. Purlys, M. Peckus, K. Staliunas,
V. Taranenko**

MICROCHIP LASER WITH INTRACAVITY CIRCULAR GRATING	62
---------------------------------------------------------	----

Ye. Krasnoshchekov, V. Yaparov, V. Taranenko

LASER EMITTING BEAM WITH ROTATING VORTICES	65
--------------------------------------------------	----

SECTION 3. LASER PROCESSING OF MATERIALS**A. Kul'ment'ev, A. Polishchuk**

IN-LINE X-RAY PHASE CONTRAST IMAGING AND WELD POOL DYNAMICS FOR LASER WELDING OF PURE ALUMINIUM	69
----------------------------------------------------------------------------------------------------------	----

M. Kuzma

LASER MELTING OF POWDER METALS AT 3D PRINTING	72
-----------------------------------------------------	----

**D. Lesyk, S. Martinez, B. Mordyuk, V. Dzhemelinskyi, A. Lamikiz,
G. Prokopenko**

IMPROVEMENT OF THE SURFACE PROPERTIES OF SLM-FABRICATED PARTS BY POST-PROCESSING	74
-------------------------------------------------------------------------------------------	----

N. Pavlovska, Yu. Pavlovskyy NEW TECHNOLOGIES OF INCREASING THE RELIABILITY OF STRUCTURAL MATERIALS.....	77
Yu. Pavlovskyy INCREASING THE STRENGTH OF THE SURFACE OF MATERIALS BY LASER METHOD.....	80
H. Czyż, P. Sarzynska, P. Ciupak, A. Barlowski, P. Sagan, T. Jasinski INTERACTION OF LASER BEAM WITH Ni ₂ MnIn ALLOY	83

SECTION 4. LASER DEPOSITION

B. Cieniek, I. Stefaniuk, I. Virt, I. Rogalska STUDY OF ZnO THIN FILMS ON A QUARTZ AND SAPPHIRE SUBSTRATE DEPOSITED BY THE PLD METHOD MEASURED BY MEANS OF ELECTRON PARAMAGNETIC RESONANCE.....	86
Yu. Pavlovskyy, I. Virt TECHNOLOGY OF OBTAINING NANO CARBON FILMS BY LASER METHOD.....	89
P. Potera, I. Virt, G. Wysz, B. Cieniek OPTICAL PROPERTIES OF ZnO:TM (TM = Cr, Mn, Co) LAYERS OBTAINED BY PLD METHOD	92
Yu. Tur, I. Virt PULSE LASER DEPOSITION OF THIN CHALCOGENIDE FILMS OF LEAD	95
I. Virt, S. Adamiak, B. Cieniek, A. Dziedzic, P. Potera, D. Zak PULSED LASER TECHNIQUES FOR DEPOSITING NANOCARBON MATERIALS.....	98

SECTION 5. LASER TECHNICAL AND TECHNOLOGY APPLICATIONS

J. Gradauskas, S. Ašmontas, A. Sužiedėlis, A. Šilėnas, E. Širmulis, A. Čerškus, V. Švedas, V. Vaičiškauskas, O. Žalys, A. Opanasyuk LASER ASSISTED HOT CARRIER EVIDENCE IN SOLAR CELLS	102
L. Muravsky, O. Kuts VISUALIZATION OF SUBSURFACE DEFECTS IN COMPOSITE STRUCTURES USING SPECKLE INTERFEROGRAMS AND DYNAMIC SPECKLE PATTERNS	105

B. Mytsyk, A. Andrushchak, N. Demyanyshyn, Ya. Kost LASER CONOSCOPIC METHOD FOR INVESTIGATION OF PHOTOELASTICITY OF CRYSTALS	108
I. Petricin APPLICATION OF LASERS IN SCIENCE AND TECHNOLOGY	111
S. Schukin, S. Frolov, R. Lymarenko, L. Litvinuk, V. Taranenko DETERMINATION OF THE CHEMICAL ELEMENTS IN THE SOIL BY LASER-INDUCED BREAKDOWN SPECTROSCOPY	114
Ye. Venger, N. Korsunska, L. Melnichuk, O. Melnichuk, L. Khomenkova INVESTIGATION OF PLASMON-PHONON INTERACTION IN THE INFRARED SPECTRAL RANGE FOR THIN Tb-DOPED ZnO FILMS GROWN ON SiO ₂ SUBSTRATES	117
V. Zemlianski, DSc. M. Gusev, S. Yegorov, S. Poliak LASER FLOWMETER FOR OPTICALLY ACTIVE LIQUID- LUBRICANT MATERIALS	120
V. Zemlianski, DSc. M. Gusev, A. Ovenko LASER DEVICE FOR MEASUREMENT OF ANGLES ATTACK AND SIDE SLIP (LDASS) OF AIRCRAFT	123
V. Zemlianski, DSc. M. Gusev, O. Zakrevskyi THE MULTIWAVE LASER MEASUREMENT OF THE CRYOGENIC LIQUIDS FLOW	126

SECTION 6. LASERS IN NANOTECHNOLOGIES

V. Adamiv, R. Gamernyk, S. Malynych LASER STIMULATED Ag NANOPARTICLES GRATING FORMATION ON THE SURFACE OF Li ₂ B ₄ O ₇ –Ag ₂ O GLASS.....	130
Yu. Azhniuk, V. Lopushansky, V. Loya, A. Gomonnai, D. Zahn SPECTROSCOPIC STUDY OF LASER-INDUCED FORMATION OF CdSe NANOCRYSTALS IN Cd-DOPED As ₂ Se ₃ FILMS	133
I. Bilynskyi, R. Leshko ELECTRICAL AND OPTICAL PROPERTIES OF THE ARRAYS DIFFERENT FORM QUANTUM DOT	136
L. Fedorenko, A. Evtukh, V. Naumov LASER-STIMULATED PROCESSES OF NANOSTRUCTURING OF THE SURFACE OF A SOLID. CURRENT STATE AND PROSPECTS	139

V. Hols'kyi ELECTRON IN MOLECULE OF THREE QUANTUM DOTS	142
Shopa Y., Jakubczyk D., Woźniak M., Derkachov G., Kolwas K., Piekarski K. DYNAMIC LIGHT SCATTERING ON EVAPORATING MICRODROPLET OF SUSPENSION WITH NANOSPHERES	145
I. Stolyarchuk, A. Stolyarchuk, I. Hadzaman STRUCTURAL AND OPTICAL PROPERTIES OF COBALT AND CHROMIUM DOPED ZnO NANOSTRUCTURES GENERATED BY PULSED LASER ABLATION IN LIQUIDS	148
T. Jasinski, A. Barlowski, P. Ciupak, G. Wisz, M. Kuzma ELECTRICAL PROPERTIES OF THIN LAYERS OF Ni ₂ MnIn OBTAINED BY PLD METHOD	151

SECTION 7. BIOMEDICAL LASER APPLICATIONS

M. Cholewa, A. Banaś, J. Cebulski, M. Obrzut, I. Zawlik DEVELOPMENT AND APPLICATIONS OF LASER TECHNIQUES IN BIOLOGY AND MEDICINE	154
Kul'ment'eva O., Kul'ment'ev A. APPLICATION OF "SOFT LASERS" IN MEDICINE.....	158
ALPHABETICAL LIST.....	161

SECTION 1. PHYSICAL AND MATHEMATICAL FUNDAMENTALS OF LASER SYSTEMS

ABSORPTION SPECTRA OF SOLID OPTICAL FILTERS

A. Czitrovsky¹, M. Veres¹, R. Holomb¹, I. Rigo¹, I. Fekeshgazi², V. Mitsa²

¹ *Research Institute for Solid State Physics and Optics, Vigner Center for Physical Investigation of HAS, Konkoly Thege M. Str. 29-33, 1121 Budapest, Hungary*

² *Research Institute of Solid State Physics and Chemistry, Ushhorod National University, Ushhorod, Ukraine*

Introduction. At the heating of liquid or solid state substances its illuminate the light beams with temperature dependence continuous spectra such as shown oneself on Fig 1.

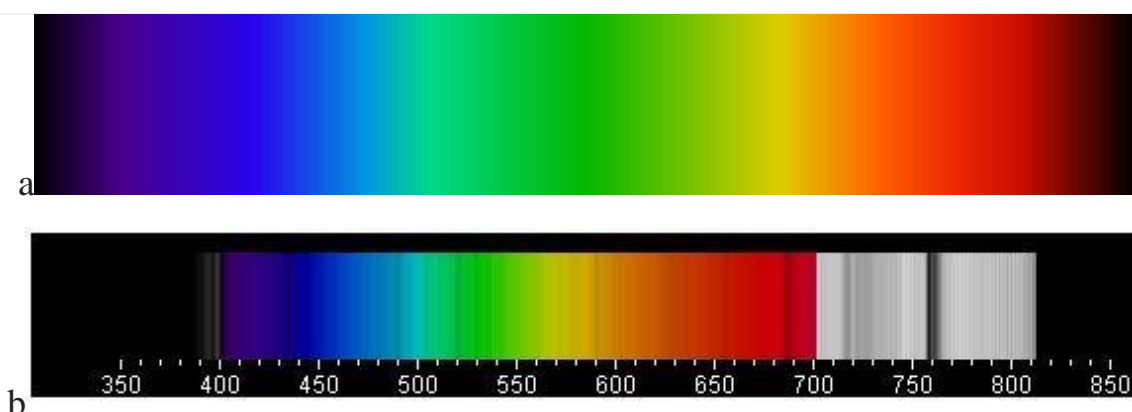


Fig 1. Continuous spectra of heated substances(a) and sunny(b).

For receiving the different colour light beam the combine of substance dispersion and mechanical systems or optical filters are used. The main properties of color glass filters, edge multicomponent and interference absorption spectra are discussed in the reports.

- The volume optical colour filters. In accordance with information from different catalogues the all optical filters are divided into four group [1-4]:

- Ultraviolet-violet (UG and VG) filters, with transmittance in 254-365 nm,
- Blue and green (BG and GG) filters, with transmittance in 400-550 nm (FIG. 2a);
- Yellow and orange (YG and OG) filters with transmittance in 580-600 nm;
- Red and Infrared (RG and IRG) filters with transmittance in 600-3000 nm (Fig. 2b).

Longpass (LP) and Shortpass (SP) filters are glass filter that attenuates shorter wavelengths and transmits (passes) longer wavelengths (LP) or attenuates longer wavelengths and transmits (passes) shorter wavelengths (SP) over the active range of the target spectrum filters. The combination of these filters give rise to constructed the Passband filters on necessary transmitted spectra.

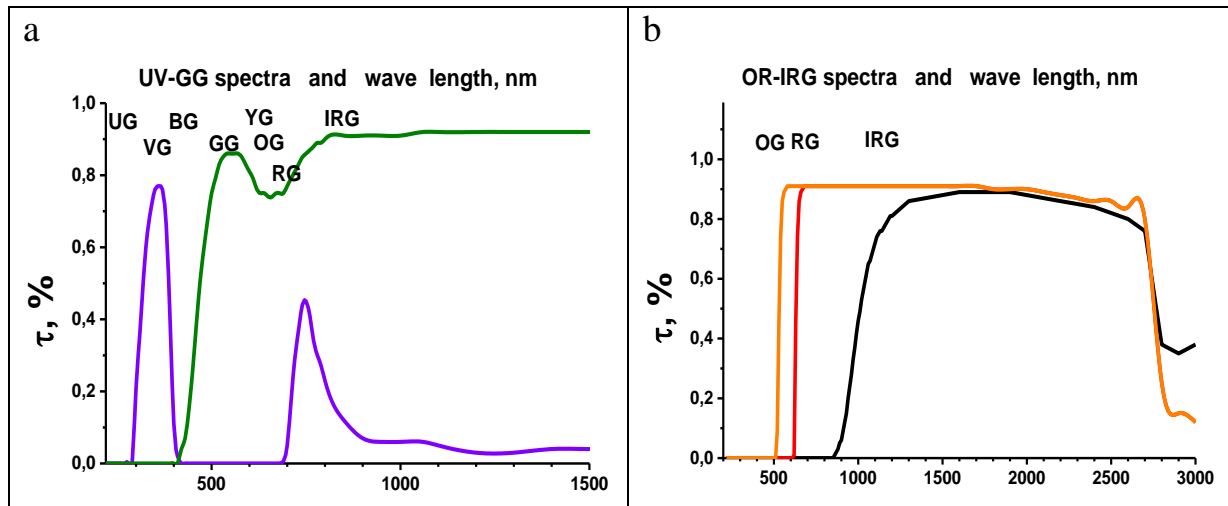
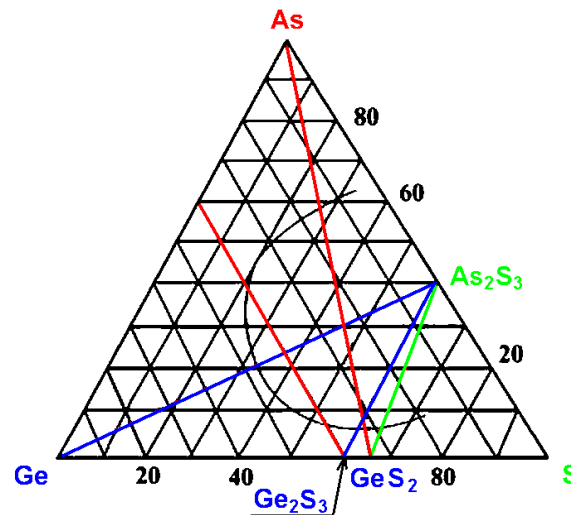


Fig. 2. Spectra of color glass filters UG (YΦC), VG(ΦC), BG(CC), GG(3C), OG(OC), RG(KC) and IRG(ИKC)

The color filters consist on transparent glasses from oxides SiO_2 , B_2O_3 , P_2O_5 , TeO_2 , GeO_2 with colored admixtures of violet NiO_2 and Mn_2O_5 , glue CuO_2 , green FeO and Fe_2O_3 , yellow SO_2 and Cr_2O_3 , red Cu_2O and Cr_2O_3 , brown V_2O_3 and V_2O_5 .

Edge multicomponent filters. The edge absorption ability of crystals and amorphous solids are often used as a long wave pass filters. The changing of $\text{CdS}_x\text{Se}_{1-x}$, $\text{ZnS}_x\text{Se}_{1-x}$, $\text{GeAs}_x\text{S}_{1-x}$ three component concentration permit the slow govern the spectra position of boundary between high and low transmittance regions. Fig 3.



Multilayer interference filters. The main advantages of interference consist in possibility receiving the sharp change of spectra that give rise to prepare narrow-band and edge filters for different transmittance and wavelength regions (Fig. 4a and 4b.)

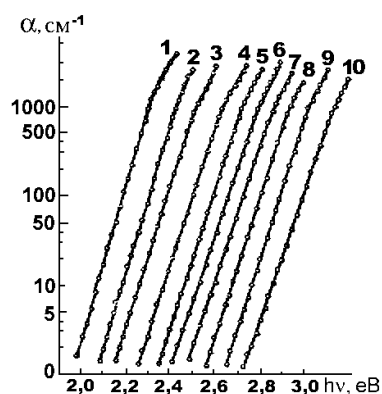


Fig. 3 Fundamental absorption spectra of $(\text{As}_2\text{S}_3)_x(\text{GeS}_2)_{1-x}$ glasses as a long wave transmittance color filters ($x = 1$; 2 - $x=0,9$; 3- $x=0,7$; 4 - $x=0,6$; 5 - $x=0,5$; 6- $x=0,4$; 7- $x=0,3$; 8- $x=0,2$; 9- $x=0,1$; 10- $x=0$).

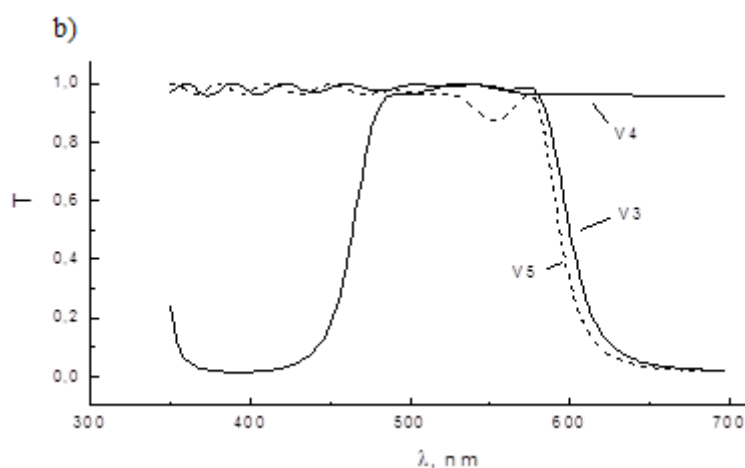
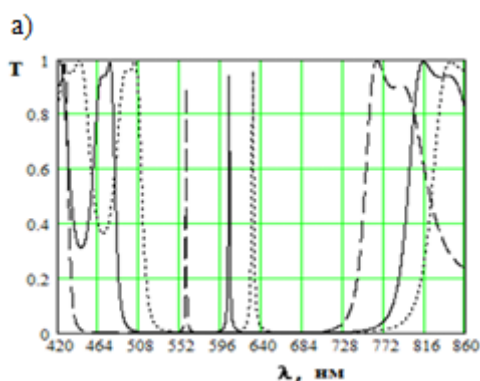


Fig 4. The transmission spectra of narrow-band filters (a) and edge (b) filters for short V_3 (solid line) and V_5 long (dotted line) and passband wavelengths V_4 (solid line)

References

1. SCHOTT GGLASWERKE Optical Glass Filters. Mainz, 2008.
2. GOST 9411-91. CATALOG COLOR GLASSES. M. 1991.
3. OPTICS 1997/98 CATALOG. Newport. USA. 1997.
4. Corion Optical filters and coatings. Holliston 1994.

TEMPERATURE-DEPENDENT RAMAN STUDIES OF LAYERED TlIn(S_{1-x}Se_x)₂ (0 ≤ x ≤ 0.25) SINGLE CRYSTALS

O. Gomonnai^{1,2}, M. Ludemann³, A. Gomonnai^{1,4}, A. Slivka¹,
I. Roman⁴, D. Zahn³

¹ *Uzhhorod National University, 46 Pidhirna Str., 88000 Uzhhorod, Ukraine*

² *Vlokh Institute of Physical Optics, 23 Dragomanov Str., 79005 Lviv, Ukraine*

³ *Semiconductor Physics, Chemnitz University of Technology,
D-09107 Chemnitz, Germany*

⁴ *Institute of Electron Physics, Ukr. Nat. Acad. Sci., 21 Universytetska Str.,
88017 Uzhhorod, Ukraine
gomonnai.o@gmail.com*

Raman spectroscopy is an efficient tool to study crystal lattice dynamics, in particular, with regard to phase transitions. TlMX₂-type crystals (M = Ga, In, X = Se, S) were the first low-dimensional semiconductors, for which a series of phase transitions with modulated structures was discovered [1]. At room temperature TlInS₂ and TlInSe₂ crystals are characterized by layered and chain-like structure, respectively [1]. For mixed TlIn(S_{1-x}Se_x)₂ crystals at $x \approx 0.7-0.75$ the crystal structure changes with x from C_{2h}⁶ to D_{4h}¹⁸ [1]. S→Se isovalent substitution results in a decrease of the structural phase transition temperatures. In the (x , T) phase diagram of TlIn(S_{1-x}Se_x)₂ a Lifshitz type point at $x = 0.05$ was reported [2]. Raman scattering studies at 30 K in the Z(XX+XY) \bar{Z} configuration were performed for TlIn(S_{1-x}Se_x)₂ (0 ≤ x ≤ 0.25) single crystals in our earlier paper [3]. The present study is devoted to the analysis of the temperature behaviour of frequencies, halfwidths, and intensities of first-order Raman-active optical phonons in sulfur-rich TlIn(S_{1-x}Se_x)₂ single crystals in the temperature interval 30 K ≤ T ≤ 293 K.

TlIn(S_{1-x}Se_x)₂ (0 ≤ x ≤ 0.25) single crystals were grown by the Bridgman technique. Raman spectra were measured using a Dilor XY 800 spectrometer equipped with a CCD camera. The instrumental resolution was in all cases better than 2 cm⁻¹. A Kr⁺ (647.1 nm) laser was used for excitation. The measurements were performed in the frequency range 16–340 cm⁻¹ in Z(XX+XY) \bar{Z} scattering configuration in the temperature range of 30 K ≤ T ≤ 293 K. The samples were placed in a cryostat coupled to a temperature control system capable of setting the sample temperature with an accuracy of ± 0.01 K.

Raman spectra of TlIn(S_{0.99}Se_{0.01})₂, TlIn(S_{0.90}Se_{0.10})₂, TlIn(S_{0.85}Se_{0.15})₂, and TlIn(S_{0.75}Se_{0.25})₂ single crystals at different temperatures are shown in Fig. 1. The number of Raman bands for the mixed crystals and their spectral positions at $T = 30$ K and $T = 293$ K are in good agreement with the data available from literature for TlInS₂ with the account of the known compositional behaviour of

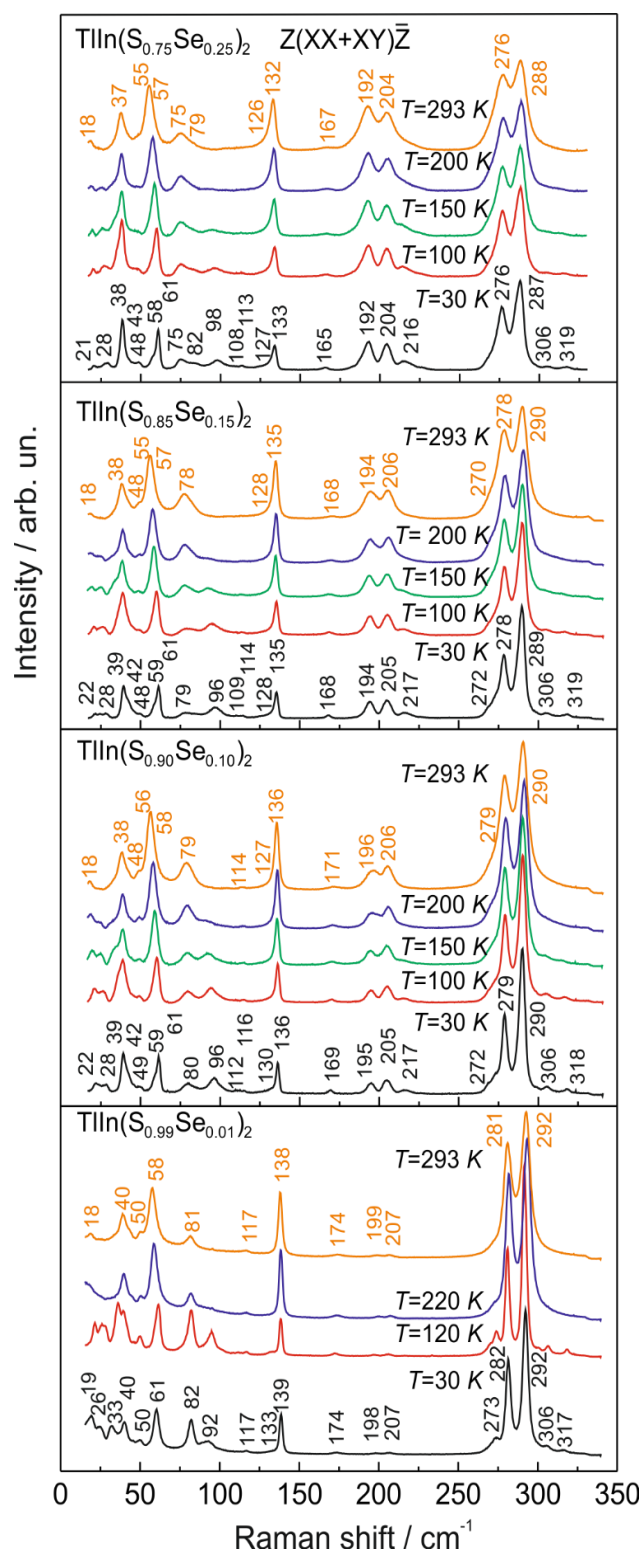


Fig.1. Raman spectra of a $\text{TlIn}(\text{S}_{1-x}\text{Se}_x)_2$ single crystals in the $Z(\text{XX}+\text{XY})\bar{Z}$ configuration at different temperatures.

the $\text{TlIn}(\text{S}_{1-x}\text{Se}_x)_2$ phonon spectra [3, 4]. An example of multi-peak simulation of the experimental $\text{TlIn}(\text{S}_{1-x}\text{Se}_x)_2$ Raman spectra by Lorentzian contours is shown in Fig. 2.

Two groups of features can be distinguished in the temperature behaviour of the $\text{TlIn}(\text{S}_{1-x}\text{Se}_x)_2$ Raman spectra: (i) typical temperature dependence of phonon band characteristics in crystals (a slight frequency downshift, increasing halfwidths and integrated intensities with increasing T) and (ii) phase transition-related transformation of the phonon spectra.

In the low-frequency spectral range of $16\text{--}50\text{ cm}^{-1}$ the Raman features undergo a complicated transformation with temperature. Among them two modes (at 28 cm^{-1} and 43 cm^{-1} at 30 K for $\text{TlIn}(\text{S}_{0.75}\text{Se}_{0.25})_2$ and similar vibrations at corresponding frequencies for other compositions) reveal the most pronounced temperature dependence in the temperature range $30\text{ K} \leq T \leq 220\text{ K}$. For other translational and "intermolecular" modes of $\text{TlIn}(\text{S}_{1-x}\text{Se}_x)_2$ crystals, the temperature-related broadening and integrated intensity increase as well as slight frequency decrease are due to the anharmonicity of the lattice vibrations and consequent thermal expansion. A similar temperature behaviour is observed for the modes in the

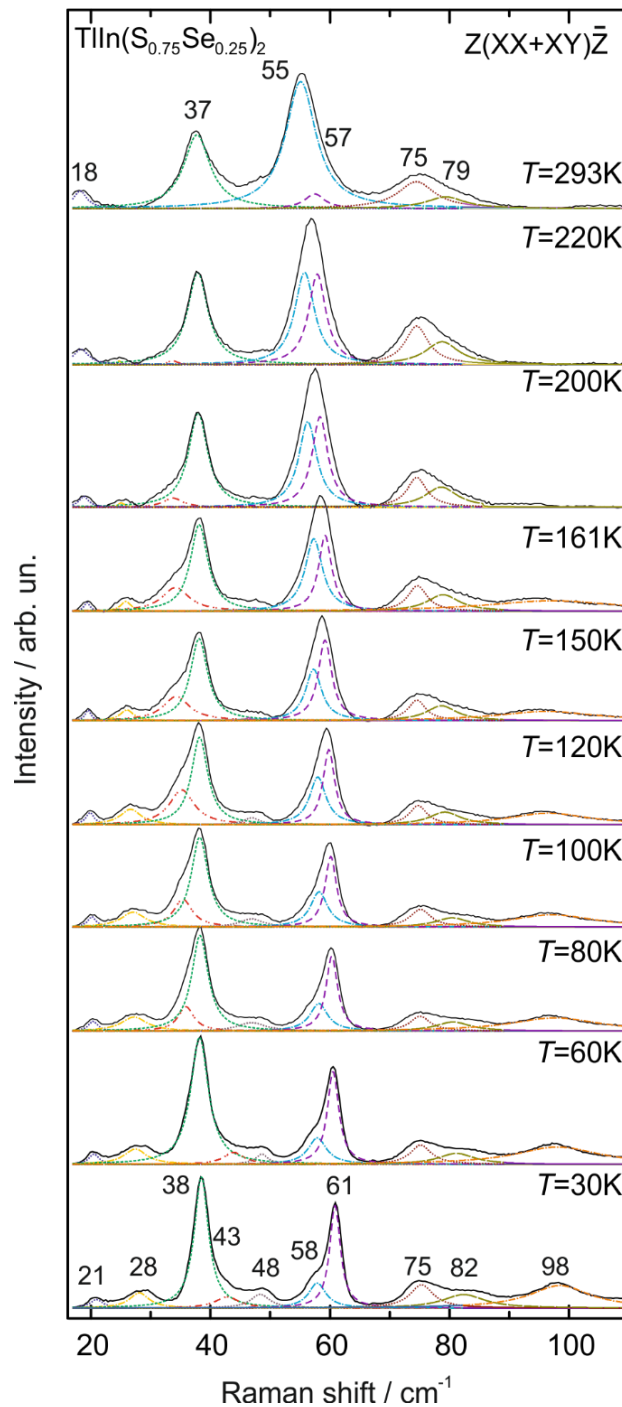


Fig. 2 Raman spectra of $\text{TIIn}(\text{S}_{0.75}\text{Se}_{0.25})_2$ single crystal in the $Z(\text{XX}+\text{XY})\bar{Z}$ configuration in the range of 16–110 cm^{-1} at 30–293 K and their multi-peak Lorentzian simulation.

high-frequency groups at 190–220 cm^{-1} and 250–350 cm^{-1} .

At temperatures above 120 K (for $x=0.25$ crystal) the number of modes in the spectra decreases. Similar effects are revealed for other crystals of the family, for which the temperatures of the observed changes differ. This can be related to phase transitions which occur at relevant temperatures. For instance, for $x=0.25$ crystal the bands at 28 cm^{-1} and 43 cm^{-1} vanish at $T > 220$ K, modes 48 cm^{-1} , 98 cm^{-1} , 108 cm^{-1} , and 113 cm^{-1} vanish at $T = 180$ K, while the bands at 306 cm^{-1} , and 319 cm^{-1} are no longer observed above 120 K which may, however, be also related to their low intensities.

[1] A.M. Panich. Electronic properties and phase transitions in low-dimensional semiconductors, *J. Phys.: Condens. Matter.*, V. 20, pp. 293202/1-42, (2008).

[2] M.Yu. Seyidov et al. Origin of structural instability in $\text{TIInS}_{2(1-x)}\text{Se}_{2x}$ solid solutions, *Phys. Scripta*, V. 84, p. 015601, (2011).

[3] O.O. Gomonnai et al. Low-Temperature Raman Studies of Sulfur-Rich $\text{TIIn}(\text{S}_{1-x}\text{Se}_x)_2$ Single Crystals, *Vibrational Spectroscopy*, V. 97, p. 114, (2018).

[4] V.M. Burlakov et al. Raman spectroscopy of soft and rigid modes in ferroelectric TIInS_2 , *Phys. Status Solidi B*, V. 153, p. 727, (1989).

**LUMINESCENCE PROPERTIES OF THE Tm³⁺-DOPED
LiKB₄O₇ GLASS**I. Kindrat^{1*}, B. Padlyak^{1,2}, R. Lisiecki³, V. Adamiv², I. Teslyuk²¹ *University of Zielona Góra, Institute of Physics, Division of Spectroscopy of Functional Materials, 4a Szafrana Str., 65-516 Zielona Góra, Poland*² *Vlokh Institute of Physical Optics, Department of Optical Materials, 23 Dragomanov Str., 79-005 Lviv, Ukraine*³ *Institute of Low Temperature and Structure Research of the Polish Academy of Sciences, Division of Optical Spectroscopy, Group for Spectroscopy of Laser Materials, 2 Okólna Str., 50-422 Wrocław, Poland*

The luminescence properties of the Tm-doped glasses with LiKB₄O₇ (0.5Li₂O–0.5K₂O–2B₂O₃) basic composition containing 0.4 mol.% Tm₂O₃ are investigated and analysed using optical absorption, emission and excitation spectra as well as luminescence kinetics studies. The LiKB₄O₇:Tm glass of high chemical purity and optical quality was obtained in the air using standard glass technology, briefly described in [1]. Based on characteristic optical spectra it was found that thulium dopant is incorporated into the LiKB₄O₇ glass network exclusively as Tm³⁺ (4f¹², ³H₆) ions.

Optical absorption spectra of the Tm-doped LiKB₄O₇ glass consist of several bands in the visible and infrared spectral ranges, which belong to 4f – 4f transitions of the Tm³⁺ ions from the ³H₆ ground state to the following excited states: ³F₄, ³H₅, ³H₄, ³F₃, ³F₂, and ¹G₄. The Tm³⁺ optical spectra were analysed in the framework of Judd–Ofelt theory [2,3]. The theoretical (f_{cal}) and experimental (f_{exp}) oscillator strengths as well as Judd–Ofelt intensity parameters (Ω_2 , Ω_4 , Ω_6) have been calculated. The evaluated Judd–Ofelt parameters have been used to estimate the radiative properties such as radiative transition probabilities (A_{rad}), luminescence branching ratios (β), and radiative lifetimes (τ_{rad}) [4].

Luminescence spectra of the LiKB₄O₇:Tm glass registered at different wavelengths of photoexcitation reveal intense blue (¹D₂ → ³F₄ transition, $\lambda_{max} = 452$ nm), red (¹G₄ → ³F₄ transition, $\lambda_{max} = 650$ nm) as well as infrared (³H₄ → ³H₆ transition, $\lambda_{max} = 786$ nm and ³F₄ → ³H₆ transition, $\lambda_{max} = 1805$ nm) emission bands (see Fig. 1). Luminescence excitation spectra of the LiKB₄O₇:Tm glass have been registered by monitoring of intensity of the ¹D₂ → ³F₄ and ³H₄ → ³H₆ emission bands. Observed excitation bands refer to transitions from the ³H₆ ground state to the ³F₃, ³F₂, ¹G₄, ¹D₂, ¹I₆, ³P₀, ³P₁, and ³P₂ excited states.

*Corresponding and presenting author, e-mail: I.Kindrat@if.uz.zgora.pl

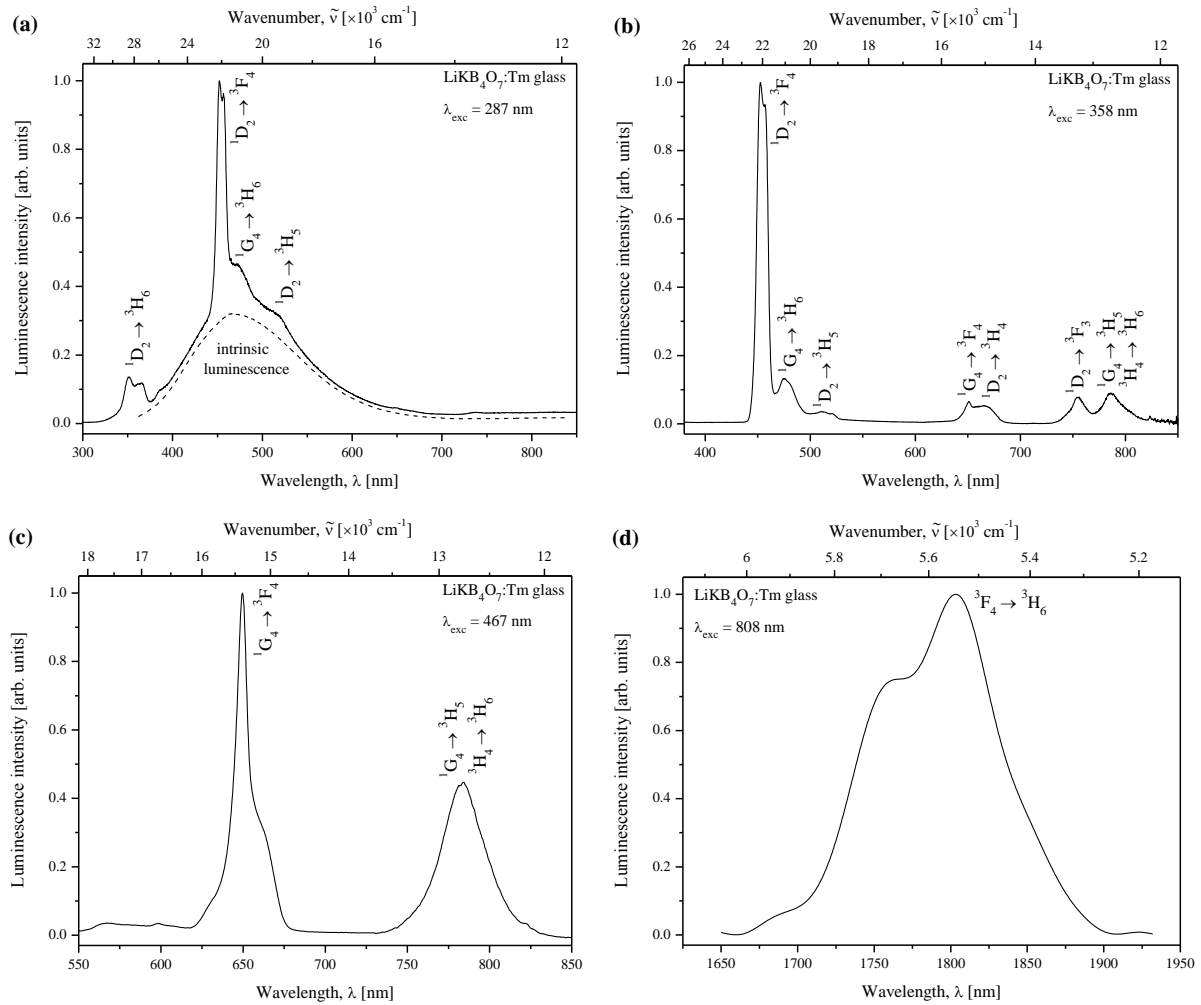


Fig. 1. Luminescence emission spectra of the $\text{LiKB}_4\text{O}_7\text{:Tm}$ glass containing 0.4 mol.% Tm_2O_3 , registered under excitation at 287 nm (a), 358 nm (b), 467 nm (c), and 808 nm (d). Observed emission bands are identified and denoted in the Figure.

The luminescence decay curves of the $^1\text{D}_2$, $^1\text{G}_4$, $^3\text{H}_4$, and $^3\text{F}_4$ excited states of Tm^{3+} ions in the $\text{LiKB}_4\text{O}_7\text{:Tm}$ glass were detailed studied and discussed. The average lifetimes were evaluated to be 14 μs , 98 μs , 81 μs , and 41 μs for the emissions originated from the $^1\text{D}_2$, $^1\text{G}_4$, $^3\text{H}_4$, and $^3\text{F}_4$ levels, respectively. The obtained experimental lifetimes are smaller than corresponding radiative lifetimes. This fact indicates non-radiative processes in the investigated $\text{LiKB}_4\text{O}_7\text{:Tm}$ glass. Based on Inokuti-Hirayama model [5] it was found that non-radiative processes mainly are related with energy transfer via cross-relaxation mechanism between Tm^{3+} ions coupled by dipole-dipole interaction. Diagram of partial energy levels of the Tm^{3+} ions in the LiKB_4O_7 glass showing luminescence emission and excitation transitions as well as energy transfer channels via cross-relaxation processes is presented in Fig. 2.

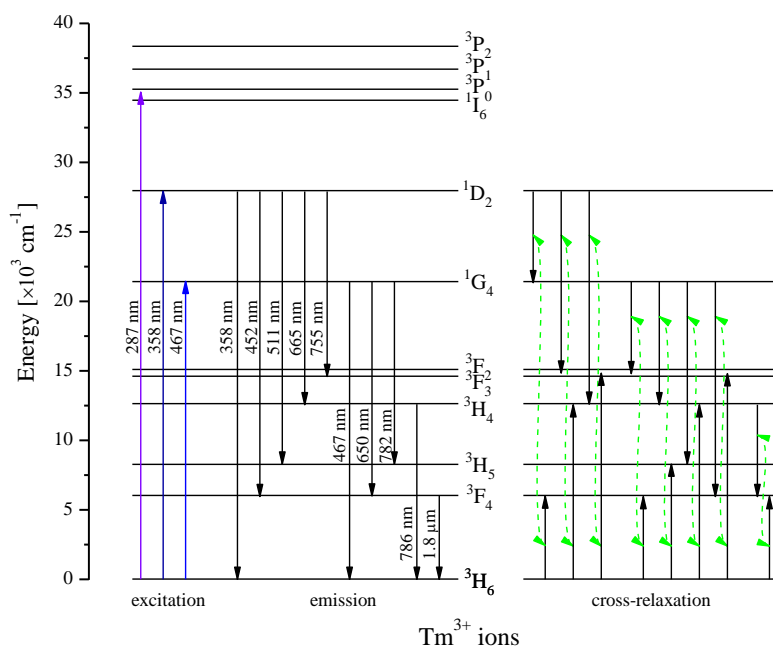


Fig. 2. The partial energy diagram of Tm^{3+} ions in the $\text{LiKB}_4\text{O}_7:\text{Tm}$ glass showing luminescence emission and excitation transitions as well as energy transfer channels via cross-relaxation mechanism.

The absorption and luminescence spectra between the ground $^3\text{H}_6$ state and first excited $^3\text{F}_4$ state were calibrated in absorption (σ_{abs}) and stimulated emission (σ_{em}) cross-section units. The highest values of absorption cross-section at 1662 nm and stimulated emission cross-section at 1805 nm have been estimated to be $0.36 \times 10^{-20} \text{ cm}^2$ and $0.45 \times 10^{-20} \text{ cm}^2$, respectively. In order to eliminate the self-absorption the effective emission cross-section (σ_{eff}) was calculated. Observed weak absorption at wavelength of emission peak and positive effective cross-section at small inversion population is useful for laser generation. Based on obtained results it was suggested that efficient laser generation around 1.8 μm can be obtained in the $\text{LiKB}_4\text{O}_7:\text{Tm}$ glass.

References

- [1] B.V. Padlyak, S.I. Mudry, Y.O. Kulyk, A. Drzewiecki, V.T. Adamiv, Y.V. Burak, I.M. Teslyuk, Synthesis and X-ray structural investigation of undoped borate glasses, *Mater. Sci. Pol.* 30 (2012) 264–273.
- [2] B.R. Judd, Optical absorption intensities of rare-earth ions, *Phys. Rev.* 127 (1962) 750–761.
- [3] G.S. Ofelt, Intensities of crystal spectra of rare-earth ions, *J. Chem. Phys.* 37 (1962) 511–520.
- [4] M.P. Hehlen, M.G. Brik, K.W. Krämer, 50th anniversary of the Judd–Ofelt theory: an experimentalist’s view of the formalism and its application, *J. Lumin.* 136 (2013) 221–239.
- [5] M. Inokuti, F. Hirayama, Influence of energy transfer by the exchange mechanism on donor luminescence, *J. Chem. Phys.* 43 (1965) 1978–1989.

APPLICATION OF THE POSITRON ANNIHILATION METHOD WITH PURPOSE IDENTIFY COMPLICATED STRUCTURE DAMAGE IN IRRADIATED GaP AND InP CRYSTALS

O. Konoreva¹, P. Lytovchenko¹, Yu. Pavlovskyy²,
V. Tartachnyk¹, V. Shlapatska³

¹*Institute for Nuclear Research, NAS of Ukraine, 47, prospect Nauky, 03028,
Kyiv, Ukraine*

²*Drohobych Ivan Franko State Pedagogical University, 24, Street Ivan Franko,
82100, Drohobych, Ukraine*

³*L.V. Pisarzhevski Physical Chemistry Institute NAS of Ukraine, 31, pr. Nauky,
03028 Kyiv, Ukraine*

It is known that the vacancy defect of the lattice is due to the absence of atoms, the electron density is sharply reduced (in aluminum, for example, on a monovacancy, it is 24% less than that of an intact matrix), which leads to a significant increase of the lifetime of the trapped positron τ_p .

In addition to an increase in τ_p , there is also a narrowing of the angular distribution of annihilation photons (ADAP).

In the work cycle performed by us, the single crystals of the $A^{III}B^V$ group grown by the Czochralski method and irradiated by electrons with $E = 1; 14; 50$ MeV; protons with $E = 35$ MeV and α -particles with $E = 80$ MeV were studied. $14; 50$ MeV. The integral particles fluctuated within the limits $10^{16} \div 10^{18} \text{cm}^{-2}$.

Experimental curves of ADAP were constructed in the form of an inverted parabola and gaussian. In the range of $0 \div 5$ mrad, parabolic dependence prevailed, with $\varphi > 5$ mrad – the Gauss distribution.

Electron irradiation.

The ratio of the area under the parabolic part of the correlation curve to the area under the Gaussian S_p/S_G is a characteristic ADAP parameter, which makes it possible to compare the probability of annihilation of positrons in vacancies and at atomic electrons.

The irradiation of GaP and InP crystals is accompanied by an increase in the rate of account in a maximum ADAP and an increase in the lifetime of positrons. The narrowing value for GaP at $E = 14$ MeV, $\Phi = 10^{18} \text{cm}^{-2}$ is $\Delta\varphi = 0,6$ mrad.

The constant σ which is included in the denominator of the Gaussian power index is related to a simple dependence with the value r_m – distance from the atomic nucleus, on which the product of the wave functions of the electron and positron is maximal ($r_m = 4,73/\sigma$).

Since the annihilation acts from the tail of the Gaussian distribution occur on the outer electron shells of the atom, r_m does not differ much from the values

of the ion radius of the elements.

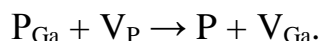
In our experiments, it was discovered that irradiation of GaP crystals by electrons with $E = 14$ MeV leads to a decrease r_m ($r_{m \text{ init}} = 1,3 \text{ \AA}$, $r_{m \text{ irradiat}} = 1,13 \text{ \AA}$).

The isochronous annealing of irradiated samples GaP (from 20°C to 200°C) reduces the rate of account in the maximum ADAP. Further heating (from 400°C to 800°C) increases it. The value of r_m initially also increases ($20 \div 200^\circ\text{C}$), decreases somewhat at $200 \div 400^\circ\text{C}$ and sharply increases reaching the original value at 600°C . Full recovery of the ADAP form occurs only at 200°C .

An increase of the intensity of the account at the maximum of the curve clearly indicates the presence of a large number of vacancy defects in the irradiated crystal. Interstitial atoms with high mobility in the presence of vacancies in both substrates contribute to the appearance of antistructural damage.

The positron which is thermalized in the region of a crystal with a high concentration of interstitial atoms annihilates mainly on atoms of a smaller radius (on atoms of P) which directly leads to a decrease of r_m .

The heating of the sample to the temperature at which the mobile V_P becomes, causes the annealing of the $P-P_4$ -centers



The main part of the antistructural defects of P_{Ga} decay within limit $400 \div 600^\circ\text{C}$.

The existence of a sharp stage of annealing makes it possible to make estimates of the activation energy of E_a according to the ratio:

$$E_a = kT_c \ln \frac{\nu k}{\alpha E_a},$$

where T_c – the center of stage, $\nu = 7 \cdot 10^{-12}$ for GaP, $\alpha = \frac{\Delta(1/T)}{\Delta t}$, k – Boltzmann constant.

The results of the calculation for the three stages were $E_{a1} = 1,19$ eV, $E_{a2} = 1,90$ eV, $E_{a3} = 2,40$ eV. The value of E_a for the 1st and 2nd stages is approximate to the values of the activation energies of migration V_P and V_{Ga} , respectively.

Proton irradiation.

Proton irradiation with $E = 35$ MeV was carried out on the isochronous cyclotron U-240 at $T = 300$ K.

The narrowing of the correlation curves and the growth of the intensity of the account at the maximum were found (Fig. 1). The radius of positron localization on radiation damage was close to 6 \AA , which indicates participation in annihilation acts of simple defects of the vacancy type. They are V_P were because the areas of the annealing of the narrow component and vacancies V_P –

coincide.

After annealing at 160°C when the V_P becomes sufficiently mobile, in the irradiated and heated sample the tendency towards the formation of the divacancies appears – the rate of account at the maximum ADAP increases again.

The peculiarity of GaP crystals is the low probability of trapping positrons by vacancies Ga, which may be due to the electrical neutrality of these defects.

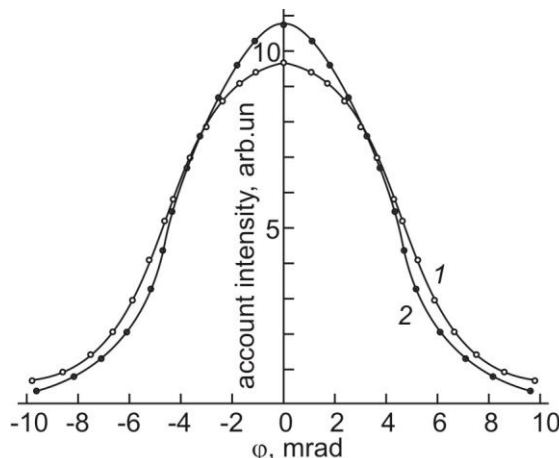


Fig. 1. Correlation curves for the initial sample GaP (1) and irradiated by protons with $E = 35$ MeV (2)

The energies of protons $E_p = 35$ MeV are quite sufficient for the creation of disordering areas in the investigated samples. Previously, it was discovered that such defects introduced in the GaP sample by neutrons irradiation of the reactor and were annealed off at a temperature greater than 500°C. Therefore, the growth of the account after 500°C obviously should be associated with the annealing of disordered areas created by proton irradiation and the formation of decay products with a large cross-section of capture of positrons.

Irradiation by α -particles.

Measurement of the lifetime of the positrons τ_p in GaP crystals irradiated by α -particles with $E = 80$ MeV was carried out by the method of coincidence of pulses of γ -quanta. The value of τ_p was equal to 225 ps and 250 ps in initial and irradiated crystals, respectively.

The recovering of this parameter proceeded during three stages: 200 ÷ 400°C; 550 ÷ 700°C; 750 ÷ 900°C. Moreover, at the first and third stages there is a decrease. The second stage is negative, annealing temperature is accompanied by a decrease of τ_p .

An important feature of the annealing of crystals irradiated with α -particles is the absence of a stage 160 ÷ 180°C where defects disappear, which compensate for the electrical conductivity of n -GaP, that is V_P . This stage also does not occur in samples irradiated by neutrons a large dose.

On the other hand, it is well appear in samples irradiated by electrons. Consequently, it is present in crystals dominated with point defects and absent –

in samples with a high concentration of complex damage.

In previously performed works it was shown that the disordering regions have a small cross-section of the absorption of positrons. Therefore, the main changes in τ_p under annealing should be associated with the influence of complex defects that can change their charge state in the process of changing the position of the Fermi level, both as a result of irradiation and as a result of annealing.

Vacancy defects in InP.

Unlike to GaP, the InP primery introduced point defects are anneal to room temperature. At temperatures greater than 300 K in the sample only complex damage and complexes of simple defects with impurities are present.

A characteristic feature of ADAP for InP is the absence of parabolic dependence in region in the maximum (Fig. 2). In the initial sample on the curve, there is a horizontal section, that is transformed in an irradiated sample in sharp peak of the so-called "narrow component", which indicates the presence of several groups of vacancy defects in the InP at 300 K. The calculations performed show that the average positron capture radius (localization radius) is close to $3 \div 4 \text{ \AA}$, but such a center can not be considered as a monovacancy of V_P or V_{In} – they do not exist at 300 K in crystals of InP. Therefore, we can assume that the process of annihilation takes place in a complex, which includes one of the vacancies.

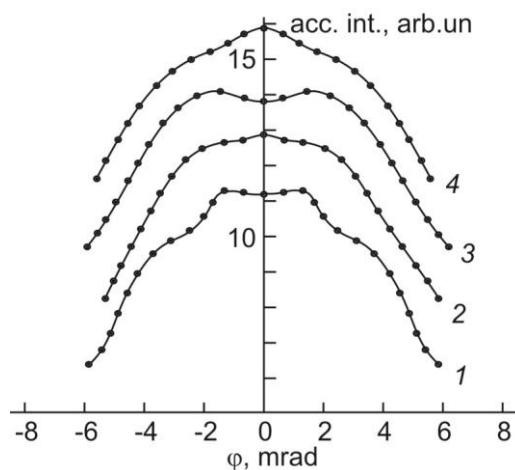


Fig. 2. Changing the fine structure of the maximum curve of the ADAP the InP sample at annealing: 1 – 180°C; 2 – 220°C; 3 – 300°C; 4 – 800°C

Using the model of diffusion capture of positrons allows us to estimate the concentration of introduced positron traps. It turned out to be small and for $\Phi = 3,3 \cdot 10^{18} \text{ cm}^{-2}$ it was $7,8 \cdot 10^{15} \text{ cm}^{-3}$. The result becomes clear when taking into account the temperature instability of simple structural disturbances in InP.

It was also found that the broad ADAP component consists of two Gaussians, the first, more intense, due to annihilation on In atoms. The second is responsible for the presence of radiation defects in the crystal.

GROWTH AND PROPERTIES OF DISORDERED BORATE SINGLE CRYSTALS FOR LASER APPLICATION

M. Kosmyna, A. Shekhovtsov

Institute for Single Crystals of the NASU, Ukraine

Solid state lasers emitting radiation in UV-VIS and IR ranges are usefully applied for telecommunication, material processing, spectroscopy, data storage, medicine and others. Explosive character of evolution of photonics stimulates search for new effective laser crystal media. The choice of laser medium under developing of laser apparatus depends on combination of different factors, like cost price of single crystal, ability of its industrial production, toxicity of technological production chain and others.

One of tasks of photonics is related to the developing of active media for eye safe lasers operating at 1.5 μm wavelength. For this task $^4\text{I}_{13/2}$ - $^4\text{I}_{15/2}$ transition of Er^{3+} can be used. But traditional crystals, like $\text{Y}_3\text{Al}_5\text{O}_{12}$ and YVO_4 do not demonstrate efficient laser operation at 1.5 μm wavelength. Most spread material of active media of commercial 1.5 μm lasers is glass having essential disadvantage – low heat conductivity (0.80 – 0.85 W/m K). Moreover, recrystallization processes of laser glass lead to degradation of functional characteristics over time.

Obviously, the search for new Er,Yb-codoped crystals combining high functional characteristics and manufacturability is actual task. The binary borate $\text{Ca}_3\text{RE}_2(\text{BO}_3)_3:\text{Er},\text{Yb}$ (RE - Y, Gd) single crystals are promising for generation of 1.5 μm radiation. Early, crystal defects, heatconductivity [1] and spectroscopic characteristics of $\text{Ca}_3\text{RE}_2(\text{BO}_3)_3:\text{Er},\text{Yb}$ (RE - Y, Gd) single crystals were studied and laser operation at 1.53 μm wavelength was demonstrated [2] for the first time in frames of joint Ukrainian – Belorussian Project. It became possible due to the developing multistage solid state synthesis based on stepped decomposition of calcium carbonate and boric acid. The developed technology of synthesis supplied production of the stoichiometric charge and crystallization up to 70% melt under the crystal growth by the Czochralski method (Fig.1).

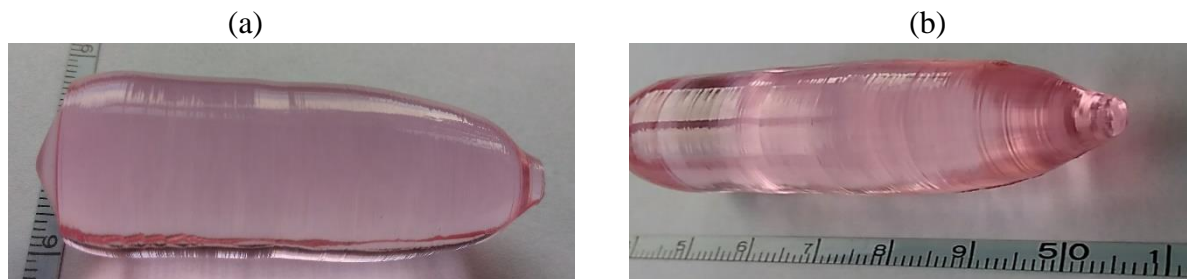


Fig.1. The $\text{Ca}_3\text{Y}_2(\text{BO}_3)_4:\text{Er},\text{Yb}$ (a) and $\text{Ca}_3\text{Gd}_2(\text{BO}_3)_4:\text{Er},\text{Yb}$ (b) crystals

Polarized absorption and emission cross-section spectra, lifetimes of $^4I_{11/2}$ and $^4I_{13/2}$ energy levels of Er^{3+} and ytterbium-erbium energy transfer efficiencies for $Ca_3RE_2(BO_3)_3:Er,Yb$ (RE - Y, Gd) crystals were investigated and presented in Table 1. Maximal laser operation efficiency of 13% was achieved at 1530 nm for $Ca_3Y_2(BO_3)_3:Er,Yb$ crystal. It should be noted that the luminescence quantum yields of the $^4I_{13/2}$ energy level was 28% for $Ca_3Gd_2(BO_3)_3:Er,Yb$ crystal. That is three times higher than for the most efficient $REAl_2(BO_3)_4:Er,Yb$ crystals applied for 1.5 μm lasers.

Table 1. – Characteristics of $Ca_3RE_2(BO_3)_3:Er,Yb$ (RE - Y, Gd) active media.

	$Ca_3Y_2(BO_3)_4:Yb,Er$	$Ca_3Gd_2(BO_3)_4:Yb,Er$
Absorption cross-section (976 nm), $10^{-20} cm^2$	1.5	1.6
Emission cross-section (1530 nm), $10^{-20} cm^2$	1.45	1.53
Quantum yield of luminescence, %	24	27.8
Efficiency of energy transfer $Yb^{3+}-Er^{3+}$, %	> 80	> 80
Slope efficiency η_{sl} , %	13	12
Pumping	diode	diode

This approach was successfully applied for synthesis and crystal growth of other borate single crystals for laser applications. In particular, Er,Yb co-doped $Ca_4YO(BO_3)_3$ crystals with optimized content of Er (1.5 at.%) and Yb (30 at.%) and free of impurity phases and gas bubble inclusions have been grown. The active elements of 1.5 μm laser have been produced (Fig. 2a). Nd doped crystals have been grown also (Fig. 2b).

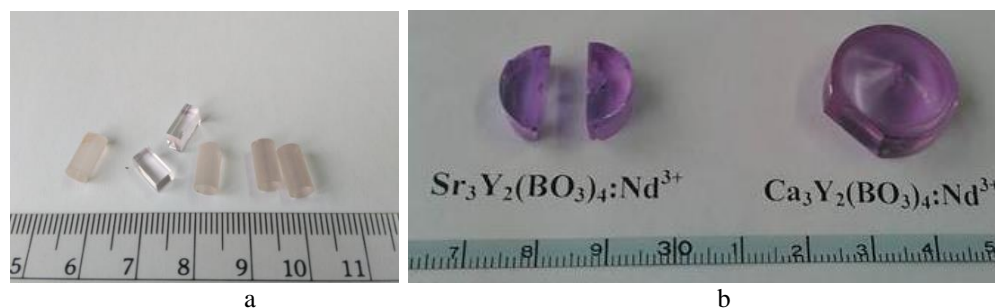


Fig. 2. The $Ca_4YO(BO_3)_3:Er,Yb$ active elements for 1.5 μm lasers (a). Nd doped $Ca_3Y_2(BO_3)_4$ and $Ca_3Y_2(BO_3)_4$ crystals (b).

Another scientific task is directed to developing of crystals for active media of solid state lasers emitting in the UV range. Application area for these lasers are wide and covers lithography, medicine, agriculture, biosensors. One of the decisions of this task is generation of anti Stokes harmonics by Raman lasers. It was shown recently, that $Ca_3(BO_3)_2$ crystal is a good candidate for Raman lasers emitting anti Stokes harmonics. $Ca_3(BO_3)_2$ crystal demonstrates outstanding third-order nonlinear optical effect. The transmission range of $Ca_3(BO_3)_2$ crystal is 180–3800 nm [3]. This compound melts congruently and can be grown by the

Czochralski method. Obviously, high optical quality single crystals are required for this application.

Multistage solid state synthesis was applied for stoichiometric charge synthesis and pure and Nd doped $\text{Ca}_3(\text{BO}_3)_2$ crystals were grown (Fig.3). It should be noted segregation coefficient of Nd is low. In our growth experiments this value was about 0.1. No impurity phases and scattering centers were detected for pure and Nd doped $\text{Ca}_3(\text{BO}_3)_2$ crystals.



Fig.3. The Nd doped and pure $\text{Ca}_3(\text{BO}_3)_2$ crystals.

This work was supported by Ukrainian-Belorussian grant.

References

1. L.V. Gudzenko, M.B. Kosmyna, A.N. Shekhovtsov, W. Paszkowicz, A. Sulich, J. Z. Domagała, P.A. Popov, S.A. Skrobov. Crystal growth and glass-like thermal conductivity of $\text{Ca}_3\text{RE}_2(\text{BO}_3)_4$ (RE-Y, Gd, Nd) single crystals // Crystals. – 2017. – V.7:88. – 9 p.
2. K.N. Gorbachenya, R.V. Deineka, V.E. Kisel, A.S. Yasukevich, A.N. Shekhovtsov, M.B. Kosmyna, N.V. Kuleshov. Er,Yb: $\text{Ca}_3\text{RE}_2(\text{BO}_3)_4$ (RE=Y, Gd) – novel 1.5 μm laser crystals // Devices and Methods of Measurements – 2019. – Vol. 10, №. 1. – P. 14–22.
3. Yanqing Liu, Fang Zhang, Zhengping Wang, Fapeng Yu, Lei Wei, Xinguang Xu and Xian Zhao. $\text{Ca}_3(\text{BO}_3)_2$, a first wide waveband borate Raman laser crystal with strong Raman effects and outstanding anti-optical damage ability // J. Material Chemistry. C. – 2015. – V. 3. – P. 10687-10694.

THERMAL CONDUCTIVITY AT LOW TEMPERATURE OF OPTICAL MATERIALS FOR IR LASERS BASED ON WIDE GAP CHALCOGENIDE GLASSES

V. Mitsa¹, A. Feher², V. Tkáč², R. Holomb^{1,3}, M. Veres³, B. Matyashovska¹

¹ *Uzhhorod National University, Voloshin str. 54, 88000 Uzhhorod, Ukraine*
e-mail: v.mitsa@gmail.com

² *Pavol Jozef Šafárik University in Košice, Park Angelinum 9, 041 54 Košice, Slovak Republic*

³ *Wigner Research Centre for Physics of the Hungarian Academy of Sciences, Konkoly-Thege, Miklós st. 29-33, 1121 Budapest, Hungary*

In addition well known intrinsic infrared (IR) properties chalcogenide glasses, they offer a wide possibilities in domains such as information technologies (ultrafast optical transmitting and information processing), photolithography, medicine, thermal imaging, sensing and biosensing etc. The numerical value of laser-induced damage of IR optical materials depends from some important critical parameters: thermal conductivity, heat capacity and high connectivity of structural matrix [1].

This investigation is based on a set of advanced techniques for the study of structure and properties of chalcogenide glassy semiconductors. The analysis of the structure of chalcogenide non-crystalline semiconductors was carried out using Raman spectroscopy. The coefficient of thermal conductivity and the dependence $k(T)$ in the range of helium temperatures were measured using the stationary method.

At a fixed temperature, the growing of mean coordination number (\bar{z}) is accompanied by a shift of the low-frequency (boson) maximum in $\text{As}_y\text{S}_{100-y}$ glasses in the high-frequency region of the spectrum from 20 cm^{-1} ($\bar{z} = 2.1$) to 26 cm^{-1} ($\bar{z} = 2.4$) (Fig.1). This relates to the lowering of the low-frequency maximum intensity. The increasing of the ultrasound longitudinal elastic modules with z (As concentration) in $\text{As}_y\text{S}_{100-y}$ glasses is in frame of the topological-cluster concept [2]. The increase of the connectivity (coordination) of the structural matrixes of glasses $\text{As}_y\text{S}_{100-y}$ with increasing z together with arsenic incorporation leads to increasing of cross-linking of one-dimensional 1D clusters (chains) to the 2D layered-chain clusters. This occurred for the case when composition is approaching $\text{As}_{40}\text{S}_{60}$, $z = 2.4$ (1D-2D transitions).

The phenomenon of hysteresis of low temperature dependence $k(T)$, first discovered in chalcogenide glasses in helium temperatures [3]. The hysteresis was found in the process of studying of the $g\text{-As}_2\text{S}_3$ $k(T)$ dependence upon cooling the sample with subsequent heating in the temperature region from 11 to 60 K with rate $v_2 = 6.9 \times 10^{-3}\text{ K/s}$ after cooling with $v_1 = 6.4 \times 10^{-3}\text{ K/s}$. In the difference curve ($k(T)$ -heating minus $k(T)$ -cooling), the energy position of the

maximum $\Delta k(T)$ is in good agreement with the position of the maximum of the “boson peak” (BP) in $g\text{-As}_2\text{S}_3$ on the scale $g(\omega)/\omega^2$. During $k(T)$ dependence study of $g\text{-As}_2\text{S}_3$ was confirmed the existence of “plateau” whose temperature interval ranges from 3.6 to 10.7 K. The quantum-mechanical theoretical calculations of low-frequency modes of the As_nS_m clusters vibrations showed that the quasi-localized vibrations [4] arise with the gradual rigid fixation number of the $\text{As}_6\text{S}_{12}\text{H}$ ring and energy of low-frequency modes correlate with the “plateau” region, where $k(T) \approx \text{const}$: 7.7 cm^{-1} (1 fixation point); 4.8 cm^{-1} (2 fixation points); 2.0 cm^{-1} (3 fixation points); 3.7 cm^{-1} (4 fixation points) (Fig.3). Such vibrations can serve as a source of resonant scattering of phonons [4] and cause a known universal weak dependence of $k(T)$ around the “plateau” region.

The dependence $k(T)$ in $g\text{-As}_2\text{S}_3$ above “plateau” from 10.7 to 111 K shows a linear temperature dependence that was theoretically predicted for chalcogenide glass in the model of the “jump mechanism” of the thermal conductivity of non-crystalline solids [5]. Quantum mechanical calculations indicate that the contribution to the dependence $k(T)$ above the “plateau” and “boson peak” are made by torsional type vibrations of ring, closed and branched As_nS_m clusters, appearing from energies (frequencies) of 1 meV (8 cm^{-1}) [6-8].

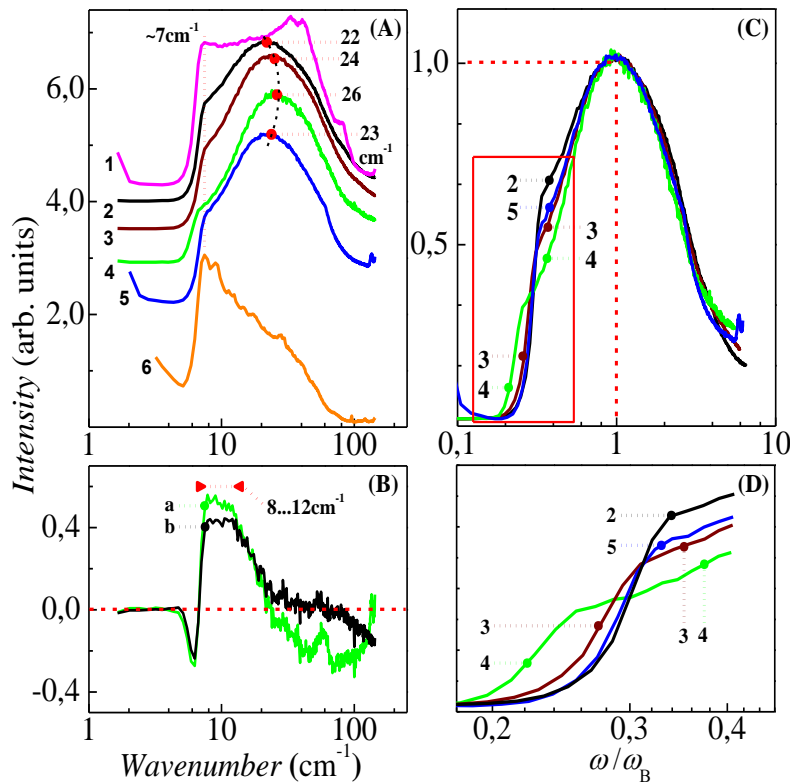


Fig. 1. (A) Depolarized room temperature LF Raman spectra of $\text{As}_x\text{S}_{100-x}$ samples measured with 632.8 nm laser excitation (samples labelling is identical as in Fig. 1.). (B) Differential LF Raman spectra of $\text{As}_{45}\text{S}_{55}$ (a) and $\text{As}_{28.6}\text{S}_{71.4}$ (b) glasses relative to $g\text{-As}_{40}\text{S}_{60}$. (C) Master curve (normalized to ω_B) of the Boson peak (BP) in the LF Raman spectra of As-S glasses (2-5). (D) Enlarged view of the selected part of BP in the region of very low-frequency tails.

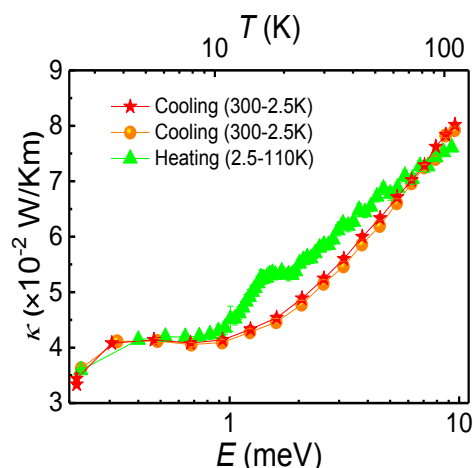


Fig. 2. Low temperature thermal conductivity glass during cooling (lower curve) lines and heating (upper curve) cycles [3].

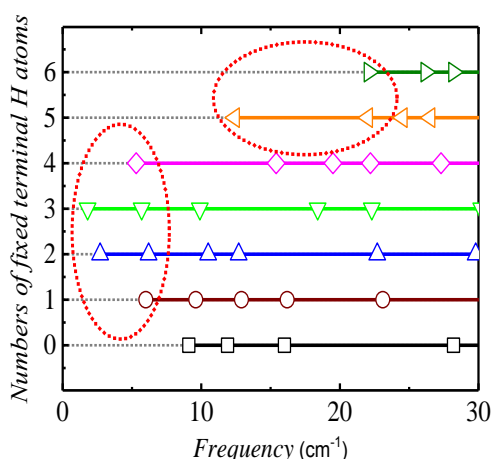


Fig. 3. Calculated vibrational modes of As_2S_3 of 12-membered ring (cluster $\text{As}_6\text{S}_{6+6/2}$). The (see details in text)

We also observed pronounced quasi-elastic scattering (QES) in the differential LF spectra (Fig.1 B). This effect can be seen in the region $8\text{--}12\text{ cm}^{-1}$ (range $0.9\text{--}1.5\text{ meV}$) with high frequency tail up to 20 cm^{-1} (2.1 meV). QES intensity in $\text{As}_y\text{S}_{100-y}$ glasses depends on level of connectivity.

Conclusions: calculated LF vibrations of main building blocks of $\text{As}_x\text{S}_{100-x}$ glasses the chain and ring-like As_nS_m nanoclusters which are flexibly fixed by one terminal heavy “H” ($\text{As}_{2+4/3}\text{S}_5$) and by up to four terminal “H” ($\text{As}_6\text{S}_{6+6/2}$ rings) are located in the same energy range as a plateau in $\kappa(T)$ and maximum in $\text{Cp}/T^3(T)$. Such “soft” LF vibrations also contribute to the formation of quasi-elastic relaxation. “Rigid” vibrations of chain and ring-like As_nS_m nanoclusters have position only in the central parts of the low-frequency BP.

References:

1. V.Mitsa, A.Feher, R.Holomb, V.Tkac, O.Mitsa, M.Ivanda, S.Petretsky, I.Fekeshgazi .Interdependence of low temperature anomalies of thermal conductivity and low-frequency Raman spectra of wide band-gap chalcogenide glasses for optical coatings of power optics. Monograph. – Uzhhorod: Ed. House TOV “RIK-Y” », 2019. – 152 p.
2. M. Thorpe, J. J. Cai, Non-Cryst. Sol. **114**, 19 (1989).
3. V. Mitsa, A. Feher, S. Petretsky, R. Holomb, V. Tkac, P. Ihnatolia, A. Laver, Nanoscale Res. Lett. **12**, 345 (2017).
4. M. I. Klinger, Theoretical and Mathematical Physics **154**, 64 (2008).
5. T. Nakayama, R. Orbach. Physica Review B. **263-264**, 261(1999).
6. R. Holomb, M. Veres, V. Mitsa, J. Optoel. Adv. Mat. **11**, 917 (2009).
7. R. Holomb, V. Mitsa Solid State Commun. **129**, 655 (2004).
8. R. Holomb, V. Mitsa, P. Johansson, M. Veres, Phys. Status Sol. C **7**, 885, (2010).

EFFECT OF THE Ag IMPURITY ON LUMINESCENT AND LASER PROPERTIES OF THE RE³⁺ IONS IN BORATE GLASSESB. Padlyak^{1,2*}, I. Kindrat¹¹*University of Zielona Góra, Institute of Physics, Division of Spectroscopy of Functional Materials, Prof. Z. Szafrana Str. 4a, 65-516 Zielona Góra, Poland,*²*Vlokh Institute of Physical Optics, Department of Optical Materials, Dragomanov Str. 23, 79-005 Lviv, Ukraine*

The study of influence of the transitional metals' ions and metallic nanoparticles (or nanoclusters) on enhancement of the rare-earth (RE) photoluminescence (PL), including Gd³⁺, Eu³⁺, Er³⁺, and other RE³⁺ ions, represents a relatively novel and very interesting scientific and applied problem. Improving of PL intensity of several RE³⁺ ions (Er³⁺, Eu³⁺, Dy³⁺, Sm³⁺, Tb³⁺, and Gd³⁺) in different glasses, co-doped with silver due to processes of excitation energy transfer from Ag⁺ to the RE³⁺ ions were studied in [1–5]. In particular, recently was obtained intense narrow-band UVB emission ($\lambda_{\max} = 311$ nm) of the Gd³⁺ ions ($^6P_J \rightarrow ^8S_{7/2}$ transition) caused by resonant excitation energy transfer from Ag⁺ to Gd³⁺ ions in the Gd-Ag co-doped phosphate [4] and lithium tetraborate (Li₂B₄O₇) [5] glasses. During last decades also intensively investigated the enhancement of the Eu³⁺ red emission in the Eu-Ag co-doped glasses, including borate glasses due to the local-field surface plasmon resonance (SPR) effect caused by the metallic silver nanoparticles [6–9]. Therefore, further investigations are necessary for enhancement of intensity of the RE³⁺ luminescence in dielectric hosts (crystals and glasses) via their co-doping with transitional metals' ions and / or introducing nanoparticles of noble metals (Ag, Au, *etc.*), which reveal intense SPR absorption band in the visible spectral region.

For the first time the co-doped with rare-earth (RE = Eu, Er) and Ag Li₂B₄O₇ tetraborate glasses have been detailed investigated by us with usage conventional electron paramagnetic resonance (EPR) and optical spectroscopy techniques. Possible types of the Ag, Eu, and Er paramagnetic and luminescence centres, their electronic and local structures in the RE-Ag co-doped Li₂B₄O₇ glasses were proposed based on the obtained by EPR and optical spectroscopy results and corresponding published data of other authors. The optical absorption, emission, and luminescence excitation spectra as well as luminescence decay kinetics of the Ag⁺, Eu³⁺, and Er³⁺ centres in the Li₂B₄O₇:Eu,Ag and Li₂B₄O₇:Er,Ag glasses were detailed studied and analysed in our articles [9] and [10], respectively.

The Li₂B₄O₇ glasses of high chemical purity and optical quality, doped

*Corresponding and presenting author, e-mail: B.Padlyak@if.uz.zgora.pl

with Eu and / or Ag were obtained in the air atmosphere using conventional glass technology [9]. Spectroscopic properties of the obtained $\text{Li}_2\text{B}_4\text{O}_7:\text{Eu}$ and $\text{Li}_2\text{B}_4\text{O}_7:\text{Eu,Ag}$ glasses were investigated with usage optical absorption, photoluminescence (excitation, emission, decay kinetics), and measurements of external quantum yield (QY) via an absolute method. Photoluminescence spectra of the $\text{Li}_2\text{B}_4\text{O}_7:\text{Eu}$ glass reveal emission bands, which correspond to the $^5\text{D}_0 \rightarrow ^7\text{F}_J$ ($J = 0 \div 6$) transitions of Eu^{3+} ions. The enhancement of Eu^{3+} luminescence in the $\text{Li}_2\text{B}_4\text{O}_7:\text{Eu,Ag}$ glass have been observed. The QY of Eu^{3+} luminescence increases from 11.7% to 26.1% in the $\text{Li}_2\text{B}_4\text{O}_7:\text{Eu,Ag}$ glass in comparison with $\text{Li}_2\text{B}_4\text{O}_7:\text{Eu}$ glass. The observed luminescence enhancement is attributed to the energy transfer from Ag^+ ions and very small molecule-like non-plasmonic silver aggregates to the Eu^{3+} ions, as the major factor, and by local field effects induced by surface plasmon resonance of the silver metallic nanoparticles. The obtained high external quantum yield shows that the $\text{Li}_2\text{B}_4\text{O}_7:\text{Eu,Ag}$ glasses can be attributed to very perspective luminescent materials in the red spectral range.

The $\text{Li}_2\text{B}_4\text{O}_7$ glasses of high chemical purity and optical quality, doped with Er and co-doped with Er and Ag were obtained in the air using standard glass technology [10]. Spectroscopic properties of the $\text{Li}_2\text{B}_4\text{O}_7:\text{Er}$ and $\text{Li}_2\text{B}_4\text{O}_7:\text{Er,Ag}$ glasses were investigated using optical absorption and photoluminescence (excitation, emission, decay kinetics) experimental techniques as well as theoretical Judd–Ofelt analysis. The theoretical and experimental oscillator strengths for observed absorption transitions as well as Judd–Ofelt intensity parameters (Ω_2 , Ω_4 , and Ω_6) have been calculated. Photoluminescence spectra of the $\text{Li}_2\text{B}_4\text{O}_7:\text{Er}$ and $\text{Li}_2\text{B}_4\text{O}_7:\text{Er,Ag}$ glasses reveal intense infrared ($^4\text{I}_{13/2} \rightarrow ^4\text{I}_{15/2}$ transition, $\lambda_{\text{max}} = 1530$ nm) and green ($^4\text{S}_{3/2} \rightarrow ^4\text{I}_{15/2}$ transition, $\lambda_{\text{max}} = 546$ nm) emission bands. Radiative properties such as transition probabilities (A_{rad}), luminescence branching ratios (β), stimulated emission cross-sections (σ_{em}), and radiative lifetimes (τ_{rad}) have been estimated. Experimental and radiative lifetimes were compared and quantum efficiency (η) has been evaluated. Considerable enhancement of the Er^{3+} green luminescence in the $\text{Li}_2\text{B}_4\text{O}_7:\text{Er,Ag}$ glasses has been observed. These results show that the $\text{Li}_2\text{B}_4\text{O}_7:\text{Er,Ag}$ glasses belong to promising laser materials of the green spectral region.

Hence, the measured values of external quantum yield (QY) and calculated values of quantum efficiency (η) clearly show significant enhancement of the Eu^{3+} (red emission) and Er^{3+} (green emission) luminescence intensity in the $\text{Li}_2\text{B}_4\text{O}_7:\text{Eu,Ag}$ ($QY = 26.1$ %) and $\text{Li}_2\text{B}_4\text{O}_7:\text{Er,Ag}$ ($\eta = 25.7$ %) glasses in comparison with $\text{Li}_2\text{B}_4\text{O}_7:\text{Eu}$ ($QY = 11.7$ %) and $\text{Li}_2\text{B}_4\text{O}_7:\text{Er}$ ($\eta = 15.4$ %) glasses. The observed high values of the Eu^{3+} quantum yield of luminescence and Er^{3+} quantum efficiency of luminescence, respectively in the $\text{Li}_2\text{B}_4\text{O}_7:\text{Eu,Ag}$ and $\text{Li}_2\text{B}_4\text{O}_7:\text{Er,Ag}$ glasses have been explained by excitation energy transfer from Ag^+ to the Eu^{3+} and Er^{3+} ions and local field effects, which are induced by surface plasmon resonance of the metallic silver nanoparticles.

Acknowledgment

The Vlokh Institute of Physical Optics (Lviv, Ukraine) financially supported this work in the framework of scientific research project No. 0119U100357 of the Ministry of Education and Science of Ukraine. The University of Zielona Góra (Poland) supported the presentation of this work in the LTLA–2019 Conference.

References

- [1] C. Strohhöfer, A. Polman, Silver as a sensitizer for erbium, *Appl. Phys. Lett.* vol. 81 (2002) pp. 1414–1416.
- [2] J.A. Jiménez, S. Lysenko, H. Liu, Enhanced UV-excited luminescence of europium ions in silver/tin-doped glass, *J. Lumin.* vol. 128 (2008) p. 831–833.
- [3] J.J. Li, R.F. Wei, X.Y. Liu, H. Guo, Enhanced luminescence via energy transfer from Ag^+ to RE ions (Dy^{3+} , Sm^{3+} , Tb^{3+}) in glasses, *Opt. Express*, vol. 20 (2012) pp. 10122–10127.
- [4] José A. Jiménez, Enhanced UV emission of Gd^{3+} in glass by Ag^+ co-doping, *Mat. Lett.*, vol. 159 (2015) pp. 193–196.
- [5] B.V. Padlyak, A. Drzewiecki, T.B. Padlyak, V.T. Adamiv, I.M. Teslyuk, Resonant excited UV luminescence of the Gd^{3+} centres in borate glasses, co-doped with Gd and Ag, *Optical Materials*, vol. 79 (2018) pp. 302–309.
- [6] O.L. Malta, P.A. Santa-Cruz, G.F. De Sá, F. Auzel, Fluorescence enhancement induced by the presence of small silver particles in Eu^{3+} doped materials, *J. Lumin.* vol. 33 (1985) pp. 261–272.
- [7] T. Hayakawa, S.T. Selvan, M. Nogami, Field enhancement effect of small Ag particles on the fluorescence from Eu^{3+} -doped SiO_2 glass, *Appl. Phys. Lett.* vol. 74, (1999) pp. 1513–1515.
- [8] R.F. Wei, J.J. Li, J.Y. Gao, H. Guo, Enhancement of Eu^{3+} luminescence by Ag species (Ag NPs, ML-Ag, Ag^+) in oxyfluoride glasses, *J. Am. Ceram. Soc.* vol. 95 (2012) pp. 3380–3382.
- [9] I.I. Kindrat, B.V. Padlyak, B. Kukliński, A. Drzewiecki, V.T. Adamiv, Enhancement of the Eu^{3+} luminescence in $\text{Li}_2\text{B}_4\text{O}_7$ glasses co-doped with Eu and Ag, *J. Lumin.* vol. 204 (2018) pp. 122–129.
- [10] I.I. Kindrat, B.V. Padlyak, R. Lisiecki, V.T. Adamiv, I.M. Teslyuk, Enhancement of the Er^{3+} luminescence in Er–Ag co-doped $\text{Li}_2\text{B}_4\text{O}_7$ glasses, *Opt. Mater.* vol. 85 (2018) pp. 238–245.

EXCITON QUASIMOLECULES IN NANOHETEROSYSTEMS CONTAINING SEMICONDUCTOR AND DIELECTRIC QUANTUM DOTS: THEORY

S. Pokutnyi

*Chuiko Institute of Surface Chemistry, National Academy of Sciences of
Ukraine, 17 General Naumov Str., Kyiv 03164, Ukraine
e-mail: pokutnyi.serg@gmail.com*

The Ge/Si heterostructures promising to create new elements silicon infrared optoelectronics are self-assembled structures with Ge/Si nanoislands. Ge/Si heterostructures with quantum dots (QDs) of Ge are heterostructures II type. In this nanosystem the lowest electronic level is in matrix, and the lowest hole level is within volume of QD. A large shift of the valence band (610 meV) generates the localization of holes in the volume of QD. A significant shift of the conduction band (about 340 meV) is a potential barrier for electrons. The electrons move in the matrix and do not penetrate in the volume of QD [1]. During investigation of the optical properties of heterostructures Ge/Si with Ge QDs in experimental papers it was found that the electron can be localized above the surface of the QD while the hole here moves in the volume of the QD [1, 2].

Using the method of electron-beam lithography obtained heterostructures which are linear chains of QDs germanium on Si substrates. The average sizes of the QD Ge is less than 60 nm. It was noted that, at such a QD content in the samples, one must take into account the interaction between charge carriers localized above the QD surfaces [3].

In [4] we show that the biexciton formation in a nanoheterosystems made up of aluminum oxide QDS synthesized in a dielectric matrix is of threshold character and can occur in a nanosystem where the distance D between the surfaces of QD is given by the condition $D_c^{(1)} \leq D \leq D_c^{(2)}$. We also demonstrate that in such nanoheterosystems acting as “exciton molecules” (or biexciton) are the quantum dots of aluminum oxide with excitons localizing over their surfaces. The position of the biexciton state energy band is shown to depend both on the mean radius of quantum dots, and the distance between their surfaces, which enables one to purposefully control it by varying these parameters of the nanoheterosystems.

It is established that at constant concentrations of biexcitons at temperatures T below a certain critical temperature T_c due to the radiative annihilation of one of the excitons forming a biexciton one can expect a new spectral band of luminescence shifted relative to the exciton band by the biexciton binding energy E_b . This new luminescence band disappears at temperatures above T_c . At a constant temperature $T < T_c$ the growth of exciton concentration brings about weakening of the exciton band and strengthening of

the biexciton band of luminescence. As follows from the results of the variational calculations, the major contribution to the biexciton binding energy is from the energy of exchange interaction of electrons and holes, which by far surpasses that from their Coulomb interaction (i.e. the ratio ≤ 0.11) [4, 5].

A review devoted to the theory of exciton quasimolecules (formed of spatially separated electrons and holes) in a nanosystems that consists of semiconductor and dielectric QDS synthesized in a dielectric (or semiconductor) matrix [4 - 8]. It is shown that exciton quasimolecule formation is of the threshold character and possible in nanosystem, in with the spacing between the QDs surfaces is larger than a certain critical spacing. It was found that the binding energy of singlet ground state of exciton quasimolecule, consisting of two semiconductor QDs is a significant large values, larger than the binding energy of the biexciton in a semiconductor single crystal almost two orders of magnitude [5 - 8].

The Ge/Si heterostructures promising to create new elements silicon infrared optoelectronics are self-assembled structures with Ge/Si nanoislands [1, 2]. Ge/Si heterostructures with quantum dots (QDs) of Ge are heterostructures II type. In this nanosystem the lowest electronic level is in matrix, and the lowest hole level is within volume of QD. The electrons move in the matrix and do not penetrate in the volume of QD. During investigation of the optical properties of heterostructures Ge/Si with Ge QDs in experimental papers it was found that the electron can be localized above the surface of the QD while the hole here moves in the volume of the QD.

Using the method of electron-beam lithography obtained heterostructures which are linear chains of QDs germanium on Si substrates. The average sizes of the QD germanium is less than 60 nm. It was noted that, at such a QD content in the samples, one must take into account the interaction between charge carriers localized above the QD surfaces [3].

Within the framework of the modified effective mass method, the theory of an exciton quasimolecule (formed from spatially separated electrons and holes) is developed in nanosystems consisting of germanium quantum dots grown in silicon matrices. In an artificial quasi-molecule, the holes are located in the volumes of germanium quantum dots, and the electrons, moving in a silicon matrix, are localized above the spherical surface of germanium quantum dots. The variational method is used to derive the dependences of the total energy, as well as the binding energy of the ground singlet state of the exciton quasimolecule, as a function of the distance D between the surfaces of the quantum dots, as well as the radius a of the quantum dot [6, 7].

It is shown that the main contribution to the binding energy of an exciton quasimolecule is made by the energy of the exchange interaction of an electron with holes, which substantially exceeds the contribution that causes the energy of the Coulomb interaction of an electron with holes. It

has been established that the appearance of an exciton quasimolecule in a nanosystem has a threshold character, and possibly in a nanosystem in which the distance D between the surfaces of quantum dots exceeds the value of a certain critical distance $D_c^{(1)}$.

In [6, 7], the theory of an exciton formed by spatially separated electron and hole is developed (the hole moves in the bulk of a germanium QD and the electron is localized above the spherical interface between the QD and the silicon matrix). It was found that the binding energy of an exciton in such nanosystem is much higher (almost an order of magnitude) than the binding energy of an exciton in a Si single crystal. A theory of exciton quasimolecule (formed from spatially separated electrons and holes) in nanosystems that consist of germanium quantum dots synthesized in a silicon matrices is developed [6, 7].

It was found that the binding energy of singlet ground state of exciton quasimolecule, consisting of two germanium quantum dots is a significant large values, larger than the binding energy of the biexciton in a silicon single crystal by almost two order of magnitude [6, 7].

It is shown that an excitonic quasimolecule in a nanosystem can exist only at temperatures below a certain critical temperature T_c . At temperatures below the critical temperature $T < T_c$, the exciton quasimolecule splits into two artificial atoms (from space-separated electrons and holes). It has been established that the binding energy of the ground singlet state of an exciton quasimolecule, consisting of two quantum dots of germanium, is an essential quantity that exceeds the binding energy of biexciton in a silicon single crystal by almost two orders of magnitude.

At a constant temperature $T < T_c$ the growth of exciton concentration brings about weakening of the exciton band and strengthening of the biexciton band of luminescence. As follows from the results of the variational calculations, the major contribution to the biexciton binding energy is from the energy of exchange interaction of electrons and holes, which by far surpasses that from their Coulomb interaction (i.e. the ratio ≤ 0.08) [6,7].

Such an effect opens up the possibility of using the exciton quasimolecules as active medium in nanolasers emitting in the infrared region and operating on exciton transitions at room temperatures in the elementary base of quantum nanocomputers.

1. A.I. Yakimov, A.V. Dvurechenskiy, A.I. Nikiforov, *JETP Lett.* **72**, 267 (2000).
2. A.I. Yakimov, A.V. Dvurechenskiy, A.I. Nikiforov, *JETP Lett.* **73**, 598 (2001).
3. J.V. Smagina, A.V. Dvurechenskiy, V.A. Seleznev, *Semiconductors* **49**, 767 (2015).
4. S.I. Pokutnyi, *J. Nanophoton.* **10**, 036008 (2016).
5. S.I. Pokutnyi, *Ukr. J. Phys. Opt.* **17**, 91 (2016).
6. S.I. Pokutnyi, *Optical Engineering*, **56**, 091603 (2017).
7. S.I. Pokutnyi, *Optical Engineering*, **56**, 067104 (2017).
8. S.I. Pokutnyi, *Low Temp. Phys.* **44**, 819 (2018).

INFRARED OPTICAL EXTINCTION IN HEAVILY DOPED CdTe:Cr SINGLE CRYSTALS

V. Popovych¹, P. Potera², M. Kuzma²

¹ *Department of Technological and Professional Education, Ivan Franko
Drogobych State Pedagogical University, Ivan Franko str. 24, 82100,
Drogobych, Ukraine; e-mail: vpopovych@yahoo.com*

² *Centre for Innovation and Transfer of Natural Sciences and Engineering
Knowledge, University of Rzeszow, Pigoia str. 1, 35-959, Rzeszow, Poland*

Cadmium telluride has a variety of applications in optical devices, such as electro-optic modulators, photorefractive components and windows for IR detectors and high-power lasers [1]. Discovery of oscillation from tetrahedrally coordinated Cr²⁺ ions in this compound stimulated interest to its doping with chromium in order to obtain a material for tunable mid-IR lasers. Concentration of substitutional Cr of the order 10¹⁹ cm⁻³ at the cation sites of CdTe lattice is needed to provide the required parameters. Room-temperature lasing in the 2 – 3 μm range has been reported from CdTe:Cr single crystals grown by Bridgman method [2]. Also, doping through thermal diffusion process was found to be an effective way to reach high Cr²⁺ content in polycrystalline CdTe:Cr windows [3]. In this paper an optical extinction in the near- and mid-IR range of spectra for the vapour grown CdTe:Cr crystals is studied.

The samples for the investigations were prepared from the CdTe single crystals, grown by the modified physical vapour transport method from the pre-synthesized charge [4]. The charge was prepared from the (Cd,Cr)Te polycrystalline ingots with 0.5, 2.5 and 5 at.% of chromium in the initial feed, which were synthesized from the melt [5]. As-grown crystals were cleaved into the wafers, and rectangular platelets with (110)-oriented wide surfaces were cut from them by a wire saw. The cleavages and the lateral faces of the samples were chemo-mechanically polished with bromine solution in the ethyleneglycol-dimethylformamide mixture, followed by rinsing in bi-distilled water and boiling in high-purity CCl₄. The transmission IR spectra were recorded using a UV-Vis-NIR CARY 5000 spectrophotometer from Agilent Technologies. The measurements were conducted at room temperature.

Extinction spectra were calculated from the experimentally obtained IR transmission spectra using the relation:

$$T = \frac{(1 - R)^2 e^{-\varepsilon d}}{1 - R^2 e^{-2\varepsilon d}} \quad (1)$$

Hence, the extinction coefficient:

$$\varepsilon = \frac{1}{d} \frac{(1 - R)^2 + \sqrt{(1 - R)^4 + 4T^2 R^2}}{2T}, \quad (2)$$

here d is the sample thickness and R is the reflectivity for the single reflection at normal incidence of the beam. The reflectivity R can be calculated by the formula:

$$R = \frac{(n-1)^2 + k^2}{(n+1)^2 + k^2}, \quad (3)$$

where n is the refractive index, $k = \alpha / 4\pi\nu$ is the extinction coefficient, and ν is the frequency of the incident beam. For the comparatively thick samples used in this study, the values of determined from the measurements were rather small; therefore, the second terms in the numerator and denominator in expression (3) can be disregarded. The refractive index was calculated by the empiric formula given in [6].

As can be seen from Fig. 1, the dependence of the extinction spectra on the nominal doping level is nonlinear in both the transparency region of CdTe (Fig. 1a) and in its optical absorption edge (Fig. 1b).

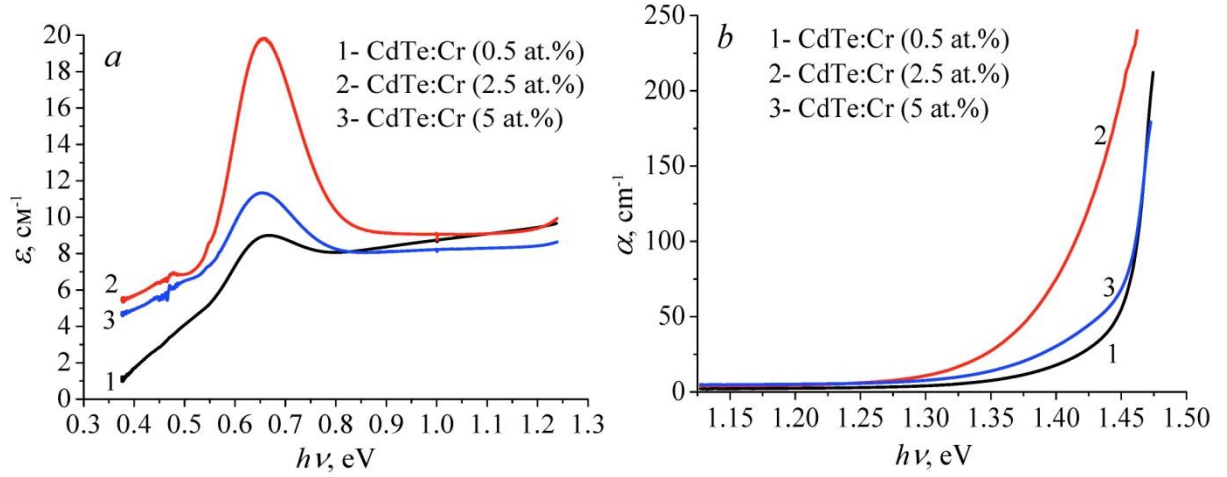


Fig. 1. Extinction spectra in the transparency region of CdTe (a) and optical absorption edge (b) of the CdTe:Cr samples

It was established that the spectral motion of the extinction coefficient in the transparency region of CdTe is determined by two processes and can be written in the form:

$$\varepsilon = \alpha + \sigma, \quad (4)$$

where α is the absorption coefficient, and σ is the scattering coefficient.

The scattering of the incident radiation occurs on the intermetallic chromium telluride precipitates, which has been detected in the grown crystals by electron microscopy and EDX methods [7]. Their density and mean size were found to be the highest for the medium doped material. The scattering can be described by the expression:

$$\sigma \sim (h\nu)^m, \quad (5)$$

where the coefficient $m > 0$. On the background of such monotonic dependence, selective peaks with a maximum at photon energy of approximately 0.65 eV are clearly indicated. It is known [7] that they are caused by the transitions between

the states $^5T_2 \rightarrow ^5E$ of Cr^{2+} ion that arise as a result of the splitting of its ground state when cadmium is replaced with chromium in CdTe crystal lattice.

Concentrations of the substitutional Cr ions, involved in the formation of $Cd_{1-x}Cr_xTe$ solid solution, can be estimated from the maximum of the absorption peaks by subtracting the scattering level. The following values were obtained: $N_{Cr} = 5.01 \cdot 10^{18} \text{ cm}^{-3}$ for the sample prepared from the charge with 2.5 at.% of nominal Cr content, $N_{Cr} = 1.56 \cdot 10^{18} \text{ cm}^{-3}$ for the sample prepared from the charge with 5 at.% of nominal Cr content and $N_{Cr} = 7.22 \cdot 10^{17} \text{ cm}^{-3}$ for the sample prepared from the charge with 0.5 at.% of nominal Cr content. For the same sample the most significant expansion of the Urbach absorption tail and shift of the absorption edge to the long-wave side were observed, which is apparently associated with so-called “elastic” interaction [8]. The lower Cr^{2+} concentration in the highest doped crystals comparing to the medium doped ones can be explained by gettering of the dopant into Te-rich inclusions during growth of the crystals with 5 at.% of nominal Cr content [4].

It can be concluded from the presented results that only a small fraction of added Cr atoms occupy anionic positions in the CdTe crystalline lattice, thus forming $Cd_{1-x}Cr_xTe$ solid solution. Because of poor solubility of chromium in the CdTe matrix, most of them are precipitated during the crystals growth and post-growth cooling, developing dopant-enriched second phase particles. However, the concentration of Cr^{2+} ions in the CdTe:Cr crystals, grown from the charge with 2.5 at.% of nominal dopant content, is sufficient for their use as a material for tunable mid-IR lasers.

- [1] R. Triboulet, P. Siffert, CdTe and Related Compounds; Physics, Defects, Hetero- and Nano-Structures, Crystal Growth, Surface and Applications. Part II: Crystal Growth, Surface and Applications, Elsevier Ltd., Amsterdam, 2010.
- [2] A.G. Bluiett, U. Hömmerich, R.T. Shan, S.B. Trivedi, S.W. Kutcher, C.C. Wang, J. Electron. Mater. 31 (2002) 806.
- [3] U. Hömmerich, I.K. Jones, Ei Ei Nyein, S.B. Trivedi, J. Cryst. Growth 287 (2006) 450.
- [4] V.D. Popovych, P. Sagan, M. Bester, B. Cieniek, M. Kuzma, J. Cryst. Growth. 426 (2015) 173.
- [5] V.D. Popovych, P. Sagan, M. Bester, M. Wierzbinska, M. Kuzma, J. Mater. Sci. 51 (2016) 4618.
- [6] P. Hlídek, J. Bok, R. Grill, J. Appl. Phys. 90 (2001) 1672.
- [7] J.T. Vallin, G.A. Slack, S. Roberts, A.E. Hughes, Phys. Rev. B 2 (1970) 4313.
- [8] M.Z. Cieplak, M. Godlewski, J.M. Baranowski, Phys. Stat. Sol. (b) 70 (1975) 323.

X- And Q-BAND ELECTRON PARAMAGNETIC RESONANCE SPECTROSCOPY OF Co-DOPED YAP CRYSTAL

I. Stefaniuk

*Faculty of Mathematics and Natural Sciences, University of Rzeszow,
Pigonia 1, Rzeszow, Poland
istef@ur.edu.pl*

1. Introduction

Yttrium aluminum perovskite YAlO_3 (YAP) crystals doped with rare-earth ions (Nd^{3+} , Tm^{3+} , Er^{3+}) belong to the most important solid-state laser materials [1], as well as they are also promising materials for scintillators (YAP:Ce) [2], and as substrates for thin films epitaxy layers [3]. Co-doped oxide crystals are attractive materials for eye-safe laser operation near $1.5 \mu\text{m}$ and as nonlinear absorbers for passive Q-switching [3].

The structural data indicate that YAP crystallizes in orthorhombically distorted perovskite structure [4,5]. The space group D_{2h}^{16} was chosen to describe the symmetry of the unit cell in YAP crystals using the Pbnm group coordinate system [5]. The structure of YAP can be represented as a grid of tilted AlO_6 octahedra with the Y ions occupying the empty space between the octahedra. The AlO_6 octahedra may be considered to be only slightly distorted. The YO_8 dodecahedra are considerably distorted [4].

2. EPR spectra

Electron paramagnetic resonance (EPR) spectra in a wide range of temperatures from 5-300 K using an EPR X- and Q-band spectrometer (Bruker multifrequency and multiresonance FT-EPR ELEXSYS E580) were investigated. The angular dependences of EPR spectra were studied using a one-degree goniometer (see fig. 1). Quantitative analysis of EPR spectra has been carried out using the program EMR-NMR [6] assuming spin Hamiltonian for a triclinic site symmetry. An extension of the computer program Superposition Model-Monte Carlo (SPM-MC) [7-9] designed for modeling of the spectroscopic and structural properties of transition ions at low symmetry sites in crystals was used. The predicted zero-field splitting (ZFS) parameters, obtained based on the SPM model, confirm the correlation between the ZFS parameters obtained from experimental EMR spectra and structural data.

3. SPIN HAMILTONIAN AND SPM ANALYSIS OF EMR SPECTRA

The only naturally abundant Co isotope is ^{59}Co with the nuclear spin $I = 7/2$. The electronic ground state of free Co^{2+} ($3d^7$) ion is ^4F , which splits in an octahedral crystal field into two orbital triplets $^4\text{T}_1$ and $^4\text{T}_2$, and a higher singlet $^4\text{A}_2$ (see [10–13]). Further splitting of the ground triplet $^4\text{T}_1$ due to the

spin-orbit coupling results in the lowest Kramers doublet with an electronic effective spin $S = 1/2$.

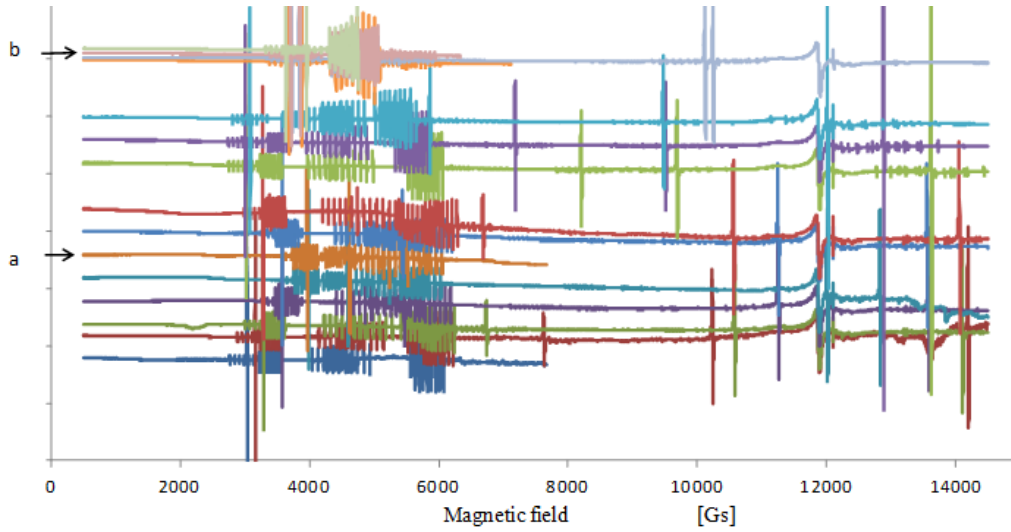


Fig.1. Angular dependence of the Q-band EPR spectra with the magnetic field in the b–a plane (at 20 K)

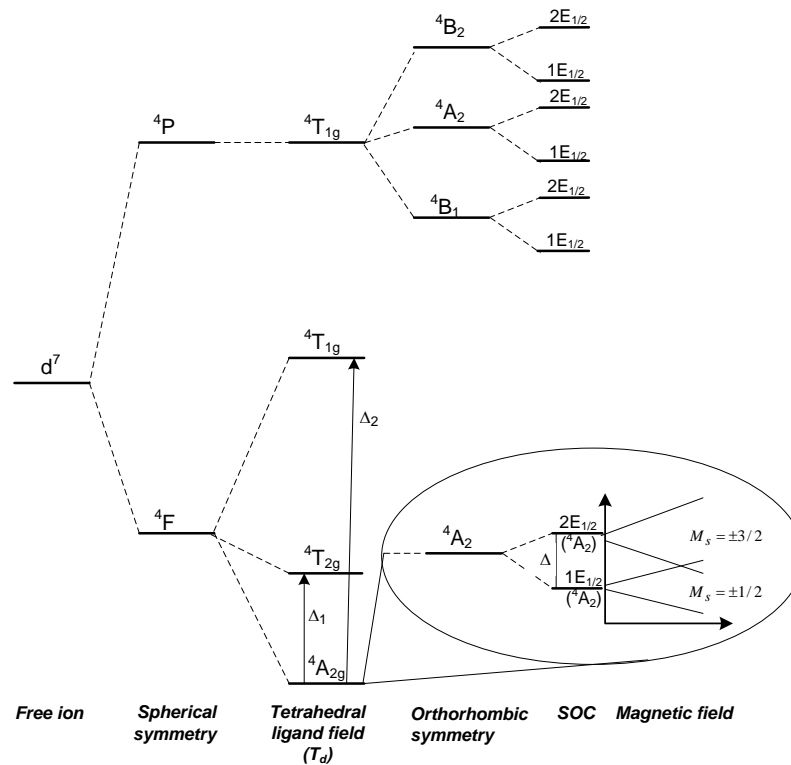


Fig. 2. Crystal-field energy levels diagram showing the origin of the fictitious spin $S' = 1/2$ from the effective spin $S = 3/2$ arising from the action of the spin-orbit coupling due to the large ZFS for the four-coordinated Co^{2+} ions in YAP [14]

This yields EPR spectra of $^{59}\text{Co}^{2+}$ ($S = 1/2$) ions with a large anisotropic g-tensor and consisting of eight hyperfine structure components due to $I = 7/2$ [10].

$$H = \mu_B B \cdot g \cdot S + S \cdot A \cdot I \quad (1)$$

Likewise, irrespective of the nature of the spin, for a paramagnetic spin $S = 3/2$ system, like Co^{2+} ($S = 3/2$), only the 2nd-rank ZFS terms exist, which for orthorhombic and lower symmetry may be expressed in the principal axis system (PAS) of the 2nd-rank ZFS terms, i.e. the D-tensor, as [10]:

$$H_{\text{ZFS}} = D(S_z^2 - \frac{1}{3}S(S+1)) + E(S_x^2 - S_y^2), \quad (2)$$

where the conventional ZFSPs D (axial) and E (rhombic) are related to those in the Stevens notation. The origin of the fictitious spin $S' = 1/2$ for $\text{Co}^{2+}:\text{YAlO}_3$ is illustrated in Fig. 2 [14].

4. Summary and Conclusions

We have used EMR spectroscopy at X- and Q-band, combined with superposition model (SPM) calculations to reveal electronic structure and establish correlations between structure, and surroundings of these complexes.

Using SPM–MC and crystallographic data, the ZFS parameters b_2q and b_4q are calculated for Co^{2+} ions ($S=3/2$) at the YAlO_3 site. Based on the obtained ZFS values, the angular dependence of the EPR spectrum was made. The relationship between the angular spectrum of the EPR spectrum in the X- and Q-band was compared, resulting in very high compliance. The interplay between the fictitious spin $S' = 1/2$ and the effective spin $S = 3/2$ for $\text{Co}^{2+}(3d^7)$ ions is considered. A better understanding of the spectroscopic properties of Co^{2+} ($S = 3/2$) ions in YAP crystal may be achieved due to the application of the SPM/Crystal Field approach.

References

- [1] A.A. Kaminskii, Laser Crystals, Springer, Berlin (1990).
- [2] A.J. Wojtowicz, J. Glodo, A. Lempicki, C. Brecher, J. Phys. Condens. Matter 10 (1998) 8401–8415.
- [3] A. Senyshyn, L. Vasylechko, Acta Phys. Polon. A 124 (2) (2013) 329–335.
- [4] L. Vasylechko, A. Matkovskii, D. Savytski, A. Suchocki, F. Wallrafen, J. Alloys Compd 291 (1–2) (1999) 57–65.
- [5] R. Diehl, G. Brant, Mater. Res Bull. 10 (1975) 85–90.
- [6] D.G. McGavin, M.Y. Mombourquette, J.A. Weil, Computer Program EPR–NMR ver. 6.5, University of Saskatchewan, Canada (2002).
- [7] I. Stefaniuk, C. Rudowicz, Curr. Top. Biophys. 33 Suppl. A (2010) 217–220.
- [8] I. Stefaniuk, C. Rudowicz, Nukleonika 58 (3) (2013) 397–400.
- [9] I. Stefaniuk, Opto-Electronics Review, vol 26, 2, (2018) 81–91.
- [10] A. Abragam, B. Bleaney, Electron Paramagnetic Resonance of Transition Ions, Clarendon (1970).
- [11] S. Altshuler, B.M. Kozyrev, Electron Paramagnetic Resonance in Compounds of Transition Elements, Wiley (1974).
- [12] F.E. Mabbs, D. Collison, Electron Paramagnetic Resonance of d Transition-Metal Compounds, Elsevier (1992).
- [13] J.R. Pilbrow, Transition-Ion Electron Paramagnetic Resonance, Clarendon (1990).
- [14] D. Piwowarska, S.M. Kaczmarek, P. Gnutek, C. Rudowicz, Acta Phys. Pol. A, 132 (2017) 73.

HIGH PRESSURE STUDIES OF PHOSPHOR MATERIALS

A. Suchocki^{1,2}¹ *Institute of Physics, Polish Academy of Sciences, Al. Lotników 32/46, 02-668 Warsaw, Poland*² *Institute of Physics, Kazimierz Wielki University, Weyssenhoffa 11, 85-072 Bydgoszcz, Poland***Abstract**

Pressure is one of the fundamental thermodynamic variables, which allows for precise changing (decreasing) the interatomic distances of materials. Therefore the strength of the crystal field experienced by emitting ions can be this way effectively increased resulting in changes of electronic structures of host materials and dopant ions. This leads to transformation of luminescence spectra of phosphors. Several examples of such effects will be presented. It will be shown, for example, that pressure: (i) transforms a broad-band luminescence of Cr^{3+} ions in low-strength crystal-field materials (e.g., $\text{LiNbO}_3:\text{Cr}$) into a sharp line type spectrum, due to a replacement of the Cr^{3+} first excited state from the strongly coupled to the lattice $^4\text{T}_2$ state to weakly coupled 2E state [1].

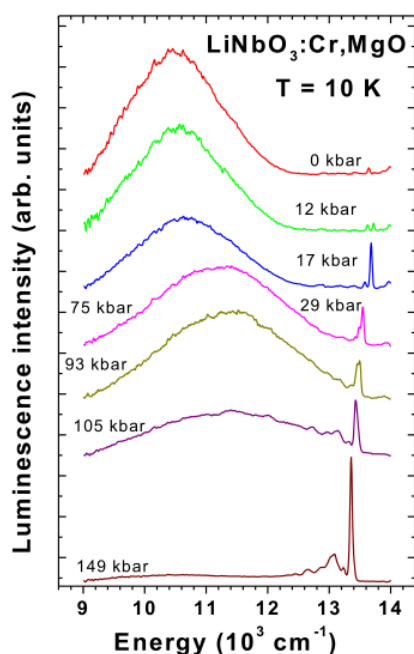


Fig. 1. The pressure dependence of the Cr^{3+} luminescence in near-stoichiometric $\text{LiNbO}_3:\text{Cr},\text{MgO}$ crystal [1]

(ii) changes non-luminescent at ambient pressure materials doped with Ce^{3+} (e.g., $\text{GGG}:\text{Ce}$) into highly efficient emitting ones, which is associated with removal of degeneracy of the $5d\text{ Ce}^{3+}$ level with conduction band of host [2];

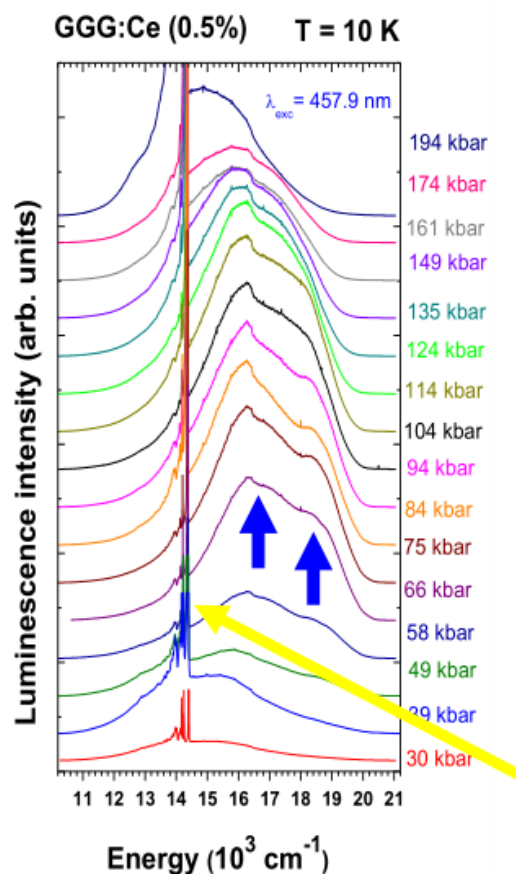


Fig. 2. The pressure dependence of the PL spectra of Ce^{3+} in GGG crystal

(iii) causes quenching of Mn^{2+} luminescence in certain materials (e.g., $\text{NaScSi}_2\text{O}_6:\text{Mn}$) due to pressure-induced crossing between $^4\text{T}_{1g}$ and $^2\text{T}_{2g}$ excited states [3].

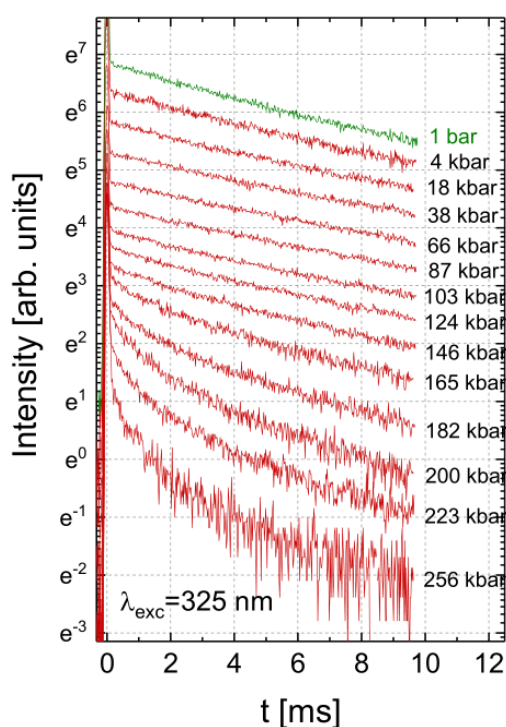


Fig. 3. Pressure dependence of the luminescence decay kinetics of Mn^{2+} in jervisite [3]

Pressure also shifts positions of certain luminescence bands changing effectively the color of emission. In this way high pressure, which can be applied in precise and controlled way, allows to check and establish the best conditions for obtaining the desired luminescence properties of the material for practical applications.

References:

- [1]. A. Kamińska, A. Suchocki, M. Grinberg, L. Arizmendi, D. Callejo, F. Jaque, Spectroscopy of near-stoichiometric LiNbO₃:MgO,Cr crystals under high pressure, *Phys. Rev. B.* 62, 10802-10811 (2000).
- [2]. A. Kamińska, A. Duzynska, M. Berkowski, S. Trushkin, A. Suchocki, Pressure induced luminescence of cerium doped gadolinium gallium garnet crystal, *Phys. Rev. B* 85, 155111 (2012)
- [3]. J. Barzowska, Zhiguo Xia, D. Jankowski, D. Włodarczyk, K. Szczodrowski, Chong-Geng Ma, M.G. Brik, Ya. Zhydashchevskii, and A. Suchocki, High pressure studies of Eu²⁺ and Mn²⁺ doped NaScSi₂O₆ clinopyroxenes, *RSC Advances* 7, 275 (2017).

SECTION 2. DEVELOPMENT OF LASERS AND LASER SYSTEMS

SIMULATION OF INSTRUMENTAL SPECTRA CdZnTe-DETECTORS FOR MEASURING THE INTRINSIC GAMMA- RADIATION OF SPENT NUCLEAR FUEL

O. Banzak, G. Banzak

*Odessa state academy of technical regulation and quality
65020, Odessa, Ukraine, street of Kuznechnay, 15*

As a result of passage gamma-radiation through detector and the subsequent processing of received signal, it is possible to obtain an instrumental spectrum, which is a direct reflection of the interactions gamma-rays with the detecting medium. It provides primary information used for further analysis of gamma radiation.

The instrumental spectrum is complex because of the peculiarities gamma-radiation detection by proportional detectors. In addition, there are both natural and technological limitations on how accurately the detection system can register the energy of gamma-radiation. The natural limitation arises mainly due to statistical fluctuations associated with charge formation processes in the detector. The positions of the total absorption peaks can also be distorted by such electronic effects as noise, imposition of pulses, incorrect installation of the “pole-zero” scheme, etc.

In addition, real gamma-ray spectrum of a sample may differ significantly from the spectra obtained under laboratory conditions.

When developing the methodology, the statement was used that linear irreversible transformations of the space of instrumental spectra correspond to changes in measurement conditions, and the spectrum of the i -th component under arbitrary measurement conditions can be represented as:

$$\varphi(a) = \sum_{i=0}^L a_i \varphi_i(a), \quad \sum a_i = 1, \quad (1)$$

where $\varphi_i(a)$ – are linearly independent spectra obtained during preliminary measurements, and the coefficients are the same for all components.

The technique for modeling the instrumental spectra is based on the following procedures:

1. The spectrum of isotopes with a large number of lines is represented as a linear combination of monoenergetic spectra taking into account the quantum yield in the "narrow beam" geometry; self-absorption in fuel assemblies is not taken into account for each isotope.

2. Simulates the change in the monoenergetic spectrum due to the interaction with the material of the technological environment and the fuel matrix.

3. The first and second procedures are used to form the instrumental spectra of a mixture of isotopes.

To represent the Compton distribution $\mu(E, E_i)$, we used method of statistical tests (Monte Carlo method), which is most effective when considering the transfer of radiation in a substance due to the statistical nature of this process. This is explained by the fact that elementary scattering events take place on a free electron and, therefore, the properties of crystal are not significant. In addition, the scattering has a continuous spectrum of secondary particles and need more statistics for its correct representation. Therefore, it is optimal to use Monte Carlo method, in which the random motion of a particle is considered as a certain trajectory, and its state at each focal point is played using random numbers from the corresponding distributions. It is shown that modern algorithms for the implementation of this method allow to achieve simulation accuracy up to 1-2% [1, 2].

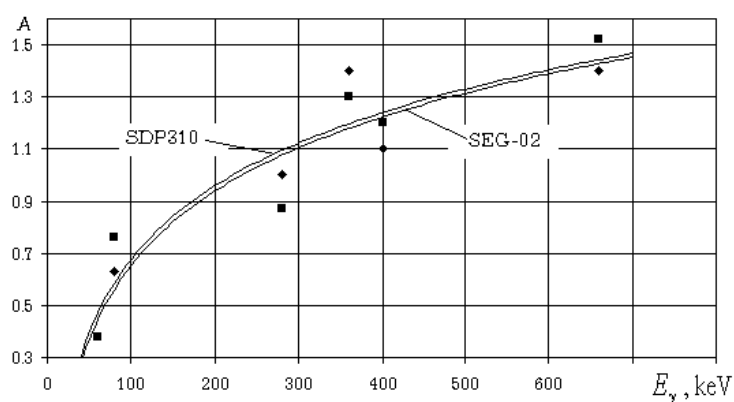


Fig. 1. The dependence of the parameter A , which determines the amplitude of function F_t , on energy of detected radiation: 1 – prototype crystal with quasispherical contact design; 2 – prototype crystal with planar contact design.

On the basis of the developed methodology and experimentally determined spectrometer characteristics, hardware spectra were simulated under various measurement conditions with subsequent processing of the obtained model spectra.

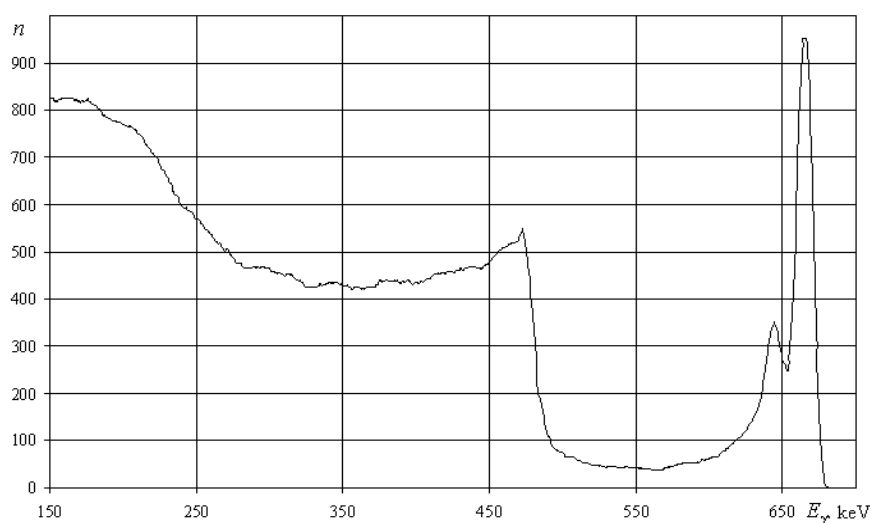


Fig. 2. Model of the instrumental spectrum when measuring a ^{137}Cs point source

To verify correctness of implementation, spectrum of a ^{137}Cs point source was simulated with the superposition of random noise (Fig. 2). For comparison, figure 3 shows the measured ^{137}Cs spectrum from a set of gamma-ray spectra. A characteristic feature of the model is a more pronounced peak in region of the maximum energy of Compton electrons.

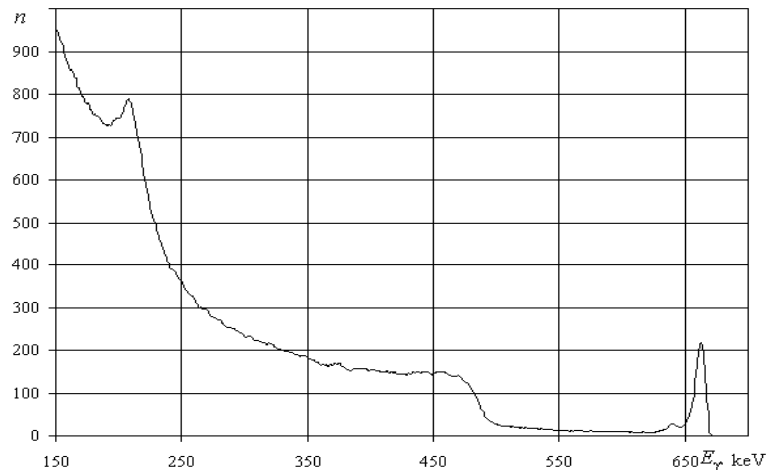


Fig. 3. Instrumental spectrum when measuring a point source ^{137}Cs .

A technique has been developed for modeling the instrumental spectra obtained by measuring the intrinsic gamma radiation of spent nuclear fuel with different burnup depths and the degree leaks of the fuel cladding. The spectrum model of the analyzed fuel assembly allowed us to determine sensitivity of the measurements and select optimal algorithm for processing the spectra. Due to this, the cost of developing the hardware and software components of the nuclear fuel condition monitoring system has been reduced.

This method differs from the known ones in that it did not use the simulation of distribution of electric field strength in the crystal volume of the sensor and did not use the Monte Carlo method to simulate electric charge induced during the primary interaction of gamma-radiation with the crystal.

Experimental verification of the methodology using example of modeling spectrum of the ^{137}Cs source confirmed the effectiveness uses of the spectrometer based on the CdZnTe-detector created in this work: compliance with requirements of monitoring the state of nuclear fuel in real time; identification of fuel assemblies containing fuel elements with a non-hermetic casing; determining fuel burnout based on fission product activity.

1. Banzak O.V. Poluprovodnikovyye detektory novogo pokoleniya dlya radiatsionnogo kontrolya i dozimetrii ioniziruyushchikh izlucheniy / O.V. Banzak, O.V. Maslov, V.A. Mokritskiy: Pod red. V.A. Mokritskogo, O.V. Maslova. – Monografiya. – Odessa, 2013. – Izd-vo «VMV». – 220 c.
2. Banzak O.V. Metodika proyektirovaniya tsifrovogo gamma-spektrometra / O.V. Banzak, A.V. Karpenko, O.V. Maslov, V.A. Mokritskiy // Sistema obrobki informatsii. – №1 (108). – Kharkiv, 2013. – S. 35-38.

ANGULAR SELECTIVE MULTILAYER DIELECTRIC STRUCTURE

S. Ilchenko, R. Lymarenko, V. Taranenko

*International Center “Institute of Applied Optics”
National Academy of Sciences of Ukraine
Kyiv, Ukraine*

The well-known SPR element on prism has wide application in sensorics [1]. The metal-multilayer structure instead thin metal layer expanding opportunities such devices for TE-polarized light and laser modulation [2, 3]. Further developing such structure is shown the perspective for using as intracavity laser angular selectors.

We propose the structure that consist of several dielectric layers, like Bragg mirror, with replacing the metal layer by boron carbide (B_4C). The peculiarity of this material is existence of the essential value of imaginary part of refractive index. For example, the relative permittivity (dielectric constants) of boron carbide at 532 nm wavelength is $\epsilon_1 = 9.9363$ and $\epsilon_2 = 3.8244$. Another material with similar behavior is titanium carbide (TiC) with refractive index $n = 2.9791$ and extinction coefficient $k = 2.4644$ at 532 nm.

The structure of sample is: the layer of B_4C put on fused silica 45-degree prism, which is following by three pair of high and low index dielectric layers of TiO_2 and SiO_2 . The thickness of boron carbide layer is about 20 nm and 25 nm for titanium carbide. Dielectric layers have 90 and 140 nm thickness respectively except last layer that 300 nm.

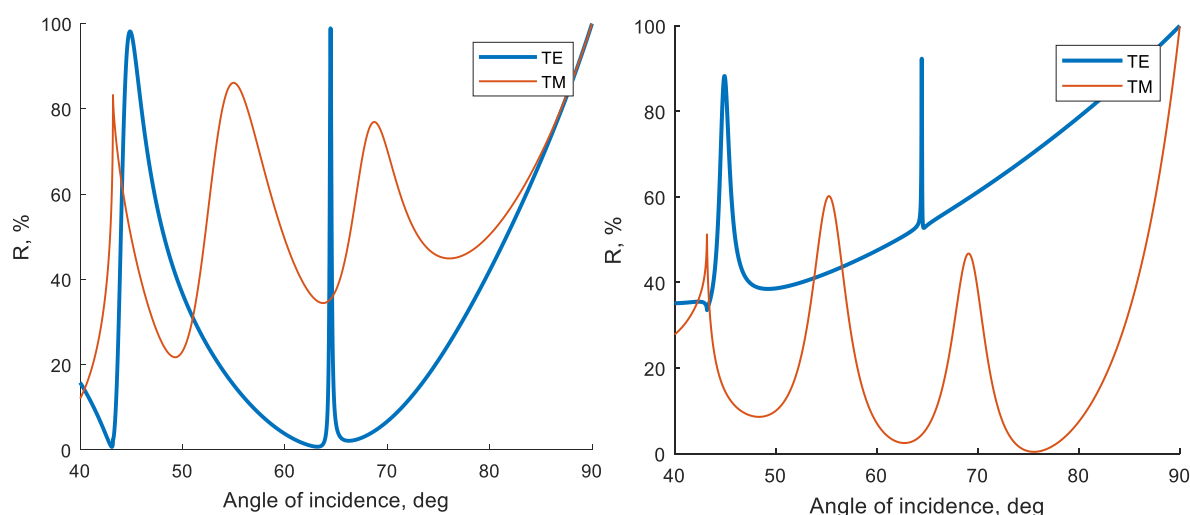


Fig. 1. The reflectance coefficient vs angle of incidence for TE and TM polarization for boron carbide (left) and titanium carbide (right)

The reflectance coefficient of this structure is shown on Fig. 1. The narrow peak at angle of incidence equal 67.1° is present for TE polarization. The width of peak is about 0.2° . The structure with titanium carbide has pick at TE-polarization and minima at TM- polarization.

Figure 2 shows the reflectance coefficient vs wavelength and incident angle. The line with a different inclination is represent the resonance with peak.

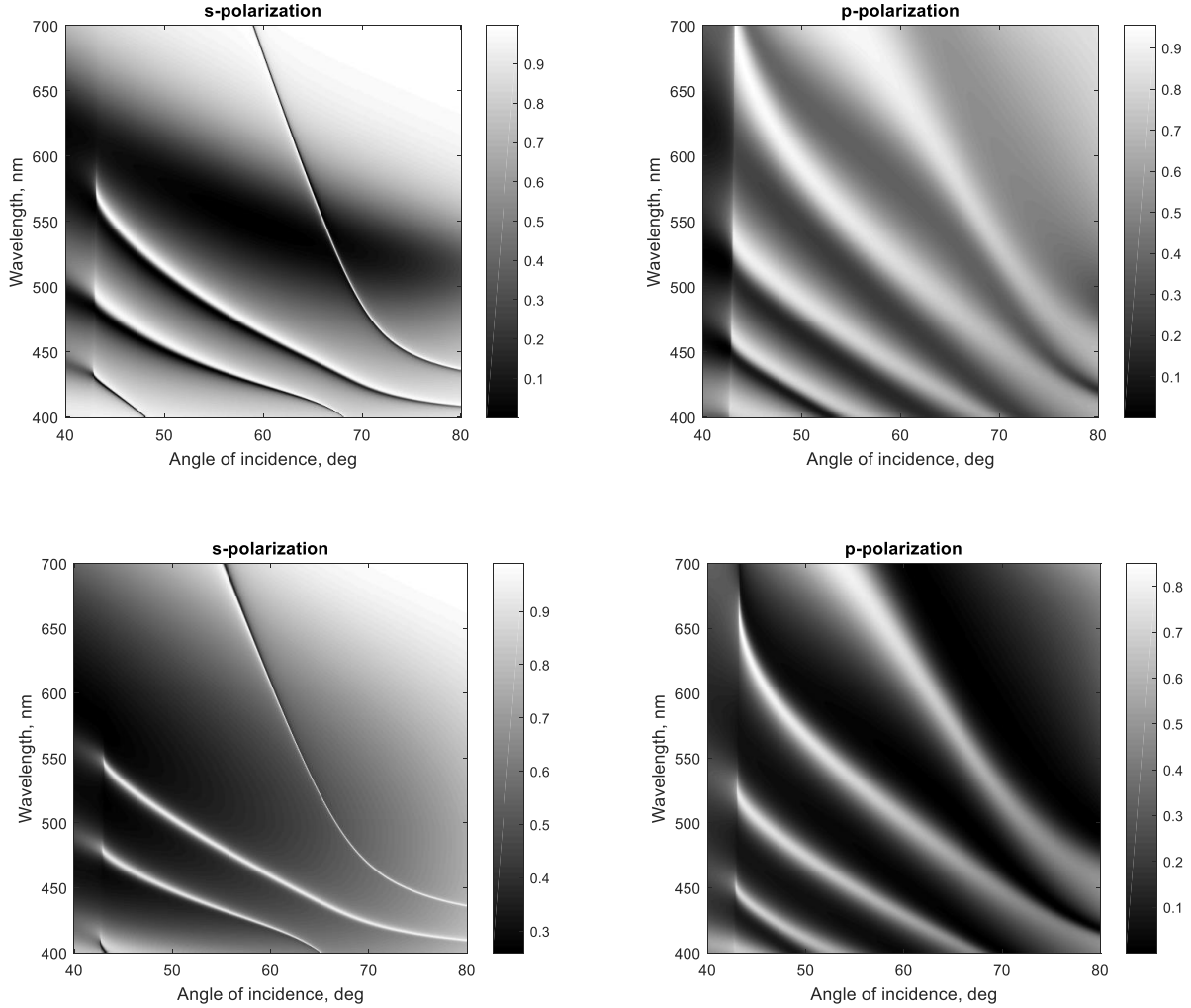


Fig. 2. The reflectance coefficient vs wavelength and incident angle: boron carbide (top) and titanium carbide (bottom).

The properties of proposed structure allow to discuss the possibility use it for laser angular selector. The optical scheme of wide-aperture laser with proposed structure as angular selectors is shows on Fig. 3. The coupling and output mirror are deposited on the sides of the prism, the multilayer structure is coating on hypotenuse.

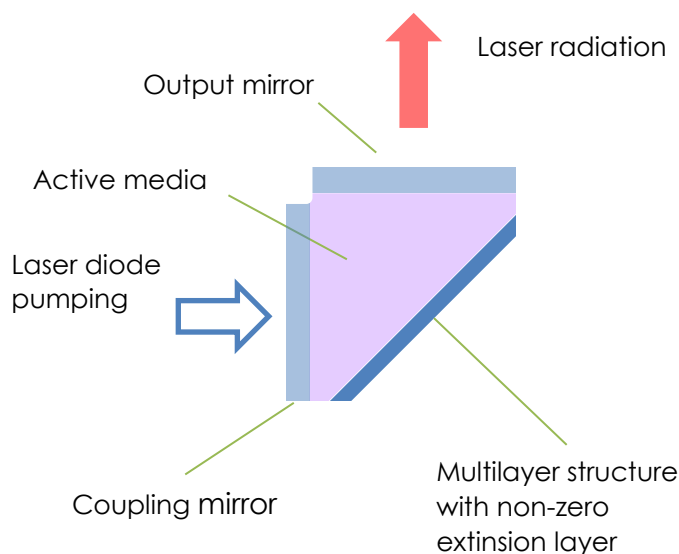


Fig. 3. The model of wide-aperture laser with proposed structure as angular selector

Summary

The combination of the layer with imaginary part of dielectric permittivity (like boron carbide or titanium carbide) and unmatched half-wavelength resonators allows to control the spectral selectivity, which give opportunities for the practical use of the proposed structures not only to improve the sensors, but also to develop the internal cavity laser angular selectors. Proposed structure has narrower angle width of resonance in reflectance. Such advantages of described structure lead to more flexible control of laser mode generation.

References

1. Piliarik M., Homola J. Surface plasmon resonance (SPR) sensors: approaching their limits? 2009, Opt. Express 17(19):16505-16517. DOI:10.1364/OE17.016505.
2. Svitlana Ilchenko, Ruslan Lymarenko, Victor Taranenko, Using Metal-Multilayer-Dielectric Structure to Increase Sensitivity of Surface Plasmon Resonance Sensor, 2017, Nanoscale Research Letters 12(1), DOI: 10.1186/s11671-017-2073-1.
3. Svitlana Ilchenko, Ruslan Lymarenko, Victor Taranenko, Metal-Multilayer-Dielectric Structure for Enhancement of s- and p-Polarized Evanescent Waves, 2016, Nanoscale Research Letters 11(1), DOI: 10.1186/s11671-016-1274-3.

DEVELOPMENT OF COMPACT ENERGY-EFFICIENT PULSE LASERS ON CERAMIC FOR LASER-LOCATION SYSTEMS OF GROUND AND SPACE BASE

A. Ostroukh, R. Lymarenko, V. Taranenko

*International Center "Institute of Applied Optics"
National Academy of Sciences of Ukraine*

One of the methods for generating subnanosecond and picosecond laser pulses is the use of semiconductor modulators. [1]. Their advantages are small thickness and short relaxation time, which allow formation high-frequency picosecond laser pulses. Compact, energy-efficient pulsed lasers on ceramics are designed for use in laser positioning systems for ground and space applications.

A typical laser design on a semiconductor modulator [2] is shown in Fig. 1. Fig. 1, right shows semiconductor modulator of type SESAM (semiconductor saturable absorber mirror) of 3×3 mm size.

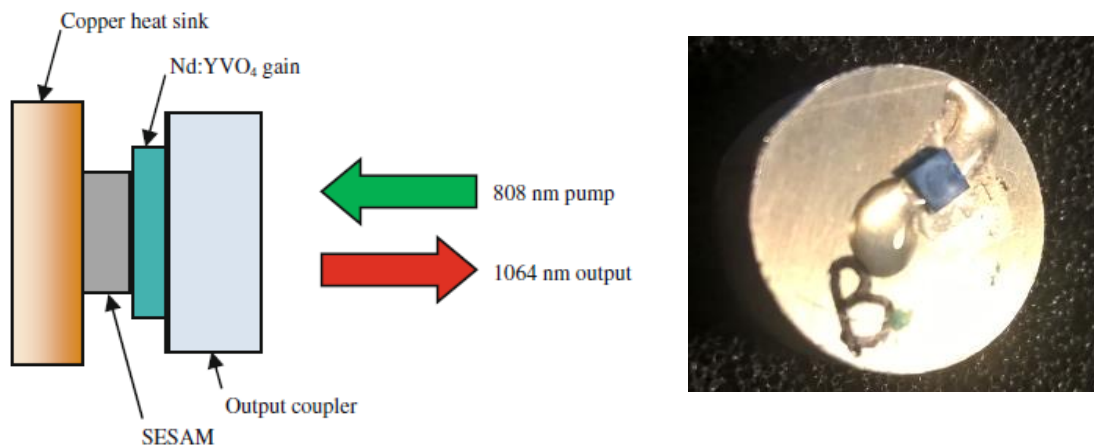


Fig. 1. (Left) Scheme of a laser with semiconductor modulator. (Right) Semiconductor modulator glued to aluminum base for heat dissipation.

To measure the modulation parameters of the semiconductor modulator, an experimental scheme was assembled (Fig. 2). A semiconductor modulator (5) is illuminated by pulses with a duration of 1 ns from a microchip laser with an energy of 1 mJ. Lens (6) serves to regulate the energy that enters the modulator through the diaphragm (7). The radiation of a cw laser (2) with a power of 100 mW is sent to SESAM as a probe beam. The Thorlabs DET10A/M high-speed photodetector (8) measures the change in the SESAM reflectance; the photodetector (9) receives the synchronization pulse signal. The signals are observed on an oscilloscope (10) Tektronix TDS-2022B.

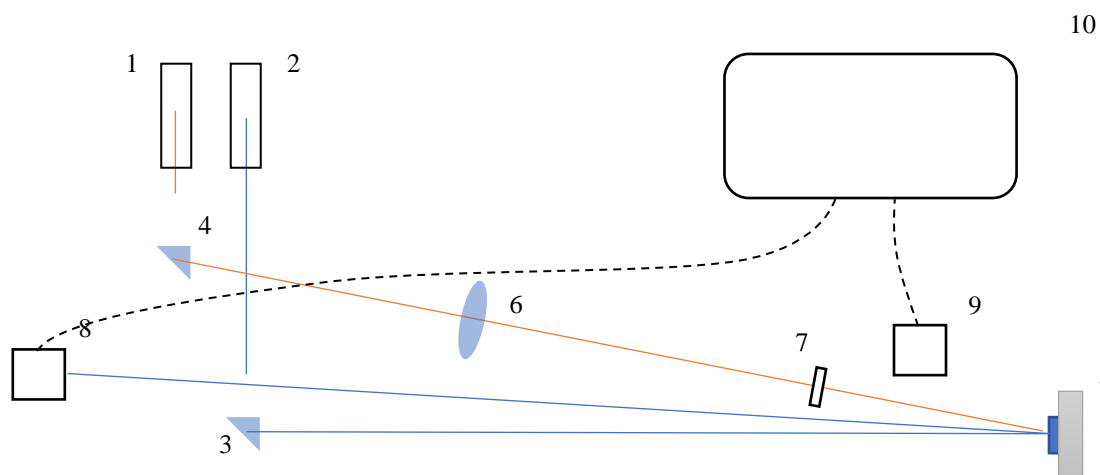


Fig. 2. Measurement of semiconductor modulator characteristics: 1-pulse microchip laser 1064 nm, 2 - continuous laser 1064 nm, 3, 4 - prisms, 5 - SESAM, 6 - lens, 7 - aperture, 8, 9 - photodetectors, 10 – oscilloscope

The results of measurements are shown in Fig. 3

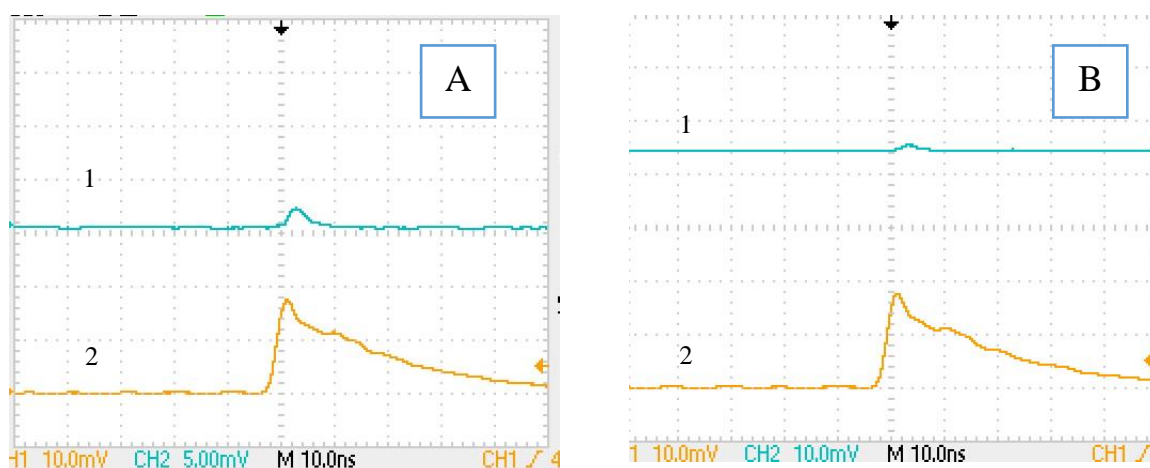


Fig. 3. Oscillograms of the probe beam (1) (change in the reflection coefficient of SESAM) and the laser pulse (2): sample A (left) and sample B (right).

As a result of the measurements we obtained the following values (Table 1)

Table 1

Parameter	Sample A	Sample B
Initial reflection coefficient, %	44	60
Modulation*, %	>10	>3
Threshold, mJ/cm ²	< 0.1	<0.1

* when illuminated by an impulse of 0.3 mJ/cm².

The laboratory model of a pulsed laser with a semiconductor modulator was created. The schematic diagram is shown in Fig. 1, left. The focused radiation of a laser pumping diode with a wavelength of 808 nm passes through a dichroic mirror and focuses on the active element Nd:YVO₄. The output mirror of the resonator has a transmittance of 0.1, a semiconductor modulator (SESAM) is used as a mirror of the resonator.

To achieve more sharp focus, a circuit with a dichroic mirror located between the collimator and the focus is used.

In the laboratory model an active element of 10 mm in length was used which corresponds to the length of laser pulses of about 3 ns. When reducing the length of the resonator (using an active element in the thickness of 0.3 - 1 mm), the length of the laser with impulses is projected to be 50 - 200 ps.

To measure the lengths of subnanosecond laser pulses, an autocorrelator was developed and assembled. To amplify laser pulses, a multi-pass amplifier based on a Nd:YAG crystal of 20×10×2 mm size with two side pumping diodes of pump MONOCROM LB-80P01-60QCW-2 with 270 W power was developed.

The work was carried out within the framework of the project 0118U004271 of the Target Complex Program of the National Academy of Sciences of Ukraine for Scientific Space Research 2018-2022.

Conclusion

The laboratory model of a laser with a promising semiconductor modulator for generating subnanosecond laser pulses is investigated. The characteristics of a semiconductor modulator are obtained experimentally. Created autocorrelator for measuring laser pulses from 10 to 1000 ps. An experimental sample of an amplifier of laser pulses was developed.

References

1. U. Keller. Ultrafast solid-state laser oscillators: a success story for the last 20 years with no end in sight. Appl Phys B (2010) 100: 15–28.
2. A. Cabasse, G. Martel and J.L. Oudar. High power dissipative soliton in an Erbium-doped fiber laser mode-locked with a high modulation depth saturable absorber mirror. 2009 / Vol. 17, No. 12 / OPTICS EXPRESS.
3. D. Nodop, J. Limpert, R.Hohmuth, W.Richter, M.Guina, and A. Tünnermann. High-pulse-energy passivelyQ-switchedquasi-monolithic microchip lasers operating inthe sub-100-ps pulse regime. 2007 / Vol. 32, No. 15 / OPTICS LETTERS.

SUPER-COLLIMATION BY CIRCULAR GRATING PAIR

R. Lymarenko¹, D. Gailevicius², V. Purlys², M. Peckus²,
K. Staliunas³, V. Taranenko¹

¹International center “Institute of Applied Optics” NAS of Ukraine,

²Laser Research Center, Vilnius University, Lithuania

³Universitat Politècnica de Catalunya, Spain

We demonstrate numerically and experimentally effect of a strong enhancement of on-axis components of a Gaussian beam (super-collimation) at the diffraction on a pair of identical circular gratings which are located coaxially at a short and fixed distance from each other.

One of the options for specifying the circular grating is determined by the following dependence of the phase modulation φ on the radius r :

$$\varphi(r) = \eta \cdot \pi \left(1 + \cos \left(\frac{2\pi r}{d} + \varphi_0 \right) \right)$$

where φ_0 is the initial phase of the structure, d is the structure period, η is the modulation coefficient. For the relief gratings the phase of the structure is related to the height of the relief h according to formula $\varphi(r) = 2\pi(n-1)h(r)/\lambda$, where n is the refractive index of the grating material, λ is the wavelength.

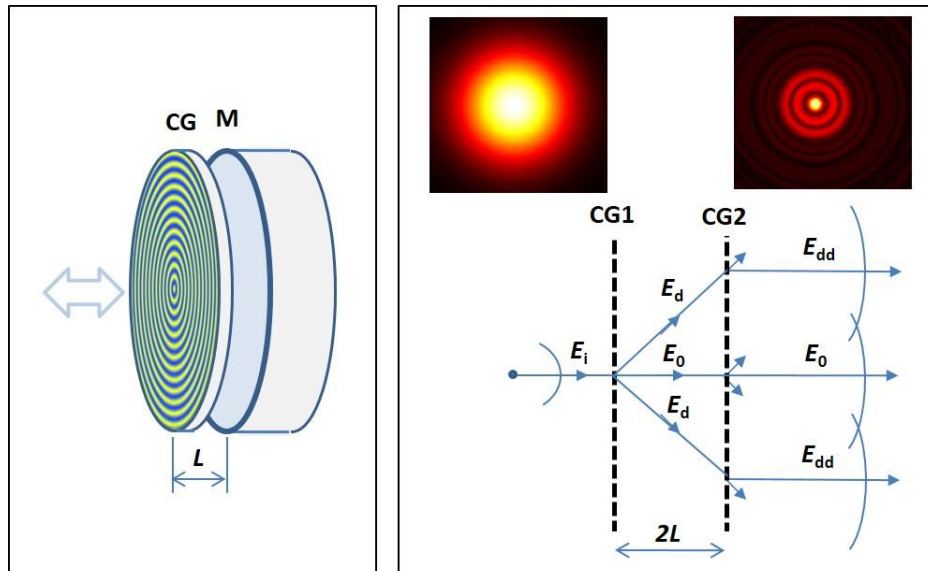


Fig. 1. Structure of circular grating in tandem with mirror (left). Collimation of diverging incident beam E_i at double diffraction on equivalent configuration of circular grating pair CG1 and CG2 (right). Arrows denote axes of diverging beams. Angular spectra of incident (top left) and double diffracted (top right) beams normalized to the maximum intensity.

We consider here effect of double diffraction of Gaussian laser beam on a pair of identical circular gratings at a distance $2L$ from each other (Fig. 1, right), which is an unfolded equivalent of a circular grating near highly reflective mirror at a distance L (Fig. 1, left). We assume that reflection from the grating is negligible, that is the grating is purely transmissive type. The first grating creates a conical diffraction order beam E_d of angle $\beta = \text{asin}(d/\lambda)$ to the grating axis. The interaction of this conical beam with the second grating produces a ring-shaped double diffraction beam E_{dd} propagating in the initial beam direction (parallel to the axis). Constructive interference of the zero-order beam E_0 and ring-shaped double diffracted beam E_{dd} produces a narrow pick of intensity in the far field.

The numerically and experimentally obtained enhancement of on-axis components of the angular spectrum of a Gaussian beam as it passes through the pair of circular gratings is shown in Fig. 2. Note that this effect of super-collimation was observed earlier for 3D axisymmetric photonic crystals [1].

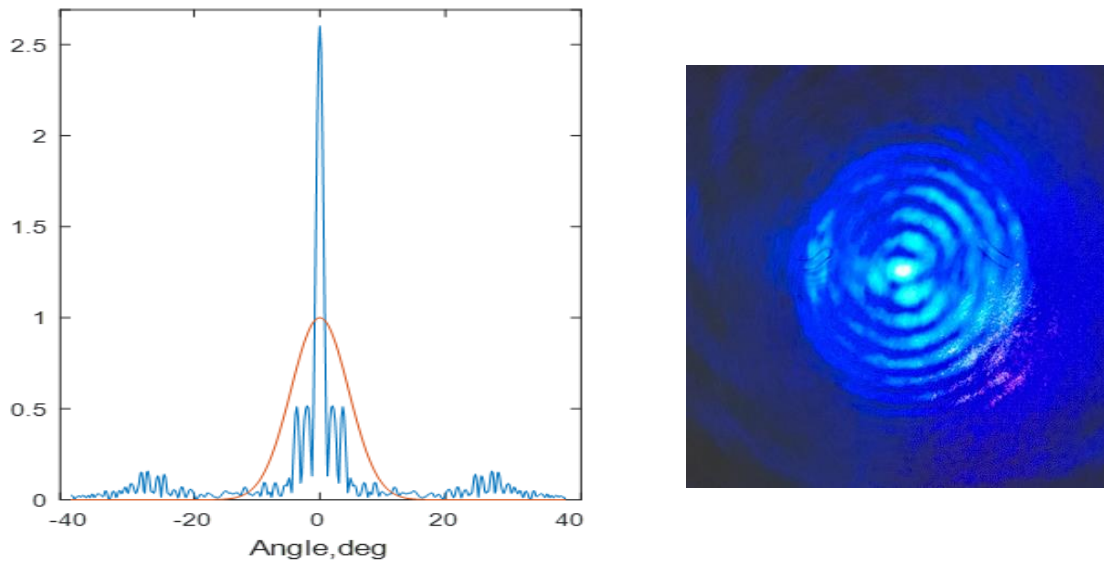


Fig. 2. Transformation of angular spectrum of a Gaussian beam at double diffraction on a pair of circular structures (effect of super-collimation) obtained numerically (left) and experimentally (right).

This research was carried out in the framework of the joint Ukrainian-Lithuanian project No 0118U004986 “High brightness photonic crystal microchip laser”.

[1] V. Purlys, L. Maigyte, D. Gailevicius, M. Peckus, R. Gadonas, and K. Staliunas, “Super-collimation by axisymmetric photonic crystals”, *Appl. Phys. Lett.* **04**, 221108 (2014)

MICROCHIP LASER WITH INTRACAVITY CIRCULAR GRATING

R. Lymarenko¹, D. Gailevicius², V. Purlys², M. Peckus²,
K. Staliunas³, V. Taranenko¹

¹International center “Institute of Applied Optics” NAS of Ukraine,

²Laser Research Center, Vilnius University, Lithuania

³Universitat Politècnica de Catalunya, Spain

Lasers with a short resonator length such as diode pumped rare-earth ions microchip lasers exhibit a number of remarkable features: they operate in single longitudinal mode regime and can generate picosecond pulses at Q-switching, they are compact, simple and cheap. However, the shorter the resonator length the smaller is its aperture for the single-transverse mode operation. For this reason, such lasers have relatively low output power and brightness. Therefore, the search for means to increase the output power and brightness of microlasers is an actual problem, especially if one takes into account that conventional means cannot be applied in this case.

One of the ways to increase the microchip laser brightness is using the axisymmetric three-dimensional photonic crystal structure inside the multimode cavity with extended pump area [1]. The axisymmetric photonic crystal has ring shaped forbidden gap in the angular spectrum, due to which it fulfills suppressing tilt angular components of the multimode laser beam. This reduces the divergence of laser beam and improves beam quality.

Here we propose using more simple two-dimensional circular grating placed inside the microlaser cavity near one of the mirrors for the brightness enhancement. For simulation of the circular grating effect on the formation of transverse structure in a wide-aperture laser with the plane-parallel cavity we consider scheme shown on Fig. 1 (M_1 and M_2 are plane mirrors, A is the gain medium, CG is the circular grating). Let's start from M_1 plane with arbitrary initial field u_0 (random noise). The L is the cavity length, Δ is the distance from CG to the mirror M_2 . The propagation operator T_1 calculates the field u_1 at CG plane: $u_1(x, y) = T_{L-\Delta}[u_0(x, y) \cdot A(x, y)]$. Then we applied the phase mask $D(x, y)$ corresponding the circular grating and next propagation operator calculate the field u_2 at the mirror M_2 : $u_2(x, y) = T_{\Delta}[u_1(x, y) \cdot D(x, y)]$. Complete round-trip pass of the cavity consists of 4 stages: $T_1 - T_4$. Repeating these steps, we get the time evaluation of transversal field distribution in the laser cavity. The amplitude-phase mask $A(x, y)$ represents the laser gain, losses

and saturation per one pass. For example, A-class laser can be described as follows:

$$A = \frac{\text{gain}}{1 + |u|^2/\text{saturation}} - \text{losses}$$

The propagation function may be written via Fourier transform (split-step method) or derived from diffraction integral.

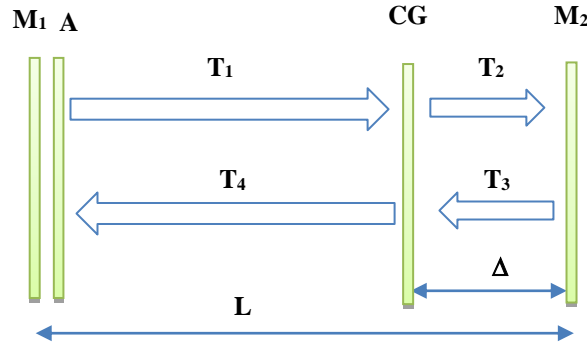


Fig. 1. Scheme of plane parallel cavity with gain and circular grating.

For numerical calculations we represent aperture as matrix of small squares. Then the result of field propagation u_{nm} in free space at distance z can be represent as

$$u_{n,m} = \sum_n \sum_m W_{nn'mm'} \cdot u_{n'm'}.$$

Indexes (n, m) and (n', m') correspond the destination (x, y) and initial (ξ, η) planes respectively. This expression can be simplified:

$$u_{n,m} = \sum_n W_{nn'} \sum_m W_{mm'} \cdot u_{n'm'}$$

due to the properties of W kernel:

$$W_{nn'mm'} = W_{nn'} \cdot W_{mm'}.$$

The expression W for numeric calculation is

$$W_{nn'} = \chi \cdot f[U(x_n - \xi_{n'} - \Delta x/2, z), U(x_n - \xi_{n'} + \Delta x/2, z)],$$

$$\xi = \frac{1-i}{\sqrt{2\pi}},$$

$$f(U_1, U_2) = \xi \int_{U_1}^{U_2} \exp(i\mu^2) d\mu,$$

$$U(x, z) = \text{sign}(x) \sqrt{\sqrt{x^2 + z^2} - z}.$$

Y-component $W_{mm'}$ is defined the same way. Results of simulation are shown in Fig. 2.

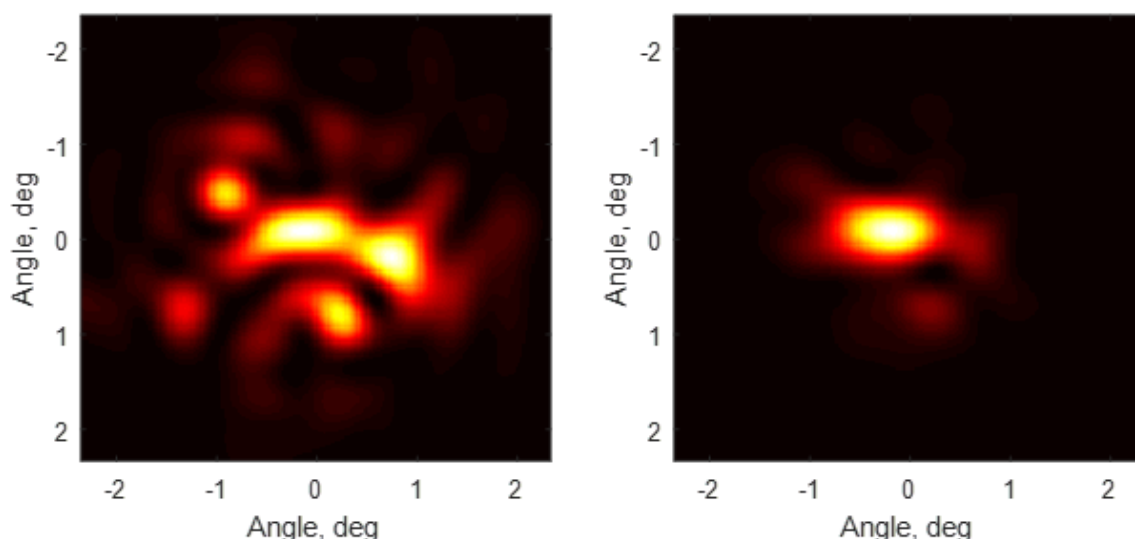


Fig. 2. Results of numerical simulation for far field laser intensity profiles without (left) and with (right) intracavity circular grating.

The surface relief grating with circular structure of $2\ \mu\text{m}$ period and $3\ \text{mm}$ diameter was fabricated by the electron beam lithography method on transparent polycarbonate slab. The grating was placed inside the cavity of diode pumped ($808\ \text{nm}$) microchip laser on Nd:YAG ceramics as shown in Fig. 3, left. The experimentally observed transverse distribution of laser beam intensity in the far field without (Fig. 3, middle) and with (Fig. 3, right) the circular grating is in qualitative agreement with theoretical predictions.

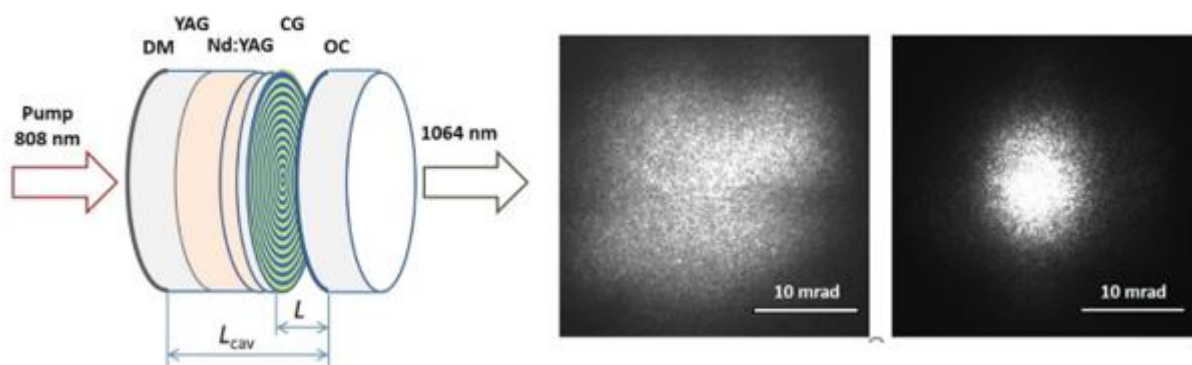


Fig. 3. Microchip laser design (left). Far field intensity distribution for microchip laser without (middle) and with (right) circular grating inside laser cavity.

This research was carried out in the framework of the joint Ukrainian-Lithuanian project No 0118U004986 “High brightness photonic crystal microchip laser”.

[1] D. Gailevicius, V. Koliadenko, V. Purlys, M. Peckus, V. Taranenko, K. Staliunas. “Photonic Crystal Microchip Laser”. *Sci. Rep.* **6**, 34173 (2016).

LASER EMITTING BEAM WITH ROTATING VORTICES

Ye. Krasnoshchekov, V. Yaparov, V. Taranenko

*International center "Institute of Applied Optics" NAS of Ukraine,
e-mail: yaparovvv@i.ua*

Lasers generate a rich variety of optical spatio-temporal structures depending on the nonlinearity of the gain medium and cavity configuration. In laser cavities characterized by a high Fresnel number those structures can be complex, even chaotic [1], while for a low laser Fresnel number they are stationary Laguerre-Gaussian modes. There are moderate laser Fresnel numbers for which spatially regular and rotating intracavity laser structures can exist. Such structures were observed experimentally in single frequency laser-like photorefractive oscillators with intracavity focusing elements [2-4]. This cavity configuration sets the formation of transverse modes of different longitudinal order families overlapping both in space and in frequency domains. In this case the rotational dynamics of the intracavity field is due to the mechanism of beating between transverse modes of different families.

In this work we demonstrate numerically and experimentally another possibility to generate laser beam with rotating structures which consist of vortices belonging to the same family of transverse modes and having the same polarization state. Vector rotating structures with frequency degenerate vortices were studied in [5] for an isotropic laser.

We consider spontaneous formation of spatio-temporal optical field structures in a single-frequency laser whose cavity is composed of plane mirrors and contains no focusing elements. A circular diaphragm with radius r is used to control the cavity Fresnel number $N_F = r^2 / L\lambda$ (L is the cavity length and λ is the laser wavelength). In this cavity configuration the transverse modes are nearly degenerated in frequency and therefore different longitudinal order families of transverse modes cannot be overlapped. For such a laser the averaging of the intracavity optical field structure over the longitudinal coordinate can be used. For class A laser, for which lifetimes of the population inversion and polarization of the active medium (transverse relaxation) are negligibly small compared with lifetime of the intracavity light field relaxation, the modified scalar laser equation has the following form:

$$\frac{\partial E}{\partial t} = g_0 \frac{E}{(1 + |E|^2)} + (1 + id)\nabla_{\perp}^2 E - \eta E, \quad (1)$$

where $E(x, y, t)$ is the transverse optical field envelope averaged over the longitudinal coordinate, x, y are the transverse coordinates normalized to the width of the effective Fresnel zone, $w_F = \left[L\lambda / 4\pi(1 - R) \right]^{1/2}$, where R is the

product of the cavity mirror reflectivity coefficients, t is the time normalized to the lifetime of light field in the laser cavity, g_0 is the unsaturated gain coefficient of the active medium, d is the coefficient of diffraction normalized to the coefficient of diffusion, $\nabla_1^2 = \partial^2/\partial x^2 + \partial^2/\partial y^2$, η is the coefficient of the intracavity losses.

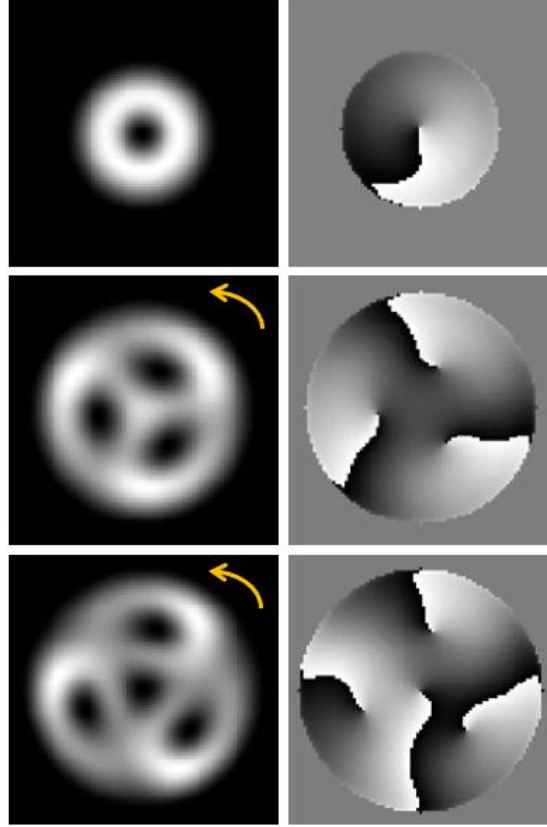


Fig. 1. Transverse distribution of laser beam intensity (left column) and phase (right column) depending on cavity Fresnel number. Arrows indicate direction of rotation.

The transverse boundary conditions are defined at the edge of the circular diaphragm which is modeled by the η parameter in the form of the six-order super-Gaussian function of the radius r . The initial conditions have been specified as a random noise which starts formation of the transversely structured vector laser field.

As expected, the solutions of Eq. (1) for a low Fresnel number have the form of Laguerre-Gaussian modes of zero-order LG_0^0 and first-order LG_0^1 (Fig. 1, top row). The latter, also called optical vortex, has a helical structure of the wave front and is characterized by a topological charge ± 1 . At higher Fresnel numbers three-vortex (Fig. 1, middle row) and four-vortex structures (Fig. 1, bottom row) form, which are rotating with permanent speed around beam axis. The vortices in the rotating structures have the same charge and frequency and are synchronized in phase.

In the experiment we use a unidirectional two-wave-mixing photorefractive

oscillator on the crystal of strontium-barium niobate (SBN) with ring cavity composed of four plane mirrors. This oscillator behaves as a class A laser [6], although the light amplification mechanism in it is completely different from the laser light amplification mechanism. It operates on a single longitudinal mode and has degenerated in frequency transverse modes. In this oscillator, formation of the transverse structures with vortices were observed (Fig. 2). The first-order Laguerre-Gaussian mode (Fig. 2, left) forms at a small size of the intracavity diaphragm. When the size of the diaphragm increased slightly, the formation of rotating three- (Fig. 2, middle) and four-vortex structure was observed (Fig. 2, right). These experimental results are consistent with the above calculations.

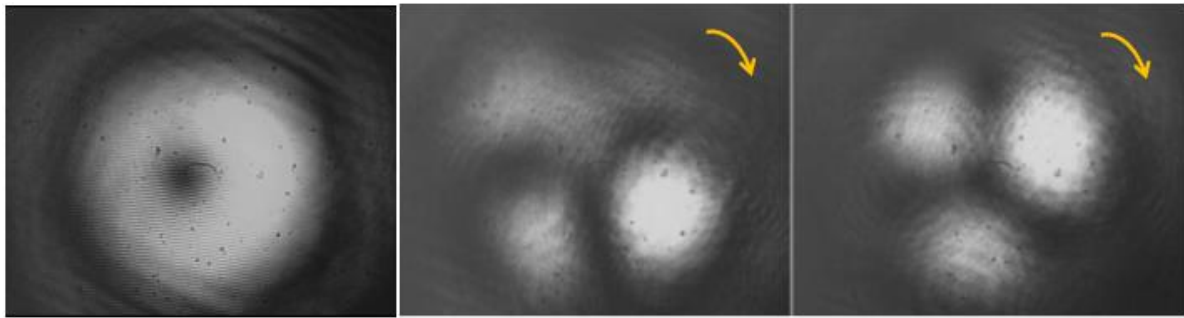


Fig. 2. Experimentally observed first order Laguerre-Gaussian mode (left), rotating three-vortex (middle) and four-vortex (right) modes. Arrow indicates direction of rotation.

[1] F.T. Arecchi, S. Bocaletti, P.L. Ramazza, S. Residori, “Transition from boundary- to bulk-controlled regimes in optical pattern formation”, *Phys. Rev. Lett.* 70, 2277-2280 (1993).

[2] M. Vaupel and C.O. Weiss, “Circling optical vortices”, *Phys. Rev. A* 51, 4078-4085 (1995).

[3] C.O. Weiss, M. Vaupel, K. Staliunas, G. Slekyš and V.B. Taranenko, “Vortices and solitons in lasers”, *Appl. Phys. B*, 68, 151-168 (1999).

[4] S.J. Jensen, R. Nicolaus and C. Denz, “Spatial-mode dynamics in a photorefractive ring oscillator with induced astigmatism”, *J. Opt. Soc. Am. B* 18, 966-973 (2001).

[5] Ye.A. Krasnoshchekov, V.V. Yaparov, V.B. Taranenko, “Rotating Full Poincaré Beams”, *Ukr.J.Phys.Opt.* 18, 1-8 (2017).

[6] K. Staliunas, M.F.H. Tarroja, G. Slekyš, C.O. Weiss, “Analogy between photorefractive oscillators and class-A lasers”, *Phys. Rev. A* 51, 4140-4151 (1995).

SECTION 3. LASER PROCESSING OF MATERIALS

IN-LINE X-RAY PHASE CONTRAST IMAGING AND WELD POOL DYNAMICS FOR LASER WELDING OF PURE ALUMINIUM

A. Kul'ment'ev*, A. Polishchuk

Institute of Applied Physics, NAS of Ukraine, Sumy

*E-mail: kulmentev@ukr.net

At present metal processing with lasers has reached high level of maturity and acceptance. It is used for cutting, drilling, welding, forming, marking, engraving, hardening and various forms of surface treatment. For example, in laser welding, a high power density can easily be obtained to achieve deeper penetration with a higher weld speed than in traditional arc welding. As a result laser welding has next advantages: 1) ultimate precision; 2) capability of creating complicated joins; 3) low heat application; 4) consistent and repeatable welds; 5) high strength welds.

At the same time laser welding creates numerous defects: 1) porosity, which is the appearance of pores in the weld metal; 2) under-fill, which is dents on the welding surface; 3) spatter, which is small pieces of weld metal flying out of the weld pool; 4) cracks in the weld metal and heat-affected zones. Despite high-level activity in the area of laser welding defect formation mechanisms are still not properly understood. It is related to the highly complicated process of mixing solid, liquid, gas, and plasma phases within weld pool.

For these weld defects investigation, analysis by X-ray imaging technology has been performed since around 2000. Although in-situ observation with X-rays is often useful for understanding laser welding phenomena, images obtained by the traditional X-ray absorption method have limited clarity.

Indeed, since the discovery of X-rays they have allowed to look inside objects without the need to damage them. This works on the principle that X-rays penetrate objects more easily than, for example, visible light. However denser object is still harder to penetrate and this leaves a shadow as fewer X-rays penetrate it. This also limits the technique because it only allows to observe objects that are relatively dense compared to the surroundings.

Unfortunately, the difference between densities of liquid and solid phases of the same metal is too low. Therefore it is difficult to distinguish clearly the solid-liquid interface and keyhole shape. As a result, the mechanism for the elementary step of laser welding remains unclear. New observation technologies are thus necessary for deep understanding of laser welding phenomena.

This is where the technique of phase contrast imaging comes in. It does not rely on how much X-rays the object absorbs, but it is based on the difference in refractive index. As an example, one can take a piece of glass in water. Both the glass and the water absorb about the same amount of X-rays so the glass would be hard to distinguish. But the refractive index of water compared to that of

glass is quite different. Therefore taking phase-contrast images it is possible to see a piece of glass in water quite well.

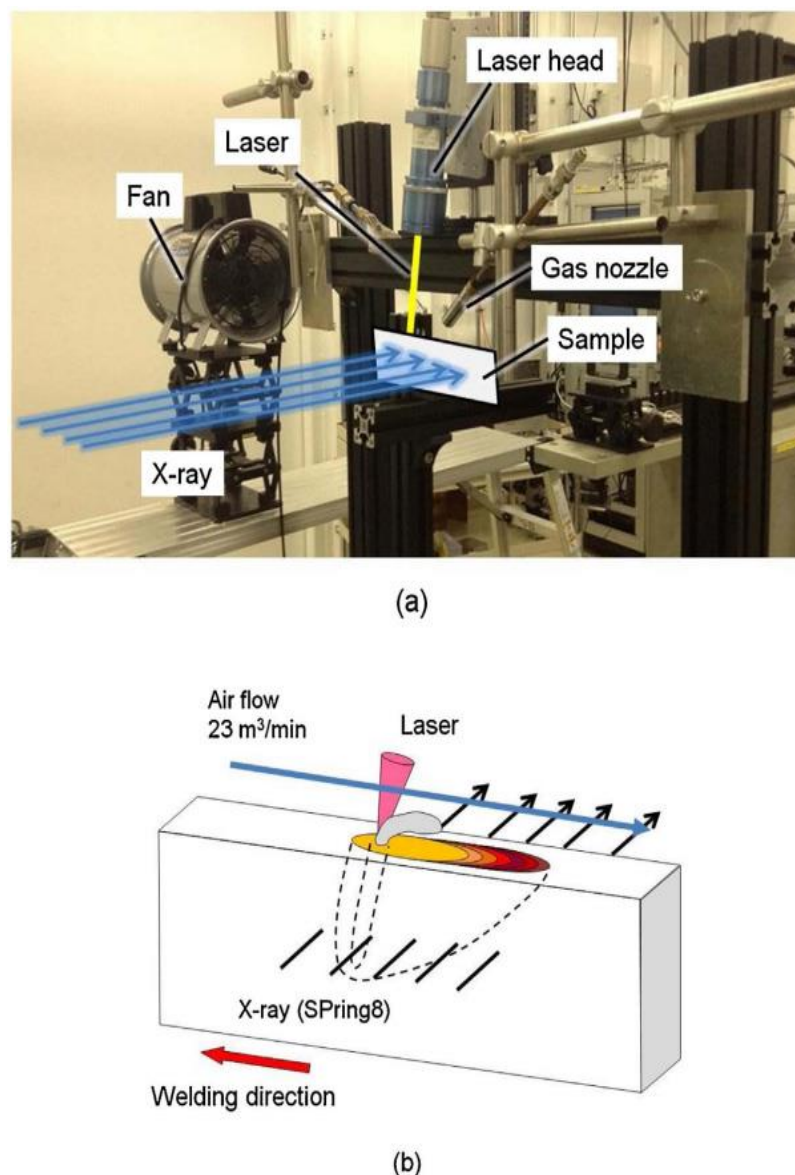


Fig.1. (a) Laser welding and X-ray observation setup at Spring-8 [1], and (b) schematic of laser welding.

As an example, in report results [1] of laser welding investigations of aluminum by applying an X-ray phase contrast method as an imaging technique [2] are considered. Fig.1 shows the general setup used in [1] for experiments, and Fig.2 shows the results in the form of a time series of consecutive images of phase-contrast X-ray images.

These results pertain to the middle of the welding process and show the weld pool evolution every 5 ms. Under experimental welding condition, the keyhole depth consist approximately 0.6 mm. Because there was no significant changes in the keyhole depth or width it meant that the keyhole was relatively

stable. However a few small bubbles formed from the keyhole bottom. At $t = 5$ ms and $t = 10$ ms, small bubbles were just about to form at the bottom.

These bubbles were formed by extra evaporation of weld metal. The space created by the extra evaporation disconnected from the keyhole and became a bubble. The bubble then moved to the back part of the weld pool and was subsequently trapped at the solid-liquid interface. After trapping, the bubble grew and developed into a teardrop-shaped void.

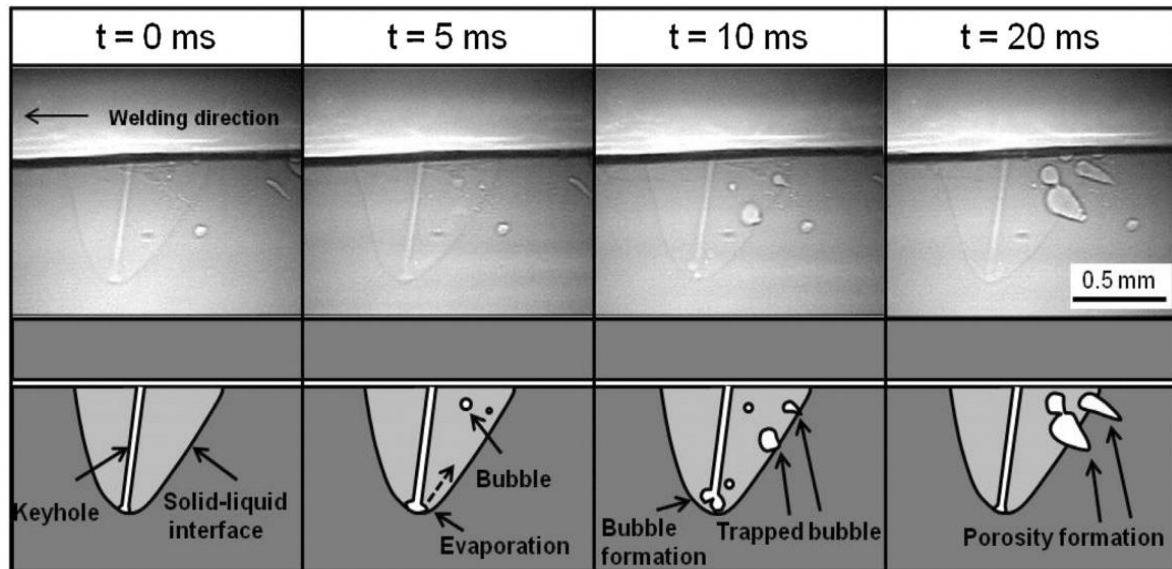


Fig.2. Images and schematics for keyhole and weld pool observation by X-ray phase contrast, for welding with fan usage [1].

Despite the large potential advantages of described approach, its wide practical application is constrained by the requirements imposed on the initial X-ray radiation, which should be quite intensive and coherent. Now this can only be achieved using a synchrotron, which is very expensive and not always available, or a microfocus X-ray tube that produces less X-rays.

In recent years a new type of particle accelerator has begun to catch the interest of a lot of researchers, so called laser wakefield accelerator. This uses a plasma to accelerate particles, usually electrons, over a very short distance. The electrons emit X-rays when accelerated and this generates a very small X-ray source, which may be suitable for phase-contrast imaging.

And again it is the laser that can help people.

References

- [1] M. Miyagi, et.al. J. of Mat. Proc. Tech. **250**, (2017), 9 – 15.
- [2] D.M. Paganin. Coherent X-ray optics. Oxford Univ. Press, 2006. 412 pp.

LASER MELTING OF POWDER METALS AT 3D PRINTING

M. Kuzma

Uniwersity of Rzeszow, Rejtana str. 16, 35-310 Rzeszow, Poland

Laser melting of solid state is commonly related to interaction of high energy fotons (laser beam) with a surface of the solid state sample. In the 3d printing , the lase melted material is in the form of thin wire or it is a powder. At both cases the thermal interaction will be modified in respect to the melting of a bulk sample. In the case of multicomponent smart materials the laser melting may change the properties of the material because they are usually sensitive on thermal history. The example are Heusler alloys [1]. Therefore, the parameters of the printing of such materials should be carefully determined and corrected. In the case of powder it is particularly actual problem while the production of powder of that materials is not known yet. The powder consists from brittle species not from small balls as in the case of ordinary metals (Fe, Cu, Zn).

Usually, two types of 3d printers are use for metal deposition. In first type, the laser head is coupled with powder delivery unit forming nozzle (Fig.1). The nozzle can move along multiple axis. This method is called Directed Energy Deposition (DED). In a second type of apparatus (SLM – selective laser melting) the laser head is moved in X Y plane according to CAD protocol. To begin of printing the powder is placed as homogenous layer (thickness of 0.1 - 0.2mm) in rectangular reservoir in which the designed object is created. Every leyer by layer laser melting new layer of powder of the same thickness is completed and reservoid is shifted up by thickness of the layer (e.g. 0.2mm). This type of printing requires large amount of power. In the case of unique materials as e.q. Ti, special semiconductors etc. economically better are DED printers.

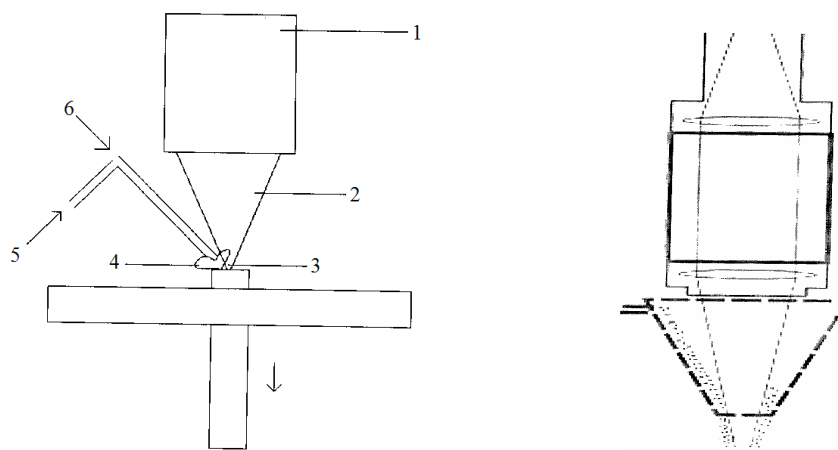


Fig.1. Scheme of nozzle in DED 3-D printer.

The proper determination of laser melting parameters for printing, the following initial parameters need to be known:

1. parameters which relates to a printer
 - laser (type, wavelength, pulse duration, energy of laser beam),
 - rate of printing,
 - the shape of grain formed by one laser pulse
2. parameters of the powder
 - average size of grains, shape of grains (Fig. 2a),
 - reflection coefficient,
3. material parameters
 - density,
 - coefficient of thermal conductivity, coefficient of temperature conductivity, intrising heat .

In theoretical modeling of the melting process the thermal model is usually used [2]. However , for powder the thermal coefficients are not known as well as the reflection coefficient is also different in respect to a bulk material. Therefore the process of melting should be determined by experiment.

In present paper we study the laser melting of powder of CrTe + Cd. In Fig.2 we show the initial powder (a) and morpooogy of melted surface (b,c). We have use the YAG:Nd³⁺ laser with duration of pulse 250 μ s.

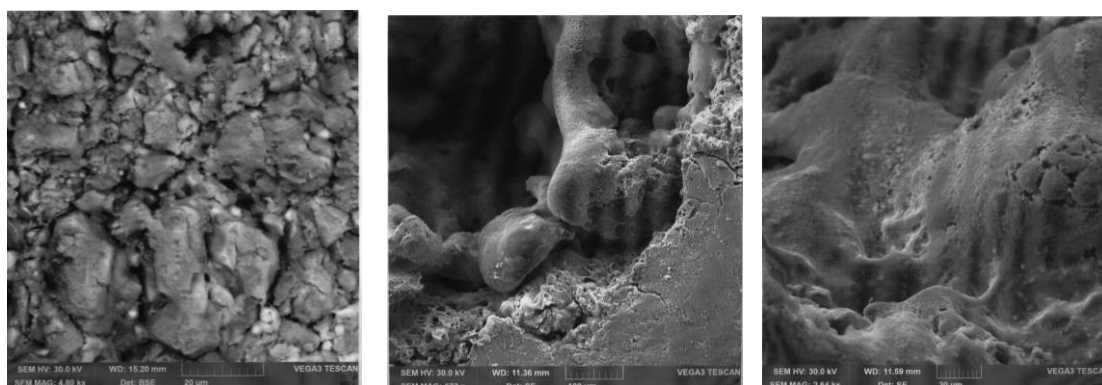


Fig.2. Powder of CrTe+ Cd (a). Melted powder (b,c).

EDS measurements of melted areas point that the synthesis occurs as well of the mixture CrTe + Te into CdCrTe.

References

1. E. Stevens, J. Toman, K. Kimes, V. Chernenko, A. Wojcik, W. Maziarz, M. Chmielus. Magnetostructural Evaluation of magnetocaloric Ni-Co-Mn-Sn Produced by Directed Energy Deposition. Microsc. Microanal. 22 (Suppl 3). 2016.
2. A.A. Wiedienow, G. Gładysz. Physical processes by laser treatment of materials, Moskov 1985 (in Rus.).

IMPROVEMENT OF THE SURFACE PROPERTIES OF SLM-FABRICATED PARTS BY POST-PROCESSING

D. Lesyk^{1*}, S. Martinez², B. Mordyuk³, V. Dzhemelinskyi¹,
A. Lamikiz², G. Prokopenko³
*Email: lesyk_d@ukr.net

¹*Laser Systems and Physical Technologies Department, National Technical University of Ukraine "Igor Sikorsky Kyiv Polytechnic Institute", Kyiv, Ukraine*

²*Aeronautics Advanced Manufacturing Center, University of the Basque Country, Zamudio, Spain*

³*Physical Principles for Surface Engineering Department, Kurdyumov Institute for Metal Physics of the NAS of Ukraine, Kyiv, Ukraine*

Nowadays, fabrication of metallic parts by different additive techniques, such as wire and arc additive manufacturing, laser metal deposition, electron beam melting, selective laser sintering or selective laser melting (SLM), etc. is very relevant. In particular, the SLM process is one of an advanced manufacturing method, which allows producing the complex 3D parts directly from 3D computer models by selectively melting successive layers of metal powder on the top of the previous one using a scanning laser beam [1–3].

Currently, the development of new post-processing technologies is very attractive since they may improve the surface properties of the components fabricated by the additive manufacturing methods. For instance, an implementation of post-processing techniques in the additive manufacturing routes, such as special heat treatment, hot isostatic pressing [1, 2], electrochemical polishing, media blasting or tumbling, ultrasonic excitation, laser shock peening, shot peening, and ultrasonic impact treatment [3–6], could minimize or eliminate the defects in the responsible metallic parts. The post-processing methods can be selected based on the application requirements, geometry complexity, size of parts, and required surface quality.

Various mechanical post-processing techniques, such as surface finishing-hardening treatment (SFHT), shot peening (SP), ultrasonic shot peening (USP), and ultrasonic impact treatment (UIT), were applied to improve the surface layer properties of the Inconel 718 alloy parts fabricated by SLM process [1–3].

The purpose of this work is to study the effects of the SFHT, SP, USP, and multi-pin UIT on the surface topography, hardness, and residual stress of the Inconel 718 alloy parts fabricated by the SLM process.

A nickel-based pre-alloyed IN 718 powder with the spherical shape and the particle size in a range of 10...55 μm was selected as feedstock material. All specimens were fabricated by the SLM process using a Renishaw AM400 machine. The build chamber was backfilled with argon gas, while the powder was melted with a 200W laser with a spot size of 70 μm , scanning speed

at 700 mm/s. Specimens were manufactured with a layer thickness of approximately 60 μm .

The SLM-built parts were subjected to four different surface treatments operated in the following regimes. During the SFHT process, the container with the processed parts was forcibly rotated by the motor with the rotation speed of 66 rpm and lasted for 4 h. The SP experiment was carried out for 5 min using the shots in diameter of 0.5 mm, a pressure of 0.55 MPa, and impact speed of 10 mm/s. The USP process was performed for 10 min in a special chamber filled with the peening media using the horn amplitude of 50 μm , and the distance between the specimen and the horn tip surface of 40 mm. The UIT experiment was carried out for 120 s using the amplitude of ultrasonic horn of 18 μm , a static load of 50 N, and a specimen feed rate of 600 mm/min.

The surface microrelief of the SLM-built specimen has a large number of manufacturing defects. Herewith, the surface is rough (R_a parameter is $\sim 5 \mu\text{m}$) having relatively high height microasperities. In comparison with the SLM-built state, the surface roughness of the post-processed specimens were respectively decreased by approximately 44.6%, 43.6%, 61.3%, and 92.4% after the SFHT, SP, USP, and UIT processes (Fig. 1a). A remarkable improvement in the surface roughness ($R_a \sim 0.38 \mu\text{m}$) was observed after the multi-pin UIT process as compared to that after the SFHT, USP and SP processes. The SFHT-processed specimens acquired relatively smoother surface compared to the shot peened ones.

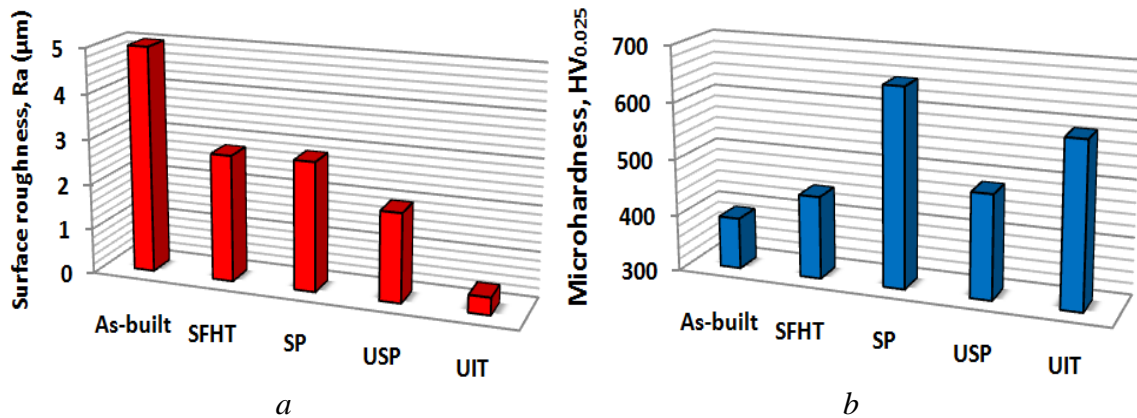


Fig. 1. Surface roughness (a) and microhardness (b) of the SLM-built and SFHT, SP, USP, and UIT processed IN 718 specimens.

The experiments show that the surface microhardness ($HV_{0.025}$) increases relative to the untreated specimen irrespective of the treatment type (Fig. 1b). The SFHT, USP, and UIT enhanced the surface hardness by 14.2%, 23.8%, and 50.97%, respectively. The SP and UIT processed specimen showed the highest hardness at the surface, followed by SFHT and USP processed specimens. The SP-processed specimens showed an increase of 66.5% from initial state, with surface hardness of 650.53 $HV_{0.025}$.

The residual stress magnitudes obtained from XRD technique are given

in Fig. 2. Conversely to the tensile stresses observed in the SLM-built part (+120 MPa) the mechanical surface treatments used led to a compressive residual stress formation. The estimated stress magnitude for the case of the SFHT processed SLM-built specimen (−201.4 MPa) is the lowest in comparison with those obtained after the USP (−313.8 MPa), multi-pin UIT (−428.7 MPa), and SP (−510.7 MPa) processes.

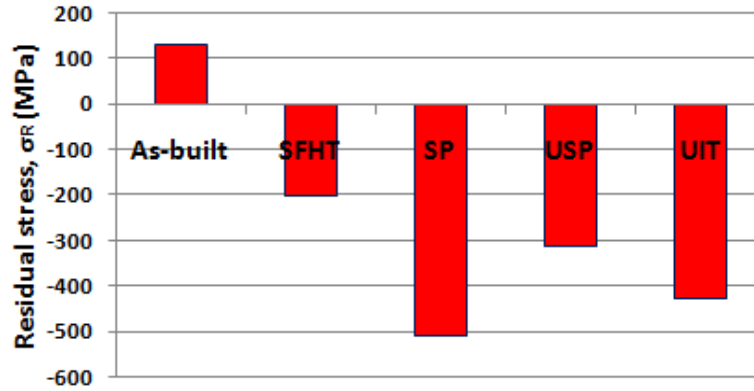


Fig. 2. Residual stress in the build direction of the SLM-built and SFHT, SP, USP, and UIT processed IN 718 specimens.

The SFHT, SP, USP, and UIT processes were applied to improve the IN 718 alloy parts fabricated by the SLM process. The obtained results allow drawing the following conclusions:

- The surface roughness of the post-processed specimens was respectively decreased by approximately 44.6%, 43.6%, 61.3%, and 92.4% after the SFHT, SP, USP, and UIT processes;
- The surface hardness was increased and compressive residual stress was formed in the near-surface layers of the processed specimens;
- The UIT and SP processes are the most effective processes regarding the surface roughness diminution, and microhardness / compressive residual stresses increase.

[1] R. Seede, et al.: Microstructural and microhardness evolution from homogenization and hot isostatic pressing on selective laser melted Inconel 718: Structure, texture, and phases, *Manuf. Mater. Process.* 2 (2018) 30–51.

[2] D. Deng, et al.: Microstructure and mechanical properties of Inconel 718 produced by selective laser melting: Sample orientation dependence and effects of post heat treatments, *Mater. Sci. Eng. A.* 713 (2018) 294–306.

[3] M. Zhang, et al.: Residual stress, defects and grain morphology of Ti-6Al-4V alloy produced by ultrasonic impact treatment assisted selective laser melting, *Appl. Sci.* 6 (2016) 304–311.

[4] M.P. Sealy, et al.: Fatigue performance of biodegradable magnesium–calcium alloy processed by laser shock peening for orthopedic implants, *Int. J. Fatigue* 82 (2016) 428–436.

[5] L. Hackel, et al.: Laser peening: A tool for additive manufacturing post-processing, *Addit. Manuf.* 24 (2018) 67–75.

[6] M. Sugavanwaran, et al.: Enhancement of surface characteristics of direct metal laser sintered stainless steel 316L by shot peening, *Surf. Interf.* 12 (2018) 31–40.

NEW TECHNOLOGIES OF INCREASING THE RELIABILITY OF STRUCTURAL MATERIALS

N. Pavlovska¹, Yu. Pavlovskyy²,

¹*Drohobych secondary school of I-III degrees №4, Drohobych, Ukraine*

²*Drohobych Ivan Franko State Pedagogical University, Drohobych, Ukraine*
yu_pavlovskyy@ukr.net

The transition of the Ukrainian industry to market relations causes the development and implementation of highly effective technological processes in the engineering industry. Achievements of modern science in many cases can radically change the technological process, sharply increase and improve new high-performance machines and machines, which ultimately allows you to improve the quality of products and improve production efficiency.

Improvement of durability and working capacity of machine parts and mechanisms, cutting tools, technological equipment, equipment and equipment is an actual problem of modern machine building. This is due to the fact that considerable material, economic and public resources are used for manufacturing, repair and maintenance of machinery, spare parts of machines and mechanisms.

The development of new branches of the national economy requires the qualitative improvement of traditionally used structural materials, as well as the creation of new materials, unique in their properties (purity, thermal and chemical resistance, hardness etc.). All this leads to intensive work on the search and development of new technological solutions in metallurgy, chemical industry, energy, engineering, electronics.

Of the six main classes of surface hardening of the metal surfaces of parts, the third-class is the most promising: the strengthening of the change in the structure of the near-surface layer. To this class there are four methods: physical and thermal treatment, electrophysical treatment, mechanical processing and surfacing with alloyed metal. Physical-thermal treatment includes processes such as laser beam processing and plasma jet. Electrophysical processing includes such processes as electrocontact, electroerosive and ultrasonic

processing [1].

The application of magnetic hydrodynamic means enables to control the processes of heat and mass transfer, interphase interactions in multicomponent rare metal systems, and also significantly influence the formation of cast billets with a given structure and unique properties and, as a result, to receive high-quality products [2].

The use of plasma technology is efficiently used in the processing of ore raw materials, the recovery of metals, the finishing of the products obtained. The developed technologies allow to improve the plasticity and durability of materials, to melt the waste from the colored alloys with the output of the suitable alloy to 90%, to remove harmful impurities from the melt, and as a result, to improve the quality of the metal products [3].

The main disadvantage of plasma technologies, which are still hampering their widespread use, is the consumption of large quantities of electricity. However, as shown by the analysis of scientific literature, in the presence of sufficiently cheap organic raw materials, electricity consumption can be significantly reduced during the burning of part of this raw material, that is to switch from pure plasma to fuel-plasma methods, and plasma generators (plasmatrons) to use only to maintain and stabilize the necessary temperature regimes with minimal electricity consumption.

In recent years, rapid growth has been achieved by laser beam technology. This technology is based on the local heating of the surface area under the action of laser radiation and the cooling of this site with supercritical velocity, due to heat transfer in the inner layers of the metal. Laser hardening is not a volumetric process, but is carried out from the surface. Laser hardening of materials has a number of advantages that distinguish it from other methods of surface hardening, namely: the possibility of using laser radiation to carry out both strengthening and smoothing of the surface of the part by controlling the processes of heating and cooling of the material; energy saving due to the strengthening location, which allows to achieve high hardness of the near-surface layer on strictly defined areas, maintaining high dynamic characteristics of the main material; high process performance; the ability to change the properties of the surface of material in hard-to-reach places; contactlessness of

the method and so on. However, this progressive method is inherent and certain disadvantages. The main ones are: the high cost of powerful laser process equipment; short-lived and high cost of lens and mirror materials used to control laser radiation in space; the need for special coatings to increase the absorption capacity of irradiated surfaces; the need to protect the staff from scattered laser radiation; low process performance during surface treatment, which has a large length; large dimensions of laser technological equipment [1].

1. Derfinka I.C. Condition and analysis of modern methods for improving the reliability of machine parts by surface hardening. Lviv: Lvivska Polytechnic Publishing House, 2007. P. 18-24.

2. Dubodelov V.I. Prospects of application of new generation magnetodynamic installations in foundry and metallurgical technologies. Technical electrodynamics. Thematic issue "Problems of Modern Electrical Engineering". 2002. Part 6. P. 100-106.

3. Tsvetkov Yu.V. Nikolayev A.V. Plasma processes in the metallurgy of the future (problems of the creation of the energy-metallurgical complex). Steel. No. 10 1998. P. 55-60.

INCREASING THE STRENGTH OF THE SURFACE OF MATERIALS BY LASER METHOD

Yu. Pavlovskyy

Drohobych Ivan Franko State Pedagogical University, Drohobych, Ukraine
yu_pavlovskyy@ukr.net

Microhardness is the resistance to plastic encrustation in a flat surface of a sample or a solid indenter product, usually diamond pyramids. Determination of microhardness differs from ordinary measurements with very small loads from 147 to 4905 mN (from 15 to 500 gf) and small sizes of the imprint.

Microhardness allows us to evaluate the properties of individual structural components, very thin layers of the surface, coatings, foils, thin wires, small parts, metal threads, artificial oxide films, as well as very fragile bodies that are cracked using conventional methods for evaluating hardness (enamel, glass etc.).

The effect of protective coating on micromechanical characteristics of silicon was experimentally investigated in this work. Titanium nitride (TiN / Si), aluminum (AlN / Si) and boron (BN / Si) films were applied to the surface of monocrystalline silicon by means of pulsed laser spraying using a laser YAG: Nd. The general view of the installation is shown in Fig. 1. The laser parameters are as follows: $\lambda = 1.06$ mm, pulse energy 0.5 J, pulse duration: in the mode of modulated Q-factor – 20 ns, in free generation mode – 200 μ s; section of beam 3 mm.

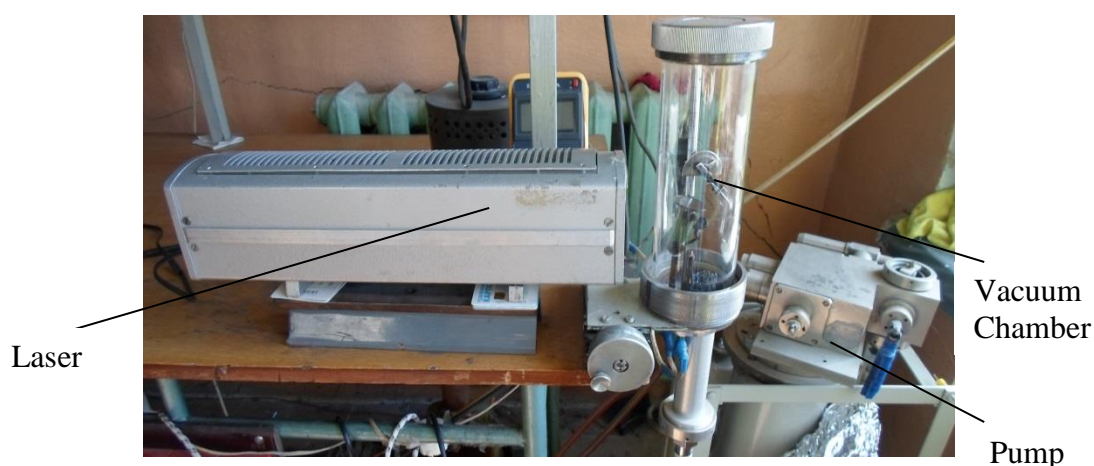


Fig. 1. Laser YAG: Nd

After that, measurements of the microhardness of the samples were carried

out using the Vickers method [1]. For each sample, the load on the indenter was selected, at which it was possible to determine the size of the diagonals of the print with a minimum error. Thus, for samples of pure silicon and silicon with a film of titanium nitride, a load of 20 g was used, and for samples with a protective coating of nitride of aluminum and boron nitride – 30 g. The value of microhardness (H , GPa) was calculated by the formula:

$$H = 1,8544 \left(\frac{P}{d^2} \right), \quad (1)$$

where P – load, mN (gf); d – the arithmetic mean value of the imprint diagonal, μm .

To determine the fracture toughness (crack resistance, K_c , $\text{MPa} \cdot \text{m}^{1/2}$) of the samples under investigation, it was necessary to remove cracks along the direction of the diagonals of the indenter print [2]. To do this, the bigger loads were selected. For pure silicon it is 100 g, for a sample with a coating of titanium nitride – 50 g, and for samples with coating AlN / Si and BN / Si – 70 g. The appearance of indenter with cracks is shown in Fig. 2. Determination of the coefficient of crack resistance was carried out by the formula:

$$K_c = 0,0089 \cdot \left(\frac{E}{H} \right)^{2/5} \cdot \frac{P}{a\sqrt{l}}, \quad (2)$$

where

P – the applied load;

E is the Young module (for silicon $1,5-1,8 \cdot 10^{10}$ GPa), we accept $1,8 \cdot 10^{10}$ GPa;

H – microhardness of Vickers;

l – length of the crack;

a – half the imprint diagonal.

The results of measurements and calculations are listed in Table 1. Compare and analyze the results.

As can be seen from Table 1, the surface coating of monocrystalline silicon with nitride films leads to an increase in the microhardness of samples, and, the maximum result is achieved in the presence of a film of aluminum nitride. At the same time, as we see from the table, in samples with a coating of nitride of

titanium and boron nitride, the coefficient of crack resistance decreases. And in samples with a film of aluminum nitride, it practically does not change.

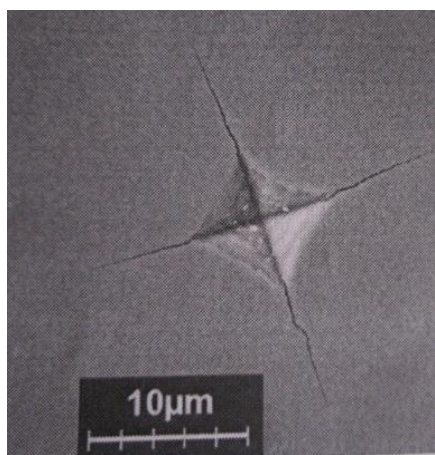


Fig. 2. The appearance of an indenter print with cracks on the Si surface

Table 1. Microhardness value and crack coefficient of investigated samples

Sample	H , GPa	K_C , $\text{MPa} \cdot \text{m}^{1/2}$
Si	7,9	1,0
TiN/Si	8,5	0,75
BN/Si	8,9	0,68
AlN/Si	10,5	0,98

Thus, the best result for strengthening the surface of monocrystalline silicon was obtained by applying a film of aluminum nitride: the growth of microhardness by one third, while maintaining the value of crack resistance.

1. Kotrechko O.O. Methods of determination of static and shock microhardness of metals and their alloys. *Young scientist*. 2016. № 6 (33). P. 203-205.

2. Robert O. Ritchie. Failure of Silicon: Crack Formation and Propagation. 13th Workshop on Crystalline Solar Cell Materials and Processes. August 2003, Vail, Colorado.

INTERACTION OF LASER BEAM WITH Ni₂MnIn ALLOY

H. Czyż¹, P. Sarzynska¹, P. Ciupak¹, A. Barłowski¹, P. Sagan², T. Jasinski¹

¹ *Physics and Biophysic Engineering Chair, Technical University of Rzeszow, Powstancow Warszawy 6, 35-900 Rzeszow, Poland*

² *Faculty of Mathematics and Natural Sciences, Department of Experimental Physics, University of Rzeszow, Pigonia 1, 35-959 Rzeszow, Poland*

Shape memory effect (SME) in ferromagnetic shape memory alloys (SMA) based on Heusler alloys of X-Y-Z type (X = Ni; Y = Mn, Co, Fe; Z = Ga, Sb, Sn, In) is attributed to the martensitic phase transition (MPT), from high-temperature austenitic phase to low-temperature martensitic phase, and to the combination of ferromagnetic properties of the martensite and thermoplastic properties of the MPT [1]. There are two groups of the classical SMA: Ni₂MnGa-type and Ni₂MnZ-type (Z = Ge, Sn In). The first family shows the SME strongly enhanced by off-stoichiometric composition of the material, whereas the second family shows martensitic transition, and therefore the SME only at off-stoichiometric conditions. Laser processing of such materials are highly desired for innovative manufacture of smart devices based on pulsed laser deposition of thin layers or on 3-d printing .

In this paper we study the interaction of high intensity pulse laser beam with surface of Ni₂Mn_{35.5}In_{14.5} Heusler alloy. The samples were manufactured by Maziarz et al [2]. The bulk pieces of alloy were prepared by induction melting of pure Ni, Mn, In elements under argon atmosphere. The product was then homogenized in vacuum at 1000°C for 6 hours [2]. The YAG:Nd³⁺ laser with 1064 nm (I harmonics) wavelength was used. The pulse time was 250 μs and the maximal fluence was 1 J per pulse. The diameter of the beam was 6mm. Therefore the energy density of the non-focused beam was 27 ·10³ J/m². In the aim to increase energy density the beam was focused on the target by 10D lens (Fig. 1).

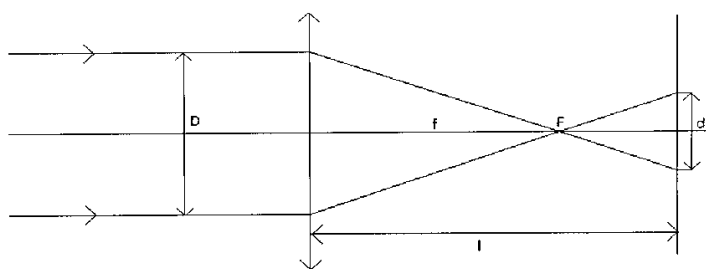


Fig.1. Scheme of the focusing of laser beam on a target.

The diameter of the spot on the target was calculated as $d = D(1 - f)/f$, where l is the distance of the lens from the target.

The spots obtained on the surface of the target, as the result of interaction of laser beam with the material, were inspected by scanning electron microscopy using VEGA3 microscopy. The examples of spots are presented in Fig. 2 at very low magnification.

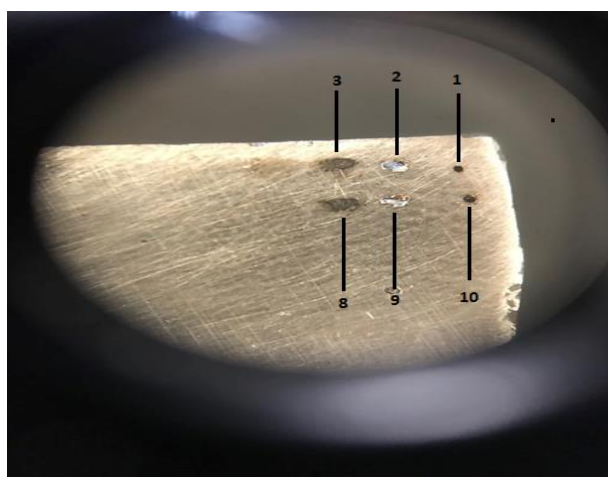


Fig. 2. Spots obtained at energy density of the laser beam: 6.26 J/mm^2 (spots 1,10), 0.514 (spots 2,9) and 0.320 J/mm^2 (spots 3,8)

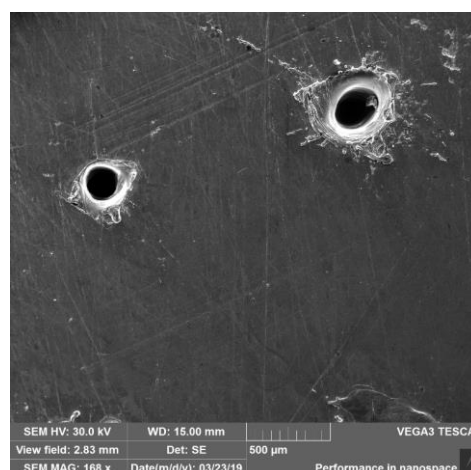


Fig. 3. Spots No 1 and 10 at high magnification

The spots observed in Fig. 2 show very different morphology. For example the spots denoted as 1 and 10 are very well formed deep holes with the circle shape of edges without effusion (see Fig. 3). From the results presented, the threshold of the energy density was determined on 4 J/mm^2 for material studied.

References

- [1]. H. Morawiec, Metale z pamięcią kształtu i ich zastosowanie, Wydawnictwo Uniwersytetu Śląskiego, Katowice 2014 (in Polish).
- [2]. W.Maziarz, Solid State Phenomena, 186, 251-254 (2012).

SECTION 4. LASER DEPOSITION

STUDY OF ZnO THIN FILMS ON A QUARTZ AND SAPPHIRE SUBSTRATE DEPOSITED BY THE PLD METHOD MEASURED BY MEANS OF ELECTRON PARAMAGNETIC RESONANCE

B. Cieniek¹, I. Stefaniuk¹, I. Virt^{1,2}, I. Rogalska¹

¹*Faculty of Mathematics and Natural Sciences, University of Rzeszow,
Pigonia 1, Rzeszow, Poland*

²*Drohobych Ivan Franko State Pedagogical University, Drohobych, Ukraine
bcieniek@ur.edu.pl*

1. Introduction

Zinc oxide (ZnO), a wide-band-gap (3.3 eV) wurtzite-phase semiconductor, is a well-known inexpensive material with wide perspective for various applications [1], such as varistors [2], sensors [3], or optoelectronic [4,5] and photonic devices [6]. It is important that some of the Zn ions can be substituted by magnetic transition metal ions to form a metastable solid solution. In addition, parameters such as transparency in visual region and piezoelectricity have generated large interest of researchers on ZnO based diluted magnetic semiconductors (DMS) [7,8]. Theoretical works using Density Functional Theory (DFT) [9,10] shows that n-type Co- and Cr-doped ZnO possesses ferromagnetism in room temperature (RTFM). Dietl et al. using the modified Zener model predicted that ZnO-based DMS could lead the transition temperature much higher than room temperature [11].

It has been reported that doping ZnO with noble metals such as silver (Ag) enhance the photocatalytic activity of the composite due to improved charge separation, and reduction in electron–hole recombination [12].

Scanning electron microscope (SEM) image was obtained on SEM/FIB Quanta 3D 200i Dual Beam microscope. The electron magnetic resonance (EPR) measurements were performed on the X-band spectrometer (Bruker multifrequency and multiresonance FT-EPR ELEXSYS E580), with the Bruker liquid nitrogen cryostats for controlling the temperature. Samples of zinc-oxide doped with Co and Cr thin films were obtained by pulsed laser deposition (PLD) method on quartz, sapphire, and quartz embed with Ag nanoparticles substrates. Silver nanoparticles were synthesized by homogeneous nucleation technique.

In the first part of this paper, a review of the investigation of ZnO:TM (TM = Co, Cr) layers on quartz and sapphire substrate is presented. In the second part the structural properties of a new series of ZnO:Co layers on quartz substrate embedded with silver nanoparticles. The aim of this work is to investigate the influence of substrates and adding of noble metals such as silver Ag to the magnetic properties of transition metal doped ZnO.

2. Short review of results

In our previous paper[13], among others, the X-band EPR studies of ZnO

thin films doped with 20% of Cr on quartz and sapphire substrate was reported. From the EPR lines the parameters: the peak-to-peak line width H_{pp} , the intensity I , as well as the resonance field H_r was determined. The results of temperature dependence of EPR spectra and linear extrapolations to the Curie–Weiss law indicate the ferromagnetic interaction between Cr ions characterized by the Curie temperature 109.6K (quartz) and 136.2 K (Al_2O_3).

In our previous papers, among others, the X-band EPR studies of thin films of ZnO doped with 4% of Co on quartz[14] and sapphire[15] substrate was reported. From the EPR lines: the peak-to-peak line width H_{pp} , the intensity I , as well as the resonance field H_r was determined. The results of temperature dependence of EPR spectra and linear extrapolations to the Curie-Weiss law indicate the ferromagnetic interaction between the Co ions characterized by the Curie temperature of 150 K for the layer on quartz. For the ZnO:Co layer on sapphire substrate, due to AFM superexchange interactions between Co ions, Co-doped ZnO prefers the spin-glass-like state. The results confirm that in the core of these nanocrystals Co has been incorporated as Co^{2+} , occupying the Zn^{2+} sites in the wurtzite structure of ZnO.

3. Structural properties of ZnO:Co layer with Ag NPs

New series of ZnO layers doped with 20% of Co on quartz substrate embedded with silver nanoparticles structural properties are described below. A detailed analysis of the magnetic properties of this layer will be presented in a separate work.

On SEM images (Fig. 1b), we can observe clusters of Ag NPs, regularly distributed on the surface of the substrate. Single Ag NP (also observed), have around 80 nm in dimensions. On EPR spectra, we can observe a wide line shifted towards the low magnetic field compared to sample without silver NPs (Fig. 1a). In addition, on this wide line, small intensity lines were observed in the field of about 340mT, probably corresponding to the silver ions Ag^{2+} and Ag^0 (described in the literature [16]).

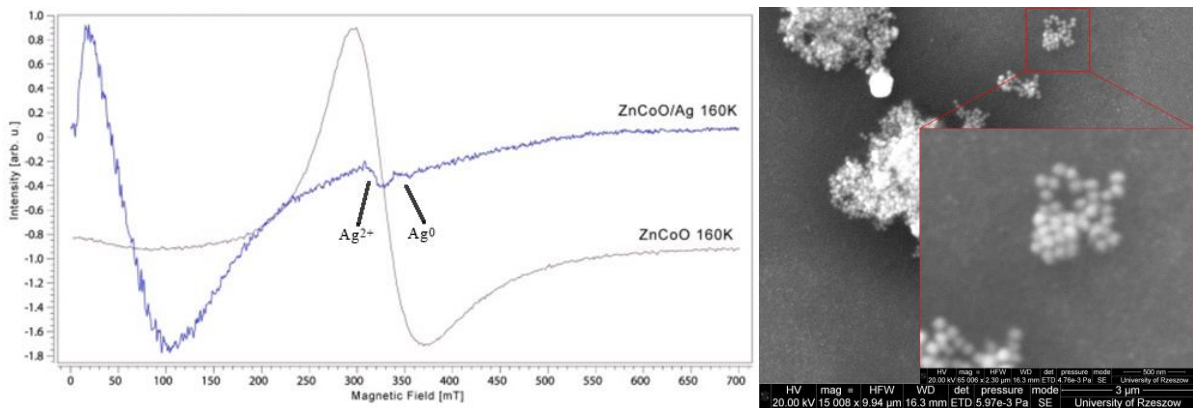


Fig. 1. ZnO layer doped with 20% of Co on quartz embedded with Ag NPs.

a) EPR spectra at temperature 160K, b) SEM image of clusters of Ag NPs

In comparison to ZnO doped with Co without Ag NPs (our works: [13,14,17]), we observe a line shift to the low-field direction (the field is smaller by about 300mT). The mechanism of this phenomenon is not yet known and further research will be carried out. It was also observed that the value of the resonance field decreases with the decreasing temperature.

4. Conclusions

Comparing data from Table 1, we can observe that the sapphire substrate affects the Curie temperature reduction. In the case of ZnO:Co with 4 % of dopant, the temperature has dropped even to the value of the Neel temperature. In conclusion, we have reported the X-band EPR studies of Cr- and Co-doped ZnO thin films with 4% and 20% of a dopant. All layers were fabricated by PLD method, on quartz, sapphire, and quartz embed with Ag NPs. We also observe a line shift to the low-field direction for samples with Ag NPs. This problem requires further research.

Table 1. Comparison of Curie/Néel temperature for layers on quartz and sapphire substrates

ZnO with 20% of Cr	
Temperature [K]	Substrate
136.2	Quartz
109.6	Sapphire
ZnO with 4% of Co	
150.0	Quartz
160.0 (Néel temperature)	Sapphire

References

- [1]. S. Pearton, *GaN and ZnO-Based Materials and Devices*, Springer (2012).
- [2]. K. X. Ya, H. Yin, T. M. De, T. M. Jing, *Mater. Res. Bull.* **33**, 1703 (1998).
- [3]. J. Xu, Q. Pan, Y. Shun, Z. Tian, *Sensors Actuators, B Chem.* **66**, 277 (2000).
- [4]. A. B. Djuriić, A. M. C. Ng, X. Y. Chen, *Prog. Quantum Electron.* **34**, 191 (2010).
- [5]. K. Harun, F. Hussain, A. Purwanto, B. Sahraoui, A. Zawadzka, A. A. Mohamad, *Mater. Res. Express* **4**, 000000 (2017).
- [6]. C. Zhou, A. Ghods, K. L. Yungans, V. G. Saravade, P. V. Patel, X. Jiang, B. Kucukgok, N. Lu, I. Ferguson, in *Oxide-Based Mater. Devices VIII*, (2017), p. 101051K.
- [7]. N. Samarth and J. K. Furdyna, *Phys. Rev. B* **37**, 9227 (1988).
- [8]. N. Volbers, H. Zhou, C. Knies, D. Pfisterer, J. Sann, D. M. Hofmann, B. K. Meyer, *Appl. Phys. A Mater. Sci. Process.* **88**, 153 (2007).
- [9]. K. Sato and H. Katayama-Yoshida, *Jap. J. Appl. Physics, P. 2 Lett.* **39**, L555 (2000).
- [10]. K. Sato and H. Katayama-Yoshida, *Jap. J. Appl. Physics, P. 2 Lett.* **40**, L334 (2001).
- [11]. T. Dietl, H. Ohno, F. Matsukura, J. Cibert, D. Ferrand, *Science* **287**, 1019 (2000).
- [12]. G. Merga, L. C. Cass, D. M. Chipman, D. Meisel, *J. Am. Chem. Soc.* **130**, 7067 (2008).
- [13]. B. Cieniek, I. Stefaniuk, I. S. Virt, *Acta Phys. Pol. A* **132**, 30 (2017).
- [14]. B. Cieniek, I. Stefaniuk, I. S. Virt, *Nukleonika* **Vol. 58, N**, 359 (2013).
- [15]. I. Stefaniuk, B. Cieniek, I. Rogalska, I. S. Virt, A. Kościak, *Mater. Sci.* **36**, 439 (2018).
- [16]. A. R. Mandal and S. K. Mandal, *J. Exp. Nanosci.* **5**, 189 (2010).
- [17]. I. Stefaniuk, B. Cieniek, and I. S. Virt, *Curr. Top. Biophys.* **33**, 221 (2010).

**TECHNOLOGY OF OBTAINING NANO CARBON FILMS
BY LASER METHOD**

Yu. Pavlovskyy, I. Virt

Drohobych Ivan Franko State Pedagogical University, Drohobych, Ukraine
yu_pavlovskyy@ukr.net**1. Introduction**

Impulse laser irradiation (ILI) is a process where laser radiation is used to "knock" multicomponent materials from the surface layers of the target and apply them to the substrate with the formation of stoichiometric mono- and multilayer coatings with special properties.

At present, ILI technology is of great interest in such fields as microelectronics, micro and nano photonics, since the reception of high-quality film structures is a priority task in these areas.

2. Short review of results

In our experiment, a neodymium laser YAG: Nd has been used with parameters: $\lambda = 1.06$ mm, pulse energy of 0.5 J, power density 100 MW/mm², pulse duration: in modulated *Q*-factor mode – 20 ns, in free generation mode – 200 μ s; section of beam 3 mm.

The films were received in two ways. The first way is to spray film in a vacuum. To do this, place on the platform in a vacuum chamber substrates (glass, silicon, quartz) to which the films will be sprayed. As a target we use carbon fiber.

A carbon nanostructured thin film on a glass substrate with an area of 1x1 cm² was obtained. The film is characterized by a bright brown color (Fig. 1).

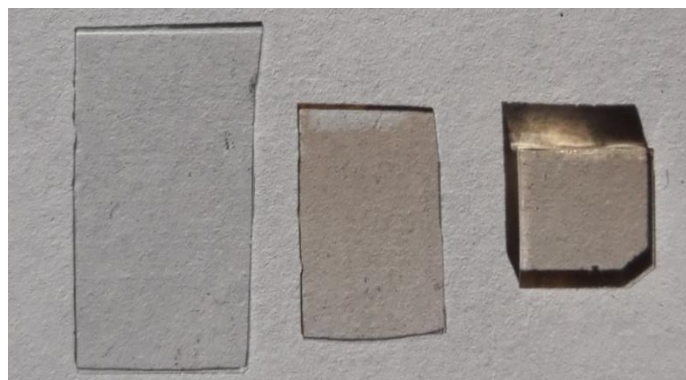


Fig. 1. Films on glass substrates

For the analysis of films, measurements of their absorption capacity in the range of waves of 200-3000 nanometers on a spectrometer were made. The obtained results are presented in Fig. 2.

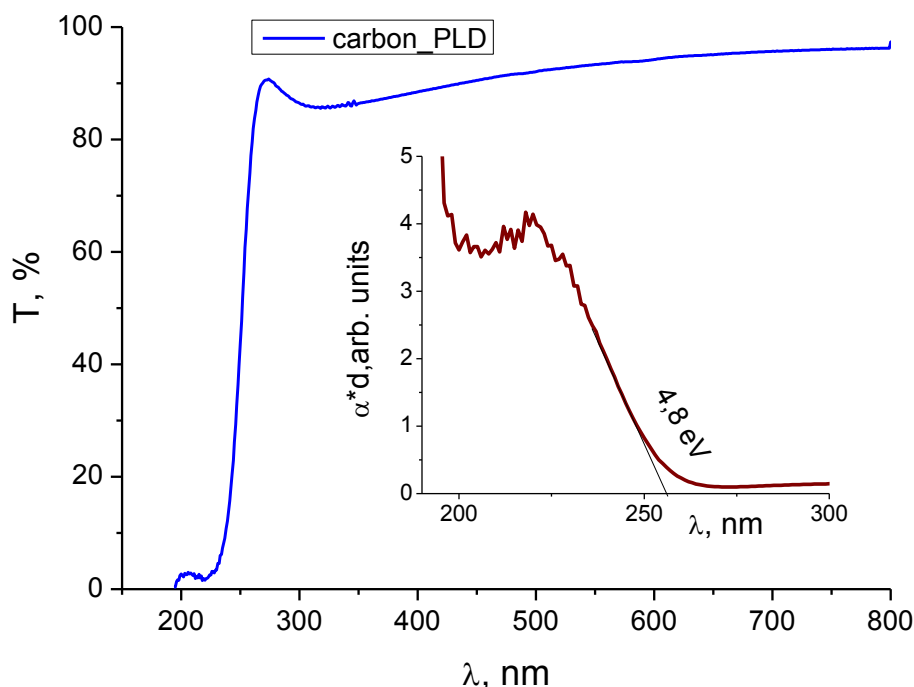


Fig. 2. Dependence of the absorption capacity on the wavelength

The absorption capacity of light is characterized by a coefficient called absorption A (this is the product of the absorption coefficient on the thickness of the film). Absorbance is determined from the ratio of intensity of light (in particular, the input I_0 and the output I). That is

$$\ln(I / I_0) = A,$$

parameter depending on the wavelength of light. If the absorption is represented not by the wavelength, but by the energy of the photons of light ($e = 1240/l$, l is the wavelength), one can estimate the energy of the photons of light at which a sharp diffusion of the absorbing layer occurs. Such a physical effect serves as one of the methods for identifying both the material and its structure. From the experiment it was established that this energy is 4.5 electron volts. Comparing with literary sources [1] (the upper curve in Fig. 2) it can be argued that the carbon thin film obtained has one of the structural modifications of the graphene-like structure.

The second method for obtaining nanoclay films was to directly fuse carbon into the glass surface. On the substrate (plate of glass) the powder of carbon nanoparticles was poured. Then the workpiece was placed in the field of

laser beam operation. As a result, a film was taken on the glass surface (Fig. 3).

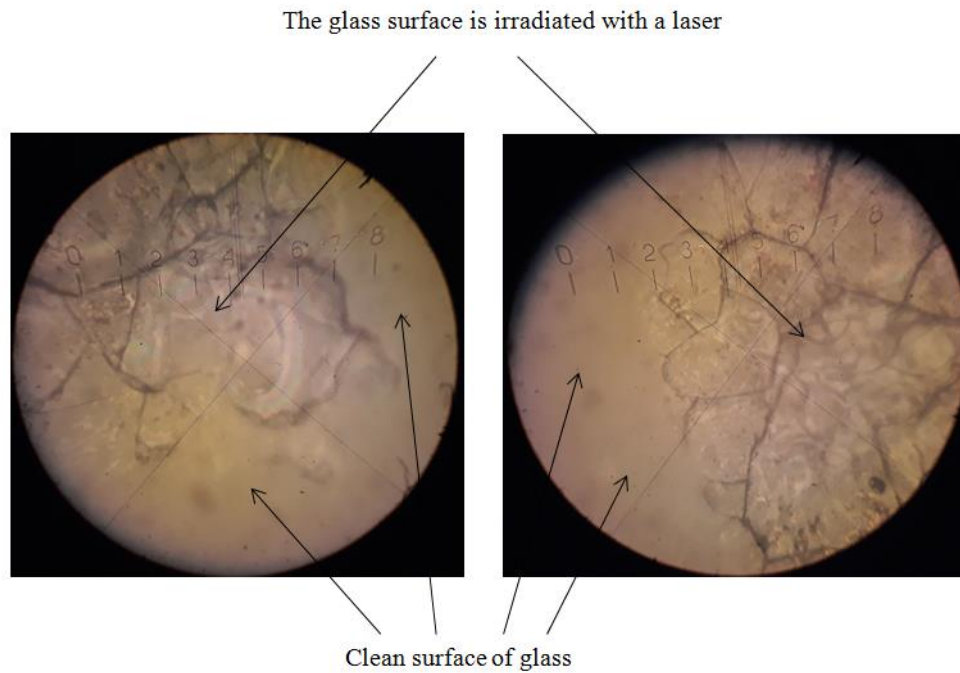


Fig. 3. Film on glass

Is this a film of womb, it is not possible to determine from a visual observation in a microscope. However, as is known, the presence of a surface film of wax leads to an increase in the microhardness of the material. Therefore, we measured the microhardness on the clean surface of the glass and on the surface with the film.

The following results are obtained: on a clean surface $HV \approx 6$ GPa, on a film – $HV \approx 7.2$ GPa. Consequently, we can assume that the film obtained on the surface of the glass can be graphene-like structure.

References

Singh S. Experimental and theoretical investigation of relative optical band gaps in graphene generations. *Materials Research Express*. 2017. 4(4):015101.

OPTICAL PROPERTIES OF ZnO:TM (TM = Cr, Mn, Co) LAYERS OBTAINED BY PLD METHOD

P. Potera¹, I. Virt^{1,2}, G. Wisz¹, B. Cieniek¹

¹ *Faculty of Mathematics and Natural Sciences University of Rzeszow,
Rzeszow, Poland*

² *Drohobych Ivan Franko State Pedagogical University,
Drohobych, Ukraine*

Introduction

Zinc oxide which is group II–IV semiconductor material exhibits many favorable properties, such as high wide band gap (~ 3.3 eV), high exciton binding energy (~ 60 meV), chemical stability, abundance in nature, and is also regarded as environment-friendly, non-toxic and low cost [1-5].

Several different physical and chemical methods are in use in literature-to fabricate high-quality ZnO thin films: molecular beam epitaxy [6], direct current and radio-frequency magnetron sputtering [7], metalorganic chemical vapor deposition [8], dip coating [9], spin coating [10], electrodeposition [11], spray pyrolysis [12], and pulsed laser deposition [5].

Doping non-magnetic semiconductors with transition metals (e.g., Co, Ti, V, Cr, Mn, Fe, Ni, and Cu) lead to the production of diluted magnetic semiconductors (DMS) which are regarded as important materials for spintronic, optoelectronic, and photonic devices.

Unfortunately, there are not many works devoted to structure, morphology and optical properties of ZnCrO, ZnMnO, and ZnCoO layers. It was shown that the transmission spectra and optical band gap energy of pure ZnO layers strongly depend on growth conditions as well as post-growth treatment [5,7,9,12]. In this way, a study of optical properties of ZnCrO, ZnMnO and ZnCoO thin films should be performed.

Experimental

The thin films of ZnO:TM (TM = Cr, Mn, and Co), with concentration of doped 4% for Cr, Mn, and Co, and 20% for Cr on the sapphire substrate were obtained by PLD method in Drohobych State University by using KWO₄:Nd laser with repetition rate of 20 pulse/min and pulse energy 0.2 J under 10^{-5} Pa vacuum. The time of deposition was 30 min with pulse duration 20 ns.

The Zn_{0.80}Mn_{0.20}O films on sapphire substrate were obtained by PLD method in University of Rzeszow by using second harmonic of YAG:Nd laser with repetition rate 50 pulse/min under $3.37 \cdot 10^{-4}$ Pa vacuum for substrate temperatures of 20°C and 250°C

The transmissions spectra of the thin films were recorded by CARY 5000 spectrophotometer. Additionally, the samples were annealed (5 min) in the air (NABERTHERM LH04 furnace) at a temperature of 400°C. After annealing (after cooling the sample) the transmissions spectra were recorded.

Results and discussion

The transmissions spectra of the as-grown ZnO:TM (TM = Cr, Mn, and Co) layers and sapphire substrate are given in Fig 1.

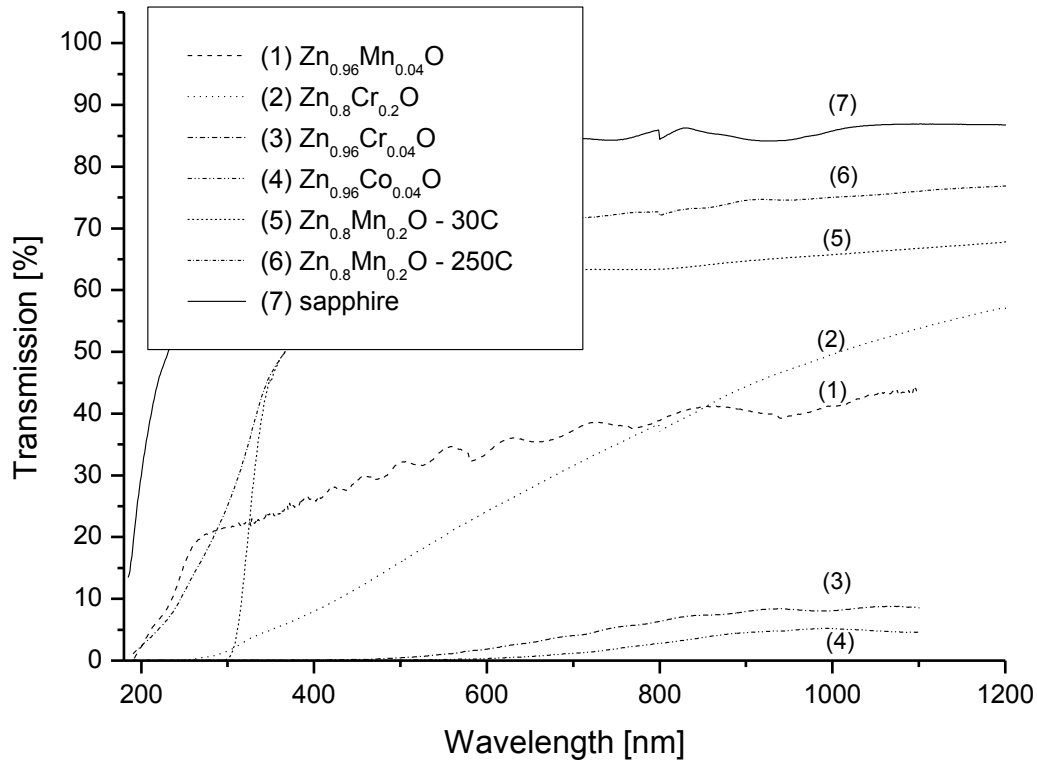


Fig 1. The transmission spectra of the as-grown $\text{Zn}_{0.96}\text{Cr}_{0.04}\text{O}$ (3), $\text{Zn}_{0.80}\text{Cr}_{0.20}\text{O}$ (2), $\text{Zn}_{0.96}\text{Mn}_{0.04}\text{O}$ (1), $\text{Zn}_{0.96}\text{Co}_{0.04}\text{O}$ (4), $\text{Zn}_{0.80}\text{Mn}_{0.20}\text{O}$ -20°C (5), $\text{Zn}_{0.80}\text{Mn}_{0.20}\text{O}$ -250°C (6), sapphire (7)

The transmission spectra of the investigated samples of ZnCrO strongly depend on target composition. The transmission of the sample obtained for 20% Cr content in the target is significantly higher than that obtained for the target with 4% Cr content. The same remark can be made for Mn dope. The sample ZnCoO was deposited from the target with 4% Co content. The transmission of this sample is smaller than for other samples.

The temperature of substrate strongly affects on optical spectra of $\text{Zn}_{0.80}\text{Mn}_{0.20}\text{O}$ layers. The layer obtained at the temperature of the substrate 250°C has higher transparency in visible region than obtained at 30°C.

The annealing of the samples in the air in the temperature of 400°C in time 5 min lead to the increase of transmission of the samples. The largest increase was observed for samples with a lower input transmission e.g. $\text{Zn}_{0.96}\text{Cr}_{0.04}\text{O}$ and $\text{Zn}_{0.96}\text{Co}_{0.04}\text{O}$.

Literature

- [1] Lee J.H., Ko K.H., Park B.O., Journal of Crystal Growth, 247(1-2), (2003)119.
- [2] Virt I.S., Hadzaman I.V., Bilyk I.S., Rudyi I.O., Kurilo I.V., Frugynskyi M.S., Potera P. Acta Physica Polonica A ,117(1), (2010) 34.
- [3] Konenkamp R., Boedecker K., Lux-Steiner M., Poschenrieder C. M., Zenia F., Levy-Clement C., Wagner S., Applied Physics Letters, 77(16), (2000) 2575.
- [4] Singh S., Kaur H., Pathak D., Bedi R.K., Journal of Nanomaterials and Biostructures 6(2), (2011), 689.
- [5] Wisz G., Virt I., Sagan P., Potera P., Yavorskyi R., Nanoscale Research Letters 12, (2017) 253.
- [6] Look D. C., Reynolds D. C., Litton C. W., Jones R. L., Eason D. B., Cantwell G., Applied Physics Letters, 81(10), (2002) 1830.
- [7] Cho S., Transactions on Electrical and Electronic Materials 10(6), (2009) 185.
- [8] Tan S. T., Chen B. J., Sun X. W., Fan W. J., Kwok H. S., Zhang X. H., Chua S. J., J. Appl. Phys. 98, (2005) 013505.
- [9] Kayani Z. N., Qbal M., Riaz S., Zia R., Naseem S., Materials Science-Poland, 33(3), (2015), 515.
- [10] Srinivasan G., Gopalakrishnan N., Yu Y. S., Kesavamoorthy R., Kumar J., Superlattices and Microstructures, 43(2), (2008) 112.
- [11] Dalchiele E. A., Giorgi P., Marotti R. Martín E F., Ayouchi R., Leinen D., Solar Energy Materials and Solar Cells, 70(3), (2001) 245.
- [12] Nadarajah K., Chee C. Y., Tan C. Y., Journal of Nanomaterials 2013 (2013), 1 (Article ID 146382).

PULSE LASER DEPOSITION OF THIN CHALCOGENIDE FILMS OF LEAD

Yu. Tur , I. Virt

*Drohobych Ivan Franko State Pedagogical University,
Drohobych, Ukraine*

Pulsed laser deposition (PLD) technique has been recently used to grow such films at moderate substrate temperatures, upto 200 °C, to investigate their structure, composition and properties. The results obtained so far indicated that the deposition of high quality PbTe films required very low residual vacuum, high purity gases, high laser fluences and repetition rates. Under such conditions, high density and nanocrystalline films that exhibited high hardness values were deposited at temperatures from 200 °C to 350 °C. Uniaxial reciprocating sliding tests were performed on such PLD grown films that exhibited very high hardness values and the results are presented below. The PLD experimental setup used to deposit the PbTe films has been extensively described previously and is only briefly described here. It uses a *Q*-switched Nd³⁺: KGd(WO₄)₂ laser ($\lambda = 1067$ nm, pulse duration $t = 20$ ns, 6–8 J/cm² fluence, 0,3 Hz repetition rate) to ablate polycrystalline targets in a quartz-steel chamber. The ultimate pressure in the deposition chamber was in the low 10⁻⁶ Pa. Films were deposited on (111) Si and Al₂O₃ substrates.

The deposition of thin films with adequate morphology and a crystalline structure is a key point in the development of many research fields. During the last two decades, the pulsed laser deposition (PLD) technique has been applied increasingly to the synthesis of thin films because of its versatility for the deposition of practically any kind of material with a relatively simple experimental set-up [1, 2]. The versatility of PLD also lies in the possibility of obtaining films very adherent to the substrates, even at room temperature and with a high predictable growth rate, which can be precisely controlled through a priori studies of the experimental parameters. Adequate selection of the irradiation conditions, as well as the chemical and physical properties of the target materials, is crucial for the production of very adherent thin films [3]. Moreover, the choice of substrate temperature may also affect the quality of thin films from the morphological and structural features point of view [4].

Pulsed laser deposition (PLD) is a growth technique in which the photon energy of a laser characterized by pulse duration and laser frequency interacts with a bulk material [1–3]. As a result, material is removed from the bulk depending on the absorption properties of the target materials. A significant removal of materials occurs above a certain threshold power density, and the ejected, partially ionized material forms a luminous ablation plume. The threshold power density required to create such a plasma depends on the

absorption properties of the target material, the laser wavelength, and pulse duration. Typical for excimer laser is a pulse length of 10 ns, for femtosecond excimer lasers it is in the range of 500 fs. The removed material is directed towards a substrate where it recondenses to form a film. The growth kinetic of such films depends on the material flux, repetition rate, growth temperature, substrate material, pressure, and background gas (vacuum, reactive). The main feature of PRCLA is the interaction between the ablated plume and a pulsed gas. The purpose of the pulsed gas valve is to use a reactive gas when transfer and deposition of material occurs, but also to provide a higher partial pressure during the interactions, yet to maintain a defined and low background pressure. This can be achieved experimentally by using a distance of at most 1 cm between the nozzle and the ablation point on the target, which results in a strong degree of scattering between the gas and the plume species also called interaction region. After passing the interaction region, the initial two beams merge and expand together almost collision-free while maintaining their reactivity for the film growth.

To use PLD for thin film growth has advantages for a number of reasons:

1. The flexibility in wavelength and power density allows to ablate almost any material or materials combination.
2. The laser is not part of the vacuum system. Therefore, a considerable degree of freedom in the ablation geometry is possible.
3. The use of a pulsed laser beam enables a precise control over the growth rate. The congruent transfer of the composition can be achieved for most ablated. Material or materials combinations.
4. Moderation of the kinetic energy of evaporated species to control the growth properties and growth modes of a film. There are also disadvantages to perform PLD.

Some of them are of a technical nature; some are intrinsic to the ablation process and the electromagnetic interaction between photons and matter [2]:

1. The large kinetic energy of some plume species causes resputtering and likewise defects in the substrate surface and growing film.
2. An inhomogeneous energy distribution in the laser beam profile gives rise to an inhomogeneous energy profile and angular energy distribution in the laser plume.
3. Light elements like oxygen or lithium have different expansion velocities and angular distributions in a plume as compared to heavier elements. Therefore, an addition source to supplement these elements to obtain the desired film composition is required, e.g., adequate background gas or an adapted target composition.

4. Due to the high laser energies involved, macroscopic and microscopic particles from the target can be ejected which can be detrimental to the desired properties of films and multilayers.

The latter point can partially be overcome by working with very dense polycrystalline or even single crystalline targets, but it also depends on the absorption and mechanical properties of the target material and laser fluence used.

- [1]. E. Rodriguez, D.Silva, L.Moya, C.L. Cesar, L.C. Barbosa, A. Schrank, C. R. Souza Filho, E. P. de Oliveira PbTe thin films grown by femtosecond pulsed laser deposition // Proc. of SPIE, Vol. 6698, 2007, pp. 669809-1-9.
- [2]. J.X. Si, H.Z.Wu, T.N. Xu, C.F. Cao, Z.C. Huang Microstructural Properties of Single Crystalline PbTe Thin Films Grown on BaF₂(111) by Molecular Beam Epitaxy// Chinese Physics Letters, Vol. 22, N.9, 2005, pp. 2353-2356.
- [3]. Virt I. S., Kurylo I. V., Rudyi I. O., Lopatynskyi I. E., Fruzhynskyi M. S. Structure and electrical properties of thin films Bi₂Te₃, Sb₂Te₃ i Bi₂S₃ and uperstructures Bi₂Te₃ - Sb₂Te₃, received by pulsed laser deposition // Visn. Nat. Univ. "Lviv Polytechnic". - 2007. - № 592: Electronics. – P. 115-121.
- [4]. Pei Y.-L. Electrical and thermal transport properties of Pb-based chalcogenides: PbTe, PbSe and PbS / Y.- L. Pei, Y. Liu // Journal of Alloys and Compounds. – 2012. – N 514 – P. 40 – 44.
- [5]. Zhu P.-W . High thermoelectric properties of PbTe doped with Bi₂Te₃ and Sb₂Te₃ / P.-W. Zhu, Y. Imai, Y. Isoda, Y. Shinohara, X.-P. Jia, G.-T. Zou. // Chin.Phys.Lett . – 2005. – V.22, N 8. – P. 2103-2105.

PULSED LASER TECHNIQUES FOR DEPOSITING NANOCARBON MATERIALS

Virt I.^{1,2}, Adamiak S.², Cieniek B.², Dziedzic A.², Potera P.², Zak D.²

¹*Drogobych State Pedagogical University, Drogobych, Ukraine*

²*University of Rzeszow, Rzeszow, Poland*

Pulsed since the discoveries of fullerenes and carbon nanotubes, there have been many exciting scientific and technological developments in the field of nanocarbon materials [1]. Single-walled carbon nanotube (SWNT) is a two dimensional graphitic nanostructures with many potential applications [2]. SWNTs were grown here on Si (and glass) substrates by pulsed laser deposition (PLD).

Results and Discussion

Laser-ablation thin films produced high yields of SWNTs by laser vaporization of carbon nanotube rods with small amounts 200°C. The X-ray diffraction and TEM showed that the synthesized nanotubes were remarkably uniform in diameters and that they formed ropes (or bundles) 5–10 nm in diameter.

X-ray diffraction. The crystalline structure of all the five SWNTs samples before and after purification treatment has been determined via XRD analysis. The corresponding spectra are illustrated in Fig. 1. a). All the diffractograms show distinct peaks: at 42° and 94° 2θ degrees. The peak at can 28° corresponds to the peak of Si.

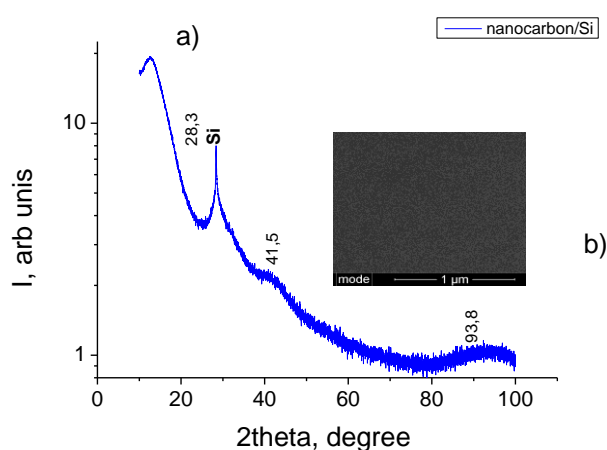


Fig. 1 a) XRD data of the SWNTs samples produced PLD. Cu-K α radiation of $\lambda = 0.15418$ nm, b) TEM data of the SWNTs samples.

The 2θ peak at around 42° can be assigned to the (100) plane nanocarbon. Its full width at the half maximum (FWHM) is rather broad, more than 2° and is typical for nanographitic carbons. From this peak, the corresponding mean domain size and plane distance was calculated.

Transmission electron microscopy. Transmission electron microscopy images were recorded for all the purified samples. Fig. 1. b) show the aggregate morphology that the carbon nanotube sample exhibits.

In the former images, graphitic domains within the SWNTs aggregates are clearly observed while the distance between layers of graphene can be estimated around 0.5 nm. The lateral size of the ordered regions exhibits values

of 10 nm. It can be seen that the agglomeration of carbon nanospheres (CNS) occur at each of the temperature variations. The agglomerates with the size of ~200 nm were observed.

Many physical properties of materials, vibrational spectra from Raman spectroscopy (RS) and specifically the optical absorption, are determined by the underlying electronic structure and lattice dynamics (fig. 2).

SWNT's between 200 cm^{-1} and 500 cm^{-1} the radial breathing modes (RBMs) of single-walled carbon nanotubes occur [3]. The position of Raman peaks ($\omega\text{ cm}^{-1}$) corresponding to individual chiralities of nanotube are determined by the diameter ($d\text{ nm}$) of the nanotube according to the relation

$$\omega(\text{cm}^{-1}) = \frac{A}{d_c(\text{nm})} + B,$$

where A and B are parameters related to the nanotube environment. Therefore, particular chiralities of nanotube may be identified from the Raman spectrum peaks at these wavenumbers. The RBM's frequency is related to the reciprocal of the nanotube diameter (d_c). In the case of an isolated SWNT, this relation is: $\omega_r = 224/d_c$. But, non isolated SWNTs are subject to inter-tube interactions which tend to boost the RBM's frequency. The D - and G -bands are understood to be due to the sp^3 and sp^2 carbon bonding, respectively. The low D -to- G -band intensity ratio suggests the presence of high-quality, low-defect CNTs. Vibration at which the nanotube diameter contracts and expands D -band: vicinity of 1098 cm^{-1} , defect-derived peak G -band: vicinity of 1516 cm^{-1} , in-plane vibration of graphite. The G mode, also known as TM- *Tangential Mode*, matches to the stretching mode of the $-C-C-$ bond in the graphite plane. This mode is placed close to 1516 cm^{-1} .

Using the empirical relationship between the Raman RBM peak frequency RBM and the SWNT diameter, $\omega_{\text{RBM}} = 224 (\text{cm}^{-1})/d_{\text{SWNT}} (\text{nm}) + 10\text{ cm}^{-1}$, one can estimate the diameters of the PLD SWNTs exhibiting the RBM spectral peaks. From the relative ratio ($R = I_D/I_G$), we are able to evaluate the change in the in-plane crystallite size after the activation using the empirical equation.

The optical spectra were obtained using instruments depending on the wavelength range. Absorption spectra of SWNTs in the visible and near IR regions contain characteristic bands due to the metallic and semiconducting species. For the VIS-NIR range (200–3300 nm) total reflectance (both specular and diffusive) and transmittance spectra were collected using. For only the transmittance measurements were conducted using (fig. 3). We then related obtained transmittance data to absorption coefficient α via equation:

$$T = \frac{(1-R)^2 \left(1 + \left(\frac{k}{n} \right)^2 \right) \cdot \exp(-\alpha d)}{1 - R^2 \exp(-2\alpha d)} \quad (1)$$

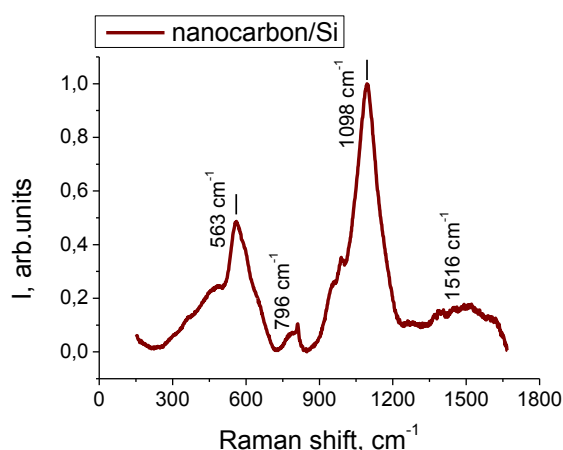


Fig. 2. Raman spectra of SWNTs samples

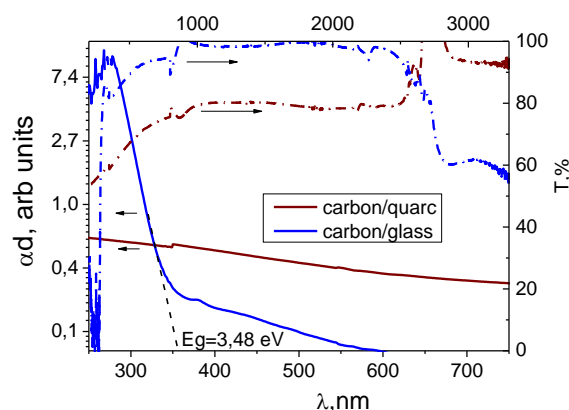


Fig. 3. Transmittance spectra of SWNTs samples in the wide spectral range (200–3300 nm)

where n is the refractive index, κ is the extinction coefficient, T – stands for transmittance, R is reflectance and d is sample thickness. To relate the transmittance and absorption coefficient to the concentration of the nanofiller, one can use the Beer-Lambert law $T \sim \exp(-ad)$, where wt represents mass fraction of the carbon nanofiller. All this provides two conclusions: first, the main mechanism responsible for blocking the light in the studied range is the absorption and secondly, only small fraction of graphene in the material is needed to fully tune its optical properties. These differences suggest different absorption mechanisms and as a result, different relation between graphene load and transmittance of the composite, depending on the wavelength of the incident radiation.

- [1]. S. Gupta and A. Saxena Nanocarbon materials: probing the curvature and topology effects using phonon spectra//J. Raman Spectrosc., 2009, **40**, p. 1127–1137.
- [2]. V.N. Popov Carbon nanotubes: properties and application // Materials Science and Engineering, R 2004, **43**, p. 61–102.
- [3]. M.S. Dresselhaus, G. Dresselhaus, R. Saito, A. Jorio Raman spectroscopy of carbon nanotubes // Physics Reports, 2005, **409**, 47–99.

SECTION 5. LASER TECHNICAL AND TECHNOLOGY APPLICATIONS

LASER ASSISTED HOT CARRIER EVIDENCE IN SOLAR CELLS

Jonas Gradauskas^{1,2}, Steponas Ašmontas¹, Algirdas Sužiedėlis¹, Aldis Šilėnas¹, Edmundas Širmulis¹, Aurimas Čerškus^{1,2}, Vitas Švedas¹, Viktoras Vaičiškauskas¹, Ovidijus Žalys¹, Anatoliy Opanasyuk³

¹ Center for Physical Sciences and Technology, Vilnius 01108, Lithuania

² Vilnius Gediminas Technical University, Vilnius 10223, Lithuania

³ Sumy State University, Sumy 40007, Ukraine

The Shockley-Queisser theory puts the limits on efficiency of a single-junction solar cell. It assumes that only photons having energy close to a semiconductor forbidden energy gap are used effectively in the formation of electrical output signal (Fig. 1; process 1). Residual energy of the high energy photons that is not used for the electron-hole generation is scored up only through the process of carrier thermalization, i.e. through the lattice heating and thus resulting effect on solar cell efficiency. Low energy photons are assumed to be not absorbed at all.

Hot carriers are free carriers with energy higher than the average one. The carriers can be heated by means of DC electric field, microwave or optical radiation. A laser is a useful tool to investigate the hot carrier phenomena for its unique features of monochromatic and wide power-range emission as well as for possibility of generating short light pulses. One way of carrier heating can be realized by laser radiation with photons having energy lower than a semiconductor forbidden energy gap. The intraband light absorption leads to rise of hot carrier photoemf across a semiconductor potential barrier (Fig. 1; process 2). Such a process has been investigated in Ge [1], Si [2], GaAs [3] i-h junctions as well as in Ge [4], Si [5], GaAs [6] and InSb [7] p-n junctions illuminated with a CO₂ laser radiation. Another possible way of carrier heating can be implemented by use of residual photon energy left over during the electron-hole pair generation due to the absorption of high energy photons.

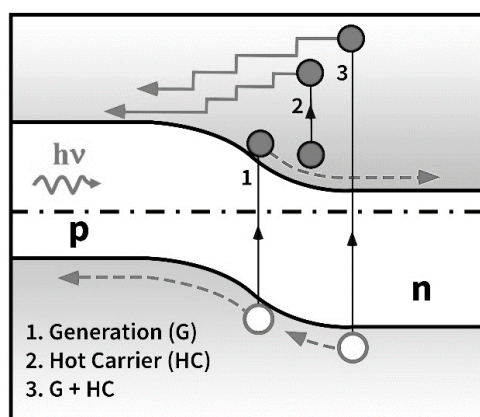


Fig. 1. Processes of generation-induced emf (1), hot carrier emf (2), and joint emf formation across a p-n junction

In this communication we present experimental evidence of hot carrier influence on the net photovoltage formation across a GaAs and Si p-n junctions as prominent candidates in solar cell production. We consider the net photovoltage consists of three components. The first one, U_G , is a relatively slow component caused by a classical electron-hole pair generation. The second one, U_{HC} , is fast and demonstrates opposite polarity what is an inherent feature of the hot carrier photovoltage. The third one, U_T , having the same polarity as U_{HC} , is also slow and is the thermoelectric voltage caused by the p-n junction lattice heating.

For direct observation of the components, they must be separated each from other. In general, the U_{HC} one could be set off by means of employing short laser pulses with photon energy lower than the semiconductor forbidden energy gap. The diode pumped solid state Nd:YAG laser NL202 (Ekspla Ltd, Lithuania) was used for direct excitation of the sample, as well as for parametric generation of longer wavelengths. The laser generated 15 ns duration pulses of the 1.064 μm radiation. Pulse repetition rate could be varied from single pulses to 1 kHz. At the laser output, irradiance could reach 2.7 MW/cm² maximum value. For spectral measurements, optical parametric oscillator (OPO) generating wavelengths from 1.43 μm to 4.8 μm was used (Fig. 2).

Investigation of photovoltage formation across the junctions exposed to short laser pulses of 1.06 – 9.2 μm spectral range reveals that predominance of each separate component depends on both light wavelength and intensity. Illumination of a p-n junction with short laser pulses having photon energy lower than the semiconductor forbidden energy gap permits to observe directly simultaneous formation of the hot carrier photovoltage and the classical photovoltage caused by two-photon absorption. As a rule, the U_{HC} component prevails at lower laser intensities and longer wavelengths (Fig. 3).

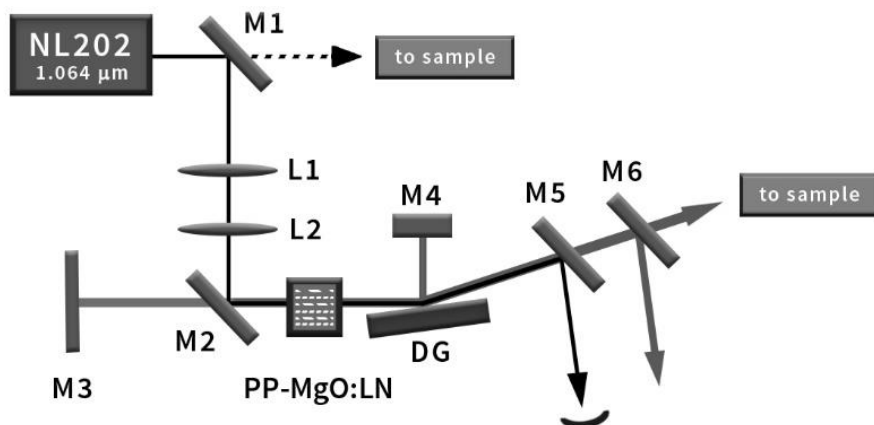


Fig. 2. Scheme of optical parametric oscillator OPO pumped by the Nd:YAG laser NL202. The 1.064 μm laser radiation is directed to the sample or, if mirror M1 is placed, is directed into the OPO; mirror M2 directs the pump radiation; L1 and L2 are lenses; mirrors M3, M4 and the gold coated optical diffraction grating DG comprise OPO's resonant cavity; mirror M5 rejects the pump and transmits the converted radiation; mirror M6 separates the signal and idler waves of parametric generation.

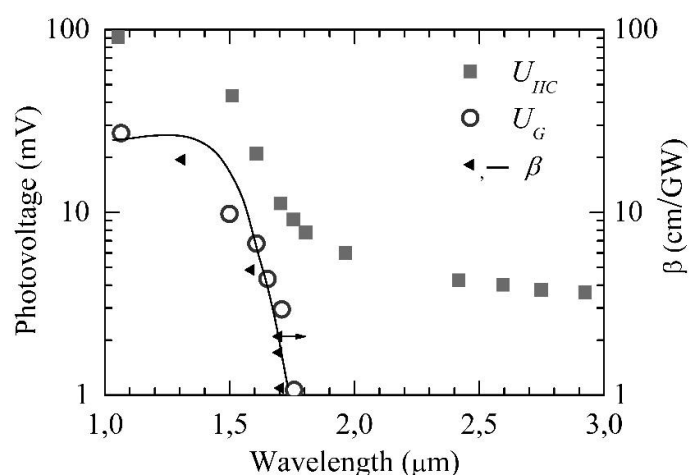


Fig. 3. Spectral dependence of U_{HC} (squares) and U_G (circles) photovoltage components across GaAs p-n junction. Triangles and solid line show distribution of GaAs two-photon absorption coefficient β (right scale).

As for conclusion, besides the usually considered thermalization of hot carriers, the magnitude of the net photovoltage depends on the result of mutual competition between the all three components. Maximum reduction of the hot carrier photovoltage contribution will boost the efficiency of a p-n junction solar cell. To reach this, several possible ways, such as formation of a graded-gap structures or porous silicon layers, are discussed in the communication. This work was supported in part by Research Council of Lithuania, Grants No. 01.2.2-LMT-K-718-01-0050 and No. S-LU-18-1.

- [1] S. Ašmontas, J. Gradauskas, D. Seliuta, A. Sužiedėlis, G. Valušis, E. Širmulis, Proc. SPIE **5123**, 221 (2003).
- [2] S. Ašmontas, E. Maldutis, E. Širmulis, Int. J. of Optoelectronics **3(3)** 263 (1988).
- [3] S. Ašmontas, J. Gradauskas, D. Seliuta, E. Širmulis, Proc. SPIE **3890**, 125 (1998).
- [4] M. Umeno, Y. Sugito, T. Jimbo, H. Hattori, Y. Amenixa, Sol. St. Electron. **21**, 191 (1978).
- [5] A.V. Andrianov, P.M. Valov, V.L. Sukhanov, V.U. Tuchkevich, N.M. Smidt, Phys. Techn. Poluprovodn. **14**, 859 (1980).
- [6] S. Ašmontas, J. Gradauskas, D. Seliuta, E. Širmulis, Proc. SPIE **4423**, 18 (2001).
- [7] S. Ašmontas, J. Gradauskas, K. Naudžius, E. Širmulis, Semiconductors **28**, 1089 (1994).

VISUALIZATION OF SUBSURFACE DEFECTS IN COMPOSITE STRUCTURES USING SPECKLE INTERFEROGRAMS AND DYNAMIC SPECKLE PATTERNS

L. Muravsky, O. Kuts

*Karpenko Physico-Mechanical Institute of the NASU,
5 Naukova str., 79060 Lviv, muravskyleon@gmail.com*

Recently, optoelectronic systems containing lasers as coherent radiation sources are used in different directions of applied research. One of such directions consists in detection of subsurface defects located in laminated composites. Some laser interferometric systems have been created that can solve this problem partially [1–4]. The common principles of these systems are based on additive-subtractive electronic speckle pattern interferometry (ESPI) combined with harmonic ultrasonic (US) excitation of a studied composite specimen with variable frequencies from tens to hundreds KHz.

To detect the subsurface defects in composite panels, we have developed the subtractive digital speckle pattern interferometry (DSPI) method with accumulation of speckle patterns, which essence is based on producing of speckle interferograms during US periodic excitation of composite panels with variable frequency [5]. In the case of composite panel is excited, each subsurface defect starts to oscillate on its own resonant frequency, if it coincides with the time variable frequency of US waves. The US excitation works in the frequency scanning mode, and all the defects that have resonant frequencies in the range from 15 to 150 KHz begin generate oscillations. So, each subsurface defect that is oscillated on the resonant frequency induces local oscillations of the surface area or the region of interest (ROI) placed directly above this defect. Thus, the ROI begins to oscillate with the same frequency. Extreme thickening of the panel within the ROI corresponds to the maximum amplitude of the harmonic wave, and the panel extreme thinning within the ROI corresponds to the minimum wave amplitude. On the other hand, surface oscillations on this frequency are absent or very small outside the ROI or ROIs. If we record speckle interferograms at different moments of the ROI oscillations, we can detect the subsurface defect by correlation comparison of these speckle interferograms.

In order to realize the proposed method, a hybrid interferometric system (HIS) intended for detection of the subsurface defects including internal debonds and delaminations in aircraft composites was created. Laminate, sandwich and honeycomb composite panels with thickness ranging from 1 to 8 mm can be tested by this system. In the HIS, the excited ROI states are recorded in a Twyman-Green interferometer as speckle interferograms of a surface region containing the ROI. Two series of speckle interferograms that fix maximum and minimum values of the US wave are accumulated by CCD camera and acousto-

optic deflector during the chosen exposure time. The obtained two accumulated speckle interferograms are subtracted in computer. The resulted fringe pattern allows visualizing the subsurface defect placed in ROI. Because the contrast of an extracted defect is low, we add the series of obtained fringe patterns. Results of the system's full-scale test using a honeycomb composite element of a trim cargo hatch aircraft AN are shown in Fig. 1.

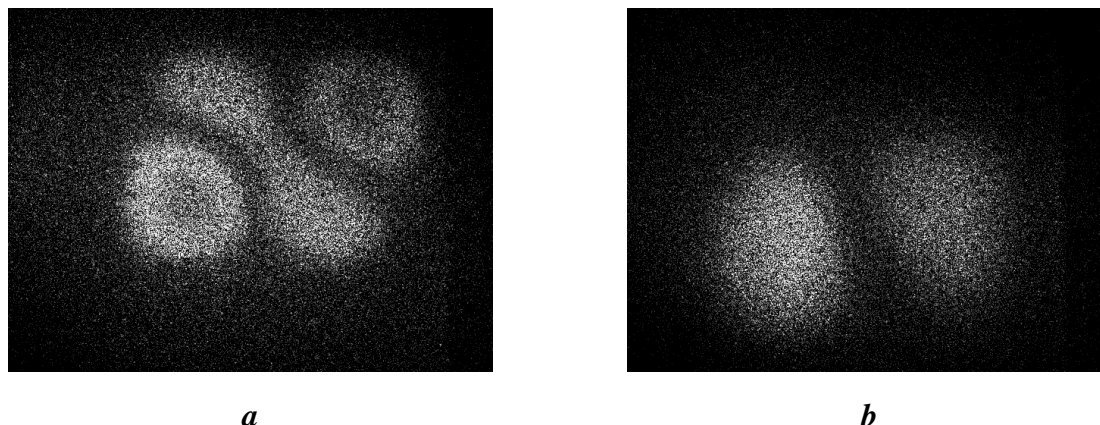


Fig. 1. Fringe patterns of delamination in a honeycomb composite element of a trim cargo hatch aircraft AN: delamination in 3-d layer, resonance frequency $f=21$ KHz (a); delamination in 5-th layer, resonance frequency $f=17.5$ KHz (b).

The interferometric systems that realize the additive-subtractive ESPI and subtractive DSPI methods are complex and very sensitive to external vibrations and air or heat fluxes. Therefore, creation of more simple systems is actual problem. One of the possible ways of its solving consists in using dynamic speckle pattern phenomena, in particular, the laser speckle contrast imaging. We offer new approach for internal defects detecting, which is based on estimation the dynamic speckle motion in different areas of a studied composite structure generated by harmonic US excitation. The differences between speckle motion amplitudes at ROI places directly above the defect and other areas of the studied composite surface allow extracting this defect and localizing it. To realize the offered approach, we have created an optical-digital system (ODS) setup, which is much simpler than any interferometric system. In the ODS setup, it is enough to use a semiconductor laser with amplitude modulation or a semiconductor laser with acousto-optical modulator. Also a laser beam expander (for example, a divergent lens), a digital camera for recording speckle patterns, a source of harmonic US excitation, and a much simpler synchronization system than the last one in the developed HIS are used. The reliability of the proposed approach was proved by the results of experiments with the composite panel containing inner holes. Results of test experiments to detect blind holes with diameters equal to 4 mm and 12 mm carved in the fiberglass laminate panel CTЭФ-1 (the analogue of FL 3240) with thickness equal to 6 mm are shown in Fig. 2.

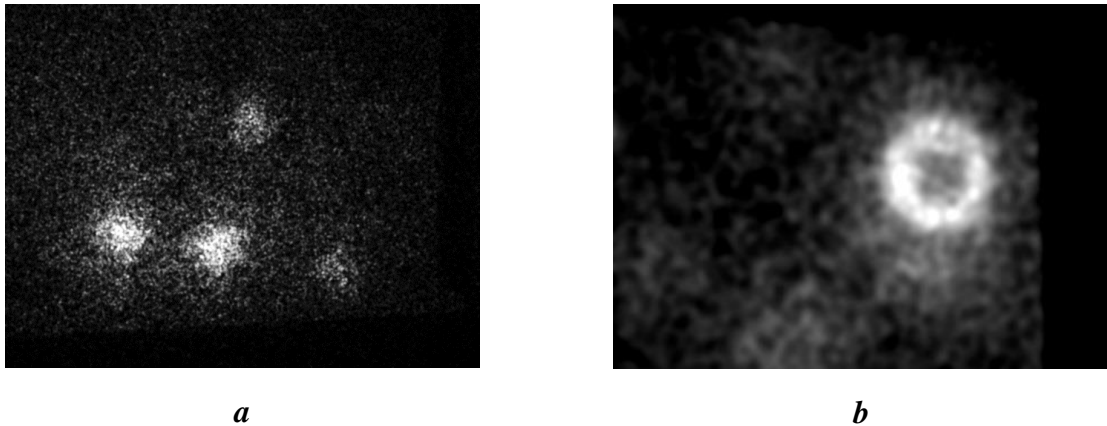


Fig. 2. Speckle patterns of blind holes in the carved in the fiberglass laminate panel (CTЭФ-1) FL 3240 located at a depth of 1 mm from the laser-probed surface, on which blind holes are invisible: blind holes with diameter 4 mm detected at resonant frequency 85 KHz (a); two blind holes with diameters 4 mm and 12 mm detected at resonant frequency 30 KHz (b).

The systems built on basis of the ODS setup can be used in field conditions, since their sensitivity to vibrations, heat and air flows and other external influences is much less than the sensitivity of interferometric systems implementing ESPI and DSPI methods.

Thus, we have developed the new methods for detecting of subsurface defects in laminated composite panels using pixel by pixel addition of subtractive speckle interferograms and dynamic speckle patterns. We have created the experimental breadboards of two systems that realize these methods, namely, the HIS and the ODS for subsurface defect detecting.

References

1. Additive/subtractive decorrelated electronic speckle pattern interferometry / B.F. Pouet, S. Krishnaswamy // Opt. Eng. – 1993. – V. 32, N 6. – P. 1360–1369.
2. Additive-subtractive phase-modulated electronic speckle pattern interferometry: analysis of fringe visibility / B.F. Pouet, S. Krishnaswamy // Appl. Opt. – 1994. – V. 33, N 28. – P. 6609–6616.
3. Additive-subtractive speckle interferometry: extraction of phase data in noisy environments // Opt. Eng. – 1996. – V. 35, N 3. – P. 794–801.
4. Fomitchov P. Advanced image-processing techniques for automatic nondestructive evaluation of adhesively-bonded structures using speckle interferometry / P. Fomitchov, L.-S. Wang, S. Krishnaswamy // J. Nondestr. Eval. – 1997. – V.16, N 4. – P. 215–227.
5. Muravs'kyy L.I., Voronyak T.I., Kmet' A.B. Lazerna interferometriya vyboru dlya potreb tekhnichnoyi diahnostyky / Nauk. red. Z.T. Nazarchuk. – L'viv: SPOLOM, 2014. – 272 s.

LASER CONOSCOPIC METHOD FOR INVESTIGATION OF PHOTOELASTICITY OF CRYSTALS

B. Mytsyk¹, A. Andrushchak², N. Demyanyshyn¹, Ya. Kost¹

¹*Karpenko Physico-Mechanical Institute, 5 Naukova St., Lviv 79601, Ukraine, mytsyk@ipm.lviv.ua*

²*Lviv Polytechnic National University, 12 Bandery St., Lviv 79000, Ukraine*

The photoelasticity of crystals (piezo- and elasto-optic effects) is studied mainly by an interferometric method (see, for example, works [1-4]). In fig. 1 shows a typical scheme of an interferometric device for determining piezo-optical coefficients (POCs) π_{im} (indices i, m denote the direction of light propagation and the action of uniaxial pressure). If $i, m = 1, 2, 3$, then the corresponding POCs are called principal, and the expression for the determination of these POCs has a simple form [2]:

$$\delta\Delta_k = -\frac{1}{2}\pi_{im}n_i^3 + S_{km}\sigma_m d_k (n_i - 1), \quad (1)$$

or

$$\pi_{im} = -\frac{2\delta\Delta_k}{\sigma_m d_k n_i^3} + 2S_{km} \frac{n_i - 1}{n_i^3}, \quad (2)$$

where the index k denotes the direction of light propagation, σ_m is uniaxial pressure (mechanical stress), $\delta\Delta_k$ is change of the optical path $\Delta = n_i d_k$; n_i is refraction index, d_k is thickness of sample in the direction of light propagation, S_{km} is elastic compliance coefficient.

If it is necessary to determine a non-principal POC π_{im} (indices $i, m = 4, 5, 6$), then the expression of type (1) is significantly complicated. For example, to determine the rotational POC π_{61} in tetragonal crystals, the ratio [5] was obtained (for sample $Z/22.5^\circ$ -cut; $\alpha = 22.5^\circ$ is the angle between the normal to the sample face and the Y axis of the optical indicatrix)

$$\begin{aligned} \delta\Delta_{6^*} = & -\frac{1}{2} \sigma d_{6^*} n_1^3 \cos^4 \alpha \cdot [\pi_{11}(1 + \tan^4 \alpha) + 2(\pi_{12} + \pi_{66}) \tan^2 \alpha + \\ & + (\pi_{16} + 2\pi_{61})(\tan^3 \alpha - \tan \alpha)] + \sigma d_{6^*} \cos^4 \alpha \cdot [(2S_{11} - S_{66}) \tan^2 \alpha + \\ & + S_{12}(1 + \tan^4 \alpha) - 2S_{16}(\tan^3 \alpha - \tan \alpha)](n_1 - 1), \end{aligned} \quad (3)$$

on the basis of which it is impossible to determine this coefficient with high accuracy, since the error of determination of POC π_{61} is formed by the error of the complex sum of the piezo-optical and elastic coefficients included in (3).

The conoscopic method is indispensable for determining the specified POC with high precision. The corresponding installation scheme is given in Fig. 1. And in fig. 2 shows conoscopic pictures of CaWO_4 crystal (symmetry class $4/m$) without stress and under the action of stress σ_1 . The expression for determining POC π_{61} has a simple form [6]:

$$\pi_{61} = (\pi_{11} - \pi_{12}) \tan \alpha_3, \quad (4)$$

where α_3 is the induced stress σ_1 the angle of rotation of the optical indicatrix around the Z axis.

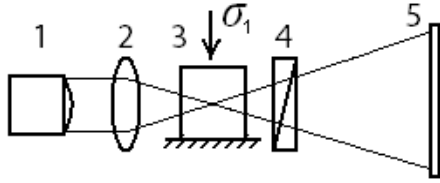


Fig 1. Installation scheme for creating a conoscopic pictures: 1 – laser, 2 – condenser, 3 – sample, 4 – analyzer, 5 – screen.

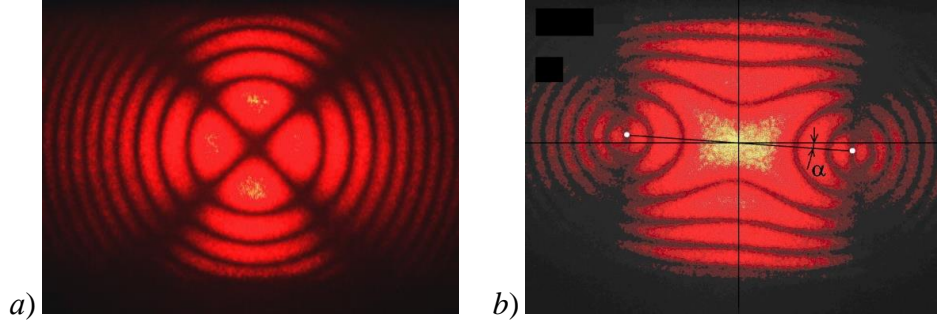


Fig. 2. Change of the conoscopic picture of CaWO₄ crystal with an increase in the mechanical stress σ_1 (in kG/cm²): a) $\sigma_1 = 0$; b) $\sigma_1 = 180$.

The conoscopic method is also useful under the condition of light propagation, perpendicular to the optical axis. An example of the corresponding conoscopic pictures are presented in fig. 3.

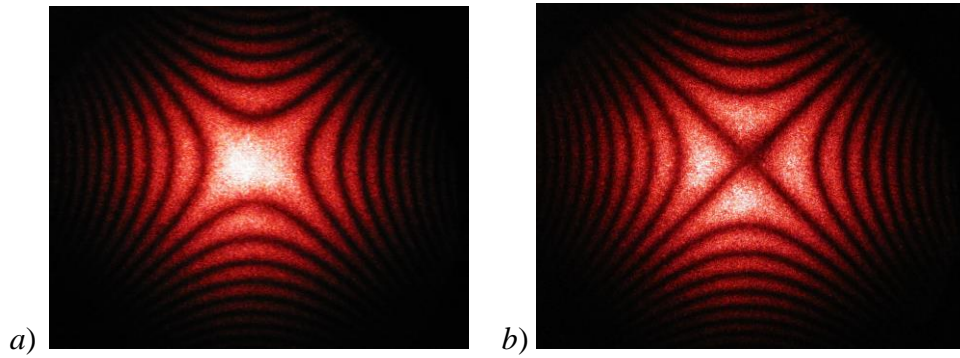


Fig. 3. Conoscopic pictures of direct cuts sample (Li₂B₄O₇ crystal) under conditions $k = 1$, $m = 2$: a) $\sigma_2 = 0$, b) $\sigma_2 = 180$ kg/cm² (this is a half-wave stress - changes the intensity of light in the center from *max* to *min*).

By changing the light intensity, in this case we can find only the combined difference of the absolute coefficients π_{im} :

$$\pi_{km}^* = \pi_{im} n_i^3 - \pi_{jm} n_j^3, \quad (5)$$

where π_{km}^* is POC, which describes the change of birefringence and is precisely determined by the experimental polarization-optical method. For example, for tetragonal crystal and for experimental conditions $k = 3$, $m = 2$ from (5) we obtain:

$$\pi_{32}^* = \pi_{12}n_2^3 - \pi_{22}n_2^3 = \pi_{12}n_2^3 - \pi_{11}n_1^3; \quad (6)$$

where it is taken into account that for 4mm symmetry class $\pi_{22} = \pi_{11}$, $n_2 = n_1$.

From (6) we find a simple expression for determining of absolute POC π_{21} :

$$\pi_{21} = \pi_{32}^* / n_1^3 + \pi_{11}. \quad (7)$$

Example: for $\text{Li}_2\text{B}_4\text{O}_7$ crystal, this method was used to find the POC π_{21} with small error, namely, $\pi_{21} = 0.46 \pm 0.11$ Br (1 Br = 10^{-12} m³/N). This coefficient is determined by the interferometric method with an error 3 times larger.

The conoscopic method is also indispensable in determining the problematic rotation coefficient of π_{53} in low-symmetric monoclinic crystals. The sample must be cut so that one face is perpendicular to one of the optical axes of the crystal. The rotation α of this axis around the Y axis of the optical indicatrix due to the actions of the mechanical stress σ_3 is easy to register using conoscopic method and determine the POC π_{53} based on the known expression

$$\tan \alpha = \frac{\pi_{53}\sigma_3}{a_1 - a_3}; \quad (8)$$

where $a_1 = 1/n_1^2$, $a_3 = 1/n_3^2$ – polarization constants.

We emphasize that the interferometric method makes it impossible to independently determine this POC.

Consequently, the conoscopic method of studying the piezo-optic effect is an excellent addition to the interferometry for fill of POC matrices of crystals of different symmetry classes. The matrices of the elasto-optical coefficients p_{in} are calculated on the basis of POC π_{im} , the elastic stiffness coefficients C_{mn} and known tensor expression $p_{in} = \pi_{im}C_{mn}$ [1, 2].

References

- [1] Narasimhamurty T.S. Photoelastic and electro-optic properties of crystals. Plenum press. New York and London (1981).
- [2] Mytsyk B. Methods for the studies of the piezo-optical effect in crystals and the analysis of experimental data. I. Methodology for the studies of piezo-optical effect. Ukr. J.Phys. Opt. **4**, 1-26 (2003).
- [3] Kaidan M.V., Zadorozhna A.V., Andrushchak A.S., Kityk A.V. Photoelastic and acousto-optical properties of Cs_2HgCl_4 crystals. Appl. Opt. **41** (25), 5341-5345 (2002).
- [4] Martynyuk-Lototska I., Mys O., Dudok T., Adamiv V., Smirnov Ye., Vlokh R. Acousto-optic interaction in $\alpha\text{-BaB}_2\text{O}_4$ and $\text{Li}_2\text{B}_4\text{O}_7$ crystals. Appl. Opt. **47** (19), 3446-3454 (2008).
- [5] Mytsyk B., Demyanyshyn N., Kost' Ya. Analytical relations describing piezo-optic effect in tetragonal crystals. Ukr. J. Phys. Opt. **14** (3), 101-118 (2013).
- [6] Mytsyk B.G., Kost' Ya.P., Demyanyshyn N.M., Gaba V.M., Sakharuk O.M. Study of piezo-optic effect of calcium tungstate crystals by the conoscopic method. Opt. Matter. **39**, 69-73 (2015).

APPLICATION OF LASERS IN SCIENCE AND TECHNOLOGY

Ivan Petricin

Drogobych State Pedagogical University, I. Franka 24, Drogobych, Ukraine
petrivan1959@gmail.com

Lasers are widely used in various fields of science and technology, such as physics, chemistry, biology, electronics and medicine. Such a widespread use of lasers is due to the special properties of laser radiation.

Laser technology is a collection of technical means for generating, transforming, transmitting, receiving and using laser radiation. Laser technology includes:

- own lasers;
- their elements - radiators, active elements, optical resonators, laser sources, load sources, power and control units, cooling systems, etc.;
- laser beam control devices - modulators of light, deflectors, frequency converters, etc.;
- to install, install, install, use lasers characteristics of their functional assignments – laser technological installations, laser rangefinders, laser sound and video players, and the like.

The physical basis of the laser is the quantum mechanical phenomenon of induced radiation. The radiation of the laser can be continuous, with constant power, or pulse, which reaches extremely high peak capacities. In some circuits, the operating element of a laser is used as an optical amplifier for radiation from another source. There are a large number of types of lasers that use as aggregates the working medium. Some types of lasers, such as dye solution lasers or polychromatic solid state lasers, can generate a set of frequencies in a wide spectral range. The dimensions of the lasers differ from the microscopic for a number of semiconductor lasers to the size of the football field for some neodymium glass lasers. The unique properties of laser radiation allowed them to be used in various fields of science and technology, as well as in everyday life, from reading and writing CDs to research in the field of controlled thermonuclear fusion.

The basis of the practical application of laser technology is the use of such fundamental differences in laser radiation from the radiation of other sources of light, such as coherence and monochromaticity, high orientation and brightness, the possibility of obtaining light pulses of short duration, unattainable when using other technical means.

The laser cuts, welds and cures, as well as hardens, drills, cuts, drills, checks the quality of parts processing, and makes a number of other, no less important cases, for which, it would seem, absolutely no good light ray. The laser allows you to easily automate welding, welding metals that can not be connected in the usual way, as well as making parts where the usual tool can not

penetrate it is impossible - to weld electronics parts directly in a vacuum flask, directing a ray through the glass.

Particularly striking changes have brought the laser in the way of processing solid materials: the ray of light cuts them like oil. The beam of light can be cut up, cut from the steel sheet the most exhausting parts. For this purpose the laser is mobile. Its motion is controlled by a digital machine. Now, in modern factories, automatic laser machines are in operation. One second - and a finished bearing. The hole in it is ideally round, the gap almost does not happen.

The most interesting thing is that only one thousandths of a second are spent on breaking the hole, and the rest of the time is to put the workpiece and to remove the finished item. The processing of materials by means of lasers has recently resulted in a powerful direction, which has got the name of laser technology.

The high temperature of the radiation allows you to weld materials that can not be cooked in conventional ways (ceramics and metal). The beam of the laser can be focused on a point about a micron diameter, which allows it to be used in microelectronics. Lasers are used to obtain surface coatings (laser surfacing, laser doping, vacuum-laser spraying) to increase their wear resistance. Wide application was also obtained by laser marking of industrial designs and engraving products from various materials. Laser processing is therefore characterized by high precision and performance.

One can formulate the main advantages of laser treatment of materials: firstly, a large variety of processing processes of various types of materials, including those that can not be machined; and secondly, the high speed of processing operations, which is sometimes a thousand times greater than mechanical; Third, the high quality of processing, the ease of automation of operations, contributing to a significant increase in productivity.

Currently, the so-called laser communication is developing rapidly. The length of the light wave is, on average, six orders of magnitude smaller than the wavelength of the radio frequency band, so laser radiation can transmit much more information. The laser communication is carried out both on open and on closed structures of light conductors, for example, on an optical fiber. The light due to the phenomenon of complete internal reflection can spread to them over long distances, practically not weakening.

Laser beams carry energy. Theoretically, they could be used, like power transmission lines, to use for energy supply in remote areas. However, the scale of the power system of the whole country is not feasible - such a method is suitable only for the energy of spacecraft and space stations of the future.

Impulse laser locators today are used not only in space, but also in aviation. In particular, they can play the role of scientific height meters. The laser altimeter was also used in the spacecraft Apollo to photograph the surface of the moon.

Of great interest are recent developments in the field of creating a TV based on laser technology. According to the expectations of specialists, such a TV should differ ultra-high quality of the image. It is also worth noting the use of lasers in already well-known high-quality printers or laser printers. In these devices, laser radiation is used to create a latent copy of a printed image on a special photosensitive drum.

In aviation, laser gyroscopes, altimeters and flight speed meters are used. It is also important that the laser helps precisely and correctly plan the aircraft, thus ensuring the safety of the crew and passengers.

Everyone knows about the laser sight, which increases the accuracy of the hit the arrow in the target. The ray is universally used in the armament of various countries of the world. With its help, not only accurately shoot, but also arrange obstacles to the enemy and the system of detection of snipers, as well as develop methods of misleading the enemy.

Today, the laser is indispensable also in medicine. It is used in surgery, ophthalmology, gynecology, oncology and cosmetic surgery. For example, in operations on the eyeball, the laser is able to weld a detached retina without injuring the eye. The laser can be a bloodless scalpel, bury both benign and malignant tumors. It is also used successfully in dentistry for teeth whitening and bloodless implantation. And very pleased with the prospect of the use of rays to stop bleeding in people with a low ability to thicken blood.

Laser astronomy can also lead to a completely different level of quality of their research. For example, with the help of ruby lasers fortified to more accurately determine the distance from Earth to other cosmic bodies. Accurate mapping of a rigorous planet is now up to a meter. With the help of semiconductor lasers, communication with satellites is carried out.

There are many other applications of lasers. In particular, they are widely used in fundamental research, for example, to study the properties of solids, liquids and gases. Without a doubt, in the future a lot of new interesting possibilities will appear in front of the lasers. Obviously only one thing - he will solve any problems, this device will never remain without a business.

The laser is one of the least instruments of today's science. It is impossible to enumerate all the fields of its application, because for a laser there are new tasks.

Such diverse tasks can be accomplished using a task laser for its properties. Coherence, monochromaticity, high energy density allow solving complex technological operations. The laser is an instrument of the future, which has become firmly established in our lives.

DETERMINATION OF THE CHEMICAL ELEMENTS IN THE SOIL BY LASER-INDUCED BREAKDOWN SPECTROSCOPY

Schukin S.¹, Frolov S.¹, Lymarenko R.¹, Litvinuk L.², Taranenko V.¹

¹ *International Center “Institute of Applied Optics”, Nat. Acad. Sci. of Ukraine, Kyiv, Ukraine, e-mail: lorlay76@gmail.com*

² *Nat. Scientific Center “Institute of Mechanization and Electrification of Agriculture”, Nat. Acad. Sci. of Ukraine*

Abstract: Capabilities, advantages and difficulties of applying laser-induced breakdown spectroscopy (LIBS) for analysis of soils are presented. For the plasma excitation a passively Q-switched pulse-periodic Nd:YAG laser laser and microlaser are used.

Keywords: LIBS; spectral analysis of soil; Q-switched YAG:Nd laser, microlaser.

There is a global actual problem of soil monitoring and agricultural chemistry. Intensification of agricultural production with an attempt to obtain maximum yield resulted in the imbalance of chemical elements in the soil environment. As a result, the destruction of soil fertility is observed, exact soil composition is locally unknown. Consequently, farmers make unnecessary fertilization and pollute soils. In order to stop the degradation and save the fertility of soil it is necessary to know the changes in the nutrient content in soil in a timely manner. Now measurements of soil composition are very time-consuming.

Therefore, it is important to have an effective technology for determining the chemical composition of the soil. The several technologies of elemental analysis are now studied for application to the rapid determination of the content of elements in soil. The LIBS looks very attractive for rapid soil analysis. This technology not needs the special sample preparation, the multi-element spectral data can be quickly obtained and processed in real-time if the correct methods and apparatus are applied, the field measurements are possible.

It is promising to develop a portable LIBS analyzer to determine the qualitative and quantitative composition of chemical elements in the soil in the field in the “on-line” mode [1].

We have used the following experimental LIBS set-up. The Q-switched Nd:YAG laser with lamp pumping provides generation of a pulse train with the pulse duration of 10 ns and the pulse energy of 30 mJ. The laser radiation has been focused on a target surface in the spot with the diameter of 100 μm with the lens of $F=75$ mm. The spectral unit is the spectrometer Ocean Optics S2000. For the purpose of the quantitative analysis, a spectrum has been detected in the

total range 200-450 nm. Measurement and processing of spectra by a computer provides conditions for performing spectral analysis in real time.

Also compact laser based on ceramics is developed, which generates sub-nano-second pulses with energy of more than 1 mJ, which corresponds to a peak power of 1 MW with a repetition rate of 200 Hz. Laser ceramics combines the best properties of laser crystals with good workability and low cost of laser glasses. It is planned to increase the energy of the microlaser pulses up to 20 mJ, which is enough for LIBS. To increase the brightness of the microlaser, the developed methods of laser filtration based on photonic crystals will be used [2].

Fig.1 shows the soil sample spectrum obtained with mentioned above technique.

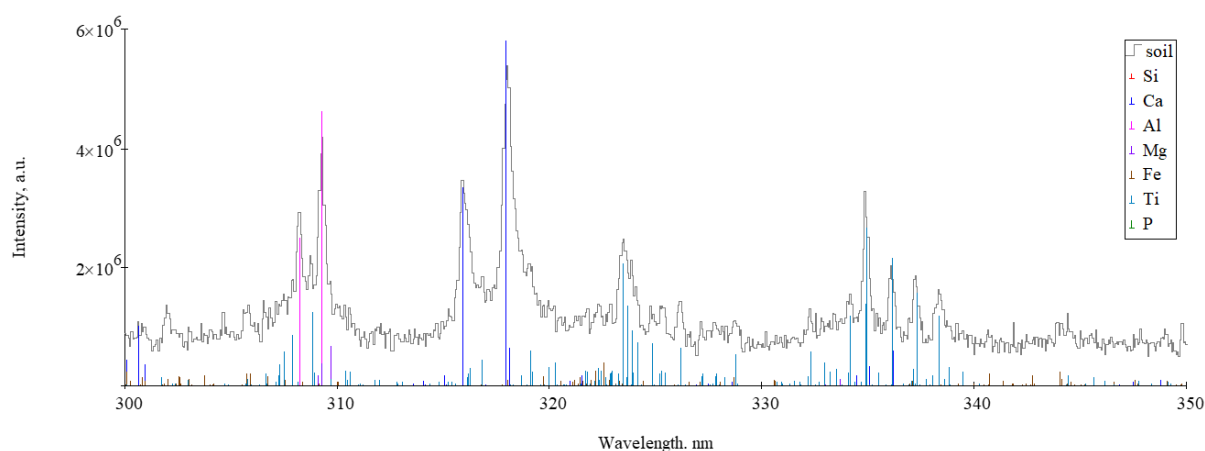


Fig.1. Qualitative analysis of LIBS spectrum of chernozem.

Up - spectrum of soil. Below - lines from the Spectra database NIST Atomic Spectra Database (temperature plasma of 1.3 eV, the electron density $7 \times 10^{18} \text{ cm}^{-3}$) [3] .

The spectrum provides qualitative information of the chemical composition of the soil. On the spectra we observe the intense lines of Si, Fe, Mg, P, Ca, Al, Ti (Fig. 1).

For the portable laser analyzer, it is expedient to use laser diode pumping to realize low power consumption, at the same time, sufficient pulse energy to excite the emission spectrum of the soil. For these purposes it is expedient to use Nd:YAG diode pumped microlaser.

But in order to determine the qualitative and quantitative composition of the sample, it is necessary to create a special catalog of analytical lines pairs obtained with the chosen mode of laser generation for LIBS [4]. Also an appropriate software is needed to be developed.

Currently, there are a number of problems of the application of the LIBS to the soil: the accuracy of elements content measurement in soil is not high, the results reproducibility is low. The influence of a physical properties of soil (humidity, granulation, density etc) on LIBS spectra is poorly understood now

[5]. The LIBS spectra are very informative, but their real-time processing needs significant amount of computer calculations and are the time-consumable.

Thus, our experimental researches have shown that the use of LIBS technology is promising for the chemical composition analysis of the soil. Nevertheless, it is necessary to conduct extensive research, overcome some difficulties, such as the creation of a database of analytical lines for soils, reference soil spectra, and develop appropriate software. The creation of a portable laser analyser will help create favourable conditions for the growth and development of cultivated crops in the soil and the climatic zones of Ukraine, restore soil fertility, improve the ecology of the soil and the environment, increase productivity, reduce production costs, reduce pathogenic microorganisms, and reduce the cost of soil analysis.

[1] Schukin S, Batrak P, Lymarenko R, Litvinuk L, Taranenko V. Laser-induced breakdown spectroscopy of soils. Laser technologies. Lasers and their application (2017) p. 112-114.

[2] Frolov S., Lymarenko R., Taranenko V., Burykin N. 1 MW subnanosecond passively Q-switched microlaser with hybrid saturable absorber. Laser technologies. Lasers and their application (2017) p. 50-52.c.

[3] National Institute of Standards and Technology Atomic Spectra Database: <http://physics.nist.gov/PhysRefData/>

[4] Anokhov S., Berezhnoy E., Zabello E., Nosov O. Spatial and spectral structure of a plasma plume induced by the multipulse laser evaporation of the material// Optics. Quantum electronics. Holography. ISSN 0503-1265. Ukr. J. Phys. V. 49. 2004, N 8, p. 763-765

[5] Capitelli F, Colao F, Provenzano M, Fantoni R, Brunetti G, Senesi N, 2002. Determination of heavy metals in soils by Laser Induced Breakdown Spectroscopy. Geoderma 106: 45-62.

INVESTIGATION OF PLASMON-PHONON INTERACTION IN THE INFRARED SPECTRAL RANGE FOR THIN Tb-DOPED ZnO FILMS GROWN ON SiO₂ SUBSTRATES

Venger Ye.¹, Korsunska N.¹, Melnichuk L.²,
Melnichuk O.², Khomenkova L.¹

¹*V. Lashkaryov Institute of Semiconductor Physics of NAS of Ukraine,
45 Pr. Nauky, 03650 Kyiv, Ukraine*

²*Mykola Gogol State University of Nizhyn, 2 Hrafska Str., Nizhyn 16600, Ukraine,
mov310310@gmail.com*

The development of modern lasers is inextricably linked with the miniaturization of certain functional components of these devices owing to the development of thin film technology. It is obvious that the properties of laser systems are extremely controlled by the quality of the grown films as well as the ability to predict and monitor their characteristics [1]. The investigation of physical, optical and electrical properties of thin semiconductor films grown on dielectric and semiconductor substrates was carried out [1-5]. However, the reports on the study of the interaction of electromagnetic radiation with different types of oscillations (such as phonons and plasmons) and the elucidation of the conditions governed phonon-plasmon interaction are not numerous. At the same time, such interaction substantially changes the nature of bulk and surface phonon and plasmon-phonon excitations, and causes significant transformation of optical properties of the entire structure.

Nowadays, ZnO-based materials attract considerable attention due to unique combination of optical, piezoelectric and mechanical properties. ZnO films doped with different elements demonstrate also plasmonic properties that can be used for optoelectronics and telecommunication. In this work, the study of Tb-doped ZnO thin films grown on fused quartz substrates was performed by means of infrared reflection (IRR) spectroscopy in the spectral range corresponding to the plasmon-phonon resonance of ZnO film.

The films were deposited by radio-frequency magnetron sputtering of composed Tb-ZnO target in argon ion plasma. More details about deposition conditions can be found in [3, 4]. The thickness of as-deposited films was ~632 nm. The films were polycrystalline with the *c*-axis orientation perpendicular to the substrate. The average Tb content in the films was about 3 at. %. The IRR spectra were recorded using Bruker Vertex 70 V FTIR spectrometer equipped with a Globar source and a deuterated triglycine sulfate (DLATGS) detector with a polyethylene window. The incidence angle was 13°. The IRR spectrum of a gold mirror was used as a reference. The orientation of electric field *E* was taken to be perpendicular to the *c*-axis of ZnO film (*E*⊥*c*). The spectral resolution was ~1 cm⁻¹. The accuracy of the determination of the reflection coefficient was ~1 %. The

experiments were carried out at room temperature.

It is known that ZnO has a strong anisotropy of phonon system and a weak anisotropy of plasma one, ZnO films are the suitable model object for investigation of anisotropy of optical and electrophysical properties of the materials in IR spectral region under the presence of the interrelation of long wavelength optical vibration of the lattice with electron plasma. Theoretical simulation of IRR spectra was performed for the range of ZnO "residual rays" (400-600 cm^{-1}) taking into account ZnO/SiO₂ structure as ZnO absorbing film grown on semi-infinite SiO₂ substrate and using the models described in Refs.[3, 5]. More details on the analysis of self-consistent parameters for a single oscillator model for ZnO films with the free carrier concentration $n_0=10^{16}$ - 10^{20} cm^{-3} can be found in Ref. [3].

The IRR spectra of SiO₂ substrate were also simulated taking into account the frequency dependence of SiO₂ dielectric constant for the $E \perp c$ reported in Ref. [5]. The presence of four oscillators in the "residual rays" range of SiO₂ substrate (350-1500 cm^{-1}) was considered [6]. They correspond to transverse (TO) and longitudinal optical (LO) phonons appeared at 457, 810, 1072 and 1160 cm^{-1} [6]. The value of the oscillator strength for i -th oscillator ($\Delta\epsilon_i$) and its attenuation coefficient (γ_{fi}) were determined by means the Kramers-Kronig method. Since the range of "residual rays" of SiO₂ substrate (350-1500 cm^{-1}) covers that of ZnO film (400-600 cm^{-1}), one can expect an appearance of some characteristic features in the experimental IRR spectra of ZnO/SiO₂ structure in the 350-1500 cm^{-1} range.

The experimental IRR spectra of the film ($RE(\nu)$, curve 1) indeed demonstrate the appearance of some maxima (Fig.1, curve 1). Taking into account the fact that the ZnO film is doped with terbium, the decrease in the $RE(\nu)$ values in this spectral range is considered to be not only due to effect of free electron concentration, but also the electron mobility.

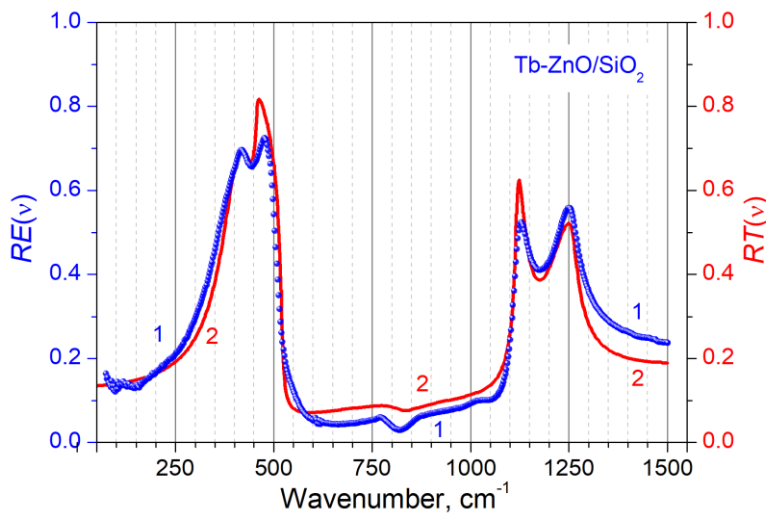


Fig.1. $RE(\nu)$ (curve 1) and $RT(\nu)$ (curve 2) spectra of Tb-doped ZnO film grown on SiO₂ substrate. The $RT(\nu)$ curve was simulated with the next parameters:
 $\gamma_f=30 \text{ cm}^{-1}$, $\nu_p=500 \text{ cm}^{-1}$,
 $\gamma_p=2500 \text{ cm}^{-1}$.

The theoretical simulation $RT(\nu)$ (Fig.1, curve 2) showed that these maxima are due to the interaction of the phonon and plasmon ZnO subsystems and the

phonon of SiO₂ subsystem. The comparison of the $RE(\nu)$ and $RT(\nu)$ curves was carried out using the least squares method. Besides, the mean square deviation of the of the $RE(\nu)$ values from the $RT(\nu)$ was determined according to the procedure described in [1, 3]. Unknown parameters in this analysis for the ZnO film were ν_p , γ_p and γ_f . They were varied in the ranges of $\nu_p=1-1000$ (with a 250 cm⁻¹ step), $\gamma_p=1-4000$ cm⁻¹ (with a 250 cm⁻¹ step) and $\gamma_f=10-50$ cm⁻¹ (with a 10cm⁻¹ step). The coincidence of the $RE(\nu)$ and $RT(\nu)$ curves was good enough and root-mean-square error was $\delta=10^{-2}$ for $\nu=50-1500$ cm⁻¹ spectral range. The best fitting was obtained for the next parameters: $\gamma_f=30$ cm⁻¹, $\nu_p=500$ cm⁻¹ and $\gamma_p=2500$ cm⁻¹ (Fig.1, curve 2).

The simulation of the $RE(\nu)$ dependence revealed that the most prominent changing of dielectric constant $\varepsilon(\nu)$ is appeared in the range of the plasmon-phonon resonance of ZnO film. It was observed a partial correlation of the features of IRR spectrum with the frequencies of TO and LO phonons of ZnO and SiO₂. The frequency shift of the TO phonon of the ZnO film affects slightly the corresponding low-frequency slope of IRR band and does not change the $RE(\nu)$ spectrum in the high-frequency range.

A good agreement between the $RE(\nu)$ and $RT(\nu)$ curves in the range of “residual rays” of the film and substrate (Fig. 1) confirms the reliability of the self-consistent parameters of bulk ZnO obtained by the authors [3] and the possibility of their use for the analysis of textured polycrystalline ZnO films.

Based on the obtained results, the electrophysical parameters of the film such as free electron concentration and their mobility were extracted. It turned out that $n_0=2.9 \cdot 10^{18}$ cm⁻³ and $\mu=90$ cm²/(V·s), respectively. Consequently, comparing the optical constants of ZnO single crystals with those of ZnO films allows us to conclude that the films investigated are of good quality, and the IRR spectroscopy is very attractive method for the determination of the lattice vibrational properties and electrophysical parameters of textured ZnO films. Being fast and non-destructive, the developed approach can be easy implemented in technology of laser materials.

References

1. Markevich I., Borkovska L., Venger Y., Korsunskaya N., Kushnirenko V., Melnichuk O., Melnichuk L., Khomenkova L., Ukr. J. Phys. (Reviews), 2018, v.13, p. 57-76.
2. Venger E.F., Melnichuk O.V., Pasechnik Yu.A., Spectroscopy of residual rays, Naukova dumka, Kyiv, 2001, 192 p.
3. Melnichuk O., Melnichuk L., Tsykaniuk B., Tsybrii Z., Lytvyn P., Guillaume C., Portier X., Strelchuk V., Venger Ye., Khomenkova L., Korsunskaya N., Thin Solid Films, 2019, v. 673, p. 136 – 140.
4. Korsunskaya N., Borkovska L., Polischuk Yu., Kolomys O., Lytvyn P., Markevich I., Strelchuk V., Kladko V., Melnichuk O., Melnichuk L., Khomenkova L., Mater. Sci. Semicond. Proces., 2019, v. 94, p. 51 – 56.
5. Kirk C.T., Phys. Rev. B, 1988, v. 38, p. 1255 – 1273.
6. Venger E.F., Melnichuk O.V., Melnichuk L.Yu., Semikina T.V., Ukr. J. Physics., 2016, v. 61, p. 1059 – 1066.

LASER FLOWMETER FOR OPTICALLY ACTIVE LIQUID-LUBRICANT MATERIALS

V. Zemlianski, DSc. M. Gusev, S. Yegorov, S. Poliak

National Aviation University, Kyiv, Ukraine

The principle of the laser speed flowmeter (LF) is based on the Doppler effect [1]. The most widespread was the differential LF scheme with two probing beams having matched polarizations. However, in the diagnostics of optically active media, the use of such a sensing scheme becomes ineffective. When two probing beams pass through the optically active medium, the azimuth of polarization changes, which leads to a low degree of polarization matching of the beams that are mixed on the photocathode, and ultimately to a decrease in the signal-to-noise ratio and accordingly to the accuracy.

The solution of the problem of increasing the accuracy of measuring the speed and flow of optically active media is proposed to be achieved by using a single laser and four probing beams that have mutually orthogonal circular polarizations in pairs.

LF works as follows [1, Fig 1].

The laser 1 emits a beam 2 that passes the polarizer 3 with a transmission axis azimuth $\alpha = 90^\circ$ and is further converted by a quarter-wave plate 4 into a left-circularly polarized beam 6 that is focused by the lens 5 at a point O located on the axis of the conduit 14. Further, the bundle 6 passing through the conduit 14, is collected by the lens 10 and, after reflection from the two mirrors 11, is focused by the lens 10 at the point O (in the measuring volume O). The lenses 5 and 10 have, respectively, the focal lengths F_1 and F_2 ($F_1 = F_2$), in addition, their optical axes coincide with the axis OX of the conduit 14. The probing beam 7 has a left-circular polarization. The beam 7 is collected by the lens 5 and, after reflection from the mirror 11, becomes circularly polarized. Further, this beam 8 is focused by the lens 5 in the measurement volume O, then collected by the lens 10 and then reflected from the two mirrors 11, this beam-9 is focused in the region D. Thus, in the measurement zone, the lens 5 focuses two beams 6 and 8, and the lens 10 two beams 7 and 9. These beams intersect at an angle γ and have mutually orthogonal circular polarizations, so when they pass through the optically active medium moving through the conduit 14, there is no change in the state of their polarization. The beam 9 is collected by a lens 5 and converted by a quarter-wave plate 4 into a horizontally polarized beam. This

beam is suppressed by the polarization filter 3 and does not enter the optical resonator of the laser 1.

Through the measurement zone O, which is an ellipsoid of revolution, the liquid medium moves at a velocity V containing micro particles (these particles have a diameter commensurable with the wavelength λ of the laser beam 2). The 26° radiation scattered on the micro particles is assembled by a receiving block consisting of 16, 18 and 20, the output of which is optically matched to the input of the light guide 22.

The second receiver unit, consisting of 15, 17 and 19, collects scattered radiation 27 which is directed to the input of the light guide 21. The outputs of the light guides 21 and 22 are optically matched to the input of the photodetector 23. Thus, by means of the light guide 21 (similarly to the light guide 22) to the photocathode Four scattered beams are sent to the photodetector: $\overline{E_{s6}}$ и $\overline{E_{s7}}$, which have left-circular polarizations, as well as beams $\overline{E_{s8}}$ и $\overline{E_{s9}}$, having right-circular polarizations.

As a result of optical mixing on the photocathode of the photodetector of four scattered beams, a signal is formed at its output, the spectrum of which contains six high-frequency components at the following Doppler frequencies:

$$W_{g67} = (\overline{K_{06}} - \overline{K_{07}})\overline{V}; \quad (1)$$

$$W_{g68} = (\overline{K_{06}} - \overline{K_{08}})\overline{V}; \quad (2)$$

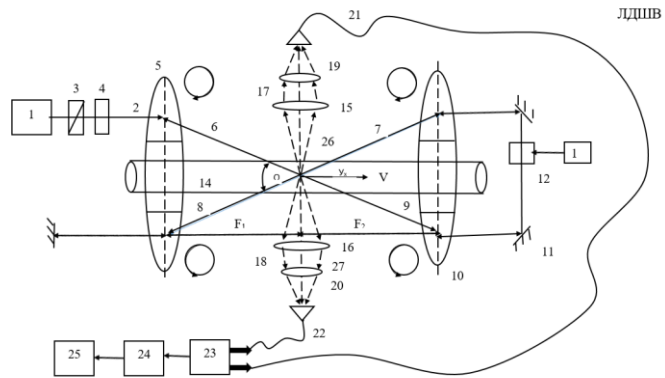
$$W_{g69} = (\overline{K_{06}} - \overline{K_{09}})\overline{V}; \quad (3)$$

$$W_{g78} = (\overline{K_{07}} - \overline{K_{08}})\overline{V}; \quad (4)$$

$$W_{g79} = (\overline{K_{07}} - \overline{K_{09}})\overline{V}; \quad (5)$$

$$W_{g81} = (\overline{K_{08}} - \overline{K_{09}})\overline{V}; \quad (6)$$

Fig.1



where $\overline{K_{0i}}$ is the wave vector of the "-i" probing beam.

If the scattered radiation 26 and 27 is collected in the direction of the OY axis at small angles, is symmetric to the OXY plane, then as shown in [3], this scattered radiation preserves the polarization state with respect to the polarization of the probing beam. Therefore, the scattered beams $\overline{E_{s6}}$ and $\overline{E_{s7}}$ have left-circular polarization, and the sheaves $\overline{E_{s8}}$ and $\overline{E_{s9}}$ are the right-circular polarization. For these pairs of beams, the polarization matching coefficient [3]

$$K_{n67}=1 \text{ and } K_{n89}=1. \quad (7)$$

For other pairs of beams, the polarization matching coefficients are close to 0:

$$K_{n68} = 0; K_{n69} = 0; K_{n78} = 0; K_{n79} = 0. \quad (8)$$

Therefore, when conditions (7) and (8) are satisfied, the high-frequency signals (crosstalk) (2), (3), (4) and (5) at the output of the photodetector 23 are suppressed, and the two useful signals (1) and (6) have same frequencies

$$W_{g67} = W_{g89} = \frac{4\pi}{\lambda} \cos \frac{\gamma}{2} V_x, \quad (9)$$

where λ is the wavelength of the laser beams;

γ is the angle between the probing beams 6 and 8, and 7 and 9.

The useful signals at the frequency (9) proportional to the speed V_x are summed and then through the bandpass filter 24 enter the meter 26, which, according to known equations, calculates the instantaneous and total flow of the optically active medium moving through the pipeline 14.

The use of the LF scheme with clarified optics (Fig. 1,[1]) with four probing beams, the total power of which is almost equal to $P\Sigma = 4P2$, where $P2$ is the power of the laser beam 2, can significantly increase the signal-to-noise ratio and, accordingly, the accuracy of measuring the velocity and flow rate of the liquid medium. In this case, in contrast to the prototype, which uses two lasers, the device uses only one laser with a power of $P2$. The nonreciprocal phase regulator 12-the Faraday cell, allows using two receiving blocks and two light guides 21 and 22 to also increase the power of the useful signal, because due to phase adjustment it provides a mode of in-phase reception of two signals (1) and (6) having the same Doppler frequencies .

In addition, the proposed LF has less weight and cost compared to the prototype, in which it is necessary to use instead of one two lasers.

References

1. Zemlyans'kyi V.M., Husyev M.O., Yehorov S.H., Polyak S.V. Lazernyy vytratimir. Zayavka na patent Ukrainy A 201806341, vid 6.06.2018.

LASER DEVICE FOR MEASUREMENT OF ANGLES ATTACK AND SIDE SLIP (LDASS) OF AIRCRAFT

V. Zemlianski, DSc. M. Gusev, A. Ovenko

National Aviation University, Kyiv, Ukraine

A new LDASS is proposed, in which the below-mentioned disadvantages [1] are eliminated. The LDASS is a laser instrument of true airspeed, angles of attack and side slip, which uses the Doppler effect and a system equations for their determinations.

The new LDASS works is follows [1, FIG1...FIG10].

Laser 1 emits a monochromatic beam 2 with a frequency ω_0 . The focusing lens 3 focuses the beam 2 at point 4 (measuring volume), through which the air flow moves at a velocity \vec{V} . Measurement zone 4 is located on the longitudinal axis of the aircraft OX, behind the sound barrier, that is, in the area of unexcited airflow. At altitudes of the aircraft from 0 to 10 km the power of the laser beam 3 is minimal. When flying at high altitudes up to 35 km, the beam power 3 is maximal.

The optical axis 7 of the first channel 5 and the optical axis 8 of the second channel 6 are placed in the same plane with the optical axis OX of the device and intersect it at point 4 at the same angles β . In this case, the first optical channel extracts scattered beams 9 and 10 located in the vertical plane OXZ at angles $\alpha / 2$ with respect to its optical axis 7, using a reception lens 32 and an opaque screen 15 with two holes. The extracted beam 9 has a frequency $\omega_0 + \omega_{d9}$, and the beam 10 has a frequency $\omega_0 + \omega_{d10}$. Here ω_{g9} and ω_{g10} are the Doppler frequency shift in the scattered beams 9 and 10, which are determined by the flow rate V in the measurement volume, the beams 9, 10 are spatially aligned by a two-beam interferometer that consists of a mirror 17 constituting the combining prisms 19. Since the beam 10, when passing through the frequency offset device 37 connected to the high frequency generator 39, receives a frequency offset by value $\omega_{ml} = 2\pi f_{ml}$, where f_{ml} is the frequency of the high frequency generator 39, then the combining beams 21 and 22, at the output component combining prism 19 have a frequency $\omega_0 + \omega_d$ and $\omega_0 + \omega_{ml} + \omega_{d10}$.

$$\omega_l = \omega_{ml} - (\omega_{g9} - \omega_{g10}) = \omega_{ml} - 2K \sin \frac{\alpha}{2} V_{xz} \cos(\gamma - \alpha_x), \quad (1)$$

where $K = 2\pi / \lambda$ – modulus of wave vector with wave length λ ; V_{xz} – projection of velocity vector of flow V on plane OXZ; γ - is the angle between the OX axis and the direction of the difference vector $\vec{K}_1 = \vec{K}_{s11} - \vec{K}_{s12}$ [FIG1], the extracted beams 9, 19 α_x - is the angle between the OX axis and the direction of the V_{xz} projection of the velocity vector. On the plane OXZ.

The second optical channel extracts scattered beams 11 and 12 located in the vertical plane OXZ also at angles $\alpha / 2$ with respect to its optical axis, with

the help of a receiving lens 32 and an opaque screen 16 with two apertures. The separated beams 11 and 12 are spatially aligned by a two-beam interferometer which consists of a mirror 18 and a component of the prism-combiner 29. Since the beam 12, when passing through the frequency offset device 28 connected to the high frequency generator 40, receives a frequency shift by an amount $\omega_{m2}=2\pi f_{m2}$, where f_{m2} ($f_{m2} > f_{m1}$) is the frequency of the high frequency generator 40, then the combining beams 23 and 24 at the output of the component of the prism-combiner 20 have frequencies $\omega_0 + \omega_{d11}$ to $\omega_0 + \omega_{m2} + \omega_{d12}$. At the output of the photo-detector 26, a signal is produced at the frequency:

$$\omega_2 + \omega_{m2} - (\omega_{g11} - \omega_{g12}) = \omega_{m2} - 2K \sin \frac{\alpha}{2} V_{xz} \cos(\gamma - \alpha_x), \quad (2)$$

γ – angle between axis OX and direction of difference vector $\vec{K}_2 = \vec{K}_{s21} - \vec{K}_{s22}$, of separated beams 11, 12. Optical circuit of dual frequency interferometer in every measurement channel provides spatial alignment of wave vector of two beams, which receives with the accuracy of seconds, whereas difference of optical path at interferometer is close to zero. High frequency signals from output of photo-detector 25 of first optical channel 5 and from output of photo-detector 26 of second optical channel 6 applies respectively at first and second input of combiner 27. Signal from the input of combiner 27 applies at inputs of first low pass filter 28 and first high pass filter 29. At the output of the first low pass filter 28; a differential frequency signal is extracted.

$$\omega_1 - \omega_2 = (\omega_{m1} - \omega_{m2}) - (8\pi)/\lambda \sin \frac{\alpha}{2} V_z \cos \beta, \quad (3)$$

Where: V_z – projection of velocity vector \vec{V} on axis OZ, this signal is applied at first input of second combiner 53 and the subsequent isolation of the frequency difference signal at the output of combiner with the help of second low pass filter 61. Signal of difference frequency is:

$$\omega_x = \left(\frac{8\pi}{\lambda} \right) \sin \frac{\alpha}{2} V_z \cos \beta, \quad (4)$$

To the first input of the first Doppler frequency meter 30 whose second input through the first frequency discriminator 57 tuned to $\omega_{m1} - \omega_{m2}$ - is connected to the output of the first low-pass filter 28. With the first Doppler frequency meter 30 the value of the projection of the velocity vector V_x is measured in real time and its sign is determined.

At the output of first high pass filter 29; the sum of frequencies signal is separated:

$$\omega_1 + \omega_2 = (\omega_{m1} + \omega_{m2}) - (8\pi)/\lambda \sin \frac{\alpha}{2} V_x \sin \beta, \quad (5)$$

where V_x is projection of vector of flow velocity V on axis OX. This signal is applied on first input of third combiner 54. On the second input of combiner 54, signal applied with frequency $\omega_{m1} + \omega_{m2}$, which is extracted through second high pass filter 60 from out of fifth combiner 55. Signal of difference frequency will be:

$$\omega_x = \left(\frac{8\pi}{\lambda} \right) \sin \frac{\alpha}{2} V_x \cos \beta, \quad (6)$$

The third optical channel 41 separates scattered beams 42 and 43 placed in the horizontal plane OXY directed to the photo-detector 26.

At the output of the photodetector 52, as a result of optical heterodyne generation, a high-frequency signal is produced at a frequency:

$$\omega_3 = \omega_{m3} - (\omega_{g42} - \omega_{g43}) = \omega_{m3} - 2K \sin \frac{\alpha}{2} V_Y, \quad (7)$$

Signal from outputs of Doppler frequency meters 30 ($\pm V_Z$), 31 ($\pm V_X$) and 62 ($\pm V_Y$) enters onboard digital processor 77, which processes through known equations with high accuracy, vector of true air speed V , angle of attack α and side slip β .

High measurement accuracy V , α , β is achieved due to the fact that the instrument uses single receive – optical unit, manufactured with high accuracy, in addition one probing laser beam, which focuses at zone of measurement on longitudinal axis of aircraft, more over its angular position with relation to longitudinal axis of aircraft is independent of measurement accuracy.

References

1. Zemlyans'kyi V.M., Husyev M.O., Ovenko A.V. Prymitka vymiryuvannya shvydkosti, kut ataky ta kovzannya. Zayavka na patent Ukrainy A201806337, vid 6.06 2018.

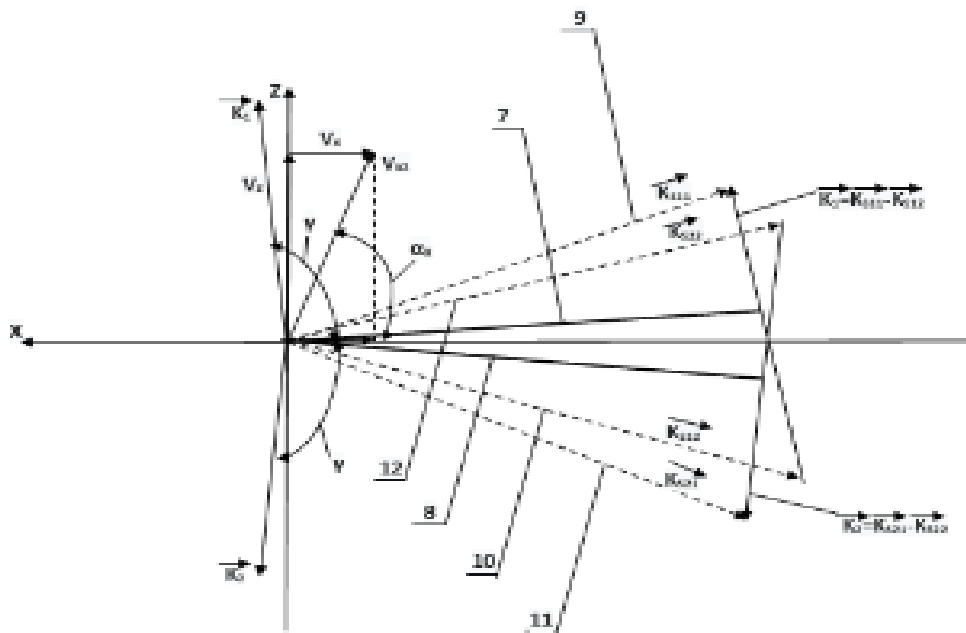


Fig. 1.

THE MULTIWAVE LASER MEASUREMENT OF THE CRYOGENIC LIQUIDS FLOW

Zemlianski V., Gusev DSc. M., Zakrevskiy O.

National Aviation University, Kyiv, Ukraine

Currently in different industries, including the aircraft-missile engineering, extensive use of cryogenic fluid (CL), as well as liquefied natural gas (LNG) at temperatures below $+53^{\circ}\text{C}$, namely hydrogen, oxygen, nitrogen, argon, helium, and others. LNG has become a priority technology in many developed countries including Japan, USA, France, Belgium, Spain, South Korea. Poland is building a terminal for LNG supplies from the USA, Ukraine also prepares a draft on the realization of similar terminal. There are different methods of liquids and gases measurement, however, in cryogenics [1] practically USA and Germany manufactured flowmeters are used. For example, the ICE Hoffer Flow Controls system (USA), consisting of the turbine flowmeter element, the permissible relative error of flow measurement $\sim 2.5\%$. The flowmeter Flowcom 2000 (Germany) uses the Venturi nozzle, the maximum flow rate depends on its diameter: $d=10, 20\ldots 65$ and corresponds accordingly: $15, 30\ldots 100 \text{ m}^3/\text{g}$, with error $\sim 2.5\%$. Inspection is carried out by ISA 483-1-2016. GSI. The Flowcom flowmeters. Verification methodology is approved at 30 September 2016 The Coriolis acceleration flowmeter OPTIMA AS28GGG (Germany), the maximum flow rate depends on diameter: $15, 40\ldots 100$ is respectively $3, 5\ldots 355\text{t}$, the measurement error $\sim 2.5\%$. The accuracy of perspective ultrasonic flowmeters for liquid rocket engines (LRE), which use hydrogen fuel, is influenced by air bubbles in the stream (cavitation), as well as restrictions on minimum flow velocities. The proposed high-precision multiwave laser method of measurement of CL flow is based on the CL flow sensing (on the axis of the transparent pipeline segment) with three pairs of colliding laser beams with corresponding wavelengths the $\lambda_1, \lambda_2, \lambda_3$ (see Fig.1). Symmetric sensing is implemented in the corners γ_1, γ_2 and γ_3 [2] (see Fig.1), as well as symmetric reception of scattered radiation by flow of CL within the range of aperture diaphragm with round hole, which center coincides with common bisector for the corners of the sensing of γ_1, γ_2 and γ_3 . Sensing beams K_1 and K_3 (wave vector $|K_i| = \frac{2\pi}{\lambda_i}$) intersecting in

the area of measurement 0 (see Fig.1) at the angle γ_1 , and have a wavelength λ_1 with vertical linear polarization. Counter-propagating beams K_2 and K_4 also intersect in the 0 measurement area at the angle γ_1 , have a horizontal polarization and wavelength λ_1 . Similar geometry of the sensing and polarization parameters have sensing beams K_5 and K_7 and counter-propagating beams K_6 and K_8 on the wavelength λ_2 , as well as the beams of K_9 and K_{11} and counter-

propagating beams of K_{10} and K_{12} on the wavelength λ_3 . These sensing beams lie in the plane OXY and velocity vector V_y of the CL flow coincides with the pipeline axis OY (see Fig. 1). They are formed from three (for example, semiconductor) lasers emitting at wavelengths $\lambda_1, \lambda, \lambda_3$, scattered CL radiation is focused in the direction of axis OX within the holes of two diaphragms D_1 and D_2 and then directed to the photoreceiver of the photocathode using light conductors. The analysis shows that in result of the optical mixing of scattered radiation at the photocathode of the photoreceiver, the output signal is formed, representing additive mixture of three low-frequency components, six useful components on one frequency $\Omega_M \pm \omega_{d1}$, where Ω_M is beam displacement: $K_1 K_5 K_9$ and $K_4 K_8, K_{12}$ (see Fig. 1), the frequency ω_{d1} is proportional to the flow velocity V_y CL; as well as twelve high-frequency crosstalk at various frequencies. Implemented geometry of the symmetric matched sensing and reception of scattered radiation provides forming of phase-conjugated useful signals [3] (symmetrical directions of reception A and B on OXZ plane), as well as formation of antiphase high frequency interference [3], (symmetrical directions of reception of A and C relative to OXY plane), as indicated by the theoretical analysis on the basis of dispersion vector theory and the results of the numerical experiment, there is an automatic suppression of all 12 high-frequency crosstalks and useful signal at a frequency $\Omega_M \pm \omega_{d1}$ has the form,

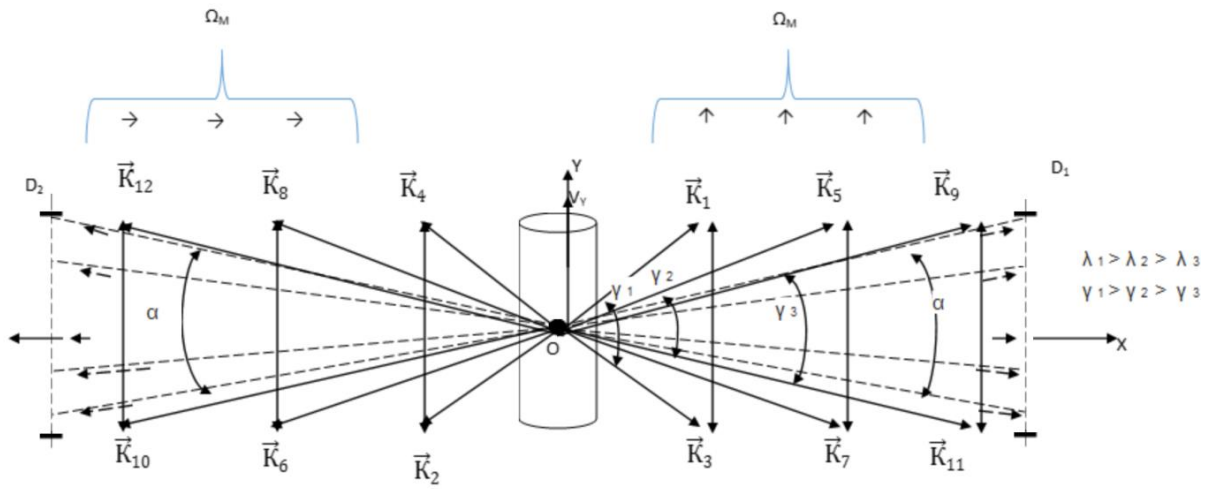


Fig.1

Where $K_i (\lambda_i, \eta_i)$ – is the coefficient of proportionality, depending on λ_i and quantum efficiency of the photocathode photodetector η_i , $K_{\pi\phi ij}$ - polarization-phase matching factor of two mixed "i" and "j" scattered waves at wavelengths $\lambda_1, \lambda_2, \lambda_3$; I_{1i}, I_{3i} – is the intensity of received scattered beams in the i-direction, respectively formed by sensing beams of K_1 and K_3 . Useful signal consists of six components on one frequency, and during matched symmetrical sensing its phases have values, as shown by the analysis and the results of the numerical experiment, either $\Phi_{\pi ij}=0^\circ$, or $\Phi_{\pi ij}=180^\circ$. Proposed method and based laser multiwave cryogenic liquid flowmeter (LMCLFM) realizes two-channel symmetric receiving of scattered radiation into two photodetectors with the implementation of spatial phase filtration (SPF) in the optical unit matching

wavelengths. The synthesis of SPF for each of the wavelengths λ_1 , λ_2 , λ_3 is carried out on PC using the program we developed according to the specified parameters of optical scheme geometry of sensing and reception of LMCLFM, as well as the flow of CL. Suggested two-channel reception with SPF provides synphased reception of useful signals [4], formed at the wavelengths λ_1 , λ_2 , λ_3 , as well as the suppression of low-frequency interference, because at the output of two photodetectors useful signals are in antiphase, and interferences are synphased. Developed scheme of LMCLFM provides high signal/noise ratio at the inlet of the calculator, connected to the output of the bandpass filter. Calculator gives high precision data about instant and total CL volume flow, and when input precise information from temperature and pressure probes, it gives data about CL mass flow. Developed LMCLFM differs from analogs by patent novelty, provides high precision of flow measurement at low rates (which is specific for flow rate measurement of hydrogen fuels, used in LRE), and at high rates of CL, for example LNG, and even so the scheme of LMCLFM sensing and reception stays the same in the whole dynamic range. LMCLFM also allows determining the direction of CL flow it is carried out with the use of frequency fixed displacement of sensing beams at wavelengths λ_1 , λ_2 , λ_3 for Ω_M using frequency displacement device. Using adequate investment Ukraine is ready to commercialize production of LMCLFM for LNG markets of Poland and Ukraine.

Literature:

1. Baranov A.S., Frolov M.A. Trofimov A.A. K voprosu vybora metoda izmereniya raskhoda kriogennykh zhidkostey. – S-P, 2015, №2 12 str.
2. Zemlyanskiy V.M. Raschet parametrov doplerovskogo signala s uchetom polarizatsionno-fazovykh effektov rasseivaniya. – M.: SHK; 1987-177 c.
3. Dyplom na Vidkryttya "Zakonomirnist' proyavy nezalezhnoyi chastoty doplerivs'koho syhnalu vid Dovzhyna khvylya EM vyprominyuvannya (Efekt Zemlyans'kyy). 30 zhovtnya 2017 r. m. Dnipro.
4. Zemlyans'kyy V.M. Doplerivs'kiy sposob elektromahnitnoho bahatokhvyly'ovykh hrunta konusu y synfaznoho pryymu. Patent Ukrayiny UA 107289 Byul. №23, 2014.

SECTION 6. LASERS IN NANOTECHNOLOGIES

**LASER STIMULATED Ag NANOPARTICLES GRATING FORMATION
ON THE SURFACE OF $\text{Li}_2\text{B}_4\text{O}_7\text{--Ag}_2\text{O}$ GLASS**V. Adamiv¹, R. Gamernyk², S. Malynych^{3,4}*¹O.G.Vlokh Institute of Physical Optics 23 Dragomanov St.,
Lviv, 79005, Ukraine**²Ivan Franko National University of Lviv 8 Kyrylo and Methodiy St.,
Lviv, 79005, Ukraine**³National University "Lviv Polytechnic" 12 S. Bandery St.,
79013 Lviv, Ukraine,**⁴Hetman Petro Sahaidachnyi National Army Academy
32 Heroes of Maidan St., 79012 Lviv, Ukraine*

The growing interest in studies of composite materials consisted of dielectric medium with embedded metal nanoparticles (NPs) is caused by significant influence of the latter on both linear and nonlinear susceptibilities of the host matrix. Those systems are considered as an effective platform for novel optical devices. Much attention in that matter is attracted to the noble metal NPs, especially silver. Silver exhibit unique frequency dependence of the dielectric function that differs from one for other noble metal (Au, Cu). Silver possesses low values of the imaginary part of dielectric function that defines electromagnetic energy dissipation. The material of a host matrix also plays role for practical applications. In optics it is necessary to deal with transparent medium, so glass is more suitable not only for its transparency, but also due to its exceptional mechanical properties and high threshold damage. Among other glasses borate glass are known for its exceptional nonlinear-optical properties associated with high nonlinear susceptibilities of boroxol groups.

Metal NPs are known for their ability to support specific excitations of conducting electrons induced by impinged electromagnetic wave. Those excitations are trapped within the nanoparticle's volume and is referred to as localized surface plasmon resonance (LSPR). The resonance frequency of electron oscillations can be effectively tuned by varying the size, shape of the NPs and dielectric environment [1]. Moreover, silver NPs exhibit LSPR in the visible spectral range. So, it seems very important to combine optical properties of glass matrix with those of noble metal NPs in order to increase performance of a composite.

Borate glasses are good candidates for Ag NPs formation. Their structure comprise boroxol groups, which are joined by the bridge oxygen atoms. The groups make borate glass structure open near the glass transition temperature T_g that simplifies the process of Ag NPs formation. Common technique for Ag NPs formation in glass relies on the reducing of Ag^+ ions to neutral Ag^0 state. Usually it is performed by thermal annealing of the glass doped with silver in

suitable atmosphere or in vacuum. Our earlier studies reveal the possibility of Ag NPs formation in borate glasses by annealing the silver doped glass in air and in vacuum [2, 3]. The annealing was performed in a furnace at the temperature $T=685 \pm 5$ K, which is close to the glassing point of $\text{Li}_2\text{B}_4\text{O}_7$. The presence of silver NPs in borate glass is evident from the extinction spectra of the samples. Interestingly, that Ag NPs tend to form close to the glass interface. That can be easily prove by polishing out approximately 1 μm layer that results in disappearing of LSPR spectral bands associated with Ag NPs [2].

In present work we use another approach to form Ag NPs in lithium tetraborate glass $\text{Li}_2\text{B}_4\text{O}_7$. Freshly prepared $\text{Li}_2\text{B}_4\text{O}_7$:Ag samples were irradiated by CW laser with $\lambda=405$ nm (1 W) at ambient conditions. The beam was split into two beams which interfered on the same spot of the sample's surface. Thus, the interference fringes appeared on the surface resulting in non-uniform heating of glass in accordance to the light intensity distribution within interference pattern. Surface regions exposed to the bright fringes experience substantial local heating in compare to dark fringes. It is naturally to expect the formation of Ag NPs along bright fringes. Indeed, as can be seen in Fig. 1 the distribution of Ag NPs on glass surface resembles interference fringes.

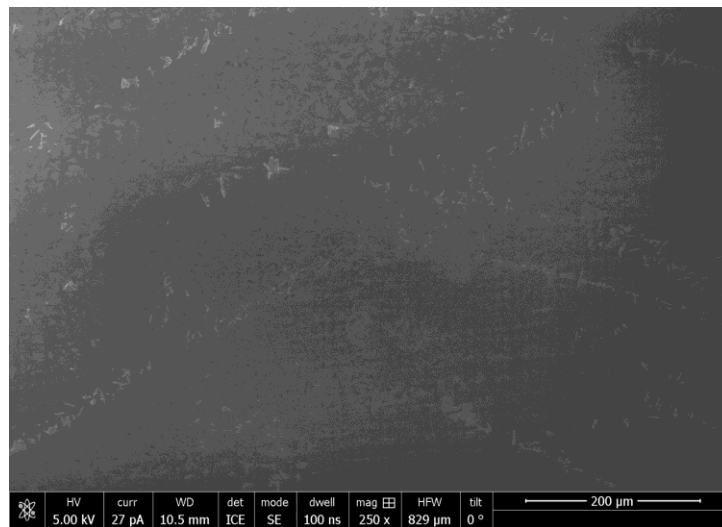


Fig. 1. SEM image of silver doped lithium tetraborate glass exposed to interfering laser radiation.

Fig. 2 depicts SEM image of the sample taken at higher magnification. It is seen that nanoparticles have spherical shape and quite narrow size distribution. Silver NPs of that size and shape should exhibit specific bands in the extinction spectra associated with LSPR in nanoparticles.

As can be seen in Fig. 3, there is a band in the spectrum of laser treated sample (dash curve). Even though the maximum is less pronounced than that for thermally annealed glass, it still confirms laser stimulated Ag NPs formation. Periodical distribution of Ag NPs across the surface was also proved by diffraction experiment (the image is not presented here).

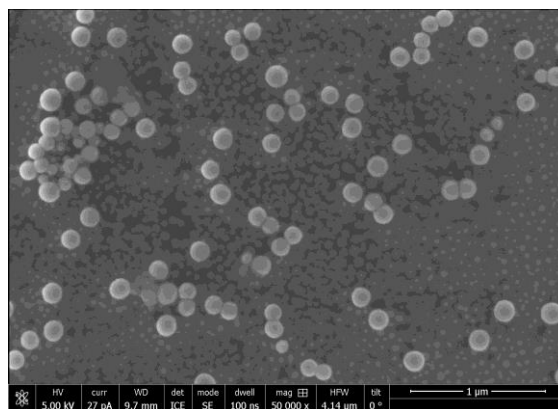


Fig. 2. SEM image of laser treated Li₂B₄O₇:Ag glass. Spherical shape of Ag NPs is clearly seen.

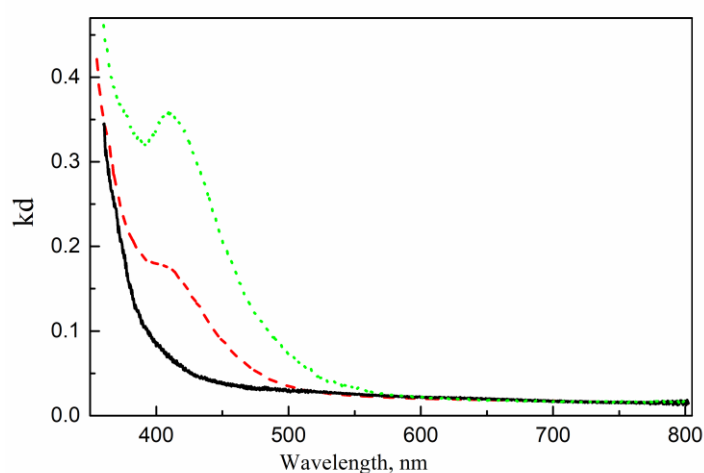


Fig. 3. Extinction spectra of non-annealed Li₂B₄O₇:Ag glass (solid line), laser treated (dash), and thermally annealed (dot).

In conclusion, we have prepared Ag NPs periodically distributed across the surface of borate glass by exposing it to laser radiation. Particle formation occurs at the regions that correspond to bright interference fringes.

References

1. N.L. Dmitruk, S.Z. Malynych. Surface plasmon resonances and their manifestation in the optical properties of nanostructures of noble metals. Ukr. J. Phys. Reviews. 9, P. 3 – 37 (2014) (in Ukrainian).
2. V. Adamiv, R. Gamernyk, I. Teslyuk. Formation of silver nanoparticles in Li₂B₄O₇-Ag₂O and Li₂B₄O₇-Gd₂O₃-Ag₂O borate glasses. Appl. Opt. Vol. 56(17), pp. 5068-5072 (2017).
3. V.T. Adamiv, Y.V. Burak, R.V. Gamernyk, S.Z. Malynych, I.E. Moroz, I.M. Teslyuk. Optical nonlinearities in LiKB₄O₇-Ag₂O and LiKB₄O₇-Ag₂O-Gd₂O₃ glasses containing Ag nanoparticles. Appl. Opt. 57(17), 4802–4808 (2018).

SPECTROSCOPIC STUDY OF LASER-INDUCED FORMATION OF CdSe NANOCRYSTALS IN Cd-DOPED As₂Se₃ FILMS

Yu.M. Azhniuk^{1,2}, V.V. Lopushansky¹, V.Yu. Loya¹,
A.V. Gomonnai^{1,2}, D.R.T. Zahn³

¹ *Institute of Electron Physics, Ukr. Nat. Acad. Sci., 21 Universytetska Str.,
88017 Uzhhorod, Ukraine*

² *Uzhhorod National University, 46 Pidhirna Str., 88000 Uzhhorod, Ukraine*

³ *Semiconductor Physics, Chemnitz University of Technology, D-09107
Chemnitz, Germany*

yu.azhniuk@gmail.com

Contrary to widely studied II–VI semiconductor nanocrystals (NCs) produced by colloidal synthesis or by diffusion-limited growth in silicate glasses, the fabrication of II–VI NCs in a matrix of another semiconductor is rather scarce [1, 2]. Recently we reported on the formation of CdSe NCs in As₂Se₃ films studied by Raman spectroscopy, atomic force microscopy (AFM), and energy-dispersive X-ray spectroscopy (EDX) [1]. The present study is devoted to *in situ* measured photoluminescence (PL) and Raman spectra of Cd-doped As₂Se₃ films, in which CdSe NCs are formed under laser illumination.

1.2–1.5 μm thick As₂Se₃:Cd films with nominal Cd content up to 12 % were prepared from additionally refined elemental components by thermal evaporation from a tantalum Knudsen cell at 770–830 °C and 10^{-6} Torr at a rate of 6 nm/s onto Si substrates kept at room temperature (RT).

Micro-Raman and PL studies were performed at RT using a Horiba LabRAM HR800 spectrometer with excitation by a solid-state laser ($\lambda_{\text{exc}} = 488.0$ nm or 514.7 nm) or a He–Ne laser ($\lambda_{\text{exc}} = 632.8$ nm). The spectral resolution was better than 2.5 cm^{-1} . The laser power was reduced down to values ensuring stability of the Raman spectra and afterwards gradually increased to observe the dynamics of photoinduced changes in the Raman spectra during the measurements. For each measurement a new spot was chosen on the film surface in order to exclude the photoinduced changes related to previous measurements.

EDX and X-ray photoelectron spectroscopy (XPS) studies show that the Cd content in Cd-doped arsenic chalcogenide films sharply decreases from the surface into the film depth [1, 2]. Hence, the nominal Cd concentrations quoted here are rather qualitative characteristics of the doping degree.

Raman spectra of undoped or weakly doped As₂Se₃:Cd films are typical for amorphous As₂Se₃ with a dominating broad asymmetric maximum near 220 cm^{-1} and a weaker broad band near 480 cm^{-1} [1]. The spectra do not change with the laser excitation wavelength λ_{exc} or power density P_{exc} . Hence, one may conclude that the amorphous undoped or weakly Cd-doped As₂Se₃ films do not undergo

any photostructural changes under laser irradiation at power densities up to 180 kW/cm² applied within this experiment.

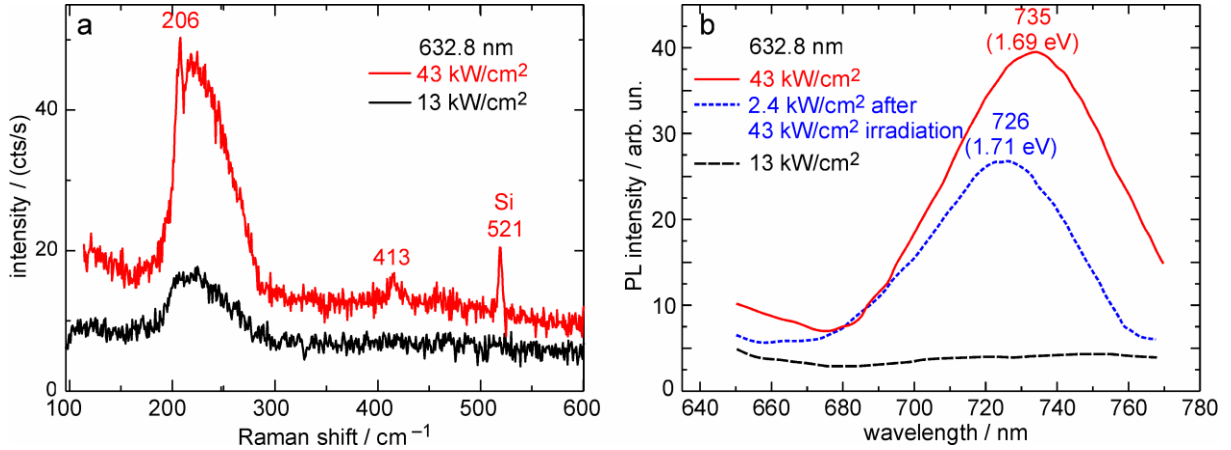


Fig. 1. Raman (a) and PL (b) spectra of As₂Se₃:Cd film with nominal Cd content of 10 at. % at the excitation with 632.8 nm at various P_{exc} .

For the films with relatively high Cd content (nominally 10 at. %), we, similarly to our earlier study [1], observed narrow peaks near 206 and 413 cm⁻¹ coinciding with the LO and 2LO phonon frequencies of CdSe, which appeared in the Raman spectra at increasing P_{exc} additionally to the broad maximum of the amorphous As₂Se₃ (Fig. 1a). They were ascribed to CdSe crystallites formed in the Cd-doped As₂Se₃ film under the laser irradiation during the Raman measurements [1]. Simultaneously we observed a PL maximum near 735 nm (1.69 eV) to appear at higher P_{exc} values corresponding to the appearance of CdSe LO and 2LO phonon features in the Raman spectra. Note that the PL maximum was also observed in the spectrum measured at much lower P_{exc} from the spot previously subjected to irradiation at a higher P_{exc} (Fig. 1b). This confirms the Raman-based conclusion on the CdSe NC formation under laser irradiation at sufficient P_{exc} .

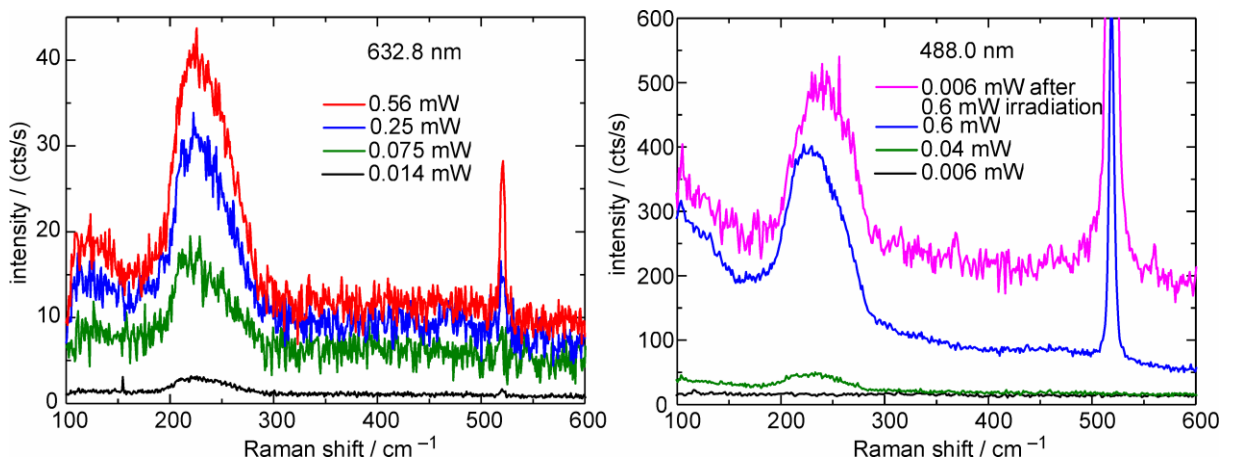


Fig. 2. Raman spectra of Cd-doped As₂Se₃ film (nominally 8 at. %) measured at the excitation with 632.8 nm (a) and 488.0 nm (b) at various P_{exc} .

For the $\text{As}_2\text{Se}_3\text{:Cd}$ film samples with nominally 8 at. % Cd no CdSe LO and 2LO phonon-related peaks were observed in the Raman spectra even at high P_{exc} (Fig. 2). Even though, in their PL spectra, which showed no luminescence at low P_{exc} , a clear maximum near 730 nm appeared at higher P_{exc} (Fig. 3). It can be attributed to the same effect of CdSe NC formation under laser irradiation. In this case PL appears to be an even more sensitive technique to detect the CdSe NCs than micro-Raman spectroscopy. The PL maximum position slightly varies for the film samples within 725–735 nm (1.69–1.71 eV), but does not show any significant dependence on λ_{exc} or P_{exc} . From the PL maximum energy, taking into account the NC bandgap size dependence [3] and the Stokes shift value of about 0.1 eV [3], one can estimate the average CdSe NC diameter as about 10–14 nm. PL mapping measurements at a reduced P_{exc} taken after the laser irradiation in the vicinity of the laser spot show that the PL signal at a distance of 2 μm from the spot is noticeably weaker and shifted by 0.03 eV towards higher energies (Fig. 4). Hence, the NCs formed directly in the laser spot are somewhat larger than those in the peripheral area.

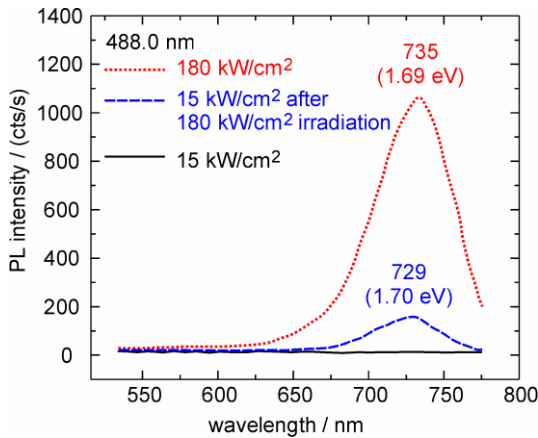


Fig. 3. PL spectra of Cd-doped As_2Se_3 film (nominally 8 at. %) at the excitation with 488.0 nm at various P_{exc} .

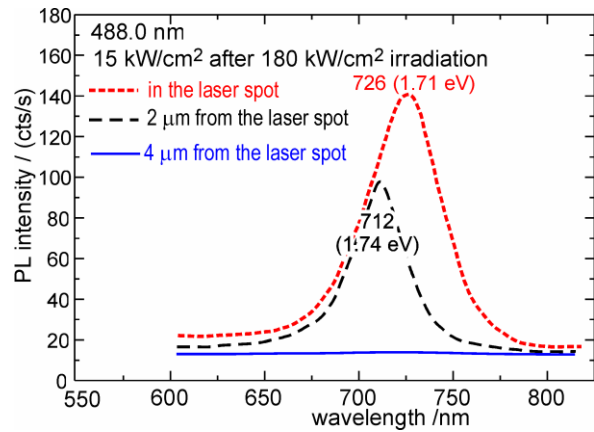


Fig. 4. PL spectra of Cd-doped As_2Se_3 film (nominally 8 at. %) after laser irradiation (488.0 nm, 180 kW/cm^2) in the laser spot and away from it.

We relate the mechanism of formation of CdSe NCs in the $\text{As}_2\text{Se}_3\text{:Cd}$ films to a drastic photoinduced increase of the film plasticity resulting in an intense material transfer from the laser spot and facilitating the diffusion of Cd and Se atoms to form the NCs. The photoplastic effect in amorphous chalcogenides is known to be of non-thermal origin [4] which is in agreement with our observations showing no NC formation upon annealing at 160°C .

References

- [1] Yu.M. Azhniuk *et al.*, Thin Solid Films 651 (2018) 163.
- [2] Yu.M. Azhniuk *et al.*, Phys. Status Solidi B 256 (2019) 1800298.
- [3] D.V. Korbutyak *et al.*, Ukr. J. Phys. – Rev. 7 (2012) 48.
- [4] S.N. Yannopoulos, M.L. Trunov, Phys. Status Solidi B 246 (2009) 1773.

**ELECTRICAL AND OPTICAL PROPERTIES OF THE ARRAYS
DIFFERENT FORM QUANTUM DOT**

I. Bilynskyi, R. Leshko

Physics Department, Drohobych Ivan Franko State Pedagogical University
email: leshkoroman@gmail.com

Investigations in physics of superlattices with quantum wells and their practical application have attracted attention of many researchers to study the systems of smaller type of dimensionality – quantum wire superlattices and quantum dot superlattices. In the past 20 years, experimenters found and actively developed the methods of growth of large ordered quantum dots arrays [1].

Methods of growth of quantum dots (QDs) under the Stranski-Krastanov technique gave the opportunity to get a three-dimensional coherent strained islands [2]. However, obtained arrays were still mixed to a considerable extent: both by size and by location.

The authors of [3] grew an *InAs* QD array on the *GaAs* substrate with small dispersion in QD size; and showed that QDs are arranged in a periodic structure along a given direction.

Multilayer arrays where QDs are located above each other, were grown and described in [4]. Such ordered arrays were named the superlattices of vertically coupled QDs. Distance between adjacent QDs within a layer is much larger than QD size and distance between adjacent layers.

The study of the electronic structure of an array, where QDs are tunnel coupled in all three dimensions, was carried out in [5] for heterostructures *GaN/AlN* and *InAs/AlAs*. Internal elastic stresses in the QD array, effect of piezoelectric and spontaneous polarizations were taken into account by perturbation theory.

In papers [6, 7] the authors proposed a modified method of connected plane waves, which correctly takes into account the complex behavior of the wave functions of quasiparticles in superlattices. This method was applied to study electronic and excitonic states, and their dependence on the geometric parameters of semiconductor superlattices of cylindrical β -*HgS* QDs in the matrix β -*CdS* and *GaAs* QDs in the matrix $Al_xGa_{1-x}As$. In [8] the electron spectrum in a QD superlattice of *GaAs* elliptic quantum wire in the matrix $Al_xGa_{1-x}As$ was studied.

The spectra of electrons and holes in 1D- and 2D-dimensional superlattices (SL) of spherical QDs are obtained and analyzed in [9 – 11].

In this report the optical properties of spherical quantum dot superlattices of heterosystem *GaAs/Al_xGa_{1-x}As* and *GaAs/AlAs* are studying theoretically for 1D, 2D, 3D dimensions (fig.1)

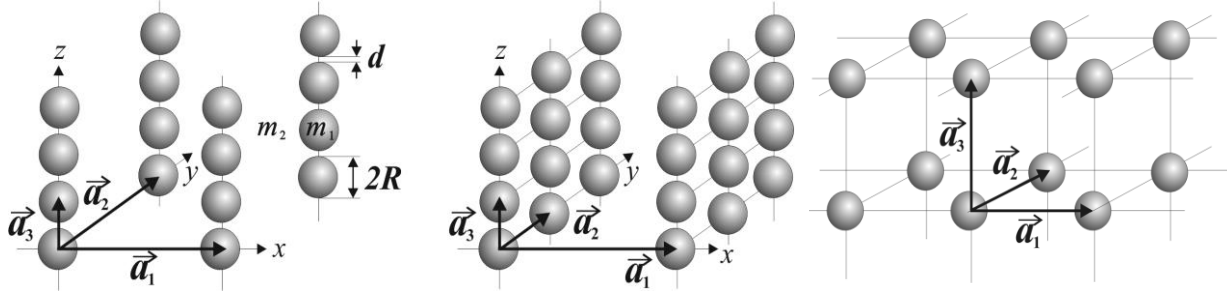


Fig. 1. Geometrical scheme of 1D-, 2D-, 3D-dimension spherical QD superlattices

In the model of strong coupling electron relations s- (fig.2) and p-type (fig.3) electronic minibands in the case under-the-barrier tunneling of electrons between quantum dots are calculated. The dependence of electron energy subbands on the wave vector, distance between QDs and parameter x are analyzed.

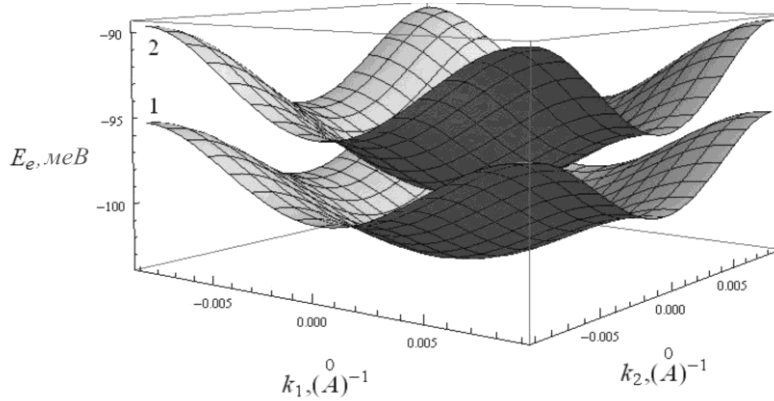


Fig. 2. The dependence of the electron s-type energy in SQDS on the two-dimensional wave vector (surface 1 corresponds to $k_3=0$; 2 - $k_3=\pi/a$, a - SQDS lattice constant)

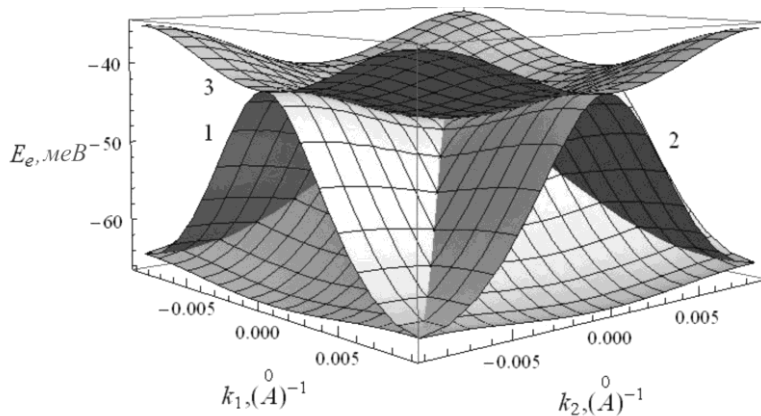


Fig. 3. The dependence of the electron energy of the p-type first excited state with quantum numbers $m = -1, 0, 1$ on two-dimensional wave vector ($k_1, k_2, k_3 = 0$)

Taking into account previous results we calculate intersubbands light absorption and electrical conductivity caused by movement of s- and p-electrons. The intersubbands light absorption for 3D-superlattice as a function

of frequency is characterized by two peaks corresponding to direct transitions of electrons with wave vectors in the center and edge of Brillouin zone (fig4)

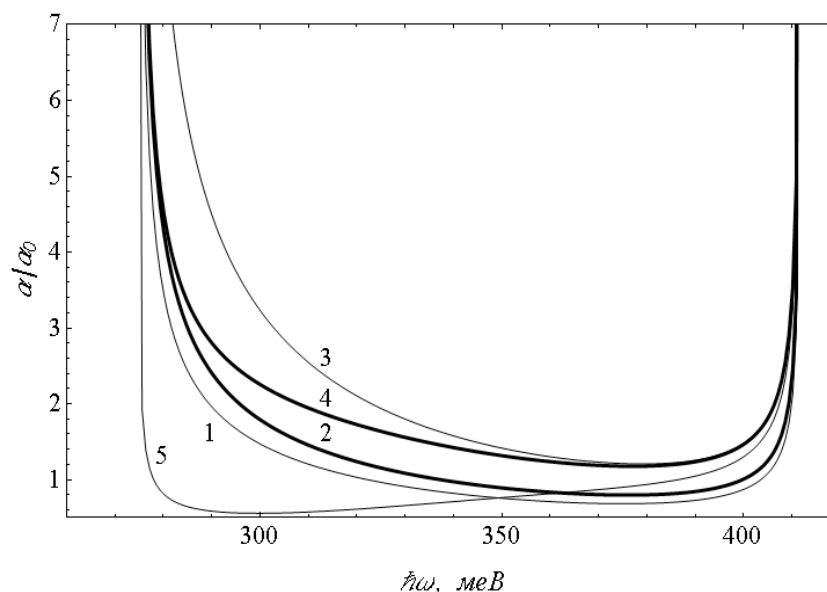


Fig. 4. The relative coefficient of intersubband light absorption in the case of linear polarization of the electromagnetic wave incidence perpendicular to QD chain if chemical potential changes from the value corresponds s-subband energy to average value of s-, p-subband regions (1-3 curves)

The coefficient of light absorption and electrical conductivity caused by Fermi level position, temperature and concentration of aluminium in the matrix.

- [1] Notzel R., Semicond. Sci. Technol., 11, 1359 (1996).
- [2] D.E. Eaglesham, M. Cerullo, Phys. Rev. Lett. 64, 1943 (1990).
- [3] T. Mano, R. Notzel, G.J. Hamhuis, Appl. Phys. Lett. 81, 1705 (2002).
- [4] T. Mano, R. Notzel, G.J. Hamhuis [et al.], Journal of applied physics 95, 109 (2004).
- [5] A.D. Andreev, E.P. O'Reilly, Appl. Phys. Lett. 87, 213106-1 (2005).
- [6] Н.В. Ткач, А.М. Маханец, Г.Г. Зегря, ФТП 36, 543 (2002).
- [7] М.В. Ткач, О.М. Маханець, Г.Г. Зегря, Укр. фіз. журн. 48, 155 (2003).
- [8] V.A. Holovatsky, V.I. Gutsul, O.M. Makhanets, Rom. Journ. Phys. 52, 327 (2007).
- [9] V. Boichuk, I. Bilynskyi, Cond. Mat. Phys. 16, 33702: 1 (2013).
- [10] В. Бойчук, І. Білінський, Р. Пазюк, І. Шаклеїна, Фізика і хімія тв.тіла, 10, №4, 752-756 (2009).
- [11] V.I. Boichuk, I.V. Bilynskyi, R.I. Pazyuk, Ukr. J. of Physics, 62, № 4, 335-342 (2017).

LASER-STIMULATED PROCESSES OF NANOSTRUCTURING OF THE SURFACE OF A SOLID. CURRENT STATE AND PROSPECTS

L. Fedorenko, A. Evtukh, V. Naumov

V.E. Lashkaryov ISP NASU, Kyiv, Ukraine,
e-mail: leonfdn@gmail.com

Development of the laser physics and study the laser interactions with materials allow, except established industrial application to realize unique advantages at the formation of high-quality and novel nanoparticles, nanotubes, and nanowires. The task of solid state structuration in the sub - wave scale was solving rather by a laser-induced self-organization. Formation of nanofragments of a given form, size and sizes distribution depends mainly on the determinism of specific self-organization process. The self-organization of these processes depends to a large extent on the laser parameters (among others factors) and material response, table 1: the pulse duration t_p , the intensity I , the wavelength λ , and polarisation.

At the processes of the thermodynamic equilibrium, the input energy ΔE is fully transferred into an increase of internal energy ΔU and an increase in temperature ΔT : $\Delta E = \Delta U = c \cdot m \cdot \Delta T$, Fig. 1 [1]. The energy introduced into the solid from laser pulses is essentially different in that the heating of the lattice occurs as a secondary process due to the electron-hole plasma as a transfer subsystem between the photons and the lattice. In most cases, the better results of nano-structurization were obtained at laser intensities before thresholds of the first-order phase transition, or close to the threshold ones. For example, this case is realized for non-destructive formation of the energy barriers and p-n junctions in semiconductor near-surface layers of sub-micron scale by nanosecond laser pulses at strong absorption [2-4], as a result of atoms transfer due to laser thermal shock (LTS) effect. LTS effect is based on the laser induced action of huge thermal gradient at conditions of strong surface absorption. A relatively small excess of the melting threshold with nanosecond pulses of an UV laser [5] made it possible to form a nanostructures on the 6H: SiC surface with a certain type of regularity in the form of a “crown” of nano-needles, Fig. 2.

Table 1. Process chart for laser action

Time scale	Material response	Observation
Femtoseconds	Electronic excitation	Electron emission
Picoseconds	Energy dissipation / core motion Bond breaking	Atom / ion emission (Plasma) plume
Nanoseconds	Surface relaxation / reorganization	

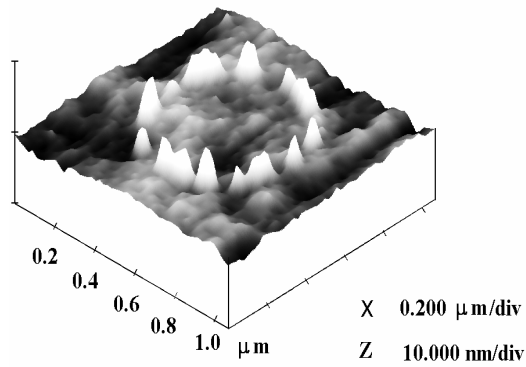


Fig.2. AFM surface image 6H-SiC: N after irradiation with pulsed N_2 laser in single mode

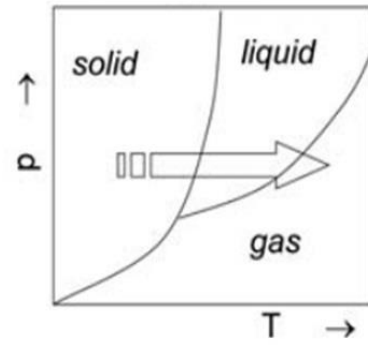


Fig.1. Schematic presentation of energy input into a solid material

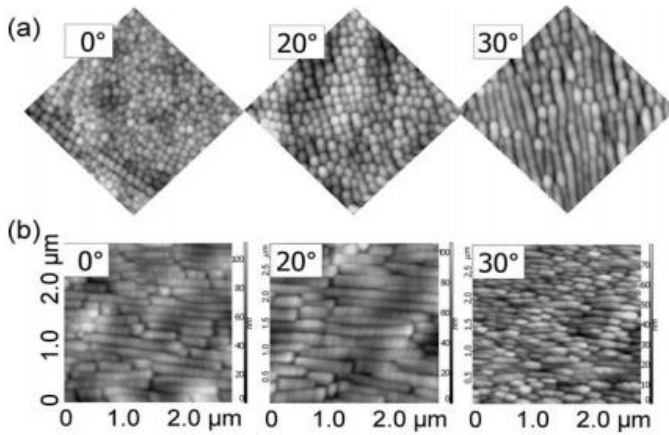


Fig.3. Artificial eccentricity, introduced by oblique incidence of circularly (a) resp. elliptically (b) polarized beam. The angle of incidence, indicated in the panels, is obtained by a rotation about the horizontal, corresponding to s -polarization (all panels are $3 \times 3 \mu m^2$ AFM pictures)

The picosecond pulses are comparable with time of thermal equilibrium established between the electrons and phonons. In the case of threshold exceeding at picosecond laser action the surface-near region will be positively charged for a considerable time because of finite time for the bulk electrons to fill that holes, which remain after electron emission from the surface. This can lead to electrostatic action is known as Coulomb

explosion [6]. At a higher excitation hot carrier absorption becomes significant, a hot electron subsystem heats the lattice via electron–phonon collisions in a large volume. Then the volume overheating begins and mechanisms such as phase burst [7] are switched on. After a picosecond pulse (usually several tens of picoseconds) the conventional heat conduction equation can be used to describe the heat flow into the bulk of the irradiated target.

Nanostructuring of surface layers makes by femtosecond (FS) laser pulses at the intensities close to the phase transition threshold, with the melting point in a small volume without any significant ablation [8]. An interesting observable effect of the dependence of the form of nanostructures and their linear order on the polarization of the laser beam, Fig.3. The sizes of the produced crystallites may be compared with an interatomic spacing. In this case, an amorphous layer

may be formed, if the cooling velocity exceeds the freezing rate. The formation of a perfect crystalline or amorphous surface structures under the action of the FS laser pulses are called in the literature “laser glazing” [9, 10]. From considered time scales, it is established that ablated part of target does not interact with ultrashort laser pulses with duration below 150 fs [11]. As shown in [12], an adequate description of the laser heating of nanoparticles provides a simple one-temperature model in femtosecond, picosecond and nanosecond modes. In conclusion, it should be noted that in the further development of methods for the formation of nanostructures with controlled sizes and shape, the prospect is viewed through the growth of the determinism of self-organization processes by reducing the number of uncontrolled factors.

- [1] Laser-Surface Interactions for New Materials Production. Springer Series in Materials Science. Editors: Antonio Miotello, Paolo M. Ossi, Springer-Verlag Berlin Heidelberg 2010, PP.130-358.
- [2] L.L. Fedorenko, V. K. Malyutenko, S. S. Bolgov. Activation of InSb Photo Conductivity by Laser Irradiation. Ukrainian Physical Journal. 1975, Vol. 20, No. 12, pp.2039-2044. (in Ukrainian).
- [3] V.P. Voronkov, G.A. Gurchenok. Impurity diffusion in semiconductors during pulsed laser annealing. FTP, 1990. Vol.14, №10. pp.1831-1834.
- [4] L. Fedorenko and A. Medvid'. Laser - induced donor centers in n-InSb. Semiconductor Physics, Quantum Electronics & Optoelectronics. 2000. V. 3, N 1. P. 31-34.
- [5] L. Fedorenko, A. Medvid', M.Yusupov [et al.] Nanostructures on SiC surface created by laser microablation. Applied Surface Science. 2008, V.254, P.2031–2036.
- [6] J. Reif. High power laser interaction with the surface of wide bandgap materials. Opt. Eng. (1989) 28, 1122-1132.
- [7] R. Kelly, A. Miotello. Comments on explosive mechanisms of laser sputtering. Appl. Sur. Sci., (1996) V. 96–98, 2, pp. 205-215.
- [8] P. Mulser. D. Bauer. High Power Laser Matter Interaction, STMP 238 (Springer. Berlin Heidelberg, 2010), DOI 10.1007/978-3-540-46065-7.
- [9] B. H. Kear, E. M. Breinan & L. E. Greenwald. Laser glazing – a new process for production and control of rapidly chilled metallurgical microstructures, Metals Technology, (1979) 6:1, pp.121-129.
- [10] V.A. Isakov , A.P. Kanavin, S.A. Uryupin. Absorption of a femtosecond laser pulse by metals and the possibility of determining effective electron – electron collision frequencies. Quantum Electronics 36 (10) 928 – 932 (2008).
- [11] J. Reif. Basic Physics of Femtosecond Laser Ablation, in book “Laser-Surface Interactions for New Materials Production”. Springer Series in Materials Science. DOI 10.1007/978-3-642-03307-0.
- [12] R. R. Letfullin, Th F. George, G. C. Duree, and B. M. Bollinger. Ultrashort Laser Pulse Heating of Nanoparticles: Comparison of Theoretical Approaches. Advances in Optical Technologies (2008) (6).

ELECTRON IN MOLECULE OF THREE QUANTUM DOTS

V. Hols'kyi

*Physics department Drohobych Ivan Franko State Pedagogical University,
Stryiska Street, 3, Drohobych, 82100, hol.wit@gmail.com*

The system quantum dot (QD) is an ideal platform for testing quantum phenomena, since the system is well described by quantum mechanics, and its properties are completely independent of the choice of material parameters. In addition, its quantum properties can be easily adjusted electrostatically. Due to these advantages, various QD systems have been widely studied over the past few decades to understand many of the phenomena, including the Coulomb blockade, the Kondo effect.

Nanosystems consisting of three tunnel-bound QDs or triatomic artificial molecules make it possible to study interesting phenomena associated with electrostatics and molecular states of triple quantum molecules (QM). Experimentally, QDs molecules are intensively studied in [1-4]. Nanocrystals in the QM can be two [1], three [2-3], four [4], and more. If we consider the geometry of a molecule, then it is linear [4], or triangular [2-3]. It can be symmetric, when the distances between quantum dots are the same and asymmetrical.

The theoretical works has shown that the base model of quantum molecules with three quantum dots is two-dimensional parabolic quantum well [5-7]. If ones solve the Schrödinger equation, the method of linear combinations of orbital quantum wells [5], the Gund-Millikan [6] and Heutler-London method [7] has been used. However, these theoretical works do not take into account the finite band offset at the boundary and the three-dimensional confinement of particles in QDs.

The paper considers a molecule of three spherical QDs that are connected with each other due to tunneling effects (Fig. 1). The spectrum of energy states of such a molecule contains the split states of individual QDs. To determine them when there is one electron in such a nanosystem, the wave function is represented as a linear combination of electron wave functions of individual QDs:

$$\Psi(r) = \sum_{i=1}^3 C_i \varphi_{is}(r), \quad i = 1, 2, 3, \quad (1)$$

$\varphi_{is}(r)$ is the wave function of the electron ground state, in i -th QD.

To obtain the energy particle levels, a substitution (1) has been made in the stationary Schrödinger equation with Hamiltonian:

$$\hat{H} = -\frac{\hbar^2}{2} \nabla^2 + U(r), \quad (2)$$

$$U(r) = \begin{cases} U_0, & \text{if } r \text{ in QDs space} \\ 0, & \text{if } r \text{ other} \end{cases}, \quad (3)$$

where m is effective mass of electron for the proper area, $U < 0$.

As a result, a system of linear homogeneous equations is obtained. To calculate the specific energy values a condition is used that the system has a solution when its determinant is zero. By adding the condition of normalization, the explicit form of the wave function of the electron is found.

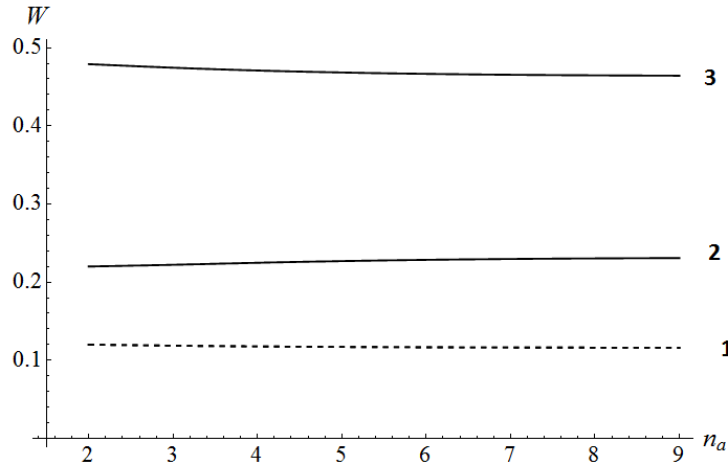


Fig. 1. The probability of finding an electron in the QM as a function of the distance between the QD at the symmetry of the equilateral triangle.

With the appearance of the wave function, one can determine the probability of a particle staying in a molecule with three QDs. In fig. 1 we consider the symmetry of the equilateral triangle. The radii of all QDs are 4 GaAs stable lattices. For the ground state (2), the probability of staying a particle in all CTs is the same and increases with increasing distance between QDs. For the excited state (1 and 3), the probability of two QDs located on the OZ axis (dashed line) is the same and smaller than in the third QD (solid line). With increasing distance, the first practically does not change, and the second slightly decreases. If we consider symmetry of an isosceles triangle, then the system is characterized by three states. The dependence of the probability of staying an electron on the symmetry of an isosceles triangle is considered if the distance between two QDs has become, and the third is removed from them (Fig. 2). Dependencies show that for all probability conditions the presence of a particle in two fixed QDs (dashed lines) is identical. For excited states, they fall (2' and 3'), and for the main state (1') - increases. If you consider the third QD, then the situation is the opposite.

In the calculation of the energy spectrum by the finite element method, graphs of the probability density of the presence of an electron in a molecule with three QDs were constructed in the case of symmetry of an equilateral triangle (Fig. 3.a). The distance between the QDs is equal to 2 steel bars of AlAs. But for the symmetry of the isosceles triangle (Fig. 3.b), the distance between the lower QDs is equal to 2 steel bars of AlAs, and the distance to the

third is equal to 4 steel bars of AlAs. The graphs are constructed in a plane section, which is determined by the centers of QD. Qualitatively results coincide, both in the first and in the second case.

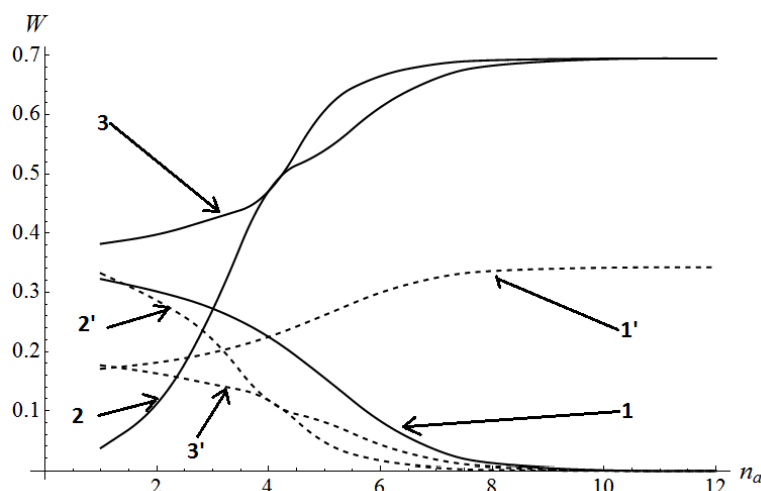


Fig. 2. The probability of finding an electron in the QM as a function of the distance of one QD to the axis on which there are two other symmetries of the isosceles triangle: 1, 1' - the ground state; 2, 2' - first excited; 3, 3' - the second excited state. The solid line is the probability of finding an electron in the QD, which was moved, dashed in QD, the placement of which was fixed.

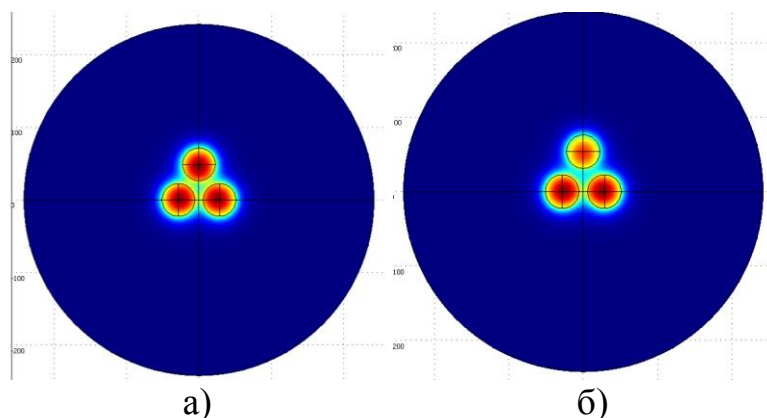


Fig. 3. The density of the probability of finding an electron in a QM in symmetry of an equilateral (a) and an isosceles (b) triangle is constructed by the finite element method for the ground state.

Reference:

1. Johnson A. C., Petta J. R., Marcus C. M., Hanson M. P., Gossard A. C. Phys. Rev. B B2, 165308 2005
2. Rogge M.C., Haug R.J. Phys. Rev. B 78, 153310 (2008)
3. Rogge M.C., Haug R.J. Physica E 40 (2008) 1656-1658
4. Takakura T., Noiri A., Obata T., Otsuka T., Yoneda J., Yoshida K., and Tarucha S. Appl. Phys. Lett. 104, 113109 (2014)
5. Gimenez I. P., Korkusinski M., Hawrylak P. Phys. Rev. B. 76, 075336 (2007)
6. Lee S.-Y., Chung Y. Phys. Rev. B. 87, 045302 (2013)
7. Ren Y.F., Wang L., Liu Z., Wu M.W. Physica E 63(2014) 329–336.

DYNAMIC LIGHT SCATTERING ON EVAPORATING MICRODROPLET OF SUSPENSION WITH NANOSPHERES

Shopa Ya.¹, Jakubczyk D.², Woźniak M.², Derkachov G.², Kolwas K.², Piekarski K.³

¹*Cardinal Stefan Wyszyński University in Warsaw. Faculty of Mathematics and
Natural Sciences, Wóycickiego 1/3, 01-938 Warsaw, Poland*
i.shopa@uksw.edu.pl

²*Institute of Physics, Polish Academy of Sciences, al. Lotników 32/46,
02-668 Warsaw, Poland.*

³*Białystok University of Technology, Faculty of Computer Science,
Wiejska 45A, 15-351 Białystok, Poland.*

Dynamic light scattering (DLS) method is widely used for measurement of the particle size and size distribution in fluids, study of the relaxation and aggregation processes, indirect viscosity measurement etc. The DLS technique is based on the measurement of intensity fluctuations of the scattered light caused by Brownian motions of particles in suspension or solution [1]. The random motion of particles in suspension is characterised by the diffusion coefficient, which by means of the well-known Stokes-Einstein relation is related to the so-called hydrodynamic radius. In order to obtain the hydrodynamic radius with the DLS method it is necessary to measure the time dependence of the autocorrelation function (ACF) $G(\tau)$ of the scattered light intensity.

The various suspensions of nanoparticles in single droplets levitated in an electrodynamic quadrupole trap are investigated by light scattering technique. Droplets of the pure host liquids with initial diameters in the 20-30 μm range were introduced into the electrodynamic trap by a droplet-on-demand injector (Fig. 1). The droplet carried an electric charge and its position was stabilized using a combination of static and oscillating electric fields. The levitated droplet was illuminated with a collimated vertically polarized blue Ar^+ laser beam (497 nm, 50 mW) or horizontally polarized red semiconductor laser beam (654 nm, 20 mW). For the detection of the fluctuations of the light scattered by a single micron-sized droplet at 90 deg we used a fast photon counter and an amplifier-discriminator that sends the TTL-level 10-ns pulses to the real-time digital correlator. The scattered light from the droplets was also collected with a CCD camera to obtain Mie-scattering patterns. As a result, we obtained a high-quality autocorrelation function after a time of only 10 s, however in order to expand the time scale of the ACF, accumulation time sometimes reached $\sim 10^3$ s. The ACF's are analyzed to obtain the corresponding characteristic times τ .

In order to prevent multiple light scattering the concentration of particles in the levitated droplet should be small. We chose different initial concentrations from 0.25 down to 0.005 wt% of the silica (SiO_2) and titania (TiO_2) guest particles in the suspensions. Using the necessary physical parameters (0.25 wt%

concentration of the 250 nm nanospheres and density values), we found that inside a 20 μm droplet the number of TiO_2 spheres was about 300 and the number of SiO_2 spheres was about 500.

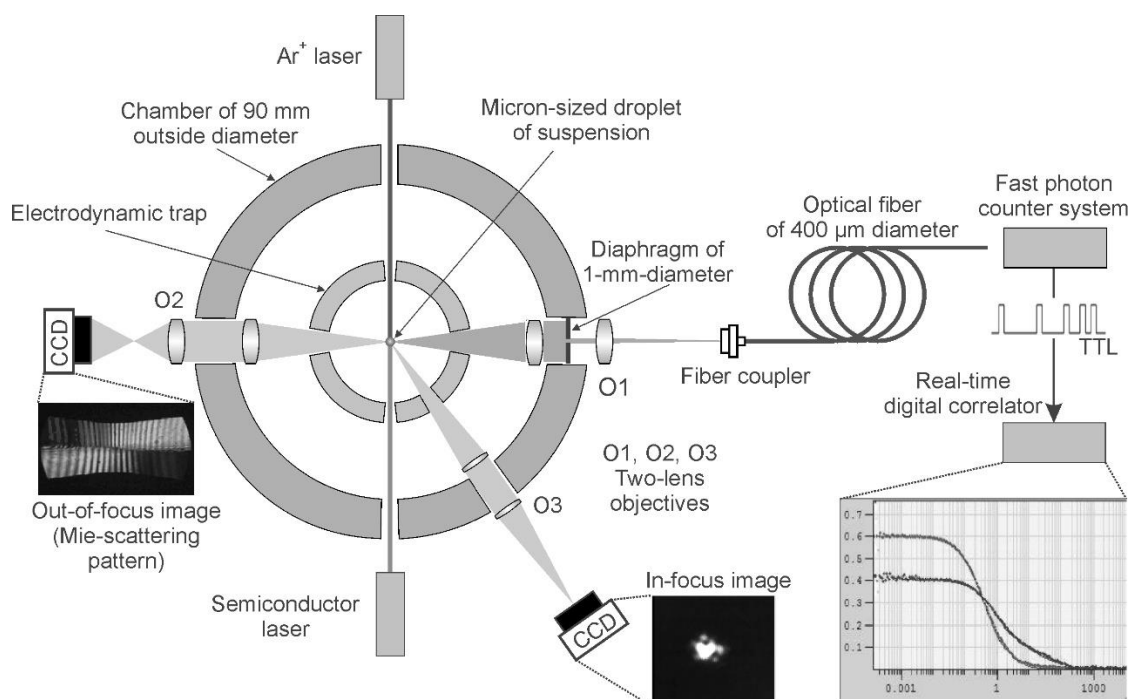


Fig. 1. Schematic of the experimental setup: electrodynamic quadrupole trap equipped with fast photon counter system and real-time correlator.

At the initial stage of a micro-droplet's evolution the optical resonances of a dielectric sphere (also known as Morphology Dependent Resonances) [2] dominate in the changes of the scattered light. Since the autocorrelation of a periodic signal from the photon counter system is also periodic with the same period, this situation significantly limits the possibilities of the ACF analysis at this stage. Only at the end of the droplet evolution the ACF with exponential decay can be obtained.

Numerous observations have shown that the ACF almost always has an exponential decay like in the case of a monodisperse scattering medium. At the final stage of the droplet evaporation the formation of non-rigid clusters consisting of nanoparticles is confirmed by the in-focus images. We obtained the ACF's of the clusters using different sizes of silica and titania spherical nanoparticles in water, diethylene and tetraethylene glycol. The regular rotational motion of a hard cluster should show a periodicity on the ACF for the large accumulation times. However, we have never found such a periodicity, only sometimes small maxima that correspond to the frequency of the AC field in the electrodynamic trap were visible. For the curves (1) and (2) in Fig. 2 we obtained the characteristic times $\tau_1(654) = 1.23 \times 10^{-3}$ s and $\tau_2(497) = 0.61 \times 10^{-3}$ s, which corresponds to the ratios of approximately 2 : 1 and differs from the classical theoretical prediction (1.8 : 1). The curves (1) and (2) in ln-lin scale (see inset in Fig. 2) also depart from linearity.

The ACF found in our standard experimental setup [3] for the DLS with the laser wavelength of 405 nm (curve (3) in Fig. 2) naturally corresponded to a monodisperse suspension.

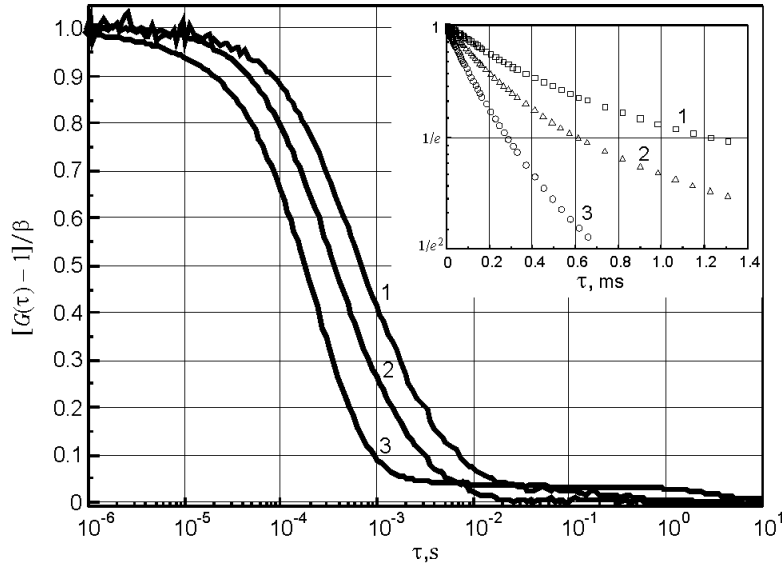


Fig. 2. The ACF's in normalized form (here β is the coherence factor) that were measured for two laser wavelengths and two different size ranges of micro-droplets with TiO_2 nanoparticles of 250 nm diameter dispersed in water with initial concentration 0.004 wt%. Curve (1) corresponds to the wavelength of 654 nm, while (2), corresponds to the wavelength of 497 nm. The ACF for the same water suspension measured in a cuvette for the wavelength of 405 nm is also shown (curve 3). The inset presents the curves (1), (2) and (3) in ln-lin scale for short delay times.

The ACF's measured with the DLS technique have properties that are like those corresponding to the light scattering by the Brownian particles. However, the temporal dependencies of these ACF's are significantly different from those found for the nanoparticle's suspension in bulk [4]. It follows from the random motions/rotations and shape changes of the final charged non-rigid aggregates in the AC electric field of the trap. The analysis showed that the dynamics of a levitated droplet is very complex and apart from ACF it requires simultaneous tracking of additional parameters such as the size, weight, number of nanoparticles, droplet electric charge (distribution), etc. Also, the theoretical basis for dynamic light scattering on a single microdroplet awaits an additional consideration.

- [1] Merkus H.G., Particle Size Measurements: Fundamentals, Practice, Quality. Springer Particle Technology Series. (2009) p 533.
- [2] Ashkin A., and Dziedzic J., Appl. Opt. **20** (1981) 1803–1814.
- [3] Derkachov G., Jakubczyk D., Kolwas K., Shopa Y., Woźniak M., Springer Proceedings in Physics. **195** (2017) 275–282.
- [4] Derkachov G., Jakubczyk D., Kolwas K., Shopa Y., Woźniak M., Proc. SPIE **10612** (2018) 106120U.

STRUCTURAL AND OPTICAL PROPERTIES OF COBALT AND CHROMIUM DOPED ZnO NANOSTRUCTURES GENERATED BY PULSED LASER ABLATION IN LIQUIDS

I. Stolyarchuk, A. Stolyarchuk, I. Hadzaman

*Department of Physics, Drohobych Ivan Franko State
Pedagogical University, 24 I. Franko str., 82100 Drohobych, Ukraine,
i.stolyarchuk@dspu.edu.ua*

Interaction of laser beam with solid target has been actively investigated for many technological applications [1]. Current trends in pulsed laser ablation (PLA) include modification of surface properties (i.e. optical absorptivity, hydrophobic properties), production of micro-components like micro-lenses for optoelectronics devices and fabrication of nanoparticles (NPs) [2]. The process of pulsed laser ablation was widely used for a large variety of semiconductor compounds including so-called diluted magnetic semiconductors (DMS). This is comparatively new class of materials with unique properties caused by spin exchange interactions between magnetic ions and band carriers (electrons and holes). On the other hand, formation of semiconductor nanostructures under pulsed laser ablation in liquid (PLAL) is less studied, although this technique has many advantages compared to other growth routes. Compared with other physical and chemical methods of synthesized of the nanomaterials, PLAL has the following advantages: PLAL is a chemically simple and clean because the process has little byproduct formation, simple starting materials, and no need for catalyst; PLAL is conducted under ambient conditions and does not require extreme temperature and pressure. PLAL is a facile general method with an almost unlimited scope of suitable materials and solvents. Because new phase formation in LAL involves both a liquid and solid, researchers can choose and combine interesting solid targets and liquids to synthesize nanocrystals and fabricate nanostructures for fundamental research and potential applications [3].

In the present work, we report on experimental investigations of structural and optical properties of two members of oxide DMS family, namely $\text{Zn}_{1-x}\text{Co}_x\text{O}$ and $\text{Zn}_{1-x}\text{Cr}_x\text{O}$, which are in form of micro- and nanoparticles generated by PLAL technique.

$\text{Zn}_{1-x}\text{Co}_x\text{O}$ and $\text{Zn}_{1-x}\text{Cr}_x\text{O}$ nanoparticles were produced by laser ablation of a ceramic target in deionized water. The target was irradiated using a frequency – quadrupled Q – switched Nd:YAG pulse laser (Continuum, Powerlite-8010). This laser was capable of producing 100 mJ of 266 nm light per pulse, laser fluence about 1.5 J/cm², operating at 10 Hz with pulse width of 7 ns. However, $\text{Zn}_{1-x}\text{Cr}_x\text{O}$ (with x range to $0 < x \leq 0.2$) and $\text{Zn}_{1-x}\text{Co}_x\text{O}$ ($0 < x \leq 0.1$) ceramic plates as targets were applied in this case.

Figure 1 shown scheme of experimental setup for deposition of DMSs nanoparticles by PLAL. The target with a diameter of 20 mm and thickness of 4 mm was immersed in a 50-ml glass cylindrical reactor filled with distilled water (about 30 ml). The laser radiation was focused using a short-focus ($F=50$ mm) collecting lens. The laser beam was introduced into the reactor through the sidewall. We produced equipment for supplying of development of laser beam to the surface of the target in horizontally and vertical planes to avoid crater formation and to expose the new surface. The ablation process duration was typically about 50 min. The layer of liquid in front of the target did not exceed 7 mm, minimizing the secondary interaction effects in the colloid between the NPs and the laser radiation. Technological experiments were carried out at room temperature and atmospheric pressure.

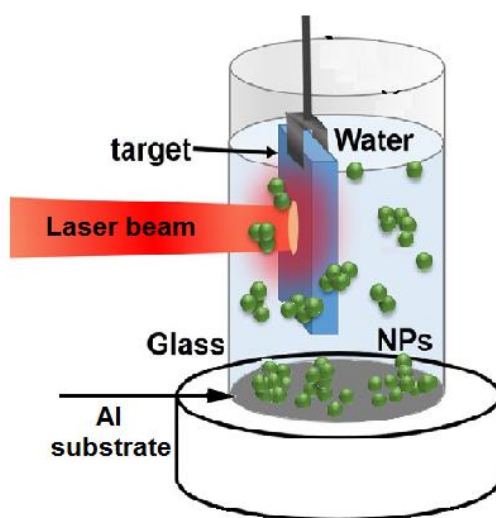


Fig. 1 Scheme of experimental setup for synthesis of NPs DMSs by PLAL

After laser ablation the colloidal aqueous solution with the produced nanoparticles or the dropped layer onto Al substrate were the samples under investigations. Additionally, polyvinylalcohol (PVA) was used as a stabilizer of colloidal solution.

The crystallographic studies were performed using X-ray Diffractometer (D8 ADVANCE X-ray Diffractometer with DAVINCI) using Cu-K_α wavelength ($\lambda = 1.54059 \text{ \AA}$) and scanning in 2θ range from 10° to 70° . Scanning electron microscopy (SEM, model JEOL-6480LV) and atomic force microscopy (AFM, Semicontact Mode with standard NT-MDT NSG03) were used for structural and morphological analysis of the fabricated nanostructures.

Optical transmission and absorption spectra between 300 and 700 nm were measured using a grating monochromator, a photodetector system and registered computer system. This setup has also served to register photoluminescence spectra. For such kind of measurements the samples were excited using a 325 nm He-Cd laser with an excitation intensity value of 10 mW. All UV-visible measurements were performed at room temperatures.

The structural analysis using X-ray diffraction (XRD) of nanocrystals reveals the standard diffraction pattern of ZnO hexagonal wurtzite with a (002) preferred orientation. With an increase of transition metal (TM) content ($x > 0.02$) additional diffraction peaks were observed, corresponding to (100), (101), and (102) of ZnO. No peaks corresponding to metal clusters or metal oxides are observed on the patterns which indicates that TM ions has entered the ZnO lattice without changing the wurtzite structures and systematically substituted the Zn^{2+} ions in the lattice

The performed scanning electron microscopy (SEM) analysis suggests of the well-defined flower-like nanostructures. In optical absorption spectra of the colloidal nanoparticles short wavelength shift of the absorption edge as compared to the bulk crystal or thin films due to confinement effect has been observed. The optical transmittance spectra showed a shift in the band edge towards lower energy side with the increase of content of magnetic impurities. This low energy shift as a function of the TM content can be explained by due to the s,p-d spin-exchange interactions between the band electrons and the localized d- electrons of the Co^{2+} (Cr^{3+}) ions. The exchange interaction between the TM ions and the band electrons give rise to a negative and a positive correction to the conduction and valence-band edges, leading to narrowing of the band gap [4]. In the room temperature photoluminescence spectra of nanostructures and nanocomposites few main peaks were revealed, which are attributed to the band - edge transitions and vacancies or defects.

1. M. Bussoli, D. Batani, T. Desai, F. Canova, M. Milani, M. Trtica, B. Gakovic, E. Krousky, Study of laser induced ablation with focused ion beam/scanning electron microscope devices, *Laser Part. Beams* 25 (2007) 121–125.
2. D. Zhang, B. Gokce, S. Barcikowski, Laser synthesis and processing of colloids: fundamentals and applications, *Chem. Rev.* 117 (5) (2017) 3990–4103.
3. J. Xiao, P. Liu, C.X. Wang, G.W. Yang, External field-assisted laser ablation in liquid: An efficient strategy for nanocrystal synthesis and nanostructure assembly // *Progress in Materials Science* 87 (2017) 140–220.
4. Introduction to the Physics of Diluted Magnetic Semiconductors // J.A. Gaj, J. Kossut (eds). – 2011. – Springer. – 469 p.

ELECTRICAL PROPERTIES OF THIN LAYERS OF Ni_2MnIn OBTAINED BY PLD METHOD

T. Jasinski¹, A. Barlowski¹, P. Ciupak¹, G. Wisz², M. Kuzma^{2,3}

¹ *Physics and Biophysics Engineering Chair, Technical University of Rzeszow,
Powstancow Warszawy 6, 35-900 Rzeszow, Poland*

² *Faculty of Mathematics and Natural Sciences, Department of Experimental
Physics, University of Rzeszow, Pigionia 1, 35-959 Rzeszow, Poland*

³ *The East European State Higher Scholl in Przemyśl, Terleckiego 6,
Przemyśl, Poland*

Metamagnetic Heusler alloys, $\text{Ni}_{50}\text{Mn}_{50-y}\text{Sb}_y$, $\text{Ni}_{50}\text{Mn}_{50-y}\text{Sn}_y$, $\text{Ni}_{50}\text{Mn}_{50-y}\text{In}_y$, $\text{Ni}_{50}\text{Mn}_{50-y}\text{Ga}_y$ demonstrate multifunctional properties: shape memory effect, giant magnetoresistance, giant magnetocaloric effect, inverse magnetocaloric effect, giant magnetothermal conductivity [1]. The magnetoresistance follows from spin dependence of the resistivity in ferromagnetic metals. At the Fermi level, electrons with spin up and spin down exhibit different conduction properties due to the splitting between the energy bands of the majority (spin up) and minority (spin down) spins what results in two channel conduction model of resistivity in magnetic field. The giant magnetoresistance in multilayered systems is applied now a day in read heads and hard discs.

We study the electrical properties of layers of $\text{Ni}_{45}\text{Co}_5\text{Mn}_{35.5}\text{In}_{14.5}$. The layers were deposited on glass substrate using pulsed deposition method (PLD) [2]. The YAG:Nd³⁺ laser with 532 nm (II harmonics) wavelength, the 6 ns pulse time and the fluence of 16 J/cm² was used. The target was bulk $\text{Ni}_{45}\text{Co}_5\text{Mn}_{35.5}\text{In}_{14.5}$ manufactured by Maziarz et al. [3]. The thickness of layers was 75 nm. The EDS and XRD measurements point on the composition of layers similar to the composition of target. The films have polycrystalline structure with lattice constant $a=6.02$ Å of cubic phase at room temperature. The temperature dependence of the resistivity of the layers were measured in the temperature range 140-280 K using helium cryostat. The dependence $R(T)$ is linear, typical for metal conductors. However, two temperature ranges: 140- 220 K and 220-280 K are observed in which the slop of R versus T differs slightly. The Hall properties of the layers were measured using Phywe set-up equipped with Cobra3 unit [4]. The four probe sample was prepared by indium soldering of silver wires. The basic results of measurements are presented in Fig. 1. We do not observe the dependence of resistance of the sample on the magnetic flux density in the range of 0 - 0.4 T (Fig. 1a).

The diagrams in Fig. 1 c, d show great asymmetry voltage U_a arising from nonsymmetrical soldering of Hall voltage probes. This voltage is demonstrated in Fig 1b ($B=0$) for sample currents 0-20mA. The asymmetry voltage modifies considerable the Hall diagrams presented in Fig. 1c, d. The conductivity, carrier

density and carrier mobility were determined from measurements. The results were addressed in the frame of the percolation model of conductivity in polycrystalline materials [5].

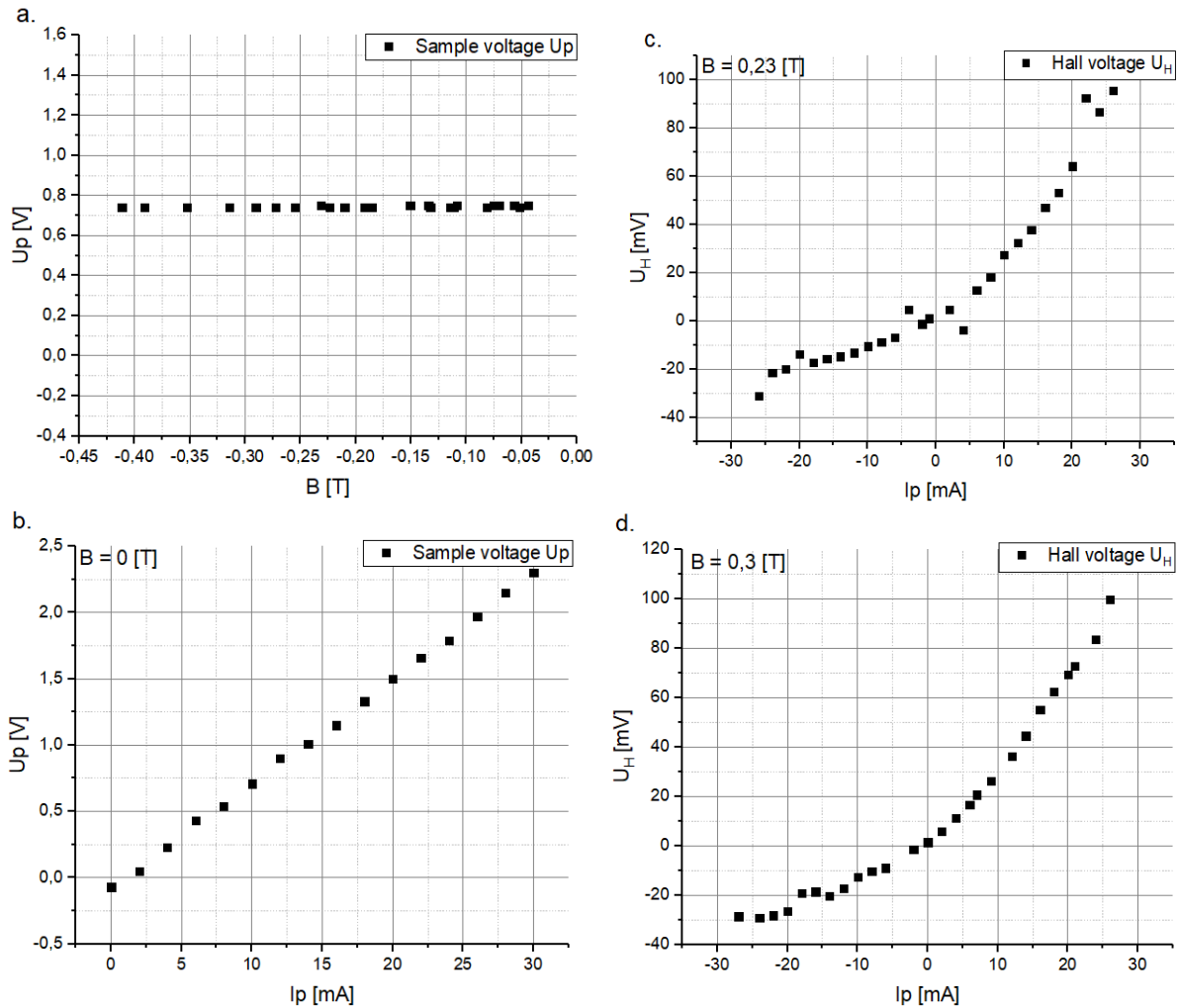


Fig. 1. Basic results of Hall measurements of $\text{Ni}_{45}\text{Co}_5\text{Mn}_{35.5}\text{In}_{14.5}$ layer using Phywe set-up. Dependence of resistance as a function of the magnetic flux density (a), Hall voltage as a function of sample current flux density of 0T, 0.23T, 0.3T (b, c, d respectively).

References

- [1]. J. Pons, E. Cesari, C. Segui, F. Masudey, R. Santamarta, Ferromagnetic shape memory alloys: Alternatives to Ni-Mn-Ga, Mater.Sc. Eng. A, 481-482 (2008) 57-65.
- [2]. G. Wisz et al. Structure and composition of layers of Ni-Co-Mn-In Heusler alloys obtained by pulsed laser deposition, EPJ Web of Conferences 133, 02006 (2017).
- [3]. W. Maziarz, Solid State Phenomena, 186, 251-254 (2012).
- [4]. Hall effect in n-germanium, Laboratory Experiments Physics, Phywe 2009.
- [5]. C. Wan, P. Sheng, Quantum interference and the giant Hall effect in percolation systems, Phys. Rev. B 66, 075209 (2002).

SECTION 7. BIOMEDICAL LASER APPLICATIONS

DEVELOPMENT AND APPLICATIONS OF LASER TECHNIQUES IN BIOLOGY AND MEDICINE

M. Cholewa^{1*}, A. Banaś², J. Cebulski¹, M. Obrzut², I. Zawlik²

¹*Faculty of Mathematics and Natural Sciences, The University of Rzeszow, Rzeszow, Poland*

²*Faculty of Medicine, The University of Rzeszow, Rzeszow, Poland*

*Email: mcholewa@ur.edu.pl

ABSTRACT

The invention of laser in 1960 was followed by a Nobel prize in 1964 received by Charles H. Townes, Nicolay G. Basov, Aleksandr M. Prokhorov. This magic device called laser have opened up vast new fields for research and applications including biology and medicine.

INTRODUCTION

The optical maser (microwave amplification by stimulated emission of radiation), that is, the laser, dates from 1958, when the possibilities of applying the maser principle in the optical region were analyzed at Columbia University at New York as well as in the Lebedev Institute in Moscow [1]. Two years later the first laser was operating.

DEVELOPMENTS & APPLICATIONS

Laser Manufacturing Processes for Medical Devices

Short pulse lasers can be used to create micropores in the millimeter and micrometer range for dosing systems and miniaturized drug depots [2]. In addition, structuring and molding processes can be applied to produce components for minimally invasive surgical and diagnostic solutions based on fundamental biological principles such as the sensory hairs of insects. Figure 1 shows a laser spotted array of biomolecules on a glass slide for functional analysis [3]. One of the other advantages of using lasers is that, in contrast to etching methods, in these applications the hole pattern can be changed in successive samples because no mask is required.

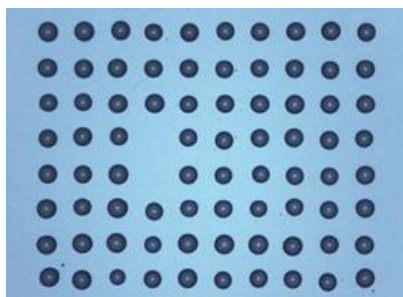


Fig.1. Laser spotted array of biomolecules on a glass slide for functional analysis [3]

Laser Techniques for Manufacturing Implants

Over the last few decades, the use of medical implants for therapeutic applications has exploded. Accordingly, the advent of laser micromachining technology has enabled many of these advances. For example, vascular implants can be used to deal with defective blood vessels in arteriosclerosis patients. This requires sufficient quantities of replacement tissue and vascular grafts. There is an increasing trend towards using personalized implants made from artificial scaffolds which are seeded in vitro with the patient's autologous cells. These scaffolds can then be developed into bio-artificial vascular prostheses in subsequent stages. This broad range of tools enables researchers to construct micro-scale structures from proteins as well as synthetic polymers.

Surface Functionalization using Laser Radiation

The cells of our body require specific biological stimuli to form tissues. With the aim of influencing and guiding cell growth researchers are investigating mechanical, topographical and molecular cues in vitro cell cultures which can be implemented on synthetic surfaces through a series of modifications. Micro and nano structures alter the substrates' roughness and wetting properties, which, in turn, affect cell adhesion, proliferation and differentiation. Applying this approach, guidance structures fostering targeted cell growth can be generated. Cell growth can also be influenced through selective modifications of surface chemistry using laser radiation. In this approach, photochemical activation of the surface generates anchor groups for covalent immobilization of biomolecules such as peptides, proteins and growth factors.

Photorelease

The targeted release of drugs in vivo – known as drug delivery – is subject of intense research at. The development of bioactive medical devices equipped with switchable drug delivery systems designed to release drugs in a controlled way regarding time and position represents a promising new form of treatment in many areas of medicine. One example from current research is the development of a photorelease system for tumor reduction which enables the release of on-demand doses of chemotherapeutic drugs from tailor-made polymer scaffolds through selective laser irradiation. Laser light of a suitable wavelength and intensity stimulates special, photoactive anchor groups, causing them to cleave and release the drug.

Laser Therapy

Working closely with medical experts, our researchers investigate and validate methods for the precision ablation of soft and hard tissue and thermal treatment of soft tissue. For fixation of wound dressings laser tissue soldering (LTS) can replace suturing techniques or using staples. This will improve the

cosmetic outcome and reduce the burden on patients. Laser soldering can be safely applied when a temperature control circuit is used to prevent the tissue from excess heating.



Fig. 2. Green laser [4]

Laser-based analytical techniques

Laser-induced breakdown spectroscopy (LIBS) is a type of atomic emission spectroscopy which uses a highly energetic laser pulse as the excitation source [5]. The laser is focused to form a plasma, which atomizes and excites samples. In principle, LIBS can analyze any matter regardless of its physical state, be it solid, liquid or gas. Because all elements emit light of characteristic frequencies when excited to sufficiently high temperatures, LIBS can (in principle) detect all elements, limited only by the power of the laser as well as the sensitivity and wavelength range of the spectrograph & detector. If the constituents of a material to be analyzed are known, LIBS may be used to evaluate the relative abundance of each constituent element, or to monitor the presence of impurities. In practice, detection limits are a function of a) the plasma excitation temperature, b) the light collection window, and c) the line strength of the viewed transition. LIBS makes use of optical emission spectrometry and is to this extent very similar to arc/spark emission spectroscopy.

LIBS is technically very similar to a number of other laser-based analytical techniques, sharing much of the same hardware. These techniques are the vibrational spectroscopic technique of Raman spectroscopy, and the fluorescence spectroscopic technique of laser-induced fluorescence (LIF). All these techniques have been successfully used in biology and medicine.

Laser-based imaging techniques

In this part, we review the imaging techniques and methods of molecular interrogation made possible by integrating laser light sources with microscopy [6]. We discuss the advantages of exciting fluorescence by laser illumination and review commonly used laser-based imaging techniques such as confocal, multiphoton, total internal reflection microscopy and super resolution microscopy. The most common imaging technology based on laser illumination

is confocal microscopy. One major concern with LSCM is that the high irradiances required to achieve high frame rates and sufficient signal-to-noise ratios adversely effects cell viability. As a solution, multiple confocal pinholes can be implemented and projected into the specimen simultaneously. As the number of pinholes increases, the dwell time per pixel increases proportionally for the same frame rate, and irradiance can be reduced. This technique is called multiphoton (multipinhole laser microscopes (MPLM)). Total internal reflection microscopy (TIRFM) is a method for imaging cell adhesions, cytoskeletal elements, and membrane components at the glass–cell interface. TIRFM induces total internal reflection between the glass and cell culture media interface sending an evanescent wave a few hundred nanometers deep into the sample with enough irradiance to excite fluorescence. A number of imaging modalities are gaining acceptance in cell biology that rely on nonlinear absorption in which the probability of an event (e.g., fluorescence) is not simply proportional to laser intensity. One such technology is MPM which was first reported in 1990.

CONCLUSIONS

Laser-based techniques have been developed and applied with great success in our everyday life, including biology and medicine. This unique discovery which was driven initially by military applications have found its role in many practical and unique areas of research and industry.

LITERATURE

- [1] Wikipedia
- [2] Elke Bremus-Koebberling & Martin Wehner http://www.ilt.fraunhofer.de/content/dam/ilt/de/documents/Leistungsangebote/Brochure_Biotechnik_and_Medicine.pdf
- [3] Arnold Gillner, *Laser Technik Journal*, Volume 5, Issue 1, Article first published online: 27 DEC 2007
- [4] Nadeem Rizvi: <http://www.med-techinnovation.com/Articles/articles/article/47>
- [5] Radziemski, Leon J.; Cremers, David A. (2006). *Handbook of laser-induced breakdown spectroscopy*. New York: John Wiley. ISBN 0-470-09299-8.
- [6] Elliot L. Botvinick and Jagesh V. Shah, *METHODS IN CELL BIOLOGY*, 2007;82:81-109

APPLICATION OF "SOFT LASERS" IN MEDICINE

Kul'ment'eva O.¹, Kul'ment'ev A.²

¹*Ukrainian branch BIONET, concern BIYOVIS, Hungary, Sumy, Ukraine,*

²*Institute of Applied Physics, Sumy, Ukraine*

E-mail: opkulm@ukr.net

About fifty years ago, the first powerful laser systems were created specifically designed for medical purposes (laser surgery). In parallel, studies were conducted to study the side effects of low-power "soft lasers" of a general orientation.

As a result of research, it turned out that the effect of a low-power laser on the body can be useful. The basis of this phenomena is the penetration into the skin and tissue of laser radiation, which has a beneficial effect on the flow of metabolic processes in cells. As a result, the biological processes in the cells are normalized, the recovery time of the body is reduced, including after sports injuries, diseases, and in the postoperative period.

At present, lasers in medicine can be divided into lasers with high and low power. The first ones, the so-called "hard lasers", create a locally high temperature. Therefore, they are used in surgery, where thermal effects are applied to cuts of muscle and bone tissue, evaporation of fluids, drying and coagulation of blood, and welding of retina. The second - "soft lasers" - are used to treat a wide range of medical diseases, in cosmetology, in sports [1,2], etc. Soft laser radiation promotes "biostimulation" of cells and tissues, regeneration (wound healing) occurs faster. Laser light promotes the acceleration of cell metabolism, promotes the renewal of the cells themselves, tissues and capillaries, and nerve endings.

Low power Safe Laser (SL) devices are referred to as "soft lasers". They are developed by Hungarian experts and have the European quality certificate [1,2]. Laser light promotes the acceleration of cell metabolism, promotes the renewal of the cells themselves, tissues and capillaries, and nerve endings. Европейский сертификат качества [1,2]. Laser certificate promotes. Their technical characteristics are given in Table 1. In this paper, practical results of using devices of this type are given.

SL devices of different power (Table 1) are made on the basis of new technologies, the essence of which is that the high-energy laser beam, which is generally dangerous for the eyes, is transformed with the help of a special optical diffuser so that it becomes safe. The front part of the diffuser "reveals" the parallel beams of the laser, and the back part helps to ensure that the laser light becomes safe for focusing the pupil of the eye [1]. That is why SL devices do not need goggles, and the devices themselves are suitable for domestic (domestic) use.

SECTION 7. BIOMEDICAL LASER APPLICATIONS

It should be noted portability (small size) SL – it fits in the human hand. Whereas, for example, the DEKA gas medical laser [3] for the MONA LISA TOUCH procedures in aesthetic gynecology for the purpose of vaginal rejuvenation [4] is about the size of a modern refrigerator.

Table 1. Technical characteristics of devices Safe Laser (SL)

	SL30 – narrow specialization	SL150 – "family doctor"	SL500 Infra – deep penetration
Maximum power, mW	30	150	500
Wavelength, nm	660	660	808
Impact location and penetration depth	The surface of the skin, the surface of the nasal mucosa, the auditory passages	The surface of the skin, the surface of the nasal mucosa, the auditory passages (with a focusing attachment), biologically active points of the body. Up to 4 cm deep into the body. Cosmetic procedures (with an optical cap)	The surface of the skin, the surface of the skin, the mucous membrane of the nose, the auditory passages (with a focusing attachment), the biologically active points of the body. Up to 8 cm deep into the body, joints and ligaments. Cosmetic procedures (with an optical cap)
Power	2 finger type batteries AA 1,5 V	2 finger type batteries AA 1,5 V or accumulator	Accumulator
Time of impact on the point	Up to 5 min	Up to 3 min	1 min
Date of patent registration	08.16.2013	04.04.2014	07.31.2014

SL belongs to the new generation of “soft lasers”, thanks to which it became possible to use the laser not only in medical institutions and medical centers, hospitals and hospitals, but also at home for all family members, as well as for pets. This laser can be used by people of any gender (men and women) and age (adults, children, the elderly).

The SL is lightweight, does not require mains power, and therefore it can be taken on the road, on business trips and travels. It can be used to treat both acute processes and chronic diseases. Laser exposure stimulates the production of large amounts of collagen and elastin, slows the aging process of skin cells. Using special tips, SL helps to care for the skin [2], removing wrinkles and smoothing the skin of the face, neck, decollete, providing deep penetration of cosmetics. It can be used by every woman in household cosmetology as a means for facial care, and for the elimination of cosmetic defects. Pigment spots and capillary nets become less noticeable. Keloid scars are absorbed. Acne go away.

In combination with an antibacterial soap, a subcutaneous mite (Demodex) is removed.

Our personal experience with the SL150 is one year. We used it for ourselves, our relatives and friends, as well as for our beloved old 18-year-old cat. By the way, on it the effect of the device manifested itself most brightly. Due to his age and illness (diabetes), he already felt not very good, was quite sluggish, ate poorly, slept a lot, retired, hid in dark places, was inactive. We tried the laser on the cat - shone it in his ears and nose for 1 minute. What was our surprise when he not only did not run away, but sat patiently, his eyes closed, but he was purring loudly. After that, when we wanted to shine our nose, the cat approached, touched with its paw and demanded that he be the first to do the procedure. He began to eat better, was vigorous, cheerful, all the time bent around and tried to be visible, lay next to us, even began to climb under the ceiling to the wall and from there on top liked to watch what was happening below.

The problems that were solved this year, were solved or significantly decreased - these are neuropathy of the legs with diabetes mellitus (reduction of pain in the toes), stabilization of blood pressure, a significant reduction in the time of a runny nose, relaxation and, in combination with magnetic therapy, the complete disappearance of sinusitis, rapid pain relief in the calf muscles after cramps and physical exertion, relief of pain in the knee joints, in the small joints of the hands, relief of pain in the ear, cheilitis, cold limbs (legs). Prolonged use of the laser normalizes sleep. Blood circulation in the vessels of the brain and the heart improved, pains in the heart ceased to bother and headaches disappeared. Using a laser without attachment to a fresh hematoma for three minutes reduced it in half. The use of a laser with an optical attachment along the facial cosmetic lines using a cream allows you to quickly inject cosmetics into the skin - it becomes moisturized and smoother.

Of course, the given examples do not cover the whole range of SL possibilities for carrying out laser therapy at home.

Summarizing, we can say that Safe Laser is a convenient, easy-to-use, multifunctional, effective, painless and safe helper in solving many medical problems and in achieving the health of all members of every family in which it is available.

References

- [1] Safe Laser.hu - Certified Medical Laser, Hungary.
- [2] Biyovis.com.ua - Medical Lasers, Hungary.
- [3] DEKA carbon dioxide laser from DEKARMARTXIDE, Italy.
- [4] MONA LISA TOUCH - Vulvo-vaginal laser rejuvenation.

ALPHABETICAL LIST

Adamiak S.	98	Konoreva O.	25
Adamiv V.	22, 130	Korsunska N.	117
Andrushchak A.	108	Kosmyna M.	29
Ašmontas S.	102	Kost Ya.	108
Azhniuk Yu.	133	Krasnoshchekov Ye.	65
Banaś A.	154	Kul'ment'ev A.	69, 158
Banzak G.	51	Kul'ment'eva O.	158
Banzak O.	51	Kuts O.	105
Barlowski A.	83, 151	Kuzma M.	41, 72, 151
Bilynskyi I.	136	Lamikiz A.	74
Cebulski J.	154	Leshko R.	136
Čerškus A.	102	Lesyk D.	74
Cholewa M.	154	Lisiecki R.	22
Cieniek B.	86, 92, 98	Litvinuk L.	114
Ciupak P.	83, 151	Lopushansky V.	133
Czitrowszky A.	16	Loya V.	133
Czyż H.	83	Ludemann M.	19
Demyanyshyn N.	108	Lymarenko R.	54, 57, 60, 62, 114
Derkachov G.	145	Lytovchenko P.	25
Dzhemelinskyi V.	74	Malynych S.	130
Dziedzic A.	98	Martinez S.	74
Evtukh A.	139	Matyashovska B.	32
Fedorenko L.	139	Melnichuk L.	117
Feher A.	32	Melnichuk O.	117
Fekeshgazi I.	16	Mitsa V.	16, 32
Frolov S.	114	Mordyuk B.	74
Gailevicius D.	60, 62	Muravsky L.	105
Gamernyk R.	130	Mytsyk B.	108
Gomonnai A.	19, 133	Naumov V.	139
Gomonnai O.	19	Obrzut M.	154
Gradauskas J.	102	Opanasyuk A.	102
Gusev DSc. M.	120, 123, 126	Ostroukh A.	57
Hadzaman I.	148	Ovenko A.	123
Holomb R.	16, 32	Padlyak B.	22, 35
Hols'kyi V.	142	Pavlovskaya N.	77
Ilchenko S.	54	Pavlovskyy Yu.	25, 77, 80, 89
Jakubczyk D.	145	Peckus M.	60, 62
Jasinski T.	83, 151	Petricin I.	111
Khomenkova L.	117	Piekarski K.	145
Kindrat I.	22, 35	Pokutnyi S.	38
Kolwas K.	145	Poliak S.	120

Polishchuk A.	69	Sužiedėlis A.	102
Popovych V.	41	Švedas V.	102
Potera P.	41, 92, 98	Taranenko V.	54, 57, 60, 62, 65, 114
Prokopenko G.	74	Tartachnyk V.	25
Purlys V.	60, 62	Teslyuk I.	22
Rigo I.	16	Tkáč V.	32
Rogalska I.	86	Tur Yu.	95
Roman I.	19	Vaičiškauskas V.	102
Sagan P.	83	Venger Ye.	117
Sarzynska P.	83	Veres M.	16, 32
Schukin S.	114	Virt I.	86, 89, 92, 95, 98
Shekhovtsov A.	29	Wisz G.	92, 151
Shlapatska V.	25	Woźniak M.	145
Shopa Ya.	145	Yaparov V.	65
Šilėnas A.	102	Yegorov S.	120
Širmulis E.	102	Zahn D.	19, 133
Slivka A.	19	Zak D.	98
Staliunas K.	60, 62	Zakrevskyi O.	126
Stefaniuk I.	44, 86	Žalys O.	102
Stolyarchuk A.	148	Zawlik I.	154
Stolyarchuk I.	148	Zemlianski V.	120, 123, 126
Suchocki A.	47		

LASER TECHNOLOGIES. LASERS AND THEIR APPLICATION

FOR NOTES

[illegible]

Scientific Edition

**MATERIALS
OF INTERNATIONAL SCIENTIFIC
AND TECHNICAL CONFERENCE**

**LASER TECHNOLOGIES.
LASERS AND THEIR APPLICATION**

Computer typing and formatting
Yuriy Pavlovskyy

Sent to printing 10.05.17. Signed for printing 17.05.17.
Format 60'90/16. Offset paper. Times Font.
Number of copies 70. Printed sheets 10. Order №124.

Operational Center Print "SHVYDKODRUK"
st. D. Galician, 1, Drohobych, 82100
Tel. (0324) 41-08-90
e-mail: drukso@gmail.com